MODELLING OF BUOYANT FLOWS ASSOCIATED WITH LARGE AREA FIRES AND INDIRECT FREE CONVECTION

A thesis submitted to the University of Manchester
for the degree of Doctor of Philosophy
in the Faculty of Engineering and Physical Sciences

2013

Vasileios Tsitsopoulos
School of Mathematics

Contents

Word count 53029

List of Tables

List of Figures

The University of Manchester

Vasileios Tsitsopoulos
Doctor of Philosophy
Modelling of Buoyant Flows Associated with Large Area Fires and Indirect Free Convection
May 8, 2013

Experimental observations indicate the presence of attached, gravity induced, horizontal buoyant currents above large area fires. Their driving mechanism is indirect and resembles the one observed above heated horizontal plates. Classic plume modelling is satisfactory for providing information for the flow far from the source. In dealing with large areas and directing attention to the flow close to the source, the classic plume theory should fail because the radial pressure gradient that is responsible for the driving of the flow is squeezed in the long and thin classic plume assumption. For this we propose a new plume structure for the description of the buoyant flow above a circular region of large radius L as "The flow field must be divided into three regions. A region where the flow is predominantly horizontal and attached to the surface, a transition region from horizontal to vertical where separation of the attached current takes place, and a region where vertical flow is established and classic plume theory can be applied". A model for the description of the gross properties of the horizontal currents is developed under the term "horizontal plume". The modified Richardson number for the horizontal plume $\mathbf{a}$, being analogous to the radius of the large area, is studied asymptotically in the limit $\mathbf{a} \to \infty$ and second order uniformly valid semi-analytical solutions are obtained. The hot plate experiment was set up in order to test the model and facilitate its improvement. A chapter is dedicated to the data analysis coming from thermocouple readings and visualisation of the flow using particle image velocimetry.

In the remainder of this thesis two classic problems of laminar natural convection are revisited. That of the first order laminar boundary layer above an isothermal circular plate of radius a and the first order laminar boundary layer above the semi-infinite plate inclined to horizontal. In both cases allowances to variable property effects were made through the introduction of a nondimensional parameter λ_{T}, with its value set to zero implying the assumption of the Boussinesq approximation. For the circular plate, fourth order series solutions were obtained valid at the edge of the plate where the effects of λ_{T} and Prandtl number Pr are studied. Furthermore a finite difference scheme for the numerical solution of the nonsimilar partial integro-differential equation was developed using the Keller Box method and compared with results obtained from the commercial finite element software COMSOL Multiphysics 3.5a. For the semi-infinite plate, fourth order series approximations valid at the edge of the plate were obtained, while an extensive analysis for the effect of λ_{T}, Pr and inclination parameter σ was performed on the flow. Positions of the separation points when the inclination is negative ($\sigma < 0$) as a function of Pr and λ_{T} were recovered.

Declaration

No portion of the work referred to in the thesis has been submitted in support of an application for another degree or qualification of this or any other university or other institute of learning.

Copyright Statement

i. The author of this thesis (including any appendices and/or schedules to this thesis) owns certain copyright or related rights in it (the “Copyright”) and s/he has given The University of Manchester certain rights to use such Copyright, including for administrative purposes.

ii. Copies of this thesis, either in full or in extracts and whether in hard or electronic copy, may be made **only** in accordance with the Copyright, Designs and Patents Act 1988 (as amended) and regulations issued under it or, where appropriate, in accordance with licensing agreements which the University has from time to time. This page must form part of any such copies made.

iii. The ownership of certain Copyright, patents, designs, trade marks and other intellectual property (the “Intellectual Property”) and any reproductions of copyright works in the thesis, for example graphs and tables (“Reproductions”), which may be described in this thesis, may not be owned by the author and may be owned by third parties. Such Intellectual Property and Reproductions cannot and must not be made available for use without the prior written permission of the owner(s) of the relevant Intellectual Property and/or Reproductions.

iv. Further information on the conditions under which disclosure, publication and commercialisation of this thesis, the Copyright and any Intellectual Property and/or Reproductions described in it may take place is available in the University IP Policy (see http://documents.manchester.ac.uk/DocuInfo.aspx?DocID=487), in any relevant Thesis restriction declarations deposited in the University Library, The University Library’s regulations (see http://www.manchester.ac.uk/library/aboutus/regulations) and in The University’s Policy on Presentation of Theses.

Acknowledgements

I had the privilege of working under the supervision of Prof John Dold, so given the opportunity I would like to thank him for the knowledge he passed on to me, his guidance, help and support throughout. Also I would like to thank Brian Bibby and Jamie Severn from AWE for sponsoring this project and for showing understanding and patience. I am grateful to Dr Will Parnell for accepting to take on the role of the internal examiner and going through the final corrections of my thesis. In addition I would like to thank my external examiner Prof John Merkin for his useful comments during my viva, and for making it an enjoyable process.

Through the Manchester ‘green years’, I was lucky to get the help of Prof Peter Eccles who allowed me to continue in the MMath, Prof Frano̧ise Tisseur who believed in me and suggested me for the MSc and Dr Joel Daou during the brief but excellent collaboration in my MSc dissertation and through his support with my PhD application.

I am filled with gratitude towards Dr I.B. GlouGlou for sponsoring me when the account ran dry, for looking after our little monster and for being patient[1] while writing this thesis. Finally a big thank to all the fantastic people I had the opportunity to share my office starting with Dr Dmitry Yumashev, Dr Haines, Dr Kwan, Dr Rudi Borsdorf, Dr Princess Kathy, La hola hola guapa Citla, and my beloved friend Imran Khan.

---

[1] That is kind of an exaggeration

To Leonardo Jack

&

Nicola

Chapter 1

Introduction

1.1 Prologue

A minimalistic but hopefully concise presentation of the basic physical laws dictating the motion of gases and fluids commences this thesis. Once the theoretical background and the mathematical description of the fluid flow have been established,a brief discussion follows regarding turbulence and its modelling, while the main part of this opening chapter is devoted to turbulent free convective flows and specifically on round plumes. By no means does this brief introductory section claim to cover the whole field of classic plume theory, instead the effort is directed towards a description of the necessary theoretical tools, as well as the introduction of the physical assumptions incorporated within the modelling of such complex turbulent flows. As it will be shown in some detail embracement of these assumptions result into a relatively simple (a system of three first order coupled differential equations) but nonetheless a versatile theoretical model, as its longevity and applications demonstrate.

As a consequence completeness is ensured regarding the fundamentals of classic plume theory. Moreover it is expected that the reader will become familiar with the principles and the philosophy of this type of turbulence modelling, which in turn allows a smooth transition to the following chapter where the derivation of the new theoretical model for the description of buoyant flows above large area fires is analytically given. That is owed to the fact that the style of modelling resembles the one of the classic round plume as the same ideas are re-employed.

The chapter concludes with a synopsis of the remaining six chapters of this thesis.

Closing, it must be emphasised that due to the nature of this work and the number of different subject matters it visits, additional introductory material is provided throughout when necessary.

1.2 The governing equations of fluid motion

Mathematically a fluid motion is considered completely determined once the velocity distribution $\vec{u} = (u(t, x_1, x_2, x_3), v(t, x_1, x_2, x_3), w(t, x_1, x_2, x_3))$, the density $\rho(t, x_1, x_2, x_3)$, the pressure $P(t, x_1, x_2, x_3)$ and the temperature field $T(t, x_1, x_2, x_3)$ are known for every point (x_1, x_2, x_3) in space at every time t. Therefore one is dealing with six unknowns and for that reason six equations are required to mathematically fully describe the problem.

The governing equations of fluid motion are due to the basic principles of conservation of mass, momentum (Newton's law) and energy (first law of thermodynamics), in addition to the invoking of the following assumptions:

(a) Macroscopic description of the flow - Incorporating the continuum hypothesis.

Enclosed by the continuum mechanics hypothesis lies the assumption that given a volume of fluid, every point is associated with a fluid particle, and that the volume can be thought of consisting by a continuous aggregate of fluid particles [95]. The terminology of a fluid particle is used to describe a small volume element part of the moving fluid exhibiting all the macroscopic properties of the fluid in a sense that should be regarded small enough such that variations of macroscopic quantities over its volume may be neglected. On the other hand, it should be large enough so that microscopic (molecular level -Brownian motion) variations are insignificant. Given a characteristic length of the flow under consideration say L and defining the molecular mean free path (the average distance a molecule travels before colliding with another molecule) as ω, then for the fluid particle with a characteristic lengthscale l the following must hold:

$$\omega \ll \ l \ll L. \tag{1.1}$$

In that way it is ensured that the fluid particle contains a great number of molecules but is still very small when compared to the volume of the fluid considered. A criterion for the suitability of the continuum hypothesis is given by the Knudsen number Kn, defined as

$$\mathrm{Kn} = \frac{\omega}{\mathrm{L}}, \tag{1.2}$$

under which the condition Kn $\ll 1$, must be satisfied for the continuum approach to be valid.

(*b*) The principle of local thermodynamic equilibrium.

Thermodynamical results expressed by the equations of state and valid for reversible processes (a fluid at rest), also hold for non-equilibrium irreversible (due to the energy dissipation introduced by viscosity and heat conduction) processes, caused by the moving fluid [98],[88][4]. In addition the local thermodynamic state is described by the state variables of pressure and temperature [80].

A detailed derivation of the fundamental equations of fluid flow from first principles can be found in the majority of fluid mechanics texts, so it was decided to put preference in a compact presentation which should be regarded sufficient for the purposes of this work, without unnecessarily extending the length of this otherwise introductory section. The interested reader can always recourse to excellent texts such as [51], [98], [80], [88], [4], and [95], to name just a few .

In Eulerian formalism, the fundamental equations for viscous, heat conducting fluid, the equation which expresses the conservation of matter in suffix notation is given as

$$\frac{\partial \rho}{\partial t} + \frac{\partial (\rho u_j)}{\partial x_j} = 0. \tag{1.3}$$

In what concerns the conservation of momentum from Newton's second law, the acceleration of a particle and the forces per unit volume are related as

$$\rho \frac{D\vec{u}}{Dt} = \Sigma \vec{F} = \vec{f} + \vec{f_s}. \tag{1.4a}$$

On the left hand side (l.h.s) the substantive derivative [1] of the velocity, while on the right hand side (r.h.s) the total force per unit volume $\Sigma\vec{F}$ is split into body forces $\vec{f}$ and surface forces $\vec{f_s}$. The only body force (acting on the whole mass) considered within the framework of this thesis is due to the influence of the gravitational field (i.e. $\rho\vec{g}$), where $\vec{g}$ is the vector for the gravity acceleration. Surface forces on the other

---

[1] $\frac{D}{Dt} = \frac{\partial}{\partial t} + (\vec{u} \cdot \nabla)$

hand are the external shear and pressure stresses applied on the surface of the element caused by the motion of the fluid particles. The total surface force can be shown to be given as [98]

$$\vec{f_s} = \frac{\partial \sigma_{ij}}{\partial x_j}, \tag{1.4b}$$

where σ_{ij} is the symmetric stress tensor. The first step in obtaining the general form of the stress tensor is by noticing that when the fluid is at rest, the shear stresses must vanish while the normal stresses have to be equal to the hydrostatic pressure. That can be expressed compactly as

$$\sigma_{ij} = -P\delta_{ij} \quad \text{when} \quad \vec{u} = \vec{0}, \tag{1.4c}$$

and δ_{ij} is the Kronecker delta ($\delta_{ij} = 1$ if $i = j$ and $\delta_{ij} = 0$ if $i \neq j$). Thus it should be expected that this property has to somehow be incorporated in the construction of the stress tensor. A way of moving forward is by decomposing the stress tensor as

$$\sigma_{ij} = \tau_{ij} - P\delta_{ij}, \tag{1.4d}$$

with τ_{ij} being the viscous/friction stress tensor having the same principal axes as σ_{ij}. In order to satisfy the hydrostatic equilibrium condition, the analytical form of the viscous stress tensor is formulated under the requirement that it vanishes when the velocity is zero. Additional postulates are necessary before proceeding further, firstly by resembling results coming from the linear elasticity theory, a linear relationship between the components of the viscous stress tensor τ_{ij} and the rate of deformation tensor e_{ij}[2] (Newtonian fluid), is suggested [88], in addition it is further presumed that the fluid is isotropic [98]. The isotropy assumption implies that the relationship between the viscous stress tensor and the tensor of rate of deformation are independent of coordinate system rotation and axis exchange [80].

The hypothesis of a linear dependence between the viscous stress and the rate of deformation tensors, provides an explicit description of the viscous stress tensor in terms of the velocity. More accurately the viscous stress tensor can be expressed as a linear combination of the velocity gradients $\frac{\partial u_i}{\partial x_j}$,$\frac{\partial u_j}{\partial x_i}$ and $\frac{\partial u_l}{\partial x_l}$ [51]. The following ansatz is suggested

$$\tau_{ij} = \mu(\frac{\partial u_i}{\partial x_j} + \frac{\partial u_j}{\partial x_i}) + \lambda\delta_{ij}\frac{\partial u_l}{\partial x_l} = 2\mu e_{ij} + \lambda\, e_{ll}\delta_{ij}, \tag{1.4e}$$

---

[2] For the rate of deformation tensor the following hold $e_{ij} = \frac{1}{2}(u_{i,j} + u_{j,i}) = \frac{1}{2}(\frac{\partial u_i}{\partial x_j} + \frac{\partial u_j}{\partial x_i})$, in addition $e_{ii} = u_{i,i} = \nabla \cdot \vec{u}$, for details see [88].

where μ is the viscosity [kg/m s], λ is the second viscosity sometimes termed as bulk viscosity due to its association with volume expansion. In that way the stress tensor σ_{ij} takes the following form

$$\sigma_{ij} = -P\delta_{ij} + 2\mu e_{ij} + \lambda\, e_{ll}\delta_{ij}. \tag{1.4f}$$

Taking the trace of the stress tensor

$$\mathrm{tr}(\sigma_{ij}) = \sigma_{11} + \sigma_{22} + \sigma_{33} = -3P + (2\mu + 3\lambda)\nabla \cdot \vec{u}, \tag{1.5a}$$

and defining the mechanical pressure as the negative one third of the trace of the stress tensor so as to obtain

$$\bar{P} = -\frac{\mathrm{tr}(\sigma_{ij})}{3} = P - \left(\frac{2\mu}{3} + \lambda\right)\nabla \cdot \vec{u}, \tag{1.5b}$$

or

$$\bar{P} = -\frac{1}{3}\sigma_{ii} = P - \left(\frac{2\mu}{3} + \lambda\right)e_{ii}. \tag{1.5c}$$

It is clear that there is a deviation between the average pressure due to the normal stresses for a viscous fluid from the thermodynamic pressure, by the term $(2\mu/3 + \lambda)e_{ii}$ [98]. This deviation vanishes when the flow is incompressible since $e_{ii} = 0$, but the same argument cannot be used when compressibility effects are taken into consideration. A direct way to overcome this anomaly comes by addressing the role of the viscosity terms, which is exactly what Stokes did in his hypothesis. According to Stokes hypothesis by setting

$$\lambda = -\frac{2\mu}{3}, \tag{1.6}$$

the problem is resolved. In that way

$$P = \frac{1}{3}\sigma_{ii} \tag{1.7}$$

and τ_{ij} is the deviator given as

$$\tau_{ij} = \mu\Big(\big(\frac{\partial u_j}{\partial x_i} + \frac{\partial u_i}{\partial x_j}\big) - \frac{2}{3}\delta_{ij}\frac{\partial u_l}{\partial x_l}\Big). \tag{1.8}$$

The validity of stokes hypothesis and the role of the secondary viscosity term λ is still an open discussion. In [51] (sections 16 and 49) the viscosity coefficients are both shown to be positive so that $\lambda > 0$ and $\mu > 0$, something that contradicts with the Stokes hypothesis, giving a negative secondary viscosity. Furthermore, as already mentioned, the second viscosity is associated to processes resulting to volume change i.e (compression-expansion). If these processes are rapid so that departures from equilibrium are short lived, the order of magnitude of the viscosity coefficients is the same which is normally the case. On the other hand when the restoration to equilibrium is slow, processes are slow the significant dissipation of energy is attributed to the second viscosity λ and is independent to μ, thus the second viscosity is noticeably larger [51]. As described in detail in [51] (section 81), the second viscosity is shown to be frequency dependent. For example in the case of expansion or compression due to to a sound wave, λ depends on the frequency of the wave. Nevertheless the momentum equations resulting after making the Stokes hypothesis have been shown to provide a good description of the actual physical processes and will be presumed within this work. In addition it must be mentioned that under the the boundary layer approximation the second viscosity and the ambiguity it introduces cease to exist since all terms containing the second viscosity can be neglected [80].

Returning to equation (1.4a), with the aid of equations (1.4b), (1.4d) and (1.8), to obtain the famous Navier-Stokes equations written compactly in suffix notation as

$$\frac{\partial(\rho u_i)}{\partial t} + \frac{\partial(\rho u_j u_i)}{\partial x_j} = f_i - \frac{\partial P}{\partial x_i} + \frac{\partial \tau_{ij}}{\partial x_j}. \tag{1.9}$$

and the viscous stress tensor is given as in equation (1.8).

Turning attention to the final conservation principle: that of energy, the first law of thermodynamics [68] states that the amount of change in the internal energy ΔU, is due to the work done W and the heat Q transferred to the system. In analogy, the continuum mechanical (fluid particle) equivalent of the first law of thermodynamics can be shown [88] to be given as

$$\rho \frac{De}{Dt} = -\frac{\partial q_i}{\partial x_i} + \sigma_{ij} \frac{\partial u_i}{\partial x_j}, \tag{1.10a}$$

where e is the internal energy per unit mass, while q_i the heat flux vector obeying Fourier's law and given as

$$q_i = -\kappa \frac{\partial T}{\partial x_i}, \tag{1.10b}$$

with κ [J/m s K], being the thermal conductivity. The minus sign corresponds to the fact that energy flux is directed from high temperatures to lower ones. Introduction of the viscous stress tensor i.e $\sigma_{ij} = -P\delta_{ij} + \tau_{ij}$ in equation (1.10a), results in

$$\rho \frac{De}{Dt} = -\frac{\partial q_i}{\partial x_i} + \tau_{ij} \frac{\partial u_i}{\partial x_j} - P \frac{\partial u_i}{\partial x_i}, \tag{1.10c}$$

furthermore by restating the continuity equation as

$$\frac{D\rho}{Dt} + \rho \frac{\partial u_i}{\partial x_i} = 0, \tag{1.10d}$$

gives

$$-P \frac{\partial u_i}{\partial x_i} = -\frac{P}{\rho} \frac{D\rho}{Dt} = -\rho \frac{D}{Dt}\Big(\frac{P}{\rho}\Big) + \frac{DP}{Dt}. \tag{1.10e}$$

Use of equation (1.10e) into (1.10c) finally results

$$\rho \frac{D}{Dt}\Big(e + \frac{p}{\rho}\Big) = -\frac{\partial q_i}{\partial x_i} + \tau_{ij} \frac{\partial u_i}{\partial x_j} + \frac{Dp}{Dt}. \tag{1.10f}$$

The enthalpy is defined as $h = e + P/\rho$, further by utilizing the thermodynamic property [98],[80] given as

$$\frac{Dh}{Dt} = c_{\mathrm{p}} \frac{DT}{Dt} + \frac{1 - \beta T}{\rho} \frac{Dp}{Dt}, \tag{1.10g}$$

with c_{p} [J/kg K], being the isobaric specific heat capacity, while

$$\beta = -\frac{1}{\rho} \left(\frac{\partial \rho}{\partial T} \right)_P, \tag{1.11}$$

is the thermal expansion coefficient, then equation (1.10f) takes the following form

$$\rho c_{\mathrm{p}} \frac{DT}{Dt} = -\frac{\partial}{\partial x_i} \left(-\kappa \frac{\partial T}{\partial x_i} \right) + \tau_{ij} \frac{\partial u_i}{\partial x_j} + \beta T \frac{DP}{Dt}. \tag{1.12}$$

The term $\tau_{ij} \partial u_i / \partial x_j$ is commonly called dissipation Φ, and expresses the rate of dissipation of mechanical energy per unit mass due to shear viscosity[4].

Up to this point five equations have been presented leaving room for one more (six unknowns), so that the general state of a moving fluid can be determined. The final equation is given by means of an equation of state

$$f(P, \rho, T) = 0, \tag{1.13}$$

where the functional form depends on the type of fluid. Collecting the fluid motion can be fully described by equations (1.3),(1.9),(1.12) and (1.13), subject to suitable boundary conditions.

1.2.1 Further discussion

When dealing with gases it is customary to employ the ideal gas law stated as

$$P = \rho R T, \tag{1.14}$$

where R is a gas constant. The ideal gas law is a reasonable approximation for most common gases and is the assumption made within the framework of this thesis. Additionally, employment of the ideal gas law introduces further simplifications within the governing equations. In particular the following holds for the gas expansion coefficient $\beta T = 1$, so that from equation (1.10g), $h = c_\mathrm{p} T$ is obtained. As a result the equation of conservation of energy changes to

$$\rho c_\mathrm{p} \frac{DT}{Dt} = -\frac{\partial}{\partial x_i}\left(-\kappa \frac{\partial T}{\partial x_i}\right) + \tau_{ij}\frac{\partial u_i}{\partial x_j} + \frac{DP}{Dt}. \tag{1.15}$$

Furthermore when the characteristic velocities are small when compared to speed of sound (which is the case here, since the essential concern is towards buoyancy driven flows) the pressure term DP/Dt contained on the r.h.s equation of can be neglected[3]. This is because the pressure variations are so small, leaving density and other thermodynamic quantities almost unaffected. In the context of what will follow, and since temperature variations are introduced to the flow, the density as well as the transport properties μ and κ are all assumed to be independent of pressure P. Moreover the secondary thermodynamic property c_p is always assumed to be constant.

Wrapping up, as a general note it must be mentioned that when there is no temperature variations instilled into the flow and the Mach number Ma is small, then the equation of state changes to $\rho = constant$. Under this assumption the governing set of equations can be simplified, that is because the coupling between momentum and energy equations is lost (that is not the case when $\rho = \rho(T)$ even if the flow can still be treated as incompressible), the flow is isothermal, thus the energy equation becomes superfluous. Thus the number of unknowns reduce to four (i.e. the three component of the velocity vector $\vec{u}$ and the pressure P), so that the continuity equation and the Navier-Stokes equation are sufficient for the description of the flow.

---

[3] Generally a criterion for that condition can be obtained by the value of the Mach number Ma defined as

$$\mathrm{Ma} = \frac{\mathrm{U}}{\mathrm{U_s}}, \tag{1.16}$$

with U being the characteristic velocity of the flow, while U_s the speed of sound for the fluid under consideration.

1.3 A brief discussion on Turbulence Modelling

Turbulence modelling is a vast topic so that a detailed discussion is forbidding. Nevertheless, since turbulent plumes and their modelling will occupy a significant portion of this work, it is advantageous to introduce some fundamental material regarding turbulence and turbulence modelling, with the aim to clarify the ideas and the philosophy behind the route of the modelling followed. Even though the notion of turbulence is clear even to the non specialist, trying to provide an accurate description of it seems to be a harder task. A detailed definition is given in the textbook of Hinze [30], but for our purposes we shall adopt the more compact one coming from Tritton: [95] '*Turbulence is a state of continuous instability*'.

Theoretically, turbulence is a continuum phenomenon so that the fundamental equations of fluid flow presented in the previous section, contain all the physics of a given turbulent flow. The nonlinearity within the Navier-Stokes equations and the fact that a turbulent flow is rotational, three dimensional and a time dependent phenomenon [99], generates huge difficulties. Since turbulence is deterministic [53],[95], it means that there is no prior difficulty in attempting a direct numerical simulation (DNS) to the unsteady three dimensional governing set of equations. However, turbulence can be thought of as consisting of a continuous spectrum of scales that the numerical solution needs to resolve. These length scales/eddies, represent the order of magnitude of the distances that the velocity varies appreciably [51], and in a turbulent flow the smaller eddies (whose order of magnitude is defined by Kolmogorov dissipation scale [53]), even though larger than the mean free path, are much smaller than larger ones whose lengthscale is of the order of a characteristic length of the flow under consideration (i.e. in the case of flow past a body the large eddies are of the same order as the body). Even with the recent advances in computing resources, and the re-emerging of parallel computing, application of DNS to most real life engineering applications of interest remain computationally intractable.

Since a complete resolution of a turbulent flow is still some way ahead, the ultimate question within turbulence modelling is how much detail is required so as to obtain the answers asked. Further it is natural to expect that there must be an analogy between detail sacrificed and the simplicity of the resulting model. Hence depending on ones needs and the physical difficulties posed by the turbulent flow studied, a careful balance between the above arguments needs taking into consideration. An advanced and fashionable technique in turbulence modelling is the Large Eddy Simulation (LES). It is based on the fact that the large eddies form the basis of a turbulent flow and are responsible for the transfer of heat and momentum which is usually of the primary interest and the energy cascade process in turbulent flows (continuous transfer of energy form large to small eddies). Large eddies are almost unaffected by viscosity so that it is safe to assume that the dissipation of energy is independent of the large eddies. The dissipation of energy is attributed to the smallest eddies which transform kinetic energy to heat. Therefore within the LES technique, the following are incorporated: i) The largest eddies are separated from the small (small frequencies from large respectively with a use of a filter); ii) Approximations are used for the energy exchanges among the small eddies which are not explicitly simulated.

Even so, LES is computationally expensive so the most common approach in turbulence modelling is to consider only statistical properties of the flowfield, and is the one that will be adopted in this work. Firstly introduced by Reynolds in 1895, the flow quantities are decomposed as the sum of mean/average and a fluctuating part.

$$u_i = \bar{u}_i + \acute{u}_i, \quad P = \bar{P} + \acute{P}, \quad T = \bar{T} + \acute{T}, \quad \text{and} \quad \rho = \bar{\rho} + \acute{\rho}. \tag{1.17}$$

The average is formed as a time average at a fixed point in space, thus for example [80], [93]

$$\bar{u}_i = \lim_{\tau \to \infty} \frac{1}{\tau} \int_{t_0}^{t_0+\tau} u_i \mathrm{d}t. \tag{1.18}$$

The limit $\tau \to \infty$, in the definition, implies that the averaging process lasts for a sufficiently long time τ, so that the average is independent of time. In this way the time averages of the fluctuating parts are zero by definition, so that $\bar{\acute{u}}_i = 0$, $\bar{\acute{P}} = 0$, etc. Therefore by assuming that the mean flow is independent of time (steady turbulent flow), the procedure to obtain Reynolds averaged equations is not hard and is a two step procedure. This starts with the governing equations for a fluid flow and the decomposition of the flow variables into their mean and fluctuating parts, followed by the time averaging procedure of the resulting equations (for detailed analysis see [80],[16],[99]).

The resulting equations contain additional unknown terms, known as Reynolds stresses, and thus the turbulence closure problem appears (i.e. coming up with additional equations for all the unknowns). Among the most popular models are the mixing length or algebraic models and the two-equations models (two additional transport differential equations are added). Focusing on turbulent free shear flows such as plumes and jets, since there are no walls, the viscosity effects are neglected because turbulent friction is much larger than the viscous friction, in addition free shear flow are slender and this results in a simplified form in the momentum equation [80]. Finally within their modelling, the turbulent closure is circumvented by making an entrainment hypothesis [52] which will be defined in the next section.

1.4 Classic Plume theory

The time averaged behaviour of low Mach number turbulent vertical convection currents, rising from maintained circular sources of buoyancy, in a surrounding environment that is still and of uniform density, is the main theme occupying this section. Depending on the manner in which buoyancy is introduced from the source in the ambient, a first categorisation of these flows can be made. The terminology of turbulent Plumes is used to describe the free convective flows induced under gravity, by a continuous density (or equivalently a temperature) contrast between the source (boundary) and the surrounding environment. When density differences are introduced in a discrete manner then the term ‘Thermal’ is adopted for their description [96]. Within the rest of this work the focus will solely lie on turbulent round plumes.

Density differences under gravitational influence give rise to a buoyancy force B which is responsible for the driving of the flow. With buoyancy being one of the main forces of our planet, plumes can be observed in a plethora of geophysical flows ranging from wildfires, volcanic eruptions and cumulus clouds to mixing in the oceans, while in the man-made environment they are encountered on a daily basis, with the most common example above chimneys. Plumes have been at the centre of intense scientific interest coming from different disciplines of science including that of meteorology, geophysics, applied mathematics, environmental and fire engineering.

The first attempts at a theoretical and experimental description of plumes dates back to Zeldovich [102] (1937) and Schmidt [81] (1941). Schmidt, by observing the conical shape of the vertical turbulent gravitational currents above point and line sources, assumed that there must be a geometrical and mechanical similarity so that the horizontal turbulent transfer of heat and momentum must balance vertical transfer by convection. His analysis was based on a mixing-length analysis hypothesis. A proposal that still dominates classic plume theory came from Taylor [92] (1945) in his work 'on the dynamics of a mass of hot gas rising in the air'. He suggested that '*The effect of turbulent mixing is represented by an inflow of surrounding air through the outer surface of the heated zone at a velocity* α *times the velocity of the heated gas.'* and he also showed that his analysis was in a good agreement with the work of Schmidt. Self similarity analysis of the turbulent buoyant plume flow came by Batchelor (1954) in his famous lecture on heat convection and buoyancy effects in fluids [3]. He went on to define the heat flux in terms of weight deficit $B = \rho_\mathrm{e} F$ as

$$Q = \frac{\mathrm{c_p} \rho_\mathrm{e} \mathrm{T_e}}{g} F, \tag{1.19}$$

where ρ_e and T_e correspond to environmental density and temperature, g is the acceleration due to gravity, while F has units of [(length)^4/(time)^3]. Based on dimensional analysis and neglecting viscosity and conductive effects since the flow is fully turbulent and self similarity is expected to be valid far from the source, he obtained the average velocity and temperature profiles

$$\bar{w} = F^{1/3}\, z^{-1/3} \times f_1(\xi), \tag{1.20a}$$

$$g\,\overline{\frac{T - T_\mathrm{e}}{T_\mathrm{e}}} = g\,\overline{\frac{\rho_\mathrm{e} - \rho}{\rho_\mathrm{e}}} = F^{2/3}\, z^{-5/3} \times f_2(\xi), \tag{1.20b}$$

$$b = \alpha z, \tag{1.20c}$$

with b the radius of the plume and $\xi = r/b$ the similarity variable. The functional form of $f_1(\xi)$ and $f_2(\xi)$ can be determined either from more detailed theories or directly from experimental measurements [97].

The first breakthrough in describing the time averaged behaviour of these vertical turbulent gravity currents came in 1956 with the publication of the model of Morton Taylor and Turner [63], frequently termed as MTT. It is based on an *ideal* point source (resulting in an axissymmetric flow) of buoyancy only, and the central point in its formulation is the entrainment hypothesis that Taylor had suggested earlier on. According to this assumption the complex process of mixing or engulfment of fresh ambient fluid within the vertical current is described as follows *'the rate at which fluid is entrained into plumes is taken to be proportional to vertical velocity on the axis of the plume'*. This hypothesis translates within the model as

$$u_{\mathrm{e}} = \alpha w \quad \text{and} \quad \alpha \simeq 0.1, \tag{1.21}$$

where u_{e} is the radial entrainment velocity, α is the entrainment coefficient and w is the vertical velocity of the plume at that height. The MTT model relies on two further assumptions; that of the Boussinesq approximation (i.e. [95] '*Variations of all fluid properties are completely ignored with the exception of the density, that its variation is taken under consideration only when it gives rise to gravitational force'*) and that of self similar profiles for the velocity and buoyancy force. Prior to the work of MTT was the plume model of Priestley and Ball [70] referred to as PB. While the classic formulation of MTT is based on the flux equations of mass, momentum, and heat, the PB model uses the flux of kinetic energy in place of the mass equation, while the closure in PB is an entrainment assumption based on Reynolds stress within the kinetic energy equation. A discussion concerning the differences between these two models is given by Morton in [61] and [63].

Given that the MTT plume model carries the Boussinesq approximation, its applicability is questionable in cases where there are large density differences between the fluid within the plume and the ambient, as for example in plumes created above a fire, or a volcanic thermal. It was in 1961, that the experimental work of Ricou and Spalding [72] showed that turbulent entrainment is dependent on the density contrast between the plume and ambient. Analytically they showed

$$u_e = \alpha \Big(\frac{\rho}{\rho_{\mathrm{e}}}\Big)^n, \quad \text{with} \quad n = \frac{1}{2}. \tag{1.22}$$

This became the most popular entrainment model, widely used until today (recent advances concerning the entrainment are given in [39]), and in what follows we shall refer to it as the R-S entrainment model. It was first applied in 1965 by Morton in [60], in his discussion concerning the modelling of fire plumes. Depending therefore on the adopted entrainment hypothesis, turbulent plumes can be categorised into Boussinesq and non-Boussinesq plumes. The first extensive study of non-Boussinesq plumes is due to Rooney and Linden [73], where similarity solution is obtained for the non-Boussinesq plumes.

Turning attention on the derivation of the MTT model, it should be emphasised that even though the flow is turbulent, it is assumed that it can adequately be described by the mean flow variables alone. Moreover the ambient will be assumed to be still and unstratified. Stratification effects can be incorporated within the MTT model and a detailed review is given by [40]. Additionally when the environment is not still but is characterised by a mean horizontal wind velocity, once more the principles of the MTT model can be applied [87],[9],[10].

In cylindrical polar coordinates the continuity of mass is expressed as

$$\frac{\partial}{\partial r}(r\bar{u}\bar{\rho}^j) + \frac{\partial}{\partial z}(r\bar{w}\bar{\rho}^j) = 0. \tag{1.23a}$$

Here superscript j is introduced so as to allow departures from the Boussinesq approximation. Therefore $j = 0$ corresponds to Boussinesq plumes while $j = 1$ implies non-Boussinesq plumes. Further assuming hydrostatic pressure distribution and that $\partial P/\partial z \gg \partial P/\partial r$, which implies that the plume is long and thin so that the pressure is constant along a cross section of a plume, then the momentum equation is given as

$$\frac{\partial}{\partial r}(r\bar{\rho}^j\bar{u}\bar{w}) + \frac{\partial}{\partial z}(r\bar{\rho}^j\bar{w}^2) = rg(\bar{\rho} - \rho_{\mathrm{e}}). \tag{1.23b}$$

When the Boussinesq approximation is adopted, conservation of energy implies conservation of buoyancy flux [17],[39], thus

$$\frac{\partial}{\partial r}(r\bar{u}\grave{g}) + \frac{\partial}{\partial z}(r\bar{w}\grave{g}) = 0, \tag{1.23c}$$

where $\grave{g}$ is the reduced gravity given by,

$$\grave{g} = g\frac{\rho_{\mathrm{e}} - \bar{\rho}}{\rho_{\mathrm{e}}}.$$

The above statement is not valid when the Boussinesq approximation is abandoned. Rooney and Linden [73], by considering the conservation of enthalpy along the plume (similarly to [20]), found that the volume flux is conserved. This allowed them to conclude that the density deficiency flux is conserved, but not the buoyancy flux. Therefore by considering the conservation of density flux

$$\frac{\partial}{\partial r}(r\bar{u}(\rho_{\mathrm{e}} - \bar{\rho})) + \frac{\partial}{\partial z}(r\bar{w}(\rho_{\mathrm{e}} - \bar{\rho})) = 0, \tag{1.23d}$$

a valid equation for the non-Boussinesq case is obtained.

By integrating radially the governing equations (1.23) from $r = 0$ to $r = \infty$, the continuity equation results in

$$\frac{\mathrm{d}}{\mathrm{d}z}\int_0^\infty r\bar{\rho}^j\bar{w}\mathrm{d}r = -r\bar{u}\bar{\rho}^j|_\infty. \tag{1.24}$$

If b is the radius of the plume, then for $b < r < \infty$ the velocity $\bar{w}$ can be neglected, so that integration of the continuity equation from b to ∞ results in $r\bar{\rho}^j\bar{u}|_{r=b} = r\bar{\rho}^j\bar{u}|_{r=\infty}$. Therefore

$$\frac{\mathrm{d}}{\mathrm{d}z}\int_0^\infty r\bar{\rho}^j\bar{w}\mathrm{d}r = -r\bar{u}\bar{\rho}^j|_b = b\rho_\mathrm{e}u_\mathrm{e}, \tag{1.25a}$$

where $u_\mathrm{e} = -u_b$. The same procedure applied to momentum and buoyancy flux results in

$$\frac{\mathrm{d}}{\mathrm{d}z}\int_0^\infty r\bar{\rho}^j\bar{w}^2\mathrm{d}r = \int_0^\infty rg(\bar{\rho} - \rho_\mathrm{e})\mathrm{d}r, \tag{1.25b}$$

$$\frac{\mathrm{d}}{\mathrm{d}z}\int_0^\infty r\bar{u}\grave{g}\mathrm{d}r = 0. \tag{1.25c}$$

Finally for the density deficiency flux, after integration it is found that

$$\frac{\mathrm{d}}{\mathrm{d}z}\int_0^\infty r\bar{w}(\rho_\mathrm{e} - \rho)\mathrm{d}r = 0. \tag{1.25d}$$

Experimental data indicate that the mean velocity and temperature distributions are Gaussian, but it is customary due to its simplicity to adopt a 'top hat' formalism. Top hat shape functions result in properties having one constant value within a cross section of the plume and another outside it [97]. For example a top hat distribution of density and vertical velocity would take the forms

$$\bar{\rho}(r,z) = \begin{cases} \rho(z) & \text{if } r \leq b(z), \\ \rho_\mathrm{e} & \text{if } r > b \end{cases}, \quad \bar{w}(r,z) = \begin{cases} w(z) & \text{if } r \leq b(z), \\ 0 & \text{if } r > b(z) \end{cases}. \tag{1.26}$$

We can now define the top hat profiles as

$$\rho^j wb^2 = 2\int_0^\infty r\bar{\rho}^j\bar{w}\mathrm{d}r, \quad \rho^j w^2b^2 = 2\int_0^\infty r\bar{\rho}^j\bar{w}^2\mathrm{d}r, \quad w(\rho_\mathrm{e}-\rho)b^2 = 2\int_0^\infty r\bar{w}(\rho_\mathrm{e}-\rho)\mathrm{d}r$$

$$g\frac{\rho - \rho_\mathrm{e}}{\rho_\mathrm{e}}wb^2 = 2\int_0^\infty r\bar{w}\grave{g}\mathrm{d}r \quad \text{and} \quad g(\rho - \rho_\mathrm{e})b^2 = 2\int_0^\infty rg(\bar{\rho} - \rho_\mathrm{e})\mathrm{d}r. \tag{1.27}$$

Collecting terms, the following set of differential equations are obtained

$$\frac{\mathrm{d}}{\mathrm{d}z}[\rho^j wb^2] = 2b\rho_\mathrm{e}u_\mathrm{e}, \tag{1.28a}$$

$$\frac{\mathrm{d}}{\mathrm{d}z}[\rho^j w^2b^2] = g(\rho - \rho_\mathrm{e})b^2, \tag{1.28b}$$

$$\frac{\mathrm{d}}{\mathrm{d}z}\left[gw\frac{(\rho_\mathrm{e}-\rho)}{\rho_\mathrm{e}}b^2\right]=0, \tag{1.28c}$$

$$\frac{\mathrm{d}}{\mathrm{d}z}[w(\rho_\mathrm{e}-\rho)b^2]=0. \tag{1.28d}$$

It can be seen that in terms of top hat formalism equations (1.28c) and (1.28d) are equivalent. Thus conservation of the density deficit is equivalent to the conservation of

$$B=\pi g(1-x)wb^2, \quad \text{with} \quad x=\frac{\rho}{\rho_\mathrm{e}}. \tag{1.29}$$

which has units of buoyancy flux. Before proceeding further it should be recalled that the entrainment hypothesis for Boussinesq and non-Boussinesq plumes is given as

$$u_\mathrm{e}=\begin{cases}\alpha w & \text{Boussinesq plumes ,}\\ \alpha\sqrt{x}w & \text{non-Boussinesq plumes.}\end{cases} \tag{1.30}$$

Therefore the entrainment method is now compactly written as

$$u_\mathrm{e}=\alpha x^{j/2}w. \tag{1.31}$$

In this way $j=0$ corresponds to MTT while $j=1$ is the R-S entrainment model.

Following Michaux & Vauquelin [58] and Bremer & Hunt [7], [32], we shall proceed with the introduction of the modified radius β [58] (termed as effective entrainment radius by [7], [32]) and a dimensionless density deficit η [58] (termed as the effective density parameter by [7], [32]) as

$$\beta=x^{\frac{j}{2}}b, \quad \eta=\frac{1-x}{x^j}, \tag{1.32}$$

the governing equations for the vertical flow can be written in terms of the new variables as

$$\frac{\mathrm{d}}{\mathrm{d}z}[w\beta^2]=2\alpha\beta w, \tag{1.33a}$$

$$\frac{\mathrm{d}}{\mathrm{d}z}[w^2\beta^2]=\eta g\beta^2, \tag{1.33b}$$

$$\frac{\mathrm{d}}{\mathrm{d}z}[\eta w\beta^2]=0. \tag{1.33c}$$

In this way a single representation is achieved encompassing both Boussinesq and non-Boussinesq plume limits. The famous MTT solutions can easily be recovered from the governing equation by simply assuming solutions for each of the variables of the form

$\beta(z) = C_\beta z^m$, $w(z) = C_w z^n$ and $\eta(z) = C_\eta z^p$ so that the similarity solutions obtained as in [58] are given below as

$$\beta(z) = \frac{6\alpha}{5} z, \tag{1.34a}$$

$$w(z) = \left(\frac{3}{4}\right)^{1/3} \left(\frac{6\alpha}{45}\right)^{-2/3} \left(\frac{B}{\pi}\right)^{1/3} z^{-1/3}, \tag{1.34b}$$

$$\eta(z) = \frac{1}{g} \left(\frac{3}{4}\right)^{-1/3} \left(\frac{6\alpha}{45}\right)^{-4/3} \left(\frac{B}{\pi}\right)^{2/3} z^{-5/3}. \tag{1.34c}$$

The fact that the classic MTT model includes an assumption of a point source of buoyancy only (zero momentum and volume flux), has already been discussed. In real life applications though the size of the source is finite, while in what concerns the conditions at the source there are many practical situations of interest where departures from the rather restrictive ‘buoyancy only source condition’ are observed, and where momentum and volume flux are present. Consequently, direct implementation of the MTT model for the prediction of the turbulent flow above a finite source would not provide the sufficient accuracy expected if the size and the source conditions are not taken into account. To overcome this difficulty a correction is required under which the finite source is related to a point source located at a virtual origin [33], before the theoretical model can be applied for predictions.

Different techniques for the determination of the virtual origin have been developed and can be classified to experimental (requiring experimental data for the prediction) and to purely theoretical ones (a more detailed categorisation and description of virtual origin recovery methods is given in [33]). A straightforward technique, that can be assigned as an experimental one, is by simply providing a best fit to the experimental data with height and then extrapolating for $z<0$ in order to find the point where the fitted function intercepts the z-axis[4]. The point of intersection can then be considered to be the virtual origin. Another simple technique belonging to this category requires a capturing of a picture of the plume once the flow has reached a steady state. With the aid of the picture and by further presuming a conic shape for the plume, the angle of spread of the axisymmetric plume, $\phi = 2\theta$ from the point source, can easily be estimated. Looking at Figure 1.1, knowledge of the angle θ allows the determination of the position of the virtual origin at $z = -z_v$ located below the source of radius R

---

[4] Where z is the axis of symmetry.

as

$$z_{\mathrm{v}} = \frac{R}{\tan\theta}. \tag{1.35}$$

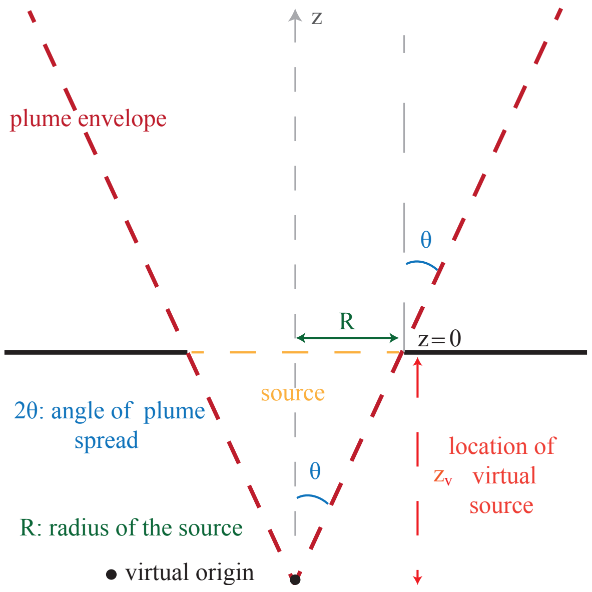

Figure 1.1: A simple technique for the recovery of the position of the virtual origin using the conic shape plume assumption. The virtual origin located at position $z = -z_v$ below the a source of radius R, and $z_{\mathrm{v}} = R/\tan\theta$.

A theoretical breakthrough for the description of the plume flow (under the Boussinesq approximation) above non ideal sources came with publication of the paper of Morton [59]. By introducing the notion of a forced plume (the term buoyant jet is also used by other authors) as a plume generated from a source of finite size which delivers flux of buoyancy B_0, momentum M_0 and volume Q_0, compactly presented as (B_0, M_0, Q_0), Morton firstly investigated the effect of discharge of momentum from a virtual source of buoyancy. By considering a forced plume from a point source of buoyancy and momentum flux only $(B_0, M_0, 0)$ he showed that it develops into a purely buoyancy driven flow (pure plume) at a height given as [33]

$$L_j = 2^{-3/2}\alpha^{-1/2}\frac{M_0^{3/4}}{B_0^{1/2}}. \tag{1.36}$$

In addition it was shown that the same behaviour of the flow above a point source $(B_0, M_0, 0)$, is exhibited by a point source of buoyancy only $(B_0, 0, 0)$, located at $z = -1.057L_j$. In other words the virtual origin is located at $z_{\mathrm{avs}} = -1.057L_j$, and this correction is termed as an asymptotic virtual source, since it is valid far from the source for $z/L_j \geq 5$ [33].

In the second part of his work, the more general case of a plume with momentum, mass and buoyancy (B_0, M_0, Q_0), rising from a finite area at $z = 0$, is shown to be related to a plume rising from a point source of modified momentum γM_0 and buoyancy B_0 only $(B_0, \gamma M_0, 0)$, with the source now located at $z = z_{\mathrm{v}}$. Though, as earlier discussed, the resulting point source plume $(B_0, \gamma M_0, 0)$ positioned at $z = z_{\mathrm{v}}$ can also be related to a plume of buoyancy only $(B_0, 0, 0)$, positioned at $z = z_{\mathrm{avs}}$. Therefore by combining the two methods, a plume generated by a finite source and general source conditions (B_0, M_0, Q_0), exhibits the same behaviour resulting from a point source plume of buoyancy only $(B_0, 0, 0)$, positioned at $z = z_{\mathrm{v}} + z_{\mathrm{avs}}$.

Morton [59],[62] firstly introduced the nondimensional parameter Γ_0 which for forced plumes, represents the balance of flow conditions imposed at the physical source as [7]

$$\Gamma_0 = \frac{5 B_0 Q_0^2}{8\alpha\sqrt{\pi} M_0^{5/2}}. \tag{1.37}$$

According to the value of that parameter he suggested the following categorisation of the plumes in [62] as

- $\Gamma_0 = 1$: Pure or simple plume. Corresponds to a plume from a virtual source of buoyancy only.
- $\Gamma_0 < 1$: In this case apart from positive buoyancy, there is additional momentum when compared with a pure plume.
- $\Gamma_0 < 0$: Negative buoyancy jets projected upwards (Fountains).
- $\Gamma_0 = 0$: Pure jets (no buoyancy effects).
- $\Gamma_0 > 1$: Lazy Plumes. Deficit of momentum when compared with a pure plume.

Recall that the Richardson number is defined as

$$\mathrm{Ri} = \frac{\grave{g} L}{U^2},$$

where U and L are the characteristic velocity and length. The Richardson number assesses the balance between free and forced convection, thus by defining the local Richardson number as $\mathrm{Ri}(z) = 2\eta g \beta / w^2$ [58], when evaluated at $z = 0$, an indication of the source conditions is obtained. Further by observing that, for any given source conditions, as $z \to \infty$ (the 'far field') the flow must be that of the self similar plume (asymptotic solution) and thus described by (1.34). Substitution of the similarity solution into the Richardson number definition on the limit $z \to \infty$ results in $R_\infty = 16\alpha/5$. By scaling the Richardson number as [58],[7]

$$\Gamma(z) = \frac{\mathrm{Ri}(z)}{\mathrm{Ri}_\infty} = \frac{5g\eta\beta}{8\alpha w^2}, \tag{1.38}$$

the categorisation of plume flows described by Morton is obtained. For example $\Gamma(0) = 1$ corresponds to a pure plume from a source, similarly according to the value of $\Gamma(0)$ we can obtain a forced plume, lazy plume, etc.

On returning to governing plume equations (1.33), with the aid of (1.38), they are rewritten in the following form

$$\frac{\mathrm{d}\beta}{\mathrm{d}z} = \frac{4\alpha}{5}\Big(\frac{5}{2} - \Gamma\Big), \tag{1.39a}$$

$$\frac{\mathrm{d}w}{\mathrm{d}z} = \frac{8\alpha}{5}\Big(\frac{w}{\beta}\Big)\Big(\Gamma - \frac{5}{4}\Big), \tag{1.39b}$$

$$\frac{\mathrm{d}\Gamma}{\mathrm{d}z} = \frac{4\alpha\Gamma}{\beta}(1 - \Gamma) \tag{1.39c}$$

and

$$\eta = \frac{8\alpha w^2 \Gamma}{5g\beta}. \tag{1.39d}$$

The form of equations (1.39) suggest the following nondimensional scalings as in [7], and given as

$$\zeta = \frac{4\alpha z}{\beta_0}, \quad \hat{\beta} = \frac{\beta}{\beta_0}, \quad \hat{w} = \frac{w}{w_0}, \tag{1.40}$$

with β_0, w_0, the modified plume radius and velocity at the source. Introduction of the above nondimensional parameters into equations (1.39) results in the Γ-plume equation given as

$$\frac{\mathrm{d}\hat{\beta}}{\mathrm{d}\zeta} = \frac{1}{5}\Big(\frac{5}{2} - \Gamma\Big), \tag{1.41a}$$

$$\frac{\mathrm{d}\hat{w}}{\mathrm{d}\zeta} = \frac{2}{5}\Big(\frac{\hat{w}}{\hat{\beta}}\Big)\Big(\Gamma - \frac{5}{4}\Big), \tag{1.41b}$$

$$\frac{\mathrm{d}\Gamma}{\mathrm{d}\zeta} = \frac{\Gamma(1 - \Gamma)}{\hat{\beta}} \tag{1.41c}$$

and

$$\eta = \frac{8\alpha w_0^2 \hat{w}^2 \Gamma}{5g\beta_0\hat{\beta}}. \tag{1.41d}$$

The system of differential equations is to be solved subject to initial conditions given as

$$\Gamma(0) = \Gamma_0, \quad \hat{w}(0) = 1 \quad \text{and} \quad \hat{\beta}(0) = 1. \tag{1.41e}$$

Depending on the value assigned to Γ_0, four of the five classes of solutions as categorised by Morton [62], jets ($\Gamma_0 = 0$); pure plumes $\Gamma_0 = 1$,;forced plumes ($0 < \Gamma_0 < 1$); and lazy plumes ($\Gamma_0 > 1$); are obtained. For the particular case of fountains ($\Gamma_0 < 0$), modifications are necessary in the formulation presented, thus attention is restricted only to the above mentioned cases. A more general treatment, so as to include the case of fountains, is given in [7].

Proceeding with a separate study for the different limiting cases of interest concerning Γ_0, it is not hard to obtain exact analytic solutions for equations (1.41a)–(1.41c), when dealing with jets and pure plumes.

- Jets, $\Gamma_0 = 0$.

For the particular case of jets the analysis is straightforward since there is no buoyancy (i.e. $\eta(\zeta) = 0$), which implies that $\Gamma(\zeta) = 0$. Therefore the solution of equations (1.41a)–(1.41c) is simply given as

$$\frac{b}{b_0} = 1 + \frac{\zeta}{2}, \quad \frac{w}{w_0} = \frac{1}{1 + \frac{\zeta}{2}} \quad \text{where} \quad \beta = b \quad \text{and} \quad \beta_0 = b_0 \tag{1.42}$$

- Pure plumes, $\Gamma_0 = 1$.

When $\Gamma_0 = 1$, then $\Gamma(z) = 1$ and the solution for pure plumes is easily obtained and given as

$$\frac{\beta}{\beta_0} = \frac{3}{10}\left(\frac{10}{3} + \zeta\right), \quad \frac{w}{w_0} = \left(\frac{10}{3}\right)^{\frac{1}{3}}\left(\frac{10}{3} + \zeta\right)^{-\frac{1}{3}}, \quad \frac{\eta}{\eta_0} = \left(\frac{10}{3}\right)^{\frac{5}{3}}\left(\frac{10}{3} + \zeta\right)^{-\frac{5}{3}}. \tag{1.43}$$

In the more general case that Γ_0 is allowed to vary (i.e. $\Gamma_0 \neq 0$,$\Gamma_0 \neq 1$), then it is not possible to obtain explicit relations for the plume variables with the height ζ. However the plume variables can be expressed in terms of Γ and Γ_0 in the following way. Starting with equations (1.41a) and (1.41c), both are solved for $\mathrm{d}\zeta$ and then combined to give the following separable differential equation

$$\frac{\mathrm{d}\hat{\beta}}{\hat{\beta}} = \left(\frac{1}{2\Gamma} + \frac{3}{10(1-\Gamma)}\right)\mathrm{d}\Gamma. \tag{1.44}$$

Integration of the above equation results in

$$\hat{\beta} = \left|\frac{\Gamma}{\Gamma_0}\right|^{\frac{1}{2}} \left|\frac{1-\Gamma_0}{1-\Gamma}\right|^{\frac{3}{10}}. \tag{1.45}$$

In a similar manner, use of equations (1.41b) and (1.41c) results in

$$\frac{\mathrm{d}\hat{w}}{\hat{w}} = \left(-\frac{1}{2\Gamma} + \frac{1}{10(1-\Gamma)}\right)\mathrm{d}\Gamma, \tag{1.46}$$

which after integration provides a general solution of $\hat{w}$ as a function of Γ, given below

$$\hat{w} = \left|\frac{\Gamma_0}{\Gamma}\right|^{\frac{1}{2}} \left|\frac{1-\Gamma}{1-\Gamma_0}\right|^{\frac{1}{10}}. \tag{1.47}$$

In order to express the plume variables as functions of height ζ, then Γ has to be related to ζ. From equation (1.41c)

$$\mathrm{d}\zeta = \frac{\hat{\beta}\mathrm{d}\Gamma}{\Gamma(1-\Gamma)}, \tag{1.48}$$

which after integration and use of equation (1.45), gives

$$\zeta = \frac{|1-\Gamma_0|^{\frac{3}{10}}}{|\Gamma_0|^{\frac{1}{2}}} \int_{\Gamma_0}^{\Gamma} \frac{|\Gamma|^{\frac{1}{2}}}{|1-\Gamma|^{\frac{3}{10}}\Gamma(1-\Gamma)}\mathrm{d}\Gamma. \tag{1.49}$$

In this way knowledge of the height as a function of Γ is obtained. Now by constraining Γ_0 within the lazy and forced plume limits and using equations (1.45) and (1.47), analytical expressions for all the plume variables as functions of Γ are given below.

- Forced plumes $0 < \Gamma(z) < 1$ and lazy plumes $\Gamma(z) > 1$

Use of equations (1.45) and (1.47) and the limiting cases for Γ considered results in

$$\frac{\beta}{\beta_0} = \sqrt{\frac{\Gamma_0}{\Gamma}}\left(\frac{1-\Gamma_0}{1-\Gamma}\right)^{\frac{3}{10}}, \quad \frac{w}{w_0} = \sqrt{\frac{\Gamma_0}{\Gamma}}\left(\frac{1-\Gamma_0}{1-\Gamma}\right)^{\frac{1}{10}}, \quad \frac{\eta}{\eta_0} = \sqrt{\frac{\Gamma_0}{\Gamma}}\sqrt{\left(\frac{1-\Gamma}{1-\Gamma_0}\right)}. \tag{1.50}$$

In addition the behaviour of Γ with height is given as

$$\zeta = \begin{cases} \frac{(1-\Gamma_0)^{3/10}}{\sqrt{\Gamma_0}} \int_{\Gamma_0}^{\Gamma} \frac{\mathrm{d}\Gamma}{\sqrt{\Gamma}(1-\Gamma)^{13/10}} & \text{for} \quad 0 < \Gamma < 1, \\ \\ \frac{(\Gamma_0-1)^{3/10}}{\sqrt{\Gamma_0}} \int_{\Gamma_0}^{\Gamma} \frac{\mathrm{d}\Gamma}{\sqrt{\Gamma_0}(1-\Gamma)^{13/10}} & \text{for} \quad \Gamma > 1. \end{cases} \tag{1.51}$$

Given any general conditions at the source the introduction of the Morton Γ function allows a characterisation of the source. When dealing with forced plume and lazy plumes far from the source it is expected that both will attain asymptotically a pure plume behaviour. The reformulation of governing plume equations (1.33) to the Γ-plume equations (1.41) provides information regarding this behaviour. From equation (1.41c) it is not hard to conclude that for a forced plume $0 < \Gamma_0 < 1$, Γ increases monotonically towards $\Gamma = 1$. On the other hand, for lazy plumes $\Gamma_0 > 1$, the Γ decreases monotonically with height to $\Gamma = 1$ [58]. From the numerical solution of equations (1.41), as shown in Figure 1.2 (*c*), above mentioned behaviour of Γ with height is illustrated. Furthermore it is clear that in general lazy plumes asymptotically attend the pure plume behaviour at lower heights than the forced plumes.

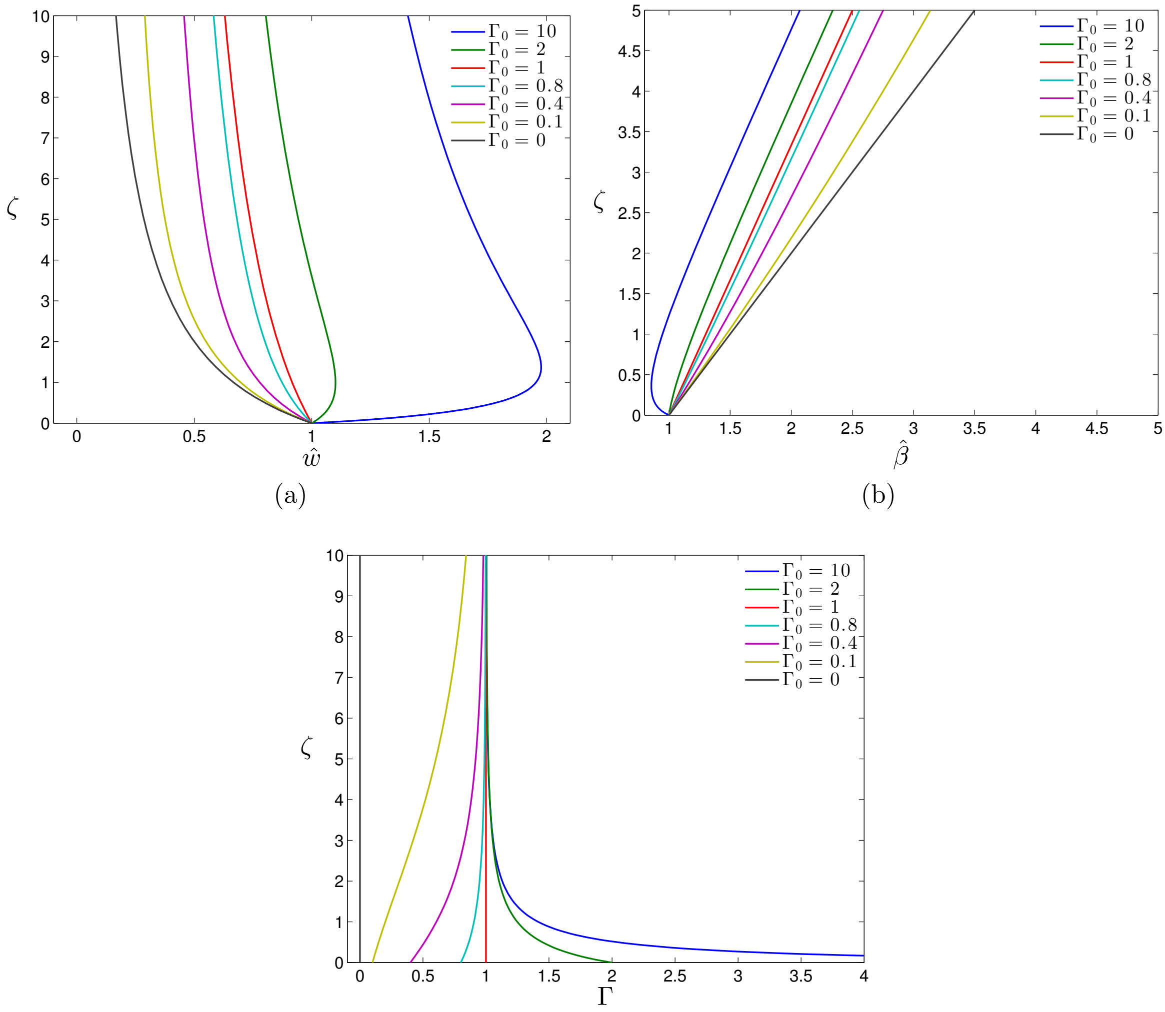

(a)

(b)

(c)

Figure 1.2: Numerical solution of the Γ-plume equations (1.41) for different values of Γ_0. (a) Nondimensional plume velocity $\hat{w}$, (b) Nondimensional modified radius $\hat{\beta}$, (c) Γ parameter variation with height.

The Γ plume equations (1.41a) and (1.41b) recover the ‘necking’ point (point of minimum radius) and the point of maximum velocity, when $\Gamma = 5/2$ and $\Gamma = 5/4$ respectively, as firstly observed by [24]. The monotonic behaviour exhibited by Γ with ζ implies that maximum and minimum velocity only exists for lazy plumes under the condition $\Gamma_0 > 5/4$ and $\Gamma_0 > 5/2$, respectively. This is also evident from the numerical solution given in Figure 1.2 (a) and (b). Clearly when $\Gamma_0 = 10$ maximum velocity and the necking are present. On the contrary for the lazy plume generated with source conditions $\Gamma_0 = 2$ only maximum velocity is observed while there is no apparent necking, as expected.

Closing, by setting $\Gamma = 5/4$ and $\Gamma = 5/2$ in equation (1.50), the maximum velocity and the minimum radius are recovered for a lazy plume. Utilisation of equation (1.51), then provides the height at which this behaviour is exhibited. Furthermore, equation (1.51) can be used to provide additional information such as the virtual source (position where $\Gamma = 0$) and the asymptotic virtual source correction, a detailed analysis is given in [7].

1.5 Outline of the thesis

It seems useful to conclude this introductory chapter by outlining the subjects visited within the rest of this work. In general, the phenomena studied can be classified as buoyancy induced flows above uniformly heated horizontal surfaces. Primarily, attention is directed towards the turbulent regime since the buoyant flows generated above large areas fires is the topic of concern. Having discussed the classic plume theory and the modelling of those vertical gravity currents, a central feature of this thesis is a theoretical suggestion for a new plume structure. Reasoning behind this proposal is the presence of attached gravity induced horizontal currents, indicated by field experimental observations of plumes generated above large area fires. Focusing on round plumes generated above sources of large radius, the long and thin assumption of classic plume theory resulting in the neglect of the radial pressure gradient within the governing equation is not justifiable, in particular when the flow close to the source is of interest. On the contrary, the horizontal driving of the flow is attributed to a radial pressure gradient result of an indirect gravity mechanism. In order to capture these horizontal buoyant currents an innovative approach is proposed regarding the plume modelling. The plume flow is divided into three regions. A region where the flow is predominantly horizontal and attached to the surface, a transition region from horizontal to vertical where separation of the attached current takes place, and a region where vertical flow is established and classic plume theory already described is adequate.

Therefore the initial objective of the thesis is the mathematical modelling of these flow regions. Analytically in **Chapter 2**, a new theoretical model termed as '*horizontal plume*' is developed, for the description of the mean flow properties of the horizontal buoyant current generated above a circular area of large radius, supplied by constant heat flux q. The assumptions within the model and its limitations are discussed. Further, a dimensionless parameter $\mathbf{a}$, termed as the modified Richardson number and present in the governing equations is introduced. This newly introduced dimensionless parameter $\mathbf{a}$ is analogous to the large radius of the source, which suggests an asymptotic study (no analytical solutions exist for the governing horizontal plume equations) in the limit $\mathbf{a} \to \infty$, which takes place in **Chapter 3**. Second order uniform valid semi-analytical approximation are obtained for the governing horizontal plume equations, also accompanied by the numerical solution. A comparison of the results obtained from the two methods is given.

It is natural to expect that within **Chapter 4** a discussion for the transition of the horizontal plume flow to the vertical to be present, but this is not the case. At that time a great deal of effort was placed in the theoretical modelling of the intermediate region, but all approaches turned out to be unsuccessful. In addition discussions were ongoing for the design of an experiment (the 'hot plate experiment'), that would test the horizontal plume model and suggest improvements along with crucial information regarding the physical mechanisms of the transition. In theory the experimental design made allowances for the laminar limit to be studied, while it also felt that the laminar study had more solid foundations to built on. Therefore **Chapter 4** commences with a brief introductory section dedicated to free/natural convective flows above horizontal plates. The main subject matter though, is that of the laminar boundary layer flow above an isothermal horizontal circular disk with the emphasis placed on variable fluid properties. Fourth order series approximations valid at the circumference of the disc are obtained. Moreover the full set of boundary layer equations is solved numerically using two methods, that of finite differences using the Keller Box method and that of finite elements. Variable fluid properties and the Prandtl number effects on the flow are studied thoroughly for the first time.

In **Chapter 5** we remain on the laminar flow regime and we revisit a classic problem, that of first order boundary layer analysis of laminar natural convection above a uniformly heated horizontal and slightly inclined semi-infinite plate. Effects of variable fluid properties, Prandtl number and inclination are studied in detail. In addition when the inclination is negative the position of the separation point is investigated when altering the Prandtl number. Furthermore, for the first time an analytic study is carried out for the position of the separation point obtained for different inclinations and for differing effects of variable fluid properties.

Chapter 6 discusses the 'hot plate' experiment designed with the collaborators and carried out by the sponsor (AWE). Unfortunately, due to technical difficulties presented, the experimental data is shown to incorporate a considerable amount of uncertainty. Nevertheless it was decided to include the detailed analysis carried, even though no safe conclusions could be reached. The chapter opens with an analytic presentation of the experimental apparatus and the methodology adopted for the conduction of the experiment, followed by a thorough discussion of the technical problems faced. Subsequently a technique is established for the analysis of the horizontal plume data, and then the experimental findings are compared with the theoretical horizontal plume model, as well as with the numerical simulation of the experiment using the two equation turbulence models $k - \epsilon$ and $k - \omega$. The chapter concludes with the visualisation of the flow using a particle image velocimetry analysis.

Chapter 7 brings this thesis to an end with a synopsis of the outcomes of this work. Finally, a brief discussion for the transition region is given while the topics of future work are presented.

Chapter 2

Buoyancy Induced Flow Above Large Area Fires

2.1 Introduction

Figure 2.1: Plume image from experimental burns in Northumberland carried out in March 2011

Observation of experimental burns indicates the presence of attached and indirectly induced, horizontal buoyant currents just above an area that is set on fire. These currents move inwardly from the edges of the area (independently of the geometry) and at certain locations depending on the wind, the topography, and the fuel, collide and separate to give rise to the routes of a vertical buoyant structure, the well known plume. Any independently formed plumes resulting from these collisions unite under the coanda effect at some height above the surface to form a dominant rising plume. It is the purpose of this chapter to describe these attached horizontal buoyant currents which we shall term as a *horizontal plume*. In trying to describe such a complex turbulent flow, where many physical processes take place simultaneously, sacrifices in modelling are necessary, especially since the scope of this work is to provide a simple model for which analytical or semi-analytical solutions are attainable and predict the gross features of the flow, rather than a more accurate state of the art multiphysics numerical simulation. Firstly combustion and radiation effects are neglected while the geometry of interest is a circular disk of radius a (so that the flow can be considered axisymmetric), supplied by constant heat flux q. Furthermore the viscosity is neglected which is a reasonable assumption to make since the flow is fully turbulent (turbulent friction is much greater than the viscous friction), while the viscous sublayer is located directly above the circular disc where many of the physical processes taking place are not modelled. Finally, the environment is assumed unstratified and still, so that the modelling focuses on the convective flow above the fire, disregarding external driving factors.

Incorporating the above assumptions, the physical mechanism responsible for the driving of the horizontal buoyant currents is in essence the one described by Stewartson [89], in his work concerning the boundary layer free convective flow above a horizontal heated semi-infinite plate. Assuming that the surrounding environment has uniform temperature T_{e} and density ρ_{e}, then in the region above the circular disk the temperature T is higher than the environmental temperature so that the fluid density ρ will be smaller i.e $(\rho < \rho_{\mathrm{e}})$. In considering the static field outside the edge of the heated disc the pressure distribution is $\partial p/\partial z = -\rho_{\mathrm{e}} g$, though above the disk the pressure gradient is reduced since $|\partial p/\partial z| = \rho g < \rho_{\mathrm{e}} g$ [80] . The decreased pressure gradient results in a pressure drop in the neighbourhood of the edge of the disc, which is responsible for a radial pressure gradient which drives the flow away from the periphery of the disk towards the centre.

The main limitation of the point source (axisymmetric) turbulent plume model, is its inability to describe the flow in the immediate neighbourhood above the source. Even when the virtual origin correction is applied satisfactory approximations with the existing experimental data are obtained everywhere except close to the source. On dimensional grounds this is reasonable, more so in the case considered here, where the radius of the disk of interest is large. Self similarity solutions must collapse near the source since the radius provides a length scale that needs to be considered. In addition it must be noted that within the classic plume model, the assumption that the flow is narrow enough so that $(\partial P/\partial z \gg \partial P/\partial r)$ is made. Therefore the radial pressure gradient can be ignored[1]. This implies that the pressure can be treated as a constant over a cross section of the plume and equal to the pressure outside the plume, which varies hydrostatically [32]. The above is a reasonable assumption to be made, but not when describing the flow close to a large area source. Therefore in considering the buoyant flow above a circular region of large radius L, a radical approach in describing the flow is proposed. The flow field is divided into three regions. A region where the flow is horizontal and attached to the surface, a transition region from horizontal to vertical where separation of the attached current takes place, and a vertical flow where the point source plume is valid and can already be described adequately by existing literature. Therefore in the coordinate system shown in Figure 2.2, the centre of the circular disk is positioned in the axis of symmetry while the horizontal plume initiates at $r = L$, moving inwards towards $r = 0$. At a point $r = r_{\mathrm{c}}$, such that $0 < r_{\mathrm{c}} < L$, the flow separates and turns into a vertical plume. In what follows the focus solely lies in the derivation of the model equations describing the horizontal flow, rather than the transition from horizontal to vertical which is briefly discussed in the final conclusions.

---

[1] Ignoring the radial pressure gradient essentially means that the vertical length scale L_{v} is much larger than the radial length scale L

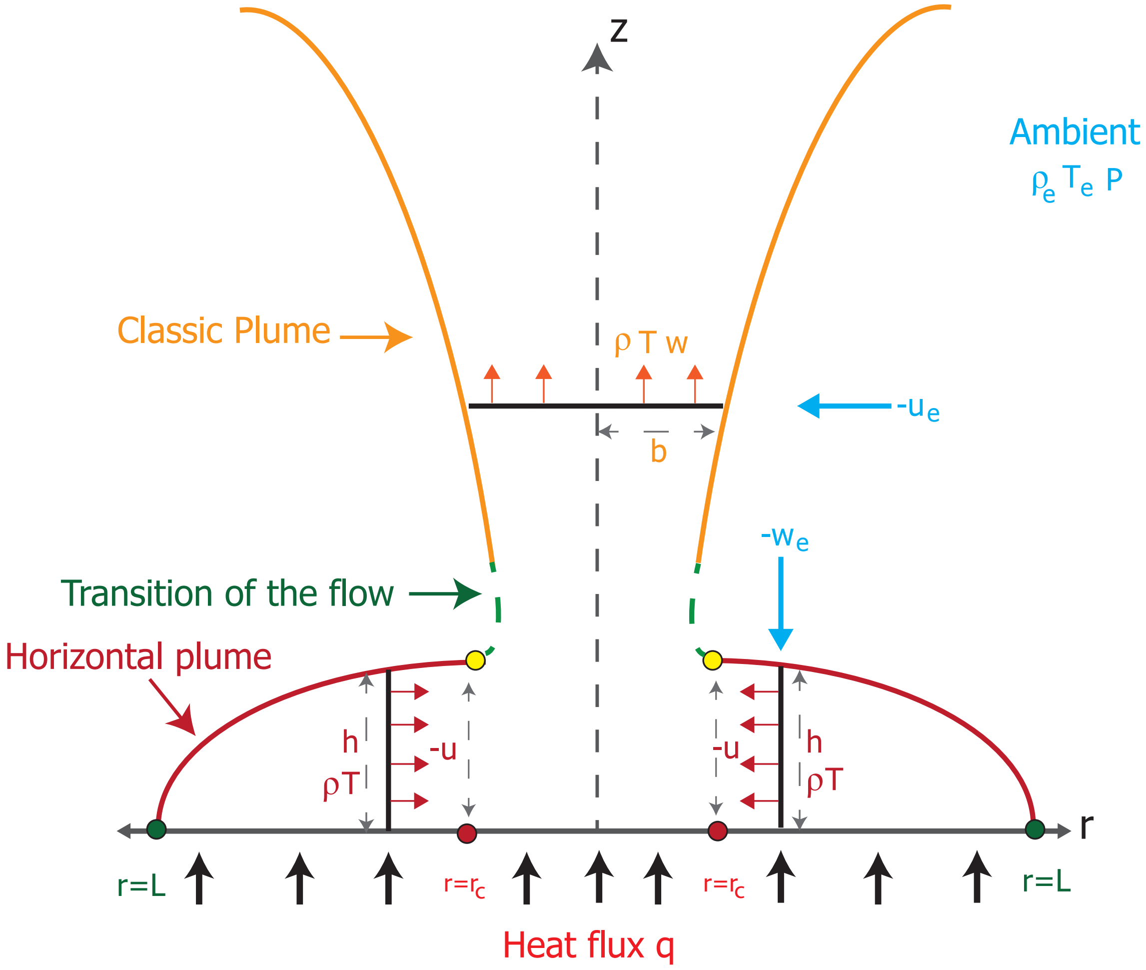

Figure 2.2: Sketch of the buoyant flow above a disc of radius L caused by an upward heat flux q, and whose centre is positioned in the axis of symmetry z. Top hat descriptions are used to describe the attached horizontal plume in a similar manner to the classic pure plume. The inward radial velocity is $-u$ while w is the vertical velocity. The temperature T and the density ρ, under the top hat formalism are constant along vertical lines of height $h(r)$ and horizontal lines of length $2b(z)$, in the respective parts of the plume. The horizontal and vertical entrainment velocities representing the engulfment of ambient fluid of density ρ_e and temperature T_e, into the classic and horizontal plume respectively, are denoted as $-u_\mathrm{e}$ and w_e. The pressure P is assumed hydrostatic, while the environment is still and unstratified. Finally $r = r_c$ represents the point at which the flow stops being horizontal, and denotes the beginning of a transition region of predominantly horizontal flow to a predominantly vertical one. The model developed here is dedicated to the description of the horizontal plume.

2.2 Horizontal plume - model equations

The methodology of deriving the horizontal plume model equations is similar to the classic MTT [63] formulation, but without making the Boussinesq approximation since the flow close to the source is modelled. The flow is turbulent but it is assumed that it can be adequately described by the mean flow variables alone [73]. Therefore based on the conservation principles of mass, momentum and energy of the mean flow properties, an entrainment assumption and adoption of top hat formalism three ordinary differential equation describing the horizontal flow will result.

In a cylindrical polar coordinate system without making the Boussinesq approximation and further assuming that there is no swirl $\bar{\mathbf{u}} = (\bar{u}, 0, \bar{w})$ in the flow, the continuity equation is expressed as

$$\frac{\partial}{\partial r}(r\bar{u}\bar{\rho}) + \frac{\partial}{\partial z}(r\bar{w}\bar{\rho}) = 0. \tag{2.1}$$

Furthermore by assuming that $h(r)$ is the height of the horizontal attached flow, and that $\bar{u}$ is negligible for $z > h$, in a similar style in which the MTT model equations were derived, we proceed by integrating the continuity equation but vertically this time.

$$\int_0^\infty \big(\frac{\partial}{\partial r}(r\bar{\rho}\bar{u}) + \frac{\partial}{\partial z}(r\bar{\rho}\bar{w})\big)\mathrm{d}z = 0, \tag{2.2a}$$

which after application of the Leibniz rule results in

$$\frac{\mathrm{d}}{\mathrm{d}r}\int_0^\infty (r\bar{\rho}\bar{u})dz = -r[\bar{\rho}\bar{w}]_0^\infty = -\bar{w}|_{z=\infty}\, r\rho_e. \tag{2.2b}$$

If the continuity equation is integrated for $h < z < \infty$, so that the contribution of $\bar{u}$ is negligible then

$$\int_h^\infty \frac{\partial}{\partial z}(r\bar{\rho}\bar{w})\mathrm{d}z = 0 \Rightarrow \bar{w}_h = \bar{w}_\infty \tag{2.2c}$$

Now defining $w_\mathrm{e}= -\bar{w}_h= -\bar{w}_\infty$, the vertical entrainment velocity at which ambient fluid of density ρ_e is submerged into the horizontal flow, then equation (2.2b) becomes

$$\frac{\mathrm{d}}{\mathrm{d}r}\int_0^\infty (r\bar{\rho}\bar{u})\mathrm{d}z = r\rho_\mathrm{e}w_\mathrm{e}. \tag{2.3}$$

The radial momentum equation is given as

$$\frac{\partial}{\partial r}(r\bar{\rho}\bar{u}^2) + \frac{\partial}{\partial z}(r\bar{\rho}\bar{u}\bar{w}) = -r\frac{\partial P}{\partial r}. \tag{2.4}$$

The pressure gradient in the r.h.s of equation (2.4) is responsible for the driving mechanism of the flow and cannot be neglected. Similarly integration of equation (2.4) results in

$$\frac{\mathrm{d}}{\mathrm{d}r}\int_0^\infty (r\bar{\rho}\bar{u}^2)\mathrm{d}z = -r\int_0^\infty \frac{\partial P}{\partial r}\mathrm{dz}. \tag{2.5}$$

Introduction of top hat variables (i.e. the mean properties will have one constant value inside the plume and another outside), is equivalent to the mass V and momentum M fluxes being replaced by mean values defined as integrals over the plume [97]. In doing so

$$V = \int_0^\infty (r\bar{\rho}\bar{u})\mathrm{d}z = r\rho u h \quad \text{and} \quad M = \int_0^\infty (r\bar{\rho}\bar{u}^2)\mathrm{d}z = r\rho u^2 h. \tag{2.6}$$

In addition the following entrainment hypothesis is made here, *the mean inflow vertical velocity at the edge of the horizontal plume is proportional to the radial velocity.* Thus the vertical velocity entrained at a given horizontal plume height h, is proportional to radial velocity u at that height. Analytically, for the horizontal plume the entrainment hypothesis is expressed as

$$w_e = -f(r)u = -\alpha\left(\frac{\rho}{\rho_\mathrm{e}}\right)^{1/2}u. \tag{2.7}$$

As can be observed $f(r)$ is chosen so as to take the classic form of R-S [72], therefore α is the entrainment coefficient. Investigation of the constant α is put on hold until **Chapter 6**. Therefore for the next two chapters the constant of entrainment is not differentiated from the one used for classic pure plumes.

The r.h.s of the momentum equation (2.5) contains a pressure gradient that needs to be expressed in terms of top hat variables. Looking at the schematic diagram given in Figure 2.3 . The pressure outside the horizontal plume is considered hydrostatic so that

$$\frac{\mathrm{d}P}{\mathrm{d}z} = P_z = -\rho_\mathrm{e} g \quad \text{with} \quad P \sim P_0 - \rho_\mathrm{e} g z \quad \text{for} \quad z > h. \tag{2.8a}$$

By considering the pressure along the vertical segment AB within the plume, with height h and top hat density ρ, then

$$P_I = -\rho g z + k_I,$$

by noting that at $z = h$, $P_I = P_0 - \rho_\mathrm{e} g h$ then $k_I = P_0 + (\rho - \rho_\mathrm{e})gh$ so that

$$P_I = P_0 + (\rho - \rho_\mathrm{e})gh - \rho g z. \tag{2.8b}$$

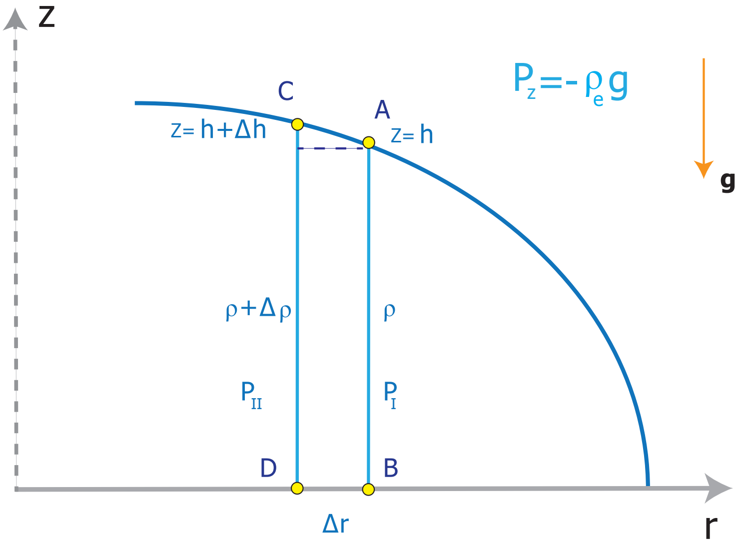

Figure 2.3: Variation of top hat properties along the vertical parallel segments AB and CD. Along AB the density is ρ, the height is of the plume is h, while the pressure varies as P_I. At distance Δr along CD, density and plume height are altered by $\Delta\rho$ and Δh respectively, while the pressure varies as P_{II}.

Similarly by considering the vertical segment CD, parallel to AB and displaced by distance Δr, the top-hat properties are slightly altered so that the height of the plume is now $h + \Delta h$, while the density is $\rho + \Delta\rho$. Along CD the pressure varies as

$$P_{II} = -(\rho + \Delta\rho)gz + k_{II}, \text{ while at the point } C \text{ i.e. } z = h + \Delta h \quad \text{then}$$

$$k_{II} = P_0 - \rho_{\mathrm{e}} g(h + \Delta h) + (\rho + \Delta\rho)g(h + \Delta h),$$

$$P_{II} = P_0 - (\rho + \Delta\rho)gz + (\rho - \rho_{\mathrm{e}})g(h + \Delta h) + \Delta\rho g h \tag{2.8c}$$

after neglecting terms of $\mathcal{O}(\Delta^2)$. Using equations (2.8b) and (2.8c), then

$$\frac{P_{II} - P_I}{-\Delta r} = -\frac{-(\rho - \rho_{\mathrm{e}})g\Delta h - \Delta\rho g(h - z)}{\Delta r}, \tag{2.8d}$$

or as $\Delta r \to 0$

$$-\frac{\partial P}{\partial r} = (\rho_e - \rho)g\frac{\mathrm{dh}}{\mathrm{dr}} + (z - h)g\frac{\mathrm{d}\rho}{\mathrm{dr}}. \tag{2.9}$$

In that way integration of equation (2.9) results in

$$\int_0^\infty -\frac{\partial P}{\partial r}\mathrm{d}z = (\rho_e - \rho)gh\frac{\mathrm{d}h}{\mathrm{d}r} - \frac{gh^2}{2}\frac{\mathrm{d}\rho}{\mathrm{d}r} = (\rho_e - \rho)gh\frac{\mathrm{d}h}{\mathrm{d}r} + \frac{gh^2}{2}\frac{\mathrm{d}}{\mathrm{d}r}\left[\rho_{\mathrm{e}} - \rho\right],$$

to finally obtain an expression for the pressure gradient with respect to (w.r.t) the top hat variables given as

$$\int_0^\infty -\frac{\partial P}{\partial r}\mathrm{d}z = \frac{1}{2}\frac{\mathrm{d}}{\mathrm{d}r}\left[g(\rho_\mathrm{e}-\rho)h^2\right]. \tag{2.10}$$

Introduction of top hat variables and the entrainment hypothesis in the conservation of mass equation (2.3) means that it is now expressed as

$$\frac{\mathrm{d}}{\mathrm{d}r}\left[r\rho u h\right] = -r\rho_\mathrm{e}\alpha\Big(\frac{\rho}{\rho_\mathrm{e}}\Big)^{1/2}u. \tag{2.11}$$

Directing attention to the momentum equation, the explicit expression of the pressure gradient in terms of top hat variables given in (2.10) in addition to the top hat expression for the momentum flux M in (2.6), generate an equivalent top hat form of the momentum equation (2.5), stated as

$$\frac{\mathrm{d}}{\mathrm{d}r}\left[r\rho u^2 h\right] = \frac{1}{2}\frac{\mathrm{d}}{\mathrm{d}r}\left[g(\rho_\mathrm{e}-\rho)h^2\right]. \tag{2.12}$$

Finally the energy equation is expressed as

$$\frac{\partial}{\partial r}(r\bar{\rho}\mathrm{c_p}\bar{\mathrm{u}}\bar{\mathrm{T}}) + \frac{\partial}{\partial \mathrm{z}}(\mathrm{r}\bar{\rho}\mathrm{c_p}\bar{\mathrm{w}}\bar{\mathrm{T}}) = -\mathrm{rQ}, \tag{2.13}$$

with $Q = q/h$. Integration of the energy equation results in,

$$\frac{\mathrm{d}}{\mathrm{dr}}\int_0^\infty (r\bar{\rho}\mathrm{c_p}\bar{\mathrm{u}}\bar{\mathrm{T}})\mathrm{dz} = \mathrm{r}\rho_\mathrm{e}\mathrm{c_p}\mathrm{w_e}\mathrm{T_e} - \mathrm{r}\int_0^\infty \mathrm{Qdz},$$

or after the introduction of top hat variables

$$\frac{\mathrm{d}}{\mathrm{dr}}\left[r\rho\mathrm{c_p}\mathrm{uTh}\right] = r\rho_\mathrm{e}\mathrm{c_p}\mathrm{w_e}\mathrm{T_e} - \mathrm{rq}. \tag{2.14}$$

The reason for the introduction of constant Q (power per unit volume) in the r.h.s of the energy equation was to inject the heat flux q into the the top hat model. Further by noting that $\rho T \approx \rho_\mathrm{e} T_\mathrm{e}$, division of equation (2.14) by $\rho_\mathrm{e}\mathrm{c_p}\mathrm{T_e}$, results in

$$\frac{\mathrm{d}}{\mathrm{dr}}\left[ruh\right] = r\left(w_\mathrm{e} - \frac{q}{\rho_\mathrm{e}\mathrm{c_p}\mathrm{T_e}}\right), \tag{2.15}$$

or after the entrainment hypothesis

$$\frac{\mathrm{d}}{\mathrm{dr}}\left[ruh\right] = -r\left(\alpha\Big(\frac{\rho}{\rho_\mathrm{e}}\Big)^{1/2}u + \frac{q}{\rho_\mathrm{e}\mathrm{c_p}\mathrm{T_e}}\right). \tag{2.16}$$

2.3 Further discussion

Thus far, based on arguments of mass, energy and momentum conservation principles, a top hat formalism, as well as an entrainment assumption, a theoretical set of model equations describing the gross properties of the attached indirectly induced buoyant horizontal flow, above a circular area of large radius has been derived. It must be pointed out that the model is ill defined at $r = 0$. Nevertheless the model by definition is designed not to be valid in the region $r \to 0$, since it is expected that the flow will not be attached anymore and that separation will have already taken place at a critical point $r_c > 0$. Therefore the purpose of the model is to describe the flow from the edge of the circular area $r = 1$ until $r = r_c$. The governing top hat equations are gathered for convenience and listed below:

- The mass equation

$$\frac{\mathrm{d}}{\mathrm{d}r}[r\rho u h] = -r\rho_e\alpha\Big(\frac{\rho}{\rho_\mathrm{e}}\Big)^{1/2}u, \tag{2.17a}$$

- The momentum equation

$$\frac{\mathrm{d}}{\mathrm{d}r}[r\rho u^2 h] = \frac{1}{2}r\mathrm{g}\frac{\mathrm{d}}{\mathrm{d}r}\big[(\rho_\mathrm{e} - \rho)h^2\big], \tag{2.17b}$$

- The energy Equation

$$\frac{\mathrm{d}}{\mathrm{d}r}[ruh] = -r\left(\alpha\Big(\frac{\rho}{\rho_\mathrm{e}}\Big)^{1/2}u + \frac{q}{c_\mathrm{p}\rho_\mathrm{e}T_\mathrm{e}}\right). \tag{2.17c}$$

The above set of differential equations will be nondimensionalised with the aid of the following scales.

$$r = L\acute{r}, \quad h = \alpha L\acute{h}, \quad u = U\acute{u} \quad \rho = \rho_e\acute{\rho}, \quad \mathbf{a} = \frac{Lg\alpha}{U^2} \quad \text{with} \tag{2.18a}$$

$$U = \frac{q}{2\alpha c_\mathrm{p}\rho_\mathrm{e}T_\mathrm{e}}, \quad \text{so that} \quad \mathbf{a} = \frac{4g\alpha^3L(c_\mathrm{p}\rho_\mathrm{e}T_\mathrm{e})^2}{q^2}. \tag{2.18b}$$

It must be noted that on dimensional grounds the Richardson number Ri is given as

$$\mathrm{Ri} = \frac{\mathrm{gL_R}}{\mathrm{V_R^2}} = \frac{1}{\mathrm{Fr}^2}. \tag{2.19}$$

Where V_R and L_R are the characteristic velocity and length scales respectively and Fr, is the Froude number. By having a closer look to the newly introduced non dimensional parameter **a**, it can be argued that **a** represents a 'modified Richardson' number for the horizontal flow. Additionally it should be pointed that it is analogous to the physical radius of the circular area L, and inversely proportional to the square of the heat flux q into the flow.

Introduction of the nondimensional variables and dropping the primes, the governing equations (2.17) results in

$$\frac{\mathrm{d}}{\mathrm{d}r}[r\rho uh] = -r\sqrt{\rho}u, \tag{2.20a}$$

$$\frac{\mathrm{d}}{\mathrm{d}r}[r\rho u^2h] = \frac{1}{2}\,\mathbf{a}r\frac{\mathrm{d}}{\mathrm{d}r}\left[(1-\rho)h^2\right], \tag{2.20b}$$

$$\frac{\mathrm{d}}{\mathrm{d}r}[ruh] = -r\sqrt{\rho}u - 2r. \tag{2.20c}$$

Subtraction of equation (2.20c) from (2.20a) gives

$$\frac{\mathrm{d}}{\mathrm{d}r}[ruh(1-\rho)] = -2r. \tag{2.21}$$

The above equation can be integrated, but before doing so it is natural to consider what are the constraints applied to the system. The problem has to be treated as an I.V.P (initial value problem) since the model is not valid at the centre of the plate. Therefore at the edge of the plate of radius $r = L$ which after the nondimensionalisation means $r = 1$, the velocity must be zero, $u(1) = 0$. Similarly the height of the horizontal plume must be set to zero i.e. $h(1) = 0$. The final constraint is applied to the density, and since the interest of this work lies in the description of flows of where $T/T_\mathrm{e} \gg 1$, the dimensional density has to be very small therefore the nondimensional density must be $\rho(1) \to 0$, or in terms of nondimensional density deficit $\delta = 1-\rho$, $\delta(1) \to 1$ must hold. Returning to equation (2.21) which can now be integrated to give

$$ruh(1-r) = -r^2 + C. \tag{2.22}$$

The constant of integration can be easily obtained once initial conditions are applied to get C=1. In that way the the system of governing equations is written in its final form as

$$\frac{\mathrm{d}}{\mathrm{d}r}[r\rho uh] = -r\sqrt{\rho}u. \tag{2.23a}$$

$$\frac{\mathrm{d}}{\mathrm{d}r}[r\rho u^2h] = \frac{1}{2}\,\mathbf{a}r\frac{\mathrm{d}}{\mathrm{d}r}\left[(1-\rho)h^2\right]. \tag{2.23b}$$

$$ruh(1-\rho) = 1 - r^2 \tag{2.23c}$$

subject to initial conditions (ICs) given as

$$\rho(1) = u(1) = h(1) = 0. \tag{2.23d}$$

As it was pointed out earlier, the Richardson number for the horizontal flow is proportional to the radius of the circular area considered. In trying to describe the attached horizontal buoyant flow, above large area fires implies that **a** has to be a large parameter, further it can be observed that as $\mathbf{a} \to \infty$ then the differential algebraic system can be treated as a singular perturbation problem. The numerical solution of the governing equations (2.23) and an asymptotic analysis based on large Richardson number is the subject that will occupy the main work of the chapter that follows.

Chapter 3

Numerical and Analytical Solution of the Horizontal Plume Flow

3.1 Introduction

The aesthetic of most natural phenomena is closely related to nonlinearities, thus it is reasonable to expect mathematical models, developed for portraying the essence of their behaviour, to commonly consist of a set of nonlinear differential equations (DEs), accompanied by a suitable set of initial (ICs) or boundary conditions (BCs). Aesthetics in this way comes at a price in mathematical terms, since most of the weaponry in dealing with linear DEs is inefficient, while recovery of an exact solution in the majority of cases is an unfeasible task. The lack of explicit solution leaves room for only two mathematical tools; direct numerical simulation and the theory of approximation.

In dealing with physical problems the conduction of nondimensionalisation is advisable though once complete, within the resulting equations and among the nondimensional dependent and independent variables features the introduction of newly nondimensional parameter(s). These parameter(s) can be characteristic of the significant competing physical processes, or characteristic of the geometry of the problem under consideration, and frequently can attain very large or very small values. A direct numerical approach to the solution of a nonlinear system of differential equations is not always an easy task, regardless of the recent computational progress, whilst the presence of a very small parameter (equivalently large) makes computations even harder.

On the contrary, the presence of a very small parameter acts as an inhibitor in tackling the problem numerically, it is blessing when an analytical approach is addressed. One of the most powerful analytical tools of modern analysis are the asymptotic methods, also termed perturbation methods, which have vastly contributed to the advances of fluid dynamics for the majority of the last century. These methods can be considered as a collection of analytical techniques that provide approximate solutions to problems containing a small (large) parameter. By means of asymptotic expansions (AE) a reduction in difficulty to the problem under consideration is achieved, so as to possibly attain an exact analytical solution, or to deal numerically with a simplified problem.

Without entering into a great deal of theoretical detail (the interested reader can turn to vast literature on perturbation methods by [66],[22],[46],[6],[18], to name a few), few definitions are necessary for the understanding of what will follow. Starting with the notion of asymptotic sequence [46],

Definition 1 *Let* $\{\Xi_n(\epsilon)\}$ *be a sequence of functions with* $n = 1, 2, \ldots$. *Such a sequence is called an asymptotic sequence if*

$$\Xi_{n+1}(\epsilon) = \mathrm{o}\left(\Xi_{\mathrm{n}}(\epsilon)\right) \quad as \quad \epsilon \to 0 \tag{3.1}$$

for each $n = 1, 2, \ldots$.

Definition 2 *An expression of the form*

$$y(x, \epsilon) = \sum_{n=0}^{N} \Xi_n(\epsilon)\, y_n(x) + \cdots, \quad n = 0, 1, 2 \ldots, \tag{3.2}$$

is an asymptotic expansion sometimes termed as Poincaré expansion, of the function $y(x, \epsilon)$ *if*

$$y(x, \epsilon) - \sum_{n=0}^{N} \Xi_n(\epsilon)\, y_n(x) = \mathrm{o}(\Xi_{\mathrm{N}}(\epsilon)) \quad as \quad \epsilon \to 0, \tag{3.3}$$

or equivalently

$$y(x, \epsilon) - \sum_{n=0}^{N} \Xi_n(\epsilon)\, y_n(x) = \mathcal{O}(\Xi_{N+1}(\epsilon)) \quad as \quad \epsilon \to 0 \tag{3.4}$$

and $\{\Xi_n(\epsilon)\}$ *is an asymptotic sequence for* $n = 0, 1, 2, \ldots$, *while* y_n *are the coefficients of the asymptotic expansion.*

Now let $y(x,\epsilon)$ be defined in a domain D, the asymptotic expansion is said to be uniformly valid in that domain provided (3.1)–(3.2) do hold. The power of the asymptotic expansions lies in the uniform validity in the domain of interest over coordinate series, i.e. Taylor or Frobenius, frequently used to approximate a solution, but their validity is often restricted to a vicinity of a point.

Returning to the previous chapter, a mathematical model was developed for the description of the attached horizontal flow above a heated circular large area. Based on 'top hat' formalism and conservation principles, we arrived at the nondimensional nonlinear set of equations listed as

$$\frac{\mathrm{d}}{\mathrm{dr}}[r\rho u h] = -r\sqrt{\rho}u, \tag{3.5a}$$

$$\frac{\mathrm{d}}{\mathrm{dr}}[r\rho u^2 h] = \frac{1}{2}\,\mathbf{a}r\frac{\mathrm{d}}{\mathrm{dr}}\big[(1-\rho)h^2\big], \tag{3.5b}$$

$$ruh(1-\rho) = 1-r^2, \tag{3.5c}$$

subject to initial conditions (ICs) given by

$$u(1)=0, \quad h(1)=0, \quad \text{and} \quad \rho(1)=0. \tag{3.6}$$

The scope of this chapter covers the numerical solution accompanied by an analytical approximation of the above nonlinear differential algebraic equations (DAEs). Numerical treatment of the above initial value problem (IVP) at first look appears to be straightforward but, as it will be shown, the DAEs are singular at the boundary $r=1$. The model is ill-defined at $r=0$ and as already mentioned, a modification of the model that will enable the capturing of the separation of the attached flow to the vertical one is required. Therefore, work in this chapter is focused on $r \in [r_0,\, 1] \subset [0,\, 1]$, while r_0 is sufficiently far from zero. Regardless, a section is dedicated to studying the behaviour of the dependent variables in the limit $r_0 \to 0$. The main part of this chapter is dedicated to the study of the governing equations for large values of the Richardson number $\mathbf{a}$. The solutions of the above equations exhibit a boundary layer character; therefore, the problem is treated as a singular perturbation problem.

In what follows, we shall start by performing local analysis at the boundaries $r=0$ and $r=1$. The asymptotic behaviour obtained around $r=1$ will be provided to the numerical solver as initial conditions in order to overcome the singularity at that point. Truncated series solutions obtained at $r=1$ provide rough approximations to the numerical solution for values of $\mathbf{a} = \mathcal{O}(1)$ and r not close to zero, but fail dramatically, when $\mathbf{a} \gg 1$. The latter case is the main interest of this work.

For the limit $\mathbf{a} \to \infty$ global analysis is carried out. A boundary layer is located at $r = 1$, therefore inner and outer asymptotic expansions are provided in terms of the small parameter $1/\mathbf{a}$. The semi-analytical approximations obtained are then analysed with the numerical results.

3.1.1 Local analysis around $r = 1$

As is typical of nonlinear differential equations, it is impossible to derive an exact closed form solution for equations (3.5). In this section local analysis ([78],[6]) is performed at the edge of the circular disc ($r = 1$), aiming at the approximation of the solution around that point. The motivation for local analysis serves a double scope, analytical as well as numerical. Focusing on the latter, suppose that a direct numerical integration is attempted. A first approach, and the one pursued here, would be to write down the index-1[1] DAEs in matrix-vector form as

$$\mathbf{M}\,\dot{\mathbf{v}}(r) = \mathbf{b}, \tag{3.7}$$

with $\dot{\mathbf{v}}(r) = (\frac{du}{dr}, \frac{dh}{dr}, \frac{d\rho}{dr})$. A key difference between DAEs and ODEs lies in the nature of the Mass matrix $\mathbf{M}$. The Mass matrix for DAEs is singular, in contrast to ODEs where it is nonsingular, and this distinctive characteristic has to be addressed numerically by the solver. Fortunately, most computational packages nowadays dedicate numerical solvers that deal with the numerical solutions of at least index-1 DAEs, without any trouble. Of course it can be argued that instead of taking the hard path, a differentiation of the algebraic equation (3.5c) would bring back equation (2.21), which historically was the equation that gave rise to the algebraic equation after integration and application of initial conditions. Dealing directly then with ODEs would overcome the singularity of $\mathbf{M}$, and classic numerical techniques can be applied. Nevertheless, because an analytical approach will be carried out in parallel to the numerical one, a preference is given to the DAEs. Bearing in mind though that a differentiation of the algebraic equations is not generally used as a computational technique, because properties of the original DAEs are often lost in numerical simulations of the differentiated

---

[1] The index of a DAE can be viewed as the number of times that the DAEs need to be differentiated, in order to obtain a system of ODEs.

equations. Having established the form of the equations to be tackled numerically, it is rather easy to implement them in **MATLAB** and compute the numerical solution using suitable methods [83]. This appears to be untrue in our case. Application of the initial conditions would result, at the initialisation of the numerical solver, in $\mathbf{M}_0 = \mathbf{0}$ and $\mathbf{b_0} = \mathbf{0}$. The consequences being a singular Jacobian Matrix, in the attempt of the solver to deal with the nonlinear system, and termination of the computation. This behaviour can be explained by the presence of a singularity at $r = 1$. The singularity becomes clear with a simple reformulation of the equations. Introduction of a new variable m given as

$$m = ruh\rho \tag{3.8a}$$

and multiplication of equation (3.5c) by ρ gives the following form

$$\rho = \frac{m}{m - r^2 + 1}. \tag{3.8b}$$

Using the above, the remaining coupled differential equations can be written in terms of u and m and expressed explicitly as

$$\frac{\mathrm{d}u}{\mathrm{d}r} = \frac{u\left(ur^2\left(2\,ru^3 + \left(r^2 - 1\right)\mathbf{a}\right)\sqrt{\dfrac{m}{m + 1 - r^2}} + 2\mathbf{a}\left(r^4 - 1 - m\right)\right)}{2r\left(rmu^3 + \mathbf{a}\left(r^2 - 1\right)\left(r^2 - m - 1\right)\right)} \tag{3.8c}$$

$$\frac{\mathrm{d}m}{\mathrm{d}r} = -ru\sqrt{\frac{m}{m + 1 - r^2}}. \tag{3.8d}$$

By noting that the new initial conditions are $m(1) = \rho(1) = u(1) = 0$, it is obvious that the system exhibits a singularity at $r = 1$. In dealing with the problem analytically, local analysis is necessary for approximating the behaviour of the solution around that point and in addition, as it will become clear on later stages, it provides information for unlocking the structure of the global solution.

Focusing on the edge of the heated surface at $r = 1$, it is assumed that the dependent variables behave as

$$\rho \sim \tilde{\rho}(1-r)^{\kappa},\ u \sim \tilde{u}(1-r)^{\mu},\ \text{and}\ h \sim \tilde{h}(1-r)^{\nu}\ \text{as}\ r \to 1, \text{for some}\ \kappa, \mu, \nu \in \Re. \tag{3.9}$$

Applying (3.9) into the governing equations (3.5) results in $\kappa = \mu = 1/5$ and $\nu = 4/5$. Proceeding with the introduction of a new independent variable s, and scalings of the dependent variables given as

$$r = 1 - s^5, \quad h = \tilde{h}s^4 \quad u = \tilde{u}s \quad \text{and} \quad \rho = \tilde{\rho}^2 s^2, \tag{3.10}$$

substitution into the governing equations gives

$$(1-s^5)\tilde{u}\tilde{h}(1-s^2\tilde{\rho}^2)=2-s^5, \tag{3.11a}$$

$$s(1-s^5)(\tilde{u}^2\tilde{h}\tilde{\rho}^2)_s+(8-13s^5)\tilde{u}^2\tilde{h}\tilde{\rho}^2=\frac{1}{2}\mathbf{a}(1-s^5)\Big[8(1-\tilde{\rho}^2s^2)\tilde{h}^2+s\big((1-\tilde{\rho}^2s^2)\tilde{h}^2\big)_s\Big], \tag{3.11b}$$

$$s(1-s^5)(\tilde{u}\tilde{h}\tilde{\rho}^2)_s+(7-12s^5)\tilde{u}\tilde{h}\tilde{\rho}^2=5(1-s^5)\tilde{u}\tilde{\rho}. \tag{3.11c}$$

As $r \to 1$, or equivalently $s \to 0$, to leading order the following is obtained

$$\tilde{u}\tilde{h}\sim 2,\ \tilde{\rho}^2\tilde{u}^2\tilde{h}\sim\frac{1}{2}\mathbf{a}\tilde{h}^2 \text{ and } 7\tilde{u}\tilde{h}\tilde{\rho}^2\sim 5\tilde{u}\tilde{\rho}. \tag{3.12}$$

Solution of the above system provides the leading order behaviour as

$$\tilde{u}\sim\tilde{u}_0=\left(\frac{14^2\mathbf{a}}{5^2}\right)^{\frac{1}{5}},\ \tilde{h}\sim\ \tilde{h}_0=\frac{2}{\tilde{u}_0},\ \tilde{\rho}\sim\tilde{\rho}_0=\frac{5\tilde{u}_0}{14}. \tag{3.13}$$

The approximations can be extended with the aid of symbolic computation package **Maple**, so in seeking truncated series expansions of the form

$$\tilde{u}\sim\tilde{u}_0+\sum_{i=1}^{n}\tilde{u}_is^i,\ \tilde{h}\sim\tilde{h}_0+\sum_{i=1}^{n}\tilde{h}_is^i,\ \tilde{\rho}\sim\tilde{\rho}_0+\sum_{i=1}^{n}\tilde{\rho}_is^i,\ \text{where } n=8, \tag{3.14}$$

and with the introduction of a scaled Richardson number A, indicated by the leading order behaviour given as

$$A=\tilde{u}_0=\left(\frac{14^2\mathbf{a}}{5^2}\right)^{1/5}, \tag{3.15}$$

the accuracy of the approximation to the local behaviour of the solution around $s=0$ can be increased. The following is obtained as $s \to 0$

$$\begin{aligned}\tilde{u}(s,A)\sim A+\frac{225}{4606}\,A^3s^2-\frac{233125}{84860944}\,A^5s^4+\frac{443}{1690}\,A\,s^5+&\\+\frac{7260453125}{27751735072544}\,A^7s^6+\frac{285305}{17125108}\,A^3s^7+\mathcal{O}(A^9s^8),&\end{aligned} \tag{3.16a}$$

$$\begin{aligned}\tilde{h}(s,A)\sim 2\,A^{-1}+\frac{725}{4606}\,A\,s^2-\frac{149375}{21215236}\,A^3s^4+\frac{402}{845}\,\frac{s^5}{A}+&\\+\frac{17243828125}{27751735072544}\,A^5s^6+\frac{234565}{4281277}\,A\,s^7+\,\mathcal{O}(A^7s^8),&\end{aligned} \tag{3.16b}$$

$$\begin{aligned}\tilde{\rho}(s,A)\sim\frac{5}{14}\,A-\frac{3375}{128968}\,A^3s^2+\frac{3646875}{1188053216}\,A^5s^4+\frac{83}{4732}\,A\,s^5-&\\-\frac{9978984375}{24282768188476}\,A^7s^6-\frac{5212975}{1438509072}\,A^3s^7+\mathcal{O}(A^9s^8).&\end{aligned} \tag{3.16c}$$

In terms of the original independent and dependent variables the above can be written as

$$\begin{aligned} u(r,A) = \tilde{u}s \sim A\,(1-r)^{1/5} + \frac{225}{4606}A^3\,(1-r)^{3/5} - \frac{233125}{84860944}A^5\,(1-r) + \\ + \frac{443}{1690}A\,(1-r)^{6/5} + \frac{7260453125}{27751735072544}A^7\,(1-r)^{7/5} + \frac{285305}{17125108}A^3\,(1-r)^{8/5} + \\ + \mathcal{O}(A^9\,(1-r)^{9/5}), \end{aligned} \tag{3.17a}$$

$$\begin{aligned} h(r,A) = \tilde{h}s^4 \sim 2\,\frac{(1-r)^{4/5}}{A} + \frac{725}{4606}A\,(1-r)^{6/5} - \frac{149375}{21215236}A^3\,(1-r)^{8/5} + \\ + \frac{402}{845}\,\frac{(1-r)^{9/5}}{A} + \frac{17243828125}{27751735072544}\,(1-r)^2\,A^5 + \frac{234565}{4281277}\,(1-r)^{\frac{11}{5}}\,A + \\ + \mathcal{O}((1-r)^{\frac{12}{5}}\,A^7), \end{aligned} \tag{3.17b}$$

$$\begin{aligned} \rho(r,A) = \tilde{\rho}^2 s^2 \sim \frac{25}{196}\,(1-r)^{2/5}\,A^2 - \frac{16875}{902776}\,(1-r)^{4/5}\,A^4 + \\ + \frac{47859375}{16632745024}\,(1-r)^{6/5}\,A^6 + \frac{415}{33124}\,(1-r)^{7/5}\,A^2 - \frac{2470519921875}{5439340074218624}\,(1-r)^{8/5}\,A^8 - \\ - \frac{4413625}{1258695438}\,(1-r)^{9/5}\,A^4 + \mathcal{O}((1-r)^2\,A^{10}), \end{aligned} \tag{3.17c}$$

as $r \to 1^-$.

We can now observe that the asymptotic behaviour of the above approximations becomes singular when $A \to \infty$ (note that the limit $A \to 0$ would also cause our approximations to be singular, but that limit is not of any physical significance, therefore we leave it as a purely mathematical curiosity). This suggests that there is a special asymptotic behaviour for $u(r)$, $h(r)$ and $\rho(r)$ that is not contained in the above representation. Nevertheless, the approximations obtained will be used so as to provide the initial conditions to the numerical solver at $r = 1^-$, and to approximate the behaviour of $u(r)$, $h(r)$ and $\rho(r)$ for $r \in [1^-,\ 1]$. In doing so the singularity at $r = 1$ is avoided and numerical solution can be obtained easily. Furthermore, it will be shown that when $A = \mathcal{O}(1)$ then (3.17) provide a roughly satisfactory approximation to the numerical solution, Figure 3.3.

3.1.2 Local analysis as $r \to 0$

Before commencing the discussion regarding the numerical solution, we shall turn our focus to the centre of the heated area. Despite the lack of credibility of the model in the neighbourhood of $r = 0$, since modifications are necessary in order to capture the expected transition (separation) of the horizontal attached flow to the well known vertical plume, the behaviour of the dependent variables in the limit ($r \to 0$) is of mathematical interest at least. For that reason this section is dedicated to the local analysis of governing equations around $r = 0$, beginning with the re-introduction of m and a transformation for the independent variable [2] given as

$$m = r\rho u h \quad \text{and} \quad r = e^{-t}. \tag{3.18}$$

In doing so, multiplication of equation (3.5c) by ρ, results in

$$m(1-\rho) = (1 - e^{-2t})\rho. \tag{3.19}$$

Now the study of limit $r \to 0$ implies $t \to \infty$; therefore, under that limit, equation (3.19) gives

$$m \sim \frac{\rho}{1-\rho}. \tag{3.20}$$

In addition, it is reasonable to expect that as the centre of the plate is approached the density attains a constant value so that, to leading order, $\rho \sim \rho_0 + \mathrm{o}(1)$. In that way equation (3.20) indicates that m to leading order must be given as $m = m_0 + \mathrm{o}(1)$ as $t \to \infty$, with m_0 being a constant. Equation (3.20) therefore changes to

$$m_0 = \frac{\rho_0}{1-\rho_0}. \tag{3.21}$$

Turning the attention to the remaining equations (3.121) and (3.5b), the introduction of transformations (3.18), results in

$$\frac{\mathrm{d}}{\mathrm{dt}}[m] = e^{-2t}\sqrt{\rho}u, \tag{3.22}$$

$$\frac{\mathrm{d}}{\mathrm{dt}}[um] = \frac{1}{2}\,\mathbf{a}e^{-t}\frac{\mathrm{d}}{\mathrm{dt}}\Big[(1-\rho)\frac{e^{2t}m^2}{\rho^2 u^2}\Big]. \tag{3.23}$$

---

[2] The reasoning behind the transformation for the independent variable is not straightforward. In the case that the independent variable remains unchanged, then equation (3.25), is given as

$$r^3 u^3 \rho_0 \frac{\mathrm{d}u}{\mathrm{d}r} \sim \mathbf{a}(u + r\frac{\mathrm{d}u}{\mathrm{d}r}).$$

Then a reasonable way to proceed is by setting (in the same style as in equation (6.30))

$$u(r) = r^{\omega}\breve{u}(r),$$

which unfortunately fails to balance the terms. Thus it is believed that the only way to proceed, is by introducing the transformation $r = e^{-t}$. Another way of looking at it, is that the term multiplying the derivative on the r.h.s (i.e. r), has to somehow vanish.

Considering the limit $t \to \infty$ it is clear that (3.22) does not contribute to any further knowledge since the outcome is that $\frac{\mathrm{d}}{\mathrm{dt}}[m_0] = 0$. Therefore the last resort is the momentum equation, so by taking into account that as $t \to \infty$, the density and subsequently m are constant so that derivatives must vanish to leading order, equation (3.23) gives

$$m_0\frac{\mathrm{du}}{\mathrm{dt}} \sim \frac{e^t\mathbf{a}}{\rho_0^4u^4}\Big[(1-\rho_0)m_0^2\rho_0^2u(u-\frac{\mathrm{du}}{\mathrm{dt}})\Big], \tag{3.24}$$

or

$$e^{-t}u^3\rho_0\frac{\mathrm{d}u}{dt} \sim \mathbf{a}(u-\frac{\mathrm{d}u}{dt}). \tag{3.25}$$

Setting

$$u(t) = e^{\omega t}\breve{u}(t), \tag{3.26}$$

so that equation (3.25) leads to

$$e^{(4\omega-1)t}\breve{u}^3\rho_0(\omega\breve{u}+\frac{\mathrm{d}\breve{u}}{dt}) \sim \mathbf{a}e^{\omega t}(\breve{u}(1-\omega)-\frac{\mathrm{d}\breve{u}}{dt}). \tag{3.27}$$

The r.h.s and l.h.s terms must balance, so the exponentials in this expression are eliminated when choosing $\omega = 1/3$, so that $u(t) = e^{1/3}\breve{u}(t)$. The above stated equation will then simplify to

$$\frac{\mathrm{d}\breve{u}}{dt} \sim \frac{\breve{u}(2\mathbf{a}-\breve{u}^3\rho_0)}{3(\mathbf{a}+\breve{u}^3\rho_0)}. \tag{3.28}$$

As $t \to \infty$, $\breve{u}$ must approach a constant equilibrium value, thus $\frac{\mathrm{d}\breve{u}}{dt} \to 0$. Thus from (3.28) it must hold that

$$\breve{u} \to \left(\frac{2\mathbf{a}}{\rho_0}\right)^{\frac{1}{3}}, \quad \text{as} \quad t \to \infty.$$

Concluding, it follows that the leading order behaviour for u, h, and ρ is given by

$$u(r) \sim (\frac{2\mathbf{a}}{\rho_0})^{\frac{1}{3}}r^{\frac{-1}{3}}, \quad h(r) \sim \left(\frac{\rho_0}{2\mathbf{a}}\right)^{\frac{1}{3}}\frac{r^{\frac{2}{3}}}{1-\rho_0}, \quad \rho \sim \rho_0 \quad \text{as} \quad t \to \infty \quad \text{or} \quad r \to 0. \tag{3.29}$$

Furthermore it should be noted that ρ_0 is a function of $\mathbf{a}$. An approximation of the behaviour of $\rho_0(\mathbf{a})$ is provided along with the numerical results, Figure 3.1.

3.2 Numerical solution

Having established the numerical procedure to be followed, the system of equations given in (3.11) is solved numerically while emphasis is placed on the variation of the dependent variables with the Richardson number of the horizontal flow. Preference is shown to the normalised s-based equations w.r.t $(\tilde{u}, \tilde{h}, \tilde{\rho})$ rather than the original $r-$ based, for reasons of numerical stability. The ICs are provided to the numerical solver by equations (3.16) at $s = 10^{-3}$, while the solution for $s \in [0,\, 10^{-3}]$ is represented by the truncated power series. Numerical integration is applied on the interval $[10^{-3}, 0.99]$. The original nondimensional dependent and independent parameters are recovered and presented in Figure 3.2, after application of the transformations $s = (1-r)^{1/5}$, $u = \tilde{u}s$, $h = \tilde{h}s^4$ and $\rho = \tilde{\rho}^2 s^2$. As $s \to 1$ (equivalently $r \to 0$), numerical results must not be fully embraced. The mathematical model fails to capture the transition of the attached horizontal flow to the vertical plume. It should be expected that a stagnation point must be located at the centre of the circle, as attached horizontal streams approach the axis of symmetry and collide. The collision that takes place must give rise to the roots of the vertical plume. Discussions regarding necessary modifications for the horizontal model, in order to capture the transition from horizontal to vertical, and concerns over the range of validity of the horizontal model are given in following chapters.

On safe grounds, far enough from the centre of the disc, numerical computations indicate that the nondimensional density ρ increases with $\mathbf{a}$, and further as $\mathbf{a} \to \infty$, not far from the edge of the plate, $\rho \to 1$ (i.e. approaches the nondimensional ambient density). Similar behaviour w.r.t $\mathbf{a}$ is observed for the velocity. The height of the horizontal plume is scaled with the constant of entrainment which (for plotting purposes only) in turn is assigned the numeric value widely used for the vertical plume $\alpha = 1/8$. It is observed that the height is decreasing as the Richardson number increases.

Further, in Figure 3.3, results of local analysis at $r = 1$ are being put under scrutiny. As already mentioned the truncated power series obtained are valid at the edge of the plate and provide a sensible approximation to the numerical solution for values of $\mathbf{a} = \mathcal{O}(1)$ whilst they collapse as the value of $\mathbf{a}$ increases. Reasons for the breakdown of the approximations are discussed in detail in the next section.

Concluding, local analysis at $r = 0$ shows that ρ attains an equilibrium value (3.29) depending on $\mathbf{a}$. Numerical solution for different values of $\mathbf{a}$, followed by the extraction of the numerical values for ρ as $r \to 0$ (collection point was set at $s = 0.97$, or equivalently at $r = 0.14127$), allows interpolation of the gathered data using a rational function. It was found that $\rho_0(\mathbf{a})$ behaves as

$$\rho_0(\mathbf{a}) \approx \frac{0.34520\,\mathbf{a} + 0.01665\,\mathbf{a}^2 + 0.00003\,\mathbf{a}^3}{1 + 0.89721\,\mathbf{a} + 0.02499\,\mathbf{a}^2 + 0.00004\,\mathbf{a}^3}. \tag{3.30}$$

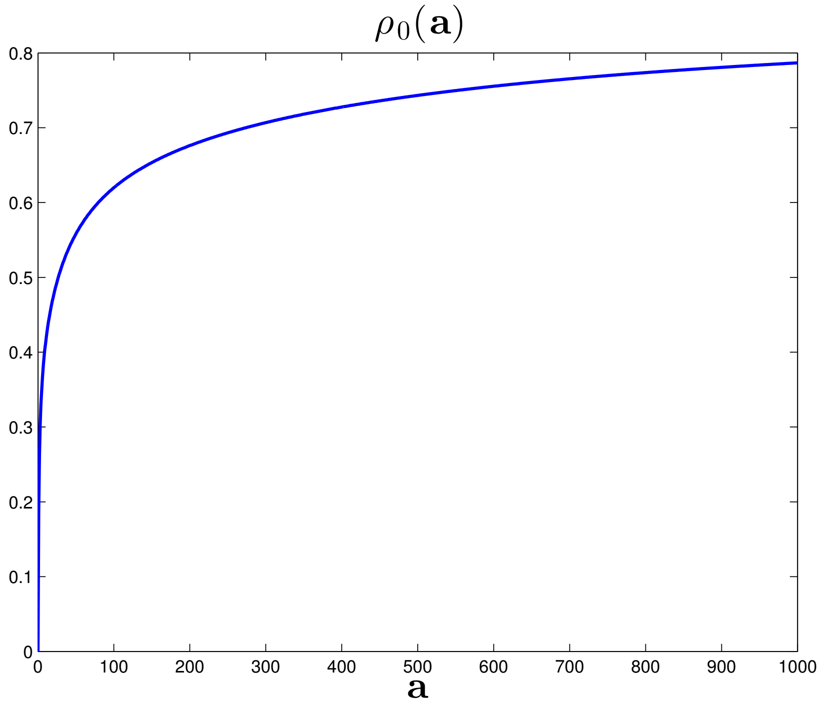

Figure 3.1: Variation of ρ_0 as a function of the Richardson number $\mathbf{a}$, with $\mathbf{a} \in [1, 1000]$. Note that the rational function captures the asymptotic behaviour of ρ_0 i.e. $\rho_0 \to 0$ as $\mathbf{a} \to 0$ and $\rho_0 \to 1$ as $\mathbf{a} \to \infty$.

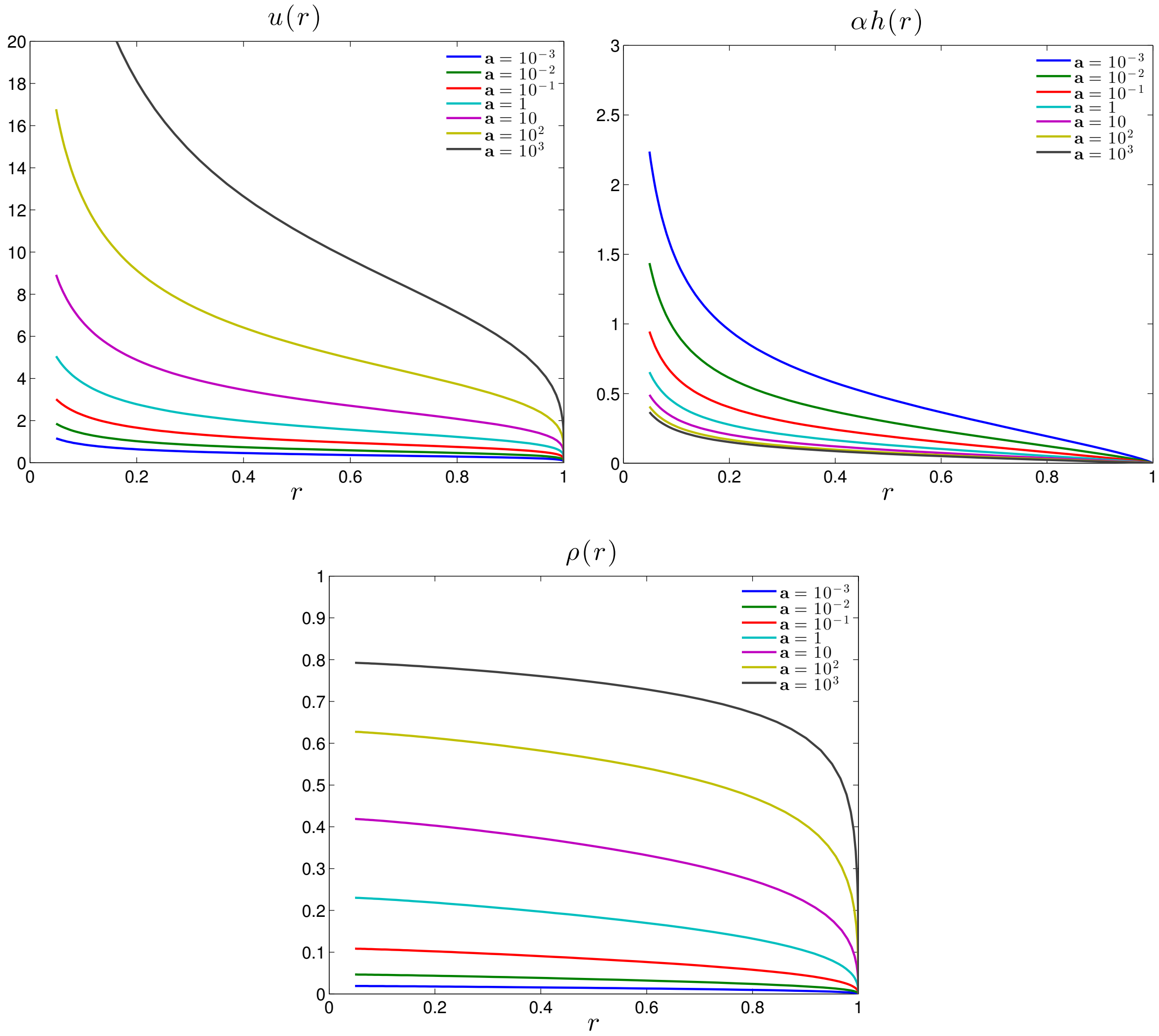

Figure 3.2: Numerical solution for $\mathbf{a} = 10^i$ and $i = -3, -2, \ldots, 2, 3$. Where α is the constant of entrainment, used for the nondimensionalisation of the height of the horizontal plume. The numerical value assigned for the plots is the one widely used for the vertical plume $\alpha = 1/8$.

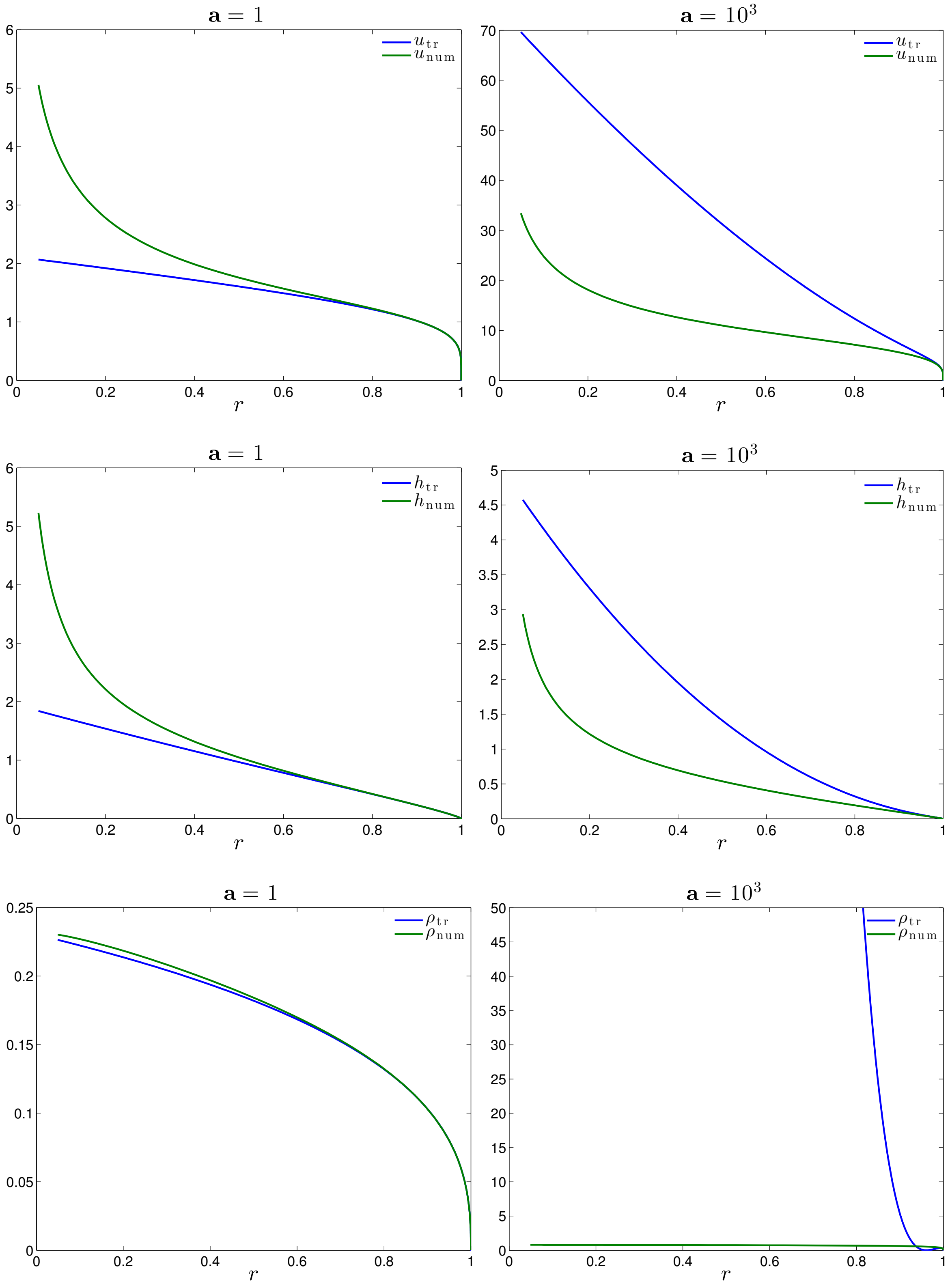

$\mathbf{a} = 1$ $\mathbf{a} = 10^3$

$\mathbf{a} = 1$ $\mathbf{a} = 10^3$

$\mathbf{a} = 1$ $\mathbf{a} = 10^3$

Figure 3.3: Comparison of the numerical solutions with the truncated power series obtained after the conduction of local analysis at $r = 1$ (3.17). It can be noted that while $\mathbf{a} = \mathcal{O}(1)$ results of local analysis provide a rough approximation to the numerical solution. The validity of the approximations collapses as $\mathbf{a}$ increases.

3.3 Inner asymptotic expansions as $A \to \infty$

3.3.1 Introduction

As it was already shown, in the limit $A \to \infty$, or equivalently $\mathbf{a} \to \infty$ the local analysis fails to capture the structure around $r = 1$. The reason for this is the existence of a boundary layer of thickness $\mathcal{O}(1/A)$, located in the neighbourhood of $s = 0$, so that the problem must be treated as a singular perturbation problem. This section is devoted to obtaining the inner and outer asymptotic expansions for large values of **a**. Moving on with the inner approximations, recall that to leading order the truncated series around $s = 0$ (3.16) indicates the following behaviour with respect to A,

$$\tilde{\rho} = A\bar{\rho}, \quad \tilde{u} = A\bar{u}, \quad \tilde{h} = \frac{\bar{h}}{A}. \tag{3.31}$$

By introducing the stretched variable ζ, as suggested by the thickness of the boundary layer (w.r.t the independent variable s), given as

$$s = \frac{\zeta}{A}, \tag{3.32}$$

where $\zeta = \mathcal{O}(1)$ as $A \to \infty$, we consider an asymptotically thin layer located at $r = 1$, or equivalently at $s = 0$, with thickness $s = \mathcal{O}(1/A)$. For that layer asymptotic analysis is carried out for the limit $A \to \infty$. Introducing the new independent variable ζ into equations (3.11a)–(3.11c) gives

$$\Big(1 - \Big(\frac{\zeta}{A}\Big)^5\Big)\tilde{u}\tilde{h}\Big(1 - \Big(\frac{\zeta}{A}\Big)^2\tilde{\rho}^2\Big) = 2 - \Big(\frac{\zeta}{A}\Big)^5, \tag{3.33a}$$

$$\begin{aligned}\zeta\Big(1 - \Big(\frac{\zeta}{A}\Big)^5\Big)(\tilde{u}^2\tilde{h}\tilde{\rho}^2)_\zeta + \Big(8 - 13\Big(\frac{\zeta}{A}\Big)^5\Big)\tilde{u}^2\tilde{h}\tilde{\rho}^2 &= \frac{1}{2}\frac{5^2A^5}{14^2}(1-\zeta^5)\times \\ &\times\left[8\left(1-\tilde{\rho}^2\frac{\zeta^2}{A^2}\right)\tilde{h}^2 + \zeta\left(\left(1-\tilde{\rho}^2\frac{\zeta^2}{A^2}\right)\tilde{h}^2\right)_\zeta\right],\end{aligned} \tag{3.33b}$$

$$\zeta\Big(1 - \Big(\frac{\zeta}{A}\Big)^5\Big)(\tilde{u}\tilde{h}\tilde{\rho}^2)_\zeta + \Big(7 - 12\Big(\frac{\zeta}{A}\Big)^5\Big)\tilde{u}\tilde{h}\tilde{\rho}^2 = 5\Big(1 - \Big(\frac{\zeta}{A}\Big)^5\Big)\tilde{u}\tilde{\rho}. \tag{3.33c}$$

Proceeding further with the substitution of the leading order behaviour $\tilde{\rho} = A\bar{\rho}$, $\tilde{u} = A\bar{u}$, $\tilde{h} = \bar{h}/A$ into equations (3.33a)–(3.33c) such that

$$\Big(1 - \Big(\frac{\zeta}{A}\Big)^5\Big)\bar{u}\bar{h}\Big(1 - \zeta^2\bar{\rho}^2\Big) = 2 - \Big(\frac{\zeta}{A}\Big)^5, \tag{3.34a}$$

$$\zeta\Big(1-\Big(\frac{\zeta}{A}\Big)^5\Big)(\bar{u}^2\bar{h}\bar{\rho}^2)_\zeta+\Big(8-13\Big(\frac{\zeta}{A}\Big)^5\Big)\bar{u}^2\bar{h}\bar{\rho}^2=\frac{1}{2}\frac{5^2}{14^2}\Big(1-\Big(\frac{\zeta}{A}\Big)^5\Big)\times \\ \times\Big[8\left(1-\zeta^2\bar{\rho}^2\right)\bar{h}^2+\zeta\left(\left(1-\zeta^2\bar{\rho}^2\right)\bar{h}^2\right)_\zeta\Big], \quad (3.34b)$$

$$\zeta\Big(1-\Big(\frac{\zeta}{A}\Big)^5\Big)(\bar{u}\bar{h}\bar{\rho}^2)_\zeta+\Big(7-12\Big(\frac{\zeta}{A}\Big)^5\Big)\bar{u}\bar{h}\bar{\rho}^2=5\Big(1-\Big(\frac{\zeta}{A}\Big)^5\Big)\bar{u}\bar{\rho}. \quad (3.34c)$$

We shall now seek inner asymptotic expansions to second order of the following form

$$\bar{\rho}\sim\bar{\rho}_1(\zeta)+A^{P_0}\bar{\rho}_2(\zeta),\quad \bar{u}\sim\bar{u}_1(\zeta)+A^{P_1}\bar{u}_2(\zeta),\quad \bar{h}\sim\bar{h}_1(\zeta)+A^{P_2}\bar{h}_2(\zeta), \quad (3.35)$$

as $A\to\infty$ with $P_0, P_1, P_2 < 0$. As it will become clear, no exact analytical solution can be obtained for leading and second order equations, thus the procedure followed will be as

- Local Analysis at $\zeta = 0$
- Study of the limit $\zeta\to\infty$
- Interpolation by rational functions applied to approximate the numerical solution.

Local analysis around $\zeta = 0$ is necessary for the provision of the ICs to the governing equations to leading and second order, while study of the limit $\zeta\to\infty$, provides the asymptotic behaviour of the dependent variables on that limit. In this manner a complete extremum behaviour w.r.t to ζ, i.e. $\zeta\to 0$ and $\zeta\to\infty$ is attained, and this knowledge will be of importance when the interpolation to the numerical solution will take place. Most importantly though, study of the limit $\zeta\to\infty$ provides the matching conditions with outer asymptotic expansions. Finally for the interpolation, preference is given to rational functions rather than polynomial, while making sure to incorporate the asymptotic structure obtained in the above steps.

3.3.2 Inner expansion and the matching condition to leading order

Substituting the sought form of asymptotic expansions given in (3.35) into equations (3.34), and by keeping leading order terms in the limit $A\to\infty$, the following is obtained

$$\bar{h}_1\bar{u}_1(1-\zeta^2\bar{\rho}_1^2)=2, \quad (3.36a)$$

$$\zeta(\bar{u}_1^2\bar{h}_1\bar{\rho}_1^2)_\zeta + 8\bar{u}_1^2\bar{h}_1\bar{\rho}_1^2 = \frac{1}{2}\frac{5^2}{14^2}\left[8\left(1-\zeta^2\bar{\rho}_1^2\right)\bar{h}_1^2 + \zeta\left(\left(1-\zeta^2\bar{\rho}_1^2\right)\bar{h}_1^2\right)_\zeta\right], \tag{3.36b}$$

$$\zeta(\bar{u}_1\bar{h}_1\bar{\rho}_1^2)_\zeta + 7\bar{u}_1\bar{h}_1\bar{\rho}_1^2 = 5\bar{u}_1\bar{\rho}_1. \tag{3.36c}$$

Local analysis is now carried out at $\zeta = 0$. The behaviour of $\bar{u}_1$, $\bar{h}_1$, $\bar{\rho}_1$ on that limit is obtained, while this information will be used to provide the initial conditions for the numerical solution of equations (3.36). Leading order behaviour can easily be obtained but for the extension of the approximation we resort again to a computer algebra system (**Maple**). Assume power series solutions of the form

$$\bar{u}_1 \sim \bar{u}_{1,0} + \sum_{i=1}^{9}\bar{u}_{1,i}\zeta^i,\ \bar{h}_1 \sim \bar{h}_{1,0} + \sum_{i=1}^{9}\bar{h}_{1,i}\zeta^i, \text{and}\, \bar{\rho}_1 \sim \bar{\rho}_{1,0} + \sum_{i=1}^{9}\bar{\rho}_{1,i}\zeta^i, \tag{3.37}$$

valid in the neighbourhood of $\zeta = 0$, to obtain

$$\bar{u}_1(\zeta) \sim 1 + \frac{225}{4606}\zeta^2 - \frac{233125}{84860944}\zeta^4 + \frac{7260453125}{27751735072544}\zeta^6 + \mathcal{O}(\zeta^8), \tag{3.38a}$$

$$\bar{h}_1(\zeta) \sim 2 + \frac{725}{4606}\zeta^2 - \frac{149375}{21215236}\zeta^4 + \frac{17243828125}{27751735072544}\zeta^6 + \mathcal{O}(\zeta^8), \tag{3.38b}$$

$$\bar{\rho}_1(\zeta) \sim \frac{5}{14} - \frac{3375}{128968}\zeta^2 + \frac{3646875}{1188053216}\zeta^4 - \frac{9978984375}{24282768188476}\zeta^6 + \mathcal{O}(\zeta^8). \tag{3.38c}$$

Note that the coefficients of the above truncated series are directly related to some of the terms given in (3.11).

3.3.3 Study of the limit $\zeta \to \infty$

As was pointed out, there is interest in the behaviour of $\bar{h}_1, \bar{u}_1, \bar{\rho}_1$ as $\zeta \to \infty$. Introducing a new independent variable t, so that $\zeta = e^t$ and $d\zeta = e^t dt$ or $d\zeta = \zeta dt$, and by noting that as $\zeta \to \infty \Rightarrow t \to \infty$, equation (3.36) are reformulated w.r.t to t to take the following form

$$\bar{h}_1\bar{u}_1(1 - e^{2t}\bar{\rho}_1^2) = 2, \tag{3.39a}$$

$$(\bar{u}_1^2\bar{h}_1\bar{\rho}_1^2)_t + 8\bar{u}_1^2\bar{h}_1\bar{\rho}_1^2 = \frac{1}{2}\frac{5^2}{14^2}\left[8\left(1-e^{2t}\bar{\rho}_1^2\right)\bar{h}_1^2 + \left(\left(1-e^{2t}\bar{\rho}_1^2\right)\bar{h}_1^2\right)_t\right], \tag{3.39b}$$

$$(\bar{u}_1\bar{h}_1\bar{\rho}_1^2)_t + 7\bar{u}_1\bar{h}_1\bar{\rho}_1^2 = 5\bar{u}_1\bar{\rho}_1. \tag{3.39c}$$

Proceed using the following *ansatz*:

$$\bar{\rho}_1 = \hat{\rho}_1 e^{-t},\quad \bar{u}_1 = \hat{u}_1 e^{\frac{2t}{3}},\quad \bar{h}_1 = \hat{h}_1 e^{t}, \tag{3.40}$$

for variables $\bar{u}_1$, $\bar{h}_1$, $\bar{\rho}_1$ as $t \to \infty$ with $\hat{\rho}, \hat{h}, \hat{u}$ being treated as constants. Starting with equation (3.39a), by keeping only leading order terms as $t \to \infty$, it must hold that

$$\hat{h}_1 \hat{u}_1 (1 - \hat{\rho}_1^2) = 0 \text{ or } \hat{\rho}_1 = 1. \tag{3.41}$$

Then turning attention to equation (3.39c) to obtain that as $t \to \infty$

$$20 \hat{u}_1 \hat{h}_1 = 15 \hat{u}_1 \text{ or } \hat{h}_1 = \frac{3}{4}. \tag{3.42}$$

Thus far $\hat{\rho}_1$, and $\hat{h}_1$ have been obtained leaving one remaining task which is the calculation of $\hat{u}_1$. Naturally we should resort to equation (3.39b) but the presence of the term $1 - e^{2t}\bar{\rho}_1^2$ on the r.h.s, indicates that no sensible result can be extracted from the information gathered so far. The way to overcome this difficulty is quite straightforward, an extension to the approximation for $\bar{\rho}_1$ needs to be obtained. Going back to equation (3.39a) we can write

$$\hat{h}_1 \hat{u}_1 e^{5t/3} (1 - e^{2t} \bar{\rho}_1^2) \sim 2 \;\Rightarrow\; (1 - e^{2t} \bar{\rho}_1^2) \sim \frac{2}{\hat{h}_1 \hat{u}_1} e^{-5t/3} \;\Rightarrow$$
$$\Rightarrow\; \bar{\rho}_1 \sim e^{-t} - \frac{1}{\hat{h}_1 \hat{u}_1} e^{-8t/3} \text{ as } t \to \infty. \tag{3.43}$$

Apply (3.43) to (3.39b) as $t \to \infty$, to obtain

$$\hat{u}_1 = \left(\frac{5}{14}\right)^{\frac{2}{3}}. \tag{3.44}$$

Collecting, the following behaviour to first order is found as $\zeta \to \infty$

$$\bar{u}_1 \sim \left(\frac{5}{14}\right)^{\frac{2}{3}} \zeta^{\frac{2}{3}},\; \bar{h}_1 \sim \frac{3}{4}\zeta,\; \bar{\rho}_1 \sim \frac{1}{\zeta} - \frac{4}{3}\left(\frac{14}{5}\right)^{\frac{2}{3}} \zeta^{-\frac{8}{3}}, \text{ as } \zeta \to \infty. \tag{3.45}$$

3.3.4 Approximation to second order

The inner solution is now extended to second order. Introducing once more the sought form of asymptotic expansions given by (3.35) into equation (3.34a) but holding on to the second order terms gives

$$\begin{aligned} &A^5 \bar{u}_1 \bar{h}_1 \Big(1 - \zeta^2 \bar{\rho}_1^2\Big) + A^5 \bar{u}_1 \bar{h}_1 \Big(- 2\zeta^2 \bar{\rho}_1 \bar{\rho}_2 A^{P_0} - \zeta^2 \bar{\rho}_2^2 A^{2P_0}\Big) + \\ &+ A^5 \Big(\bar{u}_1 \bar{h}_2 A^{P_2} + \bar{u}_2 \bar{h}_1 A^{P_1} + \bar{u}_2 \bar{h}_2 A^{P_1+P_2}\Big)\Big(1 - \zeta^2 \bar{\rho}_1^2 - 2\zeta^2 \bar{\rho}_1 \bar{\rho}_2 A^{P_0} - \zeta^2 \bar{\rho}_2^2 A^{2P_0}\Big) - \\ &- \zeta^5 \Big(\bar{u}_1 \bar{h}_1 + \bar{u}_1 \bar{h}_2 A^{P_2} + \bar{u}_2 \bar{h}_1 A^{P_1} + \bar{u}_2 \bar{h}_2 A^{P_1+P_2}\Big)\Big(1 - \zeta^2 \bar{\rho}_1^2 - 2\zeta^2 \bar{\rho}_1 \bar{\rho}_2 A^{P_0} - \zeta^2 \bar{\rho}_2^2 A^{2P_0}\Big) \\ &= 2A^5 - \zeta^5. \end{aligned} \tag{3.46}$$

The leading order equation given in (3.36a) can be brought back by keeping terms of $\mathcal{O}(A^5)$, simply by reasoning that the unknown powers P_0, P_1 and P_2 are all negative. Proceeding to second order though is slightly harder and a more detailed study of the equations is required, since full uncovering of the unknown powers is necessary. The way to go is by noting that to the next order inhomogeneous terms ζ^5 and $\zeta^5\bar{u}_1\bar{h}_1\Big(1-\zeta^2\bar{\rho}_1^2\Big)$ must be taken into account so that the trivial solution is avoided. In doing so, we arrive at the conclusion that the following constraints in terms of P_0, P_1 and P_2 must be satisfied

$$P_0 \leq -5, \quad P_1 \leq -5, \quad P_2 \leq -5. \tag{3.47}$$

With the aid of the above constraints, under the same philosophy and the use of (3.35) into equations (3.34b) and (3.34c), it can be shown that a 'meaningful' set of equations is obtained only when

$$P_0 = -5, \quad P_1 = -5, \quad P_2 = -5. \tag{3.48}$$

For the above values of P_0, P_1 and P_2, it is easily found that equations to the next order are given as

$$-\zeta^5\bar{u}_1\bar{h}_1\Big(1-\zeta^2\bar{\rho}_1^2\Big) - 2\zeta^2\bar{u}_1\bar{h}_1\bar{\rho}_1\bar{\rho}_2 + \Big(\bar{u}_1\bar{h}_2+\bar{u}_2\bar{h}_1\Big)\Big(1-\zeta^2\bar{\rho}_1^2\Big) = -\zeta^5, \tag{3.49a}$$

$$\begin{aligned}
&\zeta\Big(\bar{u}_1\bar{\rho}_1\left(2\bar{u}_1\bar{\rho}_2\bar{h}_1+\bar{u}_1\bar{\rho}_1\bar{h}_2+2\bar{u}_2\bar{\rho}_1\bar{h}_1\right)\Big)_\zeta - \zeta^6\Big(\bar{u}_1^2\bar{\rho}_1^2\bar{h}_1\Big)_\zeta - 13\zeta^5\bar{u}_1^2\bar{\rho}_1^2h_1+\\
&+8\bar{u}_1\bar{\rho}_1\left(2\bar{u}_1\bar{\rho}_2\bar{h}_1+\bar{u}_1\bar{\rho}_1\bar{h}_2+2\bar{u}_2\bar{\rho}_1h_1\right) = -\frac{1}{2}\frac{5^2}{14^2}\left[8(1-\zeta^2\bar{\rho}_1^2)\bar{h}_1^2+\zeta\Big((1-\zeta^2\bar{\rho}_1^2)\bar{h}_1^2\Big)_\zeta\right]+\\
&+\frac{1}{2}\frac{5^2}{14^2}\left[16\bar{h}_1\Big(h_2-\zeta^2\left(\bar{h}_2\bar{\rho}_1^2+\bar{h}_1\bar{\rho}_1\bar{\rho}_2\right)\Big)+2\zeta\Big(\bar{h}_1\Big(\bar{h}_2-\zeta^2\left(\bar{h}_2\bar{\rho}_1^2+\bar{h}_1\bar{\rho}_1\bar{\rho}_2\right)\Big)\Big)_\zeta\right],
\end{aligned} \tag{3.49b}$$

$$\begin{aligned}
&-\zeta^6\bar{u}_1\Big(\bar{u}_1\bar{h}_1\bar{\rho}_1^2\Big)_\zeta + \zeta\Big(\bar{u}_1\bar{h}_2\bar{h}_1\bar{\rho}_1^2+2\bar{u}_1\bar{h}_1\bar{\rho}_1\bar{\rho}_2\Big)_\zeta - 12\zeta^5\bar{u}_1\bar{h}_1\bar{\rho}_1^2+\\
&\qquad+14\bar{u}_1\bar{h}_1\bar{\rho}_1\bar{\rho}_2+7\bar{u}_1\bar{h}_2\bar{\rho}_1^2 = -5\zeta^5\bar{u}_1\bar{\rho}_1+5\Big(\bar{u}_1\bar{\rho}_2+\bar{u}_2\bar{\rho}_1\Big).
\end{aligned} \tag{3.49c}$$

Equations (3.49) do not admit exact analytic solution, therefore once more the local analysis is performed at $\zeta \to 0$, while the behaviour of $\bar{u}_2$, $\bar{h}_2$, $\bar{\rho}_2$, in the limit $\zeta \to \infty$ is examined. Beginning with the local analysis, the power series solution of the form

$$\bar{u}_2 \sim \bar{u}_{2,0} + \sum_{i=1}^{11}\bar{u}_{2,i}\zeta^i,\ \bar{h}_2 \sim \bar{h}_{2,0} + \sum_{i=1}^{11}\bar{h}_{2,i}\zeta^i, \text{and}\ \bar{\rho}_2 \sim \bar{\rho}_{2,0} + \sum_{i=1}^{11}\bar{\rho}_{2,i}\zeta^i, \tag{3.50}$$

is once more assumed. The computed approximations are listed below

$$\bar{u}_2(\zeta) \sim \frac{443}{1690}\,\zeta^5 + \frac{285305}{17125108}\,\zeta^7 - \frac{533529490625}{477371153555296}\,\zeta^9 + \mathcal{O}(\zeta^{11}), \tag{3.51a}$$

$$\bar{h}_2(\zeta) \sim \frac{402}{845}\,\zeta^5 + \frac{234565}{4281277}\,\zeta^7 - \frac{528950768375}{179014182583236}\,\zeta^9 + \mathcal{O}(\zeta^{11}), \tag{3.51b}$$

$$\bar{\rho}_2(\zeta) \sim \frac{83}{4732}\,\zeta^5 - \frac{5212975}{1438509072}\,\zeta^7 + \frac{13637575915625}{20049588449322432}\,\zeta^9 + \mathcal{O}(\zeta^{11}), \tag{3.51c}$$

valid as $\zeta \to 0$. It must be noted that the above truncated series, are necessary for the supply of ICs around $\zeta = 0$, when solving equations (3.36) and (3.49) numerically.

Turning onto the asymptotic behaviour of $\bar{u}_2$, $\bar{h}_2$ and $\bar{\rho}_2$ as $\zeta \to \infty$, by recollecting the behaviour of the leading order variables on that limit (3.45), we shall proceed with the following *ansatz*:

$$\begin{aligned} &\bar{u}_1 \sim \left(\frac{5}{14}\right)^{\frac{2}{3}} \zeta^{\frac{2}{3}},\ \bar{h}_1 \sim \frac{3}{4}\zeta,\ \bar{\rho}_1 \sim \frac{1}{\zeta} - \frac{4}{3}\left(\frac{14}{5}\right)^{\frac{2}{3}} \zeta^{-\frac{8}{3}}, \\ &\qquad \bar{u}_2 \sim \hat{u}_2 \zeta^{\frac{17}{3}}, \quad \bar{h}_2 \sim \hat{h}_2 \zeta^6, \quad \bar{\rho}_2 \sim \hat{\rho}_2 \zeta^{\frac{7}{3}} \quad \text{as} \quad \zeta \to \infty, \end{aligned} \tag{3.52}$$

with $\hat{u}_2$, $\hat{h}_2$ and $\hat{\rho}_2$ unknown constants. Substituting (3.52) into equations (3.49) and keeping leading order terms as $\zeta \to \infty$ results in a 3×3 system, listed below:

$$\begin{gathered} 18\,\lambda^2 + 27\,\lambda^3 \hat{\rho}_2 - 48\,\lambda^2 \hat{h}_2 - 36\,\hat{u}_2 \lambda = 0, \\ 252\,\lambda^3 \hat{h}_2 + 81\,\hat{u}_2 \lambda^2 - 81\,\lambda^3 = 0, \\ -4800\,\lambda\,\hat{h}_2 - 14112\,\lambda^4 + 18816\,\lambda^4 \hat{h}_2 + 28224\,\lambda^3 \hat{u}_2 + 1350\,\lambda^2 \hat{\rho}_2 + 1125\,\lambda = 0, \end{gathered} \tag{3.53}$$

with $\lambda = (5/14)^{2/3}$. From the solution of (3.53) $\hat{u}_2$, $\hat{h}_2$ and $\hat{\rho}_2$ are easily obtained as

$$\hat{u}_2 = \frac{5}{48}\left(\frac{14}{5}\right)^{\frac{1}{3}}, \quad \hat{h}_2 = \frac{51}{224}, \quad \hat{\rho}_2 = \frac{16}{45}\left(\frac{5}{14}\right)^{\frac{1}{3}}. \tag{3.54}$$

Therefore the behaviour of the variables $\bar{u}_2$, $\bar{h}_2$ and $\bar{\rho}_2$ as $\zeta \to \infty$ is known and given as

$$\bar{u}_2(\zeta) \sim \frac{5}{48}\left(\frac{14}{5}\right)^{\frac{1}{3}} \zeta^{\frac{17}{3}}, \quad \bar{h}_2(\zeta) \sim \frac{51}{224}\zeta^6, \quad \bar{\rho}_2(\zeta) \sim \frac{16}{45}\left(\frac{5}{14}\right)^{\frac{1}{3}} \zeta^{\frac{7}{3}} \quad \text{as} \quad \zeta \to \infty. \tag{3.55}$$

3.4 The matching conditions

At this point a pause might be valuable, to allow a recollection of the transformations on dependent and independent variables applied thus far, to take place. The starting point was the nondimensional independent variable $r \in (0,\, 1]$, representing the radius of the circular disk, and dependent variables $\rho(r)$, $u(r)$ and $h(r)$ representing nondimensional density, velocity and height of the horizontal attached flow respectively. On performing local analysis at the edge of the disc ($r = 1$) the following transformations were found to be appropriate,

- $r = 1 - s^5$, $A = \left(\frac{196\mathbf{a}}{25}\right)^{1/5}$, $u = \tilde{u}s$, $h = \tilde{h}s^4$ and $\rho = \tilde{\rho}^2 s^2$.

The above transformations enabled us to perform local analysis at $s = 0$, instead. Furthermore, it was found that by disregarding the significance of A, i.e $A = \mathcal{O}(1)$, the structure of the coordinate expansion for $\tilde{\rho}(s)$, $\tilde{u}(s)$ and $\tilde{h}(s)$ achieves some limited success in approximating the solution. When A is treated as it should be, a physical parameter attaining large values, the resulting parametric expansions fail dramatically to capture the behaviour of the solution. The collapse is attributed to the existence of a boundary layer of thickness of $\mathcal{O}(1/\mathbf{a})$ located at the edge of the disc ($r = 1$) or equivalently at $s = 0$. The presence of a boundary layer indicates that the problem has to be treated as singular perturbation problem with a small parameter $1/A^5$. The existence of a boundary layer required the introduction of a stretched variable ζ as is usually the case, in addition to further scaling of the dependent variables, now $\tilde{\rho}$, $\tilde{u}$, $\tilde{h}$, which were given as

- $\zeta = As$, $\tilde{u} = A\bar{u}$, $\tilde{h} = \bar{h}/A$ and $\tilde{\rho} = A\bar{\rho}$.

In this way it was found that to second order the inner asymptotic expansions take the following form

$$\bar{u}(\zeta) \sim \bar{u}_1 + A^{-5}\bar{u}_2,\ \bar{h}(\zeta) \sim \bar{h}_1 + A^{-5}\,\bar{h}_2\bar{\rho}(\zeta) \sim \bar{\rho}_1 + A^{-5}\bar{\rho}_2. \tag{3.56}$$

The above inner asymptotic expansions were constructed in the limiting procedure $\zeta = \mathcal{O}(1)$ and $1/\mathbf{a} \to 0$, in order to approximate the solution in the thin strip (boundary layer) placed at the edge of the plate. The validity of these asymptotic expansions can be extended by making use of **Kaplun's Extension Theorem** [77],[18], formulated w.r.t the current problem[3] as:

Theorem 1 *Let* $\bar{u}(\zeta, 1/\boldsymbol{a})$, $\bar{h}(\zeta, 1/\boldsymbol{a})$, $\bar{\rho}(\zeta, 1/\boldsymbol{a})$ *be functions of coordinate* ζ *and a small parameter* $1/\boldsymbol{a}$. *In addition, allow the following*

$$\bar{u}(\zeta, 1/\boldsymbol{a}) = \sum_{j=0}^{k} \psi_j(1/\boldsymbol{a}) x_j(\zeta) + ..., \ \bar{h}(\zeta, 1/A) = \sum_{j=0}^{k} \phi_j(1/A) y_j(\zeta) + ...,$$

$$\bar{\rho}(\zeta, 1/\boldsymbol{a}) = \sum_{j=0}^{k} \mu_j(1/\boldsymbol{a})_j \nu_j(\zeta) + ... \quad (3.57)$$

to be asymptotic expansions of the Poincaré type valid on the interval $\zeta \in [\zeta_0,\, 1]$, *where* $\zeta_0 > 0$ *and* $1 - \zeta_0 = \mathcal{O}(1/\boldsymbol{a})$. *Then the above are valid in an extended interval* $\zeta \in [\zeta_1,\, 1]$ *such that* $1 - \zeta_1 = \epsilon(1/\boldsymbol{a}) \to 0$ *as* $1/\boldsymbol{a} \to 0$ *and* $1/\boldsymbol{a} \ll \epsilon(1/\boldsymbol{a}) \ll 1$.

In other words the validity of the inner approximations is not restricted in the inner region but can penetrate further into the left of the original domain of uniformity. The new extended domain includes the famous overlap region. It is the existence of this region that allows the matching procedure, since the inner asymptotic expansions do not hold the monopoly of validity, in addition the outer asymptotic expansions are valid in this region. Based now on Prandtl's Matching rule, which can be thought of as continuity to the sought solution in this region, we shall require that as $1/\mathbf{a} \to 0$

$$\lim_{\zeta\to\infty} u(\zeta) = \lim_{r\to1} u(r), \ \lim_{\zeta\to\infty} h(\zeta) = \lim_{r\to1} h(r), \ \text{and} \ \lim_{\zeta\to\infty} \rho(\zeta) = \lim_{\rho\to1} u(r), \quad (3.58)$$

In examining the limit $\zeta \to \infty$ it was found that

$$\bar{u}(\zeta) \sim \bar{u}_1 + A^{-5}\bar{u}_2 = \left(\frac{5}{14}\right)^{\frac{2}{3}} \zeta^{\frac{2}{3}} + A^{-5}\frac{5}{48}\left(\frac{14}{5}\right)^{\frac{1}{3}} \zeta^{\frac{17}{3}}, \quad (3.59a)$$

$$\bar{h}(\zeta) \sim \bar{h}_1 + A^{-5}\bar{h}_2 = \frac{3}{4}\zeta + A^{-5}\frac{51}{224}\zeta^6, \quad (3.59b)$$

$$\bar{\rho}(\zeta) \sim \bar{\rho}_1 + A^{-5}\bar{\rho}_2 = \frac{1}{\zeta} - \frac{4}{3}\left(\frac{14}{5}\right)^{\frac{2}{3}} \zeta^{-\frac{8}{3}} + A^{-5}\frac{16}{45}\left(\frac{5}{14}\right)^{\frac{1}{3}} \zeta^{\frac{7}{3}}. \quad (3.59c)$$

Expressing equations (3.59a)-(3.59c) in terms of the original variables gives

$$u(r) \sim \left[(1-r)^{\frac{1}{3}} + \frac{7}{24}(1-r)^{\frac{4}{3}}\right]\mathbf{a}^{\frac{1}{3}}, \quad (3.60a)$$

---

[3] Even though here the theorem is applied to the inner asymptotic expansion, it is a general result for asymptotic expansions, so that it holds for the outer asymptotic expansions.

$$h(r) \sim \frac{3}{4}\,(1-r) + \frac{51}{224}\,(1-r)^2, \tag{3.60b}$$

$$\begin{aligned}\rho(r) \sim 1 - \left[\frac{8}{3}\,(1-r)^{-\frac{1}{3}} - \frac{16}{63}\,(1-r)^{\frac{2}{3}}\right]\mathbf{a}^{-\frac{1}{3}} + \\ + \left[\frac{16}{9}\,(1-r)^{-\frac{2}{3}} - \frac{64}{189}\,(1-r)^{\frac{1}{3}} + \frac{64}{3969}(1-r)^{\frac{4}{3}}\right]\mathbf{a}^{-\frac{2}{3}}.\end{aligned} \tag{3.60c}$$

The above being valid in a range of the form $1/\mathbf{a} \ll 1-r \ll 1$ for $\mathbf{a} \gg 1$, will provide the matching conditions with the outer expansions. Being more precise the above conditions do provide the matching with the leading order terms for u and h, while qualitative information is provided for ρ to the second order. Knowledge of the above will be valuable in constructing the outer asymptotic expansions.

3.5 Semi-analytical solutions for the inner asymptotic expansions

Having obtained inner asymptotic expansions to second order, this section is dedicated to the interpolation of the dependent variables $\bar{u}_1, \bar{u}_2$, $\bar{h}_1, \bar{h}_2$ and $\bar{\rho}_1, \bar{\rho}_2$. For the interpolation, rational functions will be preferred over polynomial functions in order to avoid unnecessary oscillations [11] . The construction of the rational functions though, say $Q(\zeta)/M(\zeta)$, is not straightforward. Caution is required not to neglect the nature of the variables that are being interpolated. Recall that the validity of the inner approximations is not restricted only for $\zeta = \mathcal{O}(1)$, inner approximations are also valid in the overlap region so that the behaviour of the dependent variables on the limit $\zeta \to \infty$ somehow needs to be included in the analytical approximations. Furthermore, local analysis at $\zeta = 0$ provided the ICs for the numerical solution of systems (3.36)–(3.49). Thus it is additionally important to incorporate that behaviour into the approximations.

The methodology followed consists of three steps. Starting with the construction of a function of the same limiting behaviour at $\zeta = 0$ and $\zeta \to \infty$ as the dependent variable under consideration, proceeding with a normalisation of the numerical solution with the newly introduced function and finally interpolating the resulting normalised function using a rational function.

3.5.1 Approximation for $\bar{u}_1$, $\bar{h}_1$ and $\bar{\rho}_1$

It was found that the behaviour of $\bar{u}_1$ in the the two 'extreme' limiting values of ζ is given as:

$$\bar{u}_1(\zeta) = \begin{cases} 1 & \text{as} \quad \zeta \to 0 \\ \left(\frac{5}{14}\right)^{\frac{2}{3}} \zeta^{\frac{2}{3}} & \text{as} \quad \zeta \to \infty. \end{cases} \tag{3.61}$$

We begin with the introduction of z, where

$$z = \frac{\zeta}{\zeta+1} = \begin{cases} 0 & \text{as} \quad \zeta \to 0 \\ 1 & \text{as} \quad \zeta \to \infty. \end{cases} \tag{3.62}$$

A function that has the same limiting behaviour as $\bar{u}_1$ is listed below:

$$U_1(\zeta) = 1 - z + \left(\frac{5}{14}\right)^{\frac{2}{3}} z\, \zeta^{\frac{2}{3}}. \tag{3.63}$$

As it was discussed earlier this limiting behaviour has to be taken into account in the analytical approximation. Thus $\bar{u}_1$ is approximated as

$$\bar{u}_{1\mathrm{apr}} = U_1 \bar{u}_{1\mathrm{rat}}. \tag{3.64}$$

A suitable rational function $\bar{u}_{1\mathrm{rat}}$ was found to be

$$\bar{u}_{1rat} = 1 + \frac{(0.97796 - 1.0764\, z + 0.33330\, z^2)\, z\, (1-z)}{1 - 2.6042\, z + 2.5885\, z^2 - 0.98384\, z^3}. \tag{3.65}$$

In Figure 3.4, a comparison between numerical and analytical approximation is displayed. In a similar manner for $\bar{h}_1$ the following limiting behaviour was found

$$\bar{h}_1(\zeta) = \begin{cases} 2 & \text{as} \quad \zeta \to 0 \\ \frac{3\zeta}{4} & \text{as} \quad \zeta \to \infty. \end{cases} \tag{3.66}$$

A function that captures this limiting behaviour is

$$H_1 = 2 - 2z + z\,\frac{3\zeta}{4}. \tag{3.67}$$

Using this information, $\bar{h}_1$ is approximated as

$$\bar{h}_{1\mathrm{apr}} = H_1 \bar{h}_{1\mathrm{rat}}, \tag{3.68}$$

where $\bar{h}_{1rat}$ is given by

$$\bar{h}_{1\mathrm{rat}} = 1 + \frac{(1.0218 - 0.53137\, z)\, z\, (1-z)}{1 - 2.0836\, z + 1.5088\, z^2}. \tag{3.69}$$

A comparison between the approximate and numerical solution is plotted in Figure 3.4. Solving for $\zeta^2\bar{\rho}_1$, in equation (3.36a), to obtain

$$\zeta^2\bar{\rho}_1^2 = 1 - \frac{2}{\bar{h}_1\bar{u}_1}. \tag{3.70}$$

Thus usage of the approximations obtained so far for $\bar{u}_{1\text{apr}}$, $\bar{h}_{1\text{apr}}$ allows for an approximation for $\bar{\rho}_1$ as

$$\zeta^2\bar{\rho}_{1\text{apr}} = 1 - \frac{2}{\bar{h}_{1\text{apr}}\bar{u}_{1\text{apr}}}. \tag{3.71}$$

In Figure 3.4 the numerical solution obtained for $\zeta^2\bar{\rho}_1^2$ is compared with the analytical approximation $\zeta^2\bar{\rho}_{1\text{apr}}^2$. Note that the oscillations evident as $z \to 0$ are due to very small numerical oscillations exaggerated by the fine-scale of the vertical axis. Errors are typically of the order of 0.1% with a maximum below 1%.

3.5.2 Approximation for $\bar{u}_2$, $\bar{h}_2$ and $\bar{\rho}_2$

The same methodology is now applied to the next order terms. Starting with $\bar{u}_2$ it was found that $\bar{u}_2$ has the following asymptotic behaviour in the distinct limits of $\zeta \to 0$ and $\zeta \to \infty$:

$$\bar{u}_2(\zeta) = \begin{cases} \dfrac{443}{1690}\zeta^5 & \text{as} \quad \zeta \to 0 \\[2ex] \dfrac{5}{48}\left(\dfrac{14}{5}\right)^{\frac{1}{3}}\zeta^{\frac{17}{3}} & \text{as} \quad \zeta \to \infty. \end{cases} \tag{3.72}$$

Defining as U_2, a function that contains the above limiting behaviour is:

$$U_2 = \frac{443}{1690}\zeta^5\frac{1}{\zeta+1} + \frac{5}{48}\left(\frac{14}{5}\right)^{\frac{1}{3}} z\,\zeta^{\frac{17}{3}}, \tag{3.73}$$

the analytical approximation to $\bar{u}_2$ will be of the form

$$\bar{u}_{2\text{apr}} = U_2\bar{u}_{2\text{rat}}, \tag{3.74}$$

where $\bar{u}_{2\text{rat}}$ was computed to be given as

$$\bar{u}_{2rat} = 1 + \frac{(0.93670 - 0.18821\,z)\,z\,(1-z)}{1 - 1.4630\,z + 1.2882\,z^2}. \tag{3.75}$$

Moving to $\bar{h}_2$ the following has been obtained thus far

$$\bar{h}_2(\zeta) = \begin{cases} \dfrac{402}{845}\zeta^5 & \text{as} \quad \zeta \to 0 \\[2ex] \dfrac{51}{224}\zeta^6 & \text{as} \quad \zeta \to \infty. \end{cases} \tag{3.76}$$

Once more, defining a function H_2 which incorporates the above behaviour

$$H_2 = \frac{402}{845}\,\zeta^5 \frac{1}{\zeta+1} + \frac{51}{224}\,z\zeta^6, \tag{3.77}$$

the approximation for $\bar{h}_2$ will be given as

$$\bar{h}_{2apr} = H_2 \bar{h}_{2rat}, \tag{3.78}$$

and

$$\bar{h}_{2rat} = 1 + \frac{(0.98710 - 0.29557\,z)\,z\,(1-z)}{1 - 1.9856\,z + 1.6486\,z^2}. \tag{3.79}$$

Concluding for $\bar{\rho}_2$, equation (3.49a) can be simplified with the aid of equation (3.36a) i.e.

$$\bar{\rho}_2 = \frac{\left(\bar{u}_1 \bar{h}_2 + \bar{u}_2 \bar{h}_1\right)\left(1 - \zeta^2 \bar{\rho}_1{}^2\right) - \zeta^5}{2\zeta^2 \bar{u}_1 \bar{h}_1 \bar{\rho}_1}. \tag{3.80}$$

Direct application of the analytical approximations ($\bar{u}_{1\mathrm{apr}}$,$\bar{u}_{2\mathrm{apr}}$, $\bar{\rho}_{1\mathrm{apr}}$ and $\bar{h}_{1apr}$, $\bar{h}_{2\mathrm{apr}}$) obtained so far into (3.80) gives an analytical approximation for $\bar{\rho}_2$.

The performance of the second order analytical approximations are given in Figure 3.5. Further maximum absolute and relative errors are listed on Table 3.1

f	$\max\lvert \mathrm{f} - \mathrm{f_{ap}} \rvert$	$\max \frac{\lvert \mathrm{f} - \mathrm{f_{ap}} \rvert}{\lvert \mathrm{f} \rvert}$
$\bar{u}_1$	6.5027e-03	1.2248e-03
$\bar{u}_2$	9.5122e-03	2.6580e-03
$\bar{h}_1$	3.1893e-02	1.2445e-03
$\bar{h}_2$	1.9899e-02	4.6018e-03
$\bar{\rho}_1$	9.5613e-01	2.7131e-03

Table 3.1: Maximum values of Absolute and Relative Erros of the approximations. The values are obtained for $z \in [10^{-3} 0.97143]$.

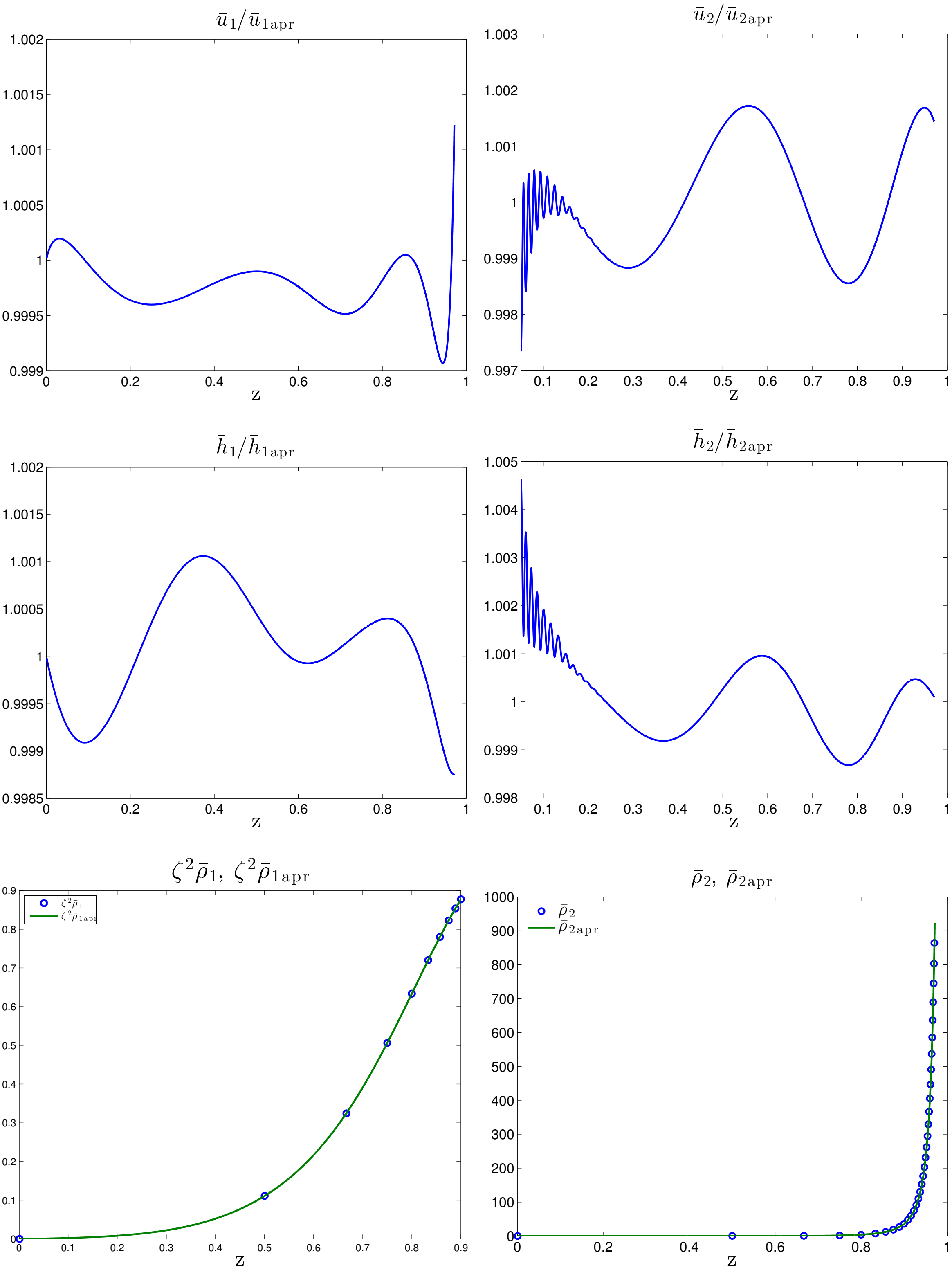

Figure 3.4: Comparison of the numerical solutions with analytic approximations, while $z \in [10^{-3}, 0.97143]$. The oscillations evident as $z \to 0$ are due to very small numerical oscillations exaggerated by the fine-scale of the vertical axis.

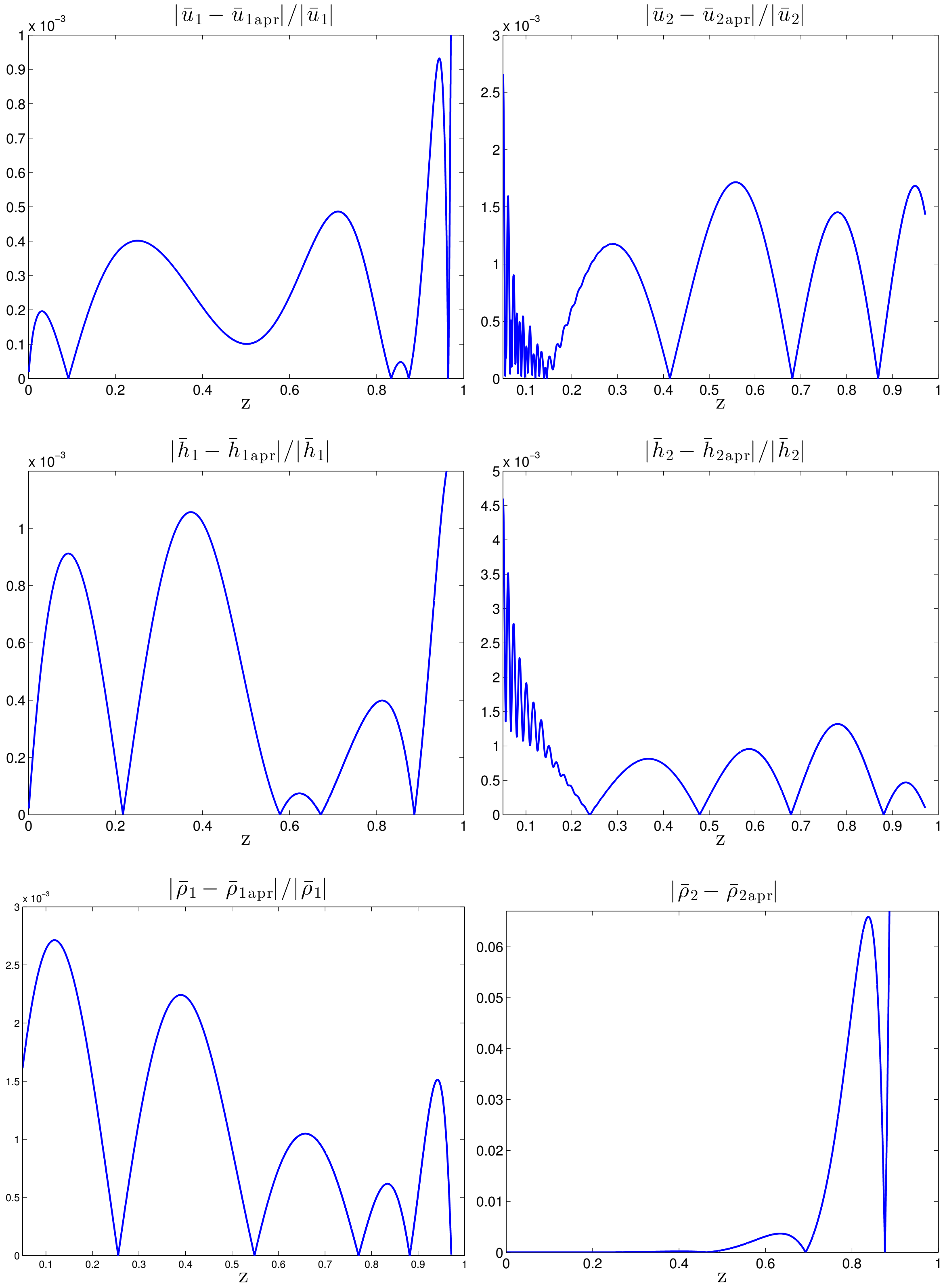

$|\bar{u}_1 - \bar{u}_{1\mathrm{apr}}|/|\bar{u}_1|$

$|\bar{u}_2 - \bar{u}_{2\mathrm{apr}}|/|\bar{u}_2|$

$|\bar{h}_1 - \bar{h}_{1\mathrm{apr}}|/|\bar{h}_1|$

$|\bar{h}_2 - \bar{h}_{2\mathrm{apr}}|/|\bar{h}_2|$

$|\bar{\rho}_1 - \bar{\rho}_{1\mathrm{apr}}|/|\bar{\rho}_1|$

$|\bar{\rho}_2 - \bar{\rho}_{2\mathrm{apr}}|$

Figure 3.5: Comparison of the numerical solutions with analytic approximations, while $z \in [10^{-3}, 0.97143]$. The oscillations evident as $z \to 0$ are due to very small numerical oscillations exaggerated by the fine-scale of the vertical axis.

3.6 Outer asymptotic expansions $\mathbf{a} \to \infty$

We begin by recalling that the system of the governing equations in nondimensional form was found to be given as

$$ruh(1-\rho) = 1 - r^2,$$

$$\frac{\mathrm{d}}{\mathrm{dr}}\left[ru^2h\rho\right] = \frac{1}{2}\mathbf{a}r\frac{\mathrm{d}}{\mathrm{dr}}\left[(1-r^2)h^2\right],$$

$$\frac{\mathrm{d}}{\mathrm{dr}}[ruh\rho] = -r\sqrt{\rho}u.$$

In this section the asymptotic analysis of the governing equations is based on the distinguished limit $\mathbf{a} \to \infty$ and $r = \mathcal{O}(1)$. In seeking outer asymptotic expansion in the limit $\mathbf{a} \to \infty$, the matching with inner solutions (3.60) suggests the following behaviour to leading order

$$u(r) \sim \mathbf{a}^{\frac{1}{3}}u_1(r), \quad h(r) \sim h_1(r), \quad \rho(r) \sim 1 - \mathbf{a}^{-\frac{1}{3}}\rho_1(r). \tag{3.81}$$

Further examination of the matching conditions indicate that when trying to extend the approximation to second order, available information exists only for the density i.e. $\mathcal{O}(\mathbf{a}^{-2/3})$. Therefore the general form of the outer asymptotic solutions to second order can be assumed to be given as

$$\rho(r) \sim 1-\mathbf{a}^{-\frac{1}{3}}\rho_1(r)+\mathbf{a}^{-\frac{2}{3}}\rho_2(r),\ u(r) \sim \mathbf{a}^{\frac{1}{3}}u_1(r)+\mathbf{a}^{P_u}u_2(r),\ \text{and}\, h(r) \sim h_1(r)+\mathbf{a}^{P_h}h_2(r),$$
$$\text{as} \quad \mathbf{a} \to \infty \,\text{with}\, r \,\text{fixed while}\, P_u < \frac{1}{3} \,\text{and}\, P_h < 0. \tag{3.82}$$

Applying the proposed form of the asymptotic expansions given in (3.82) into the algebraic equation (3.5c) gives

$$r\Big(u_1h_1\rho_1 - u_1h_1\rho_2\mathbf{a}^{-\frac{1}{3}}\Big) + r\Big(u_1h_2\mathbf{a}^{\frac{1}{3}+P_h} + u_2h_1\mathbf{a}^{P_u} + u_2h_2\mathbf{a}^{P_u+P_h}\Big)\times$$
$$\times\left(\rho_1\mathbf{a}^{-\frac{1}{3}} - \rho_2\mathbf{a}^{-\frac{2}{3}}\right) = 1 - r^2. \tag{3.83}$$

By keeping in mind the constraints $P_u < 1/3$, and $P_h < 0$, it is not hard to see that to leading order, terms of $\mathcal{O}(1)$ must be retained. When considering the terms that must be kept to the next order approximation, a more careful analysis is required. Contenders for the second order approximation must be terms having either one of the the following orders $\mathcal{O}(\mathbf{a}^{P_u-1/3})$, $\mathcal{O}(\mathbf{a}^{P_h})$ and $\mathcal{O}(\mathbf{a}^{-1/3})$, a combination of these or all of them. Distinguishing between different cases, we start by assuming that one term dominates over the others. For example lets say $P_u - 1/3 > P_h > -1/3$, in which case to second order the resulting equation should be given as $u_2 h_1 \rho_1 = 0$. Similar homogeneous equations which would lead to the trivial zero solution would be obtained by keeping only one dominant term. Considering now the option that two terms balance and dominate over the remaining one, i.e say that $P_u - 1/3 = P_h > -1/3$, which would result to second order that the following is valid, $\rho_1(u_1 h_2 + u_2 h_1) = 0$ or simply $u_1 h_2 + u_2 h_1 = 0$. To see where this causes a problem another governing equation needs to be brought in. By substituting (3.82) in the conservation of mass equation (3.121) the following is obtained

$$\left[r\left(u_1 h_1 \mathbf{a}^{\frac{1}{3}} + u_1 h_2 \mathbf{a}^{\frac{1}{3}+P_h} + u_2 h_1 \mathbf{a}^{P_u} + u_2 h_2 \mathbf{a}^{P_u+P_h}\right)\left(1 - \rho_1 \mathbf{a}^{-\frac{1}{3}} + \rho_2 \mathbf{a}^{-\frac{2}{3}}\right)\right]_r = \\ = -r\left(u_1 \mathbf{a}^{\frac{1}{3}} + u_2 \mathbf{a}^{P_u} - \frac{1}{2} u_1 \rho_1 - \frac{1}{2} u_2 \rho_1 \mathbf{a}^{-\frac{1}{3}+P_u}\right). \quad (3.84)$$

Note that the r.h.s term in equation (3.84) is acquired after the following approximation

$$\sqrt{\rho} \sim \left(1 - \mathbf{a}^{-\frac{1}{3}}\rho_1 + \mathbf{a}^{-\frac{2}{3}}\rho_2\right)^{1/2} \sim 1 - \frac{1}{2}\rho_1 \mathbf{a}^{-\frac{1}{3}} + \mathcal{O}(\mathbf{a}^{-\frac{2}{3}}) \quad \text{as} \quad \mathbf{a} \to \infty. \quad (3.85)$$

To leading order, we shall hold on to terms of $\mathbf{a}^{1/3}$, while to second order the resulting equation will be $[r(u_1 h_2 + u_2 h_1)]_r = -r u_2$, but by recalling that $(u_1 h_2 + u_2 h_1) = 0$ this would result again in a trivial solution $u_2 = 0$. The concluding remark is that all terms must balance and be included. Therefore the following must hold

$$Pu - \frac{1}{3} = P_h = -\frac{1}{3} \quad \text{or} \quad P_u = 0 \quad \text{and} \quad P_h = -\frac{1}{3}. \quad (3.86)$$

Now the outer asymptotic structure to second order has been established to be of the following form

$$\rho(r) \sim 1 - \mathbf{a}^{-\frac{1}{3}}\rho_1(r) + \mathbf{a}^{-\frac{2}{3}}\rho_2(r),\ u(r) \sim \mathbf{a}^{\frac{1}{3}} u_1(r) + u_2(r) \quad \text{and} \\ h(r) \sim h_1(r) + \mathbf{a}^{-\frac{1}{3}} h_2(r) \quad \text{as} \quad \mathbf{a} \to \infty. \quad (3.87)$$

3.6.1 Approximation to leading and second order

Knowledge of the form of the asymptotic expansions to second order enables us to proceed. Therefore, substituting the sought form of the solution (3.87) into the governing equations (3.5), to obtain as $\mathbf{a} \to \infty$ to leading order

$$r u_1 h_1 \rho_1 = 1 - r^2 \quad (3.88a)$$

$$\left(ru_1^2h_1\right)_r = \frac{1}{2}r\frac{\mathrm{d}}{\mathrm{dr}}\left[\rho_1 h_1^2\right] \tag{3.88b}$$

$$\left(ru_1h_1\right)_r = -ru_1, \tag{3.88c}$$

while to second order the governing equations will be given as

$$-u_1h_1\rho_2 + (u_1h_2 + u_2h_1)\rho_1 = 0 \tag{3.89a}$$

$$\left(r\left(u_1^2(h_2 - h_1\rho_1) + 2u_1u_2h_1\right)\right)_r = \frac{1}{2}r\left(2\rho_1h_1h_2 - \rho_2h_1^2\right)_r \tag{3.89b}$$

$$\left(r\left(u_1\left(h_2 - h_1\rho_1\right) + u_2h_1\right)\right)_r = -r\left(u_2 - \frac{1}{2}u_1\rho_1\right). \tag{3.89c}$$

The above listed system of equations does not admit an exact analytical solution, thus a numerical approach is required. The problem though appears when one considers the ICs under which the system will be solved. For the system of equations to leading order (3.88), ICs for u_1, h_1 and ρ_1, are provided by the Matching Conditions obtained in studying the limit $\zeta \to \infty$ for the inner solution. But what about the second order dependent variables? Matching conditions do provide information to second order only for the dependent variable ρ_2, but indicate nothing about u_2 and h_2. The way to overcome this difficulty and to obtain the additional information when Prandtl's rule and the intermediate layer expansions fail, is a subject of the next section. The principle is simple, in requiring the limiting behaviour of our dependent variables at $r \to 1^-$, local analysis at $r = 1$ can provide answers to the questions asked. Furthermore by making the assumption that no prior knowledge is on hold for leading order terms, local analysis will serve as a validation tool to what has been derived so far w.r.t the Matching Conditions.

Once ICs for all dependent variables are known, the system of equations (3.88)–(3.89) is solved numerically. The numerical solution obtained is then interpolated using once more rational functions. In that way semi-analytical approximations for the outer asymptotic expansions, is accomplished.

3.6.2 Obtaining the matching conditions for u_2, h_2

Start with the introduction of a new independent variable $\xi^3 = 1 - r$, so that study of the limit $r \to 1$ is equivalent to the limit $\xi \to 0$. Leading order equations (3.88) are written in terms of ξ as

$$(1 - \xi^3)u_1h_1\rho_1 = 2\xi^3 - \xi^6 \tag{3.90a}$$

$$\Big((1-\xi^3)u_1^2h_1\Big)_\xi = \frac{1}{2}(1-\xi^3)\Big(\rho_1h_1^2\Big)_\xi \tag{3.90b}$$

$$\Big((1-\xi^3)u_1h_1\Big)_\xi = 3\xi^2(1-\xi^3)u_1. \tag{3.90c}$$

Disregarding knowledge of the form of the dependent variables u_1 , h_1 and ρ_1 as $\xi \to 0$, we shall assume the following behaviour

$$u_1 \sim \boldsymbol{\alpha}\xi^{k_1},\ h_1 \sim \boldsymbol{\beta}\xi^{k_2},\ \rho_1 \sim \boldsymbol{\gamma}\xi^{k_0},\ \text{ as } \xi \to 0. \tag{3.91}$$

Substituting (3.91) into (3.90) and keeping leading order terms, we obtain the following values for $\boldsymbol{\alpha}$, $\boldsymbol{\beta}$, $\boldsymbol{\gamma}$, k_0 k_1 and k_2, as $\xi \to 0$

$$\boldsymbol{\alpha} = 1,\ \boldsymbol{\beta} = \frac{3}{4},\ \boldsymbol{\gamma} = \frac{8}{3} \text{ while } k_0 = -1,\ k_1 = 1,\ k_2 = 3. \tag{3.92}$$

So that (3.91) is given as

$$u_1 \sim \xi = (1-r)^{\frac{1}{3}},\ h_1 \sim \frac{3}{4}\xi^3 = \frac{3}{4}(1-r),\ \rho_1 \sim \frac{8}{3}\xi^{-1} = \frac{8}{3}(1-r)^{-\frac{1}{3}},\ \text{ as } \xi \to 0. \tag{3.93}$$

A comparison now of the Matching Conditions (3.60) with (3.93) is encouraging. The leading order terms obtained by performing local analysis at $r = 1$ or $\xi = 0$, results in the leading order terms obtained after the study of the limiting behaviour of inner solutions as $\zeta \to \infty$. A similar approach is now applied to the second order equations (3.89) which in terms of the new independent variable ξ are given as

$$-u_1h_1\rho_2 + (u_1h_2 + u_2h_1)\rho_1 = 0 \tag{3.94a}$$

$$\left((1-\xi^3)\Big(u_1^2(h_2 - h_1\rho_1) + 2u_1u_2h_1\Big)\right)_\xi = \frac{1}{2}(1-\xi^3)\Big(2\rho_1h_1h_2 - \rho_2h_1^2\Big)_\xi \tag{3.94b}$$

$$\left((1-\xi^3)\Big(u_1\left(h_2 - h_1\rho_1\right) + u_2h_1\Big)\right)_\xi = 3\xi^2(1-\xi^3)\Big(u_2 - \frac{1}{2}u_1\rho_1\Big). \tag{3.94c}$$

On the assumption that to leading order as $\xi \to 0$, the dependent variables attain the following form

$$u_1 \sim \boldsymbol{\alpha}\xi^{k_1},\ h_1 \sim \boldsymbol{\beta}\xi^{k_2},\ \rho_1 \sim \boldsymbol{\gamma}\xi^{k_0},\ u_2 \sim \boldsymbol{\delta}\xi^{k_3},\ h_2 \sim \boldsymbol{\epsilon}\xi^{k_4},\ \rho_2 \sim \boldsymbol{\lambda}\xi^{k_5}, \text{ as } \xi \to 0, \tag{3.95}$$

then substituting and keeping leading order and balancing powers gives

$$k_3 = 0,\ k_4 = 2 \text{ and } k_5 = -2. \tag{3.96}$$

In addition to the 3×3 system

$$\begin{aligned} \boldsymbol{\gamma}\,(\boldsymbol{\alpha\epsilon} + \boldsymbol{\delta}\,\boldsymbol{\beta}) &= \boldsymbol{\lambda}\,\boldsymbol{\alpha\beta} \\ -\boldsymbol{\alpha}^2\boldsymbol{\beta}\,\boldsymbol{\gamma} + 2\,\boldsymbol{\alpha\delta}\,\boldsymbol{\beta} + \boldsymbol{\alpha}^2\boldsymbol{\epsilon} &= 1/2\,\boldsymbol{\beta}\,(2\,\boldsymbol{\gamma}\,\boldsymbol{\epsilon} - \boldsymbol{\lambda}\,\boldsymbol{\beta}) \\ -\boldsymbol{\alpha\beta}\,\boldsymbol{\gamma} + \boldsymbol{\delta}\,\boldsymbol{\beta} + \boldsymbol{\alpha\epsilon} &= -\frac{1}{2}\,\boldsymbol{\gamma}\,\boldsymbol{\alpha} + \boldsymbol{\delta} \end{aligned} \tag{3.97}$$

or

$$\begin{aligned} -9\boldsymbol{\lambda} + 32\boldsymbol{\epsilon} + 24\boldsymbol{\delta} &= 0 \\ 32\boldsymbol{\epsilon} - 9\boldsymbol{\lambda} - 48\boldsymbol{\delta} &= -64 \\ 12\boldsymbol{\epsilon} - 3\boldsymbol{\delta} &= 8, \end{aligned} \tag{3.98}$$

solution of the above gives

$$\boldsymbol{\delta} = \boldsymbol{\epsilon} = \frac{8}{9} \text{ and } \boldsymbol{\lambda} = \frac{448}{81}. \tag{3.99}$$

The ICs for the second order dependent variables will thus be given as

$$u_2 = \frac{8}{9},\ h_2 = \frac{8}{9}\,\xi^2 = \frac{8}{9}\,(1-r)^{\frac{2}{3}},\ \rho_2 = \frac{448}{81}\,\xi^{-2} = \frac{448}{81}\,(1-r)^{-\frac{2}{3}} \text{ as } r \to 1^-. \tag{3.100}$$

The system of equations (3.90)–(3.94) can now be solved numerically subject to constraints given in (3.93) and (3.100). Further on, analytical approximations to the numerical solution can easily be obtained using interpolation via rational functions which is a subject that is dealt with in the following section.

3.6.3 Semi-analytical results for the outer approximations

This section is finalised with the construction of analytical approximations for the dependent variables of the outer asymptotic expansions. The methodology used, mimics the one employed, when approximations were performed for the inner solutions. The dependent variables are normalised with their limiting behaviour as $\xi \to 0$, so that in that limit the resulting normalised function attains a limiting value of one. Interpolation using rational function is then applied to the normalised function.

Start with the leading order terms, thus for u_1, it is found that

$$u_{1\text{apr}} = \xi\left(1 + \frac{(0.00753 + 0.23197\,\xi - 0.15742\,\xi^2)\,\xi^2}{1 - 0.97077\,\xi - 0.00568\,\xi^2}\right) \tag{3.101}$$

while h_1 is approximated by

$$h_{1\mathrm{apr}} = \frac{3}{4}\xi^3\left(1 + \frac{(-0.0019710 + 0.27719\,\xi - 0.20403\,\xi^2)\,\xi^2}{1 - 0.97251\,\xi - 0.016482\,\xi^2}\right) \tag{3.102}$$

Finally ρ_1 can be expressed explicitly using equation (3.90a)

$$\rho_1 = \frac{2\xi^3 - \xi^6}{(1-\xi^3)u_1 h_1}. \tag{3.103}$$

Therefore by application of the approximations $u_{1\mathrm{apr}}$ and $h_{1\mathrm{apr}}$ into (3.90a) directly leads to the approximate solution $\rho_{1\mathrm{apr}}$. Proceeding to the second order dependent variables starting with u_2, which is approximated by

$$u_{2\mathrm{apr}} = \frac{8}{9}\left(1 + \frac{(0.02484\; + 0.06601\,\xi - 0.06121\,\xi^2)\,\xi^2}{1 - 1.5418\,\xi + 0.55062\,\xi^2}\right) \tag{3.104}$$

whereas h_2 is approximated by

$$h_{2\mathrm{apr}} = \frac{8}{9}\xi^2\left(1 + \frac{(-0.01411 + 0.21671\,\xi - 0.08928\,\xi^2)\,\xi^2}{1 + 0.25291\,\xi - 1.2364\,\xi^2}\right). \tag{3.105}$$

Concluding, ρ_2 is given using equation (3.89a) as

$$\rho_2 = \rho_1\left(\frac{h_2}{h_1} + \frac{u_2}{u_1}\right). \tag{3.106}$$

Therefore utilisation of the analytical approximations found so far, are enough for the approximation for ρ_2 to be made.

The behaviour of the leading order analytical approximations when compared with numerical is given in Figure 3.6, while Figure 3.7 presents the behaviour of second order analytical approximations. Finally in Table 3.2 the maximum values of absolute and relative errors of the analytical approximations is presented.

	$\max\lvert \mathrm{f} - \mathrm{f_{ap}} \rvert$	$\max\frac{\lvert \mathrm{f} - \mathrm{f_{ap}} \rvert}{\lvert \mathrm{f} \rvert}$
u_1	6.9077e-03	3.5319e-03
h_1	5.0843e-03	3.7125e-03
ρ_1	1.8480e-02	7.2051e-03
u_2	2.7394e-03	1.6206e-03
h_2	1.7019e-03	1.1758e-03
ρ_2	4.213e-02	9.4458e-03

Table 3.2: Maximum values of Absolute and Relative Errors of the approximations. Values are obtained while $\xi \in [10^{-4}, 0.9]$. It must be noted that the maximum absolute error for ρ_2 is obtained for $\xi \in [0.1, 0.9]$, since it is singular at $\xi = 0$ (3.106).

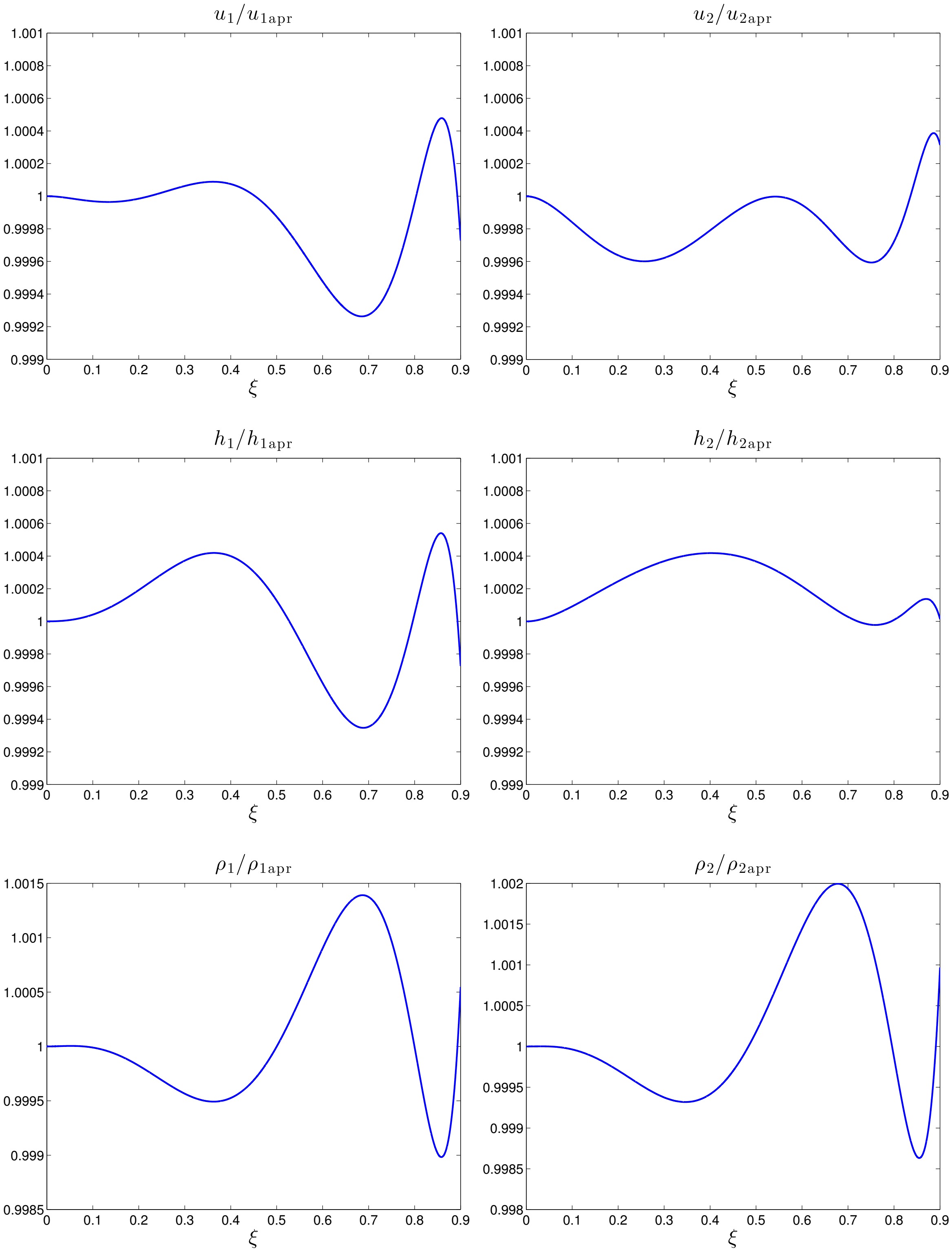

Figure 3.6: Comparison of the numerical solutions with analytic approximations, while $\xi \in [10^{-4}, 0.9]$.

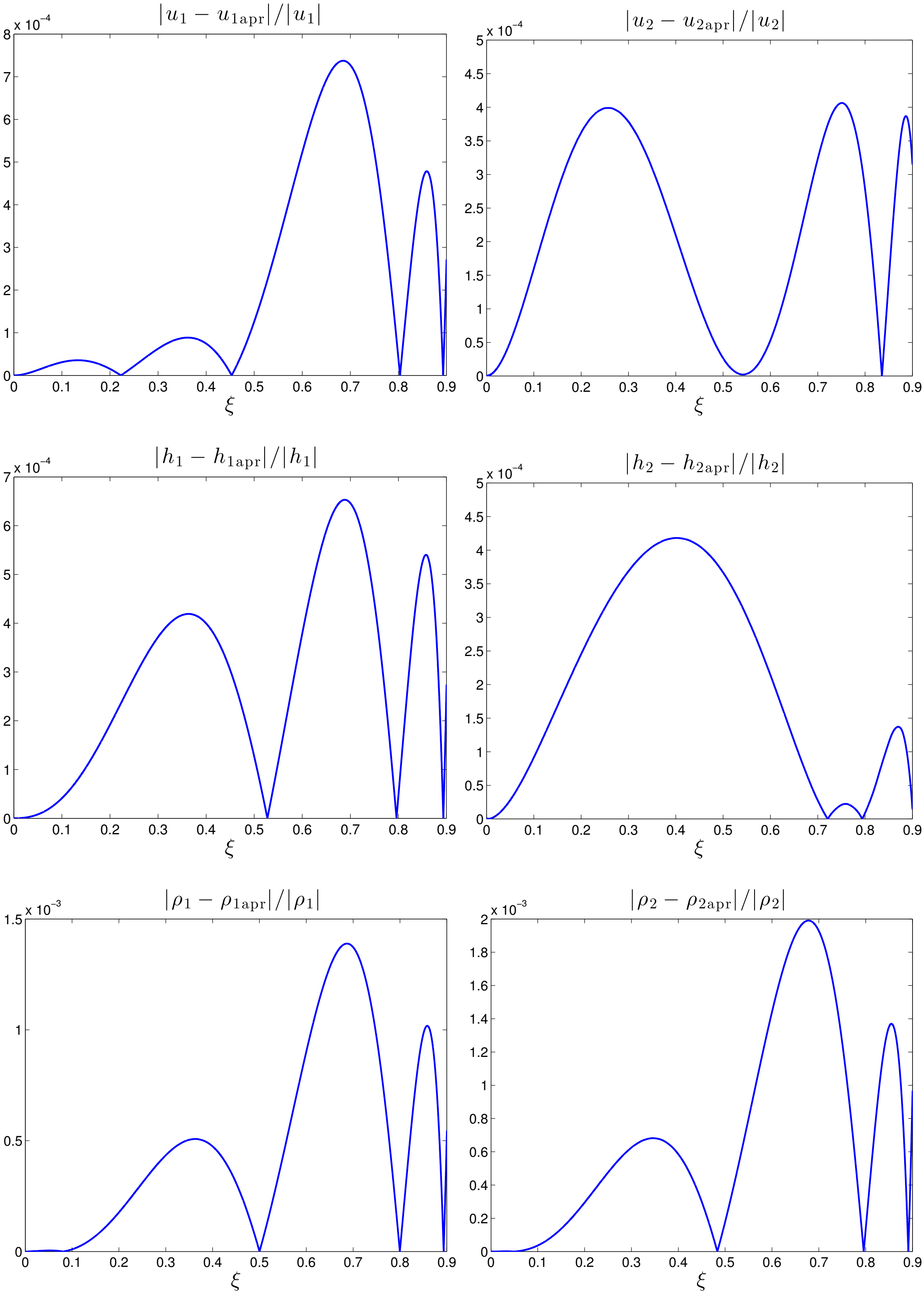

Figure 3.7: Relative Error of the approximations while $\xi \in [10^{-4}, 0.9]$.

3.7 Global solution

The chapter is finalised with the construction of a global solution. So far in studying the flow analytically as $\mathbf{a} \to \infty$, a three layer structure has been uncovered (Figure 3.8). For the region around the centre of the disc $r = 0$, a leading order analytical approximation has been provided, being valid as $r \to 0$. This qualitative information serves as an indication of the model behaviour in the region where it fails around $r = 0$. The main analytical results though were obtained in the remaining two layer regions which are of primary interest. For the boundary layer structure, inner asymptotic expansions valid in a thin strip of thickness $1 - r = \mathcal{O}(1/\mathbf{a})$ positioned at edge of the plate where obtained as

$$u(\zeta) \sim \zeta(\bar{u}_1 + A^{-5}\bar{u}_2), \quad h(\zeta) \sim \frac{\zeta^4}{A^5}(\bar{h}_1 + A^{-5}\bar{h}_2), \quad \rho(\zeta) \sim \zeta^2(\bar{\rho}_1 + A^{-5}\bar{\rho}_2)^2, \tag{3.107}$$

while outer asymptotic expansions in the final remaining distinguished layer of thickness $1 - r = \mathcal{O}(1)$ were found to be given as

$$u(r) \sim \mathbf{a}^{\frac{1}{3}} u_1 + u_2, \quad h(r) \sim h_1 + \mathbf{a}^{-\frac{1}{3}} h_2, \quad \rho(r) \sim 1 - \mathbf{a}^{-\frac{1}{3}} \rho_1 + \mathbf{a}^{-\frac{2}{3}} \rho_2. \tag{3.108}$$

From Kaplun's extension theorem it is known that the local character of validity of these approximations can be extended to include an intermediate region (overlap region), where both inner and outer expansions are valid. Nevertheless even after extension of the domain of their validity, distinguished regions are still present, so that a global solution cannot be attained by a single usage of inner or outer asymptotic expansions.

It is natural to expect that a global solution needs to implement information from both inner and outer asymptotic expansion. That is achieved through the uniform valid composite solution, valid for $1 - r = \mathcal{O}(1/\mathbf{a})$ and $1 - r = \mathcal{O}(1)$ obtained in the following way as

$$\begin{aligned} u(r, 1/\mathbf{a}) &= u_{\text{outer}} + u_{\text{inner}} - u_{\text{common}}, \\ h(r, 1/\mathbf{a}) &= h_{\text{outer}} + h_{\text{inner}} - h_{\text{common}}, \\ \rho(r, 1/\mathbf{a}) &= \rho_{\text{outer}} + \rho_{\text{inner}} - \rho_{\text{common}}. \end{aligned} \tag{3.109}$$

Thus a global solution, uniformly valid in the whole domain of interest can be obtained by summing inner and outer asymptotic expansions and subtracting their common

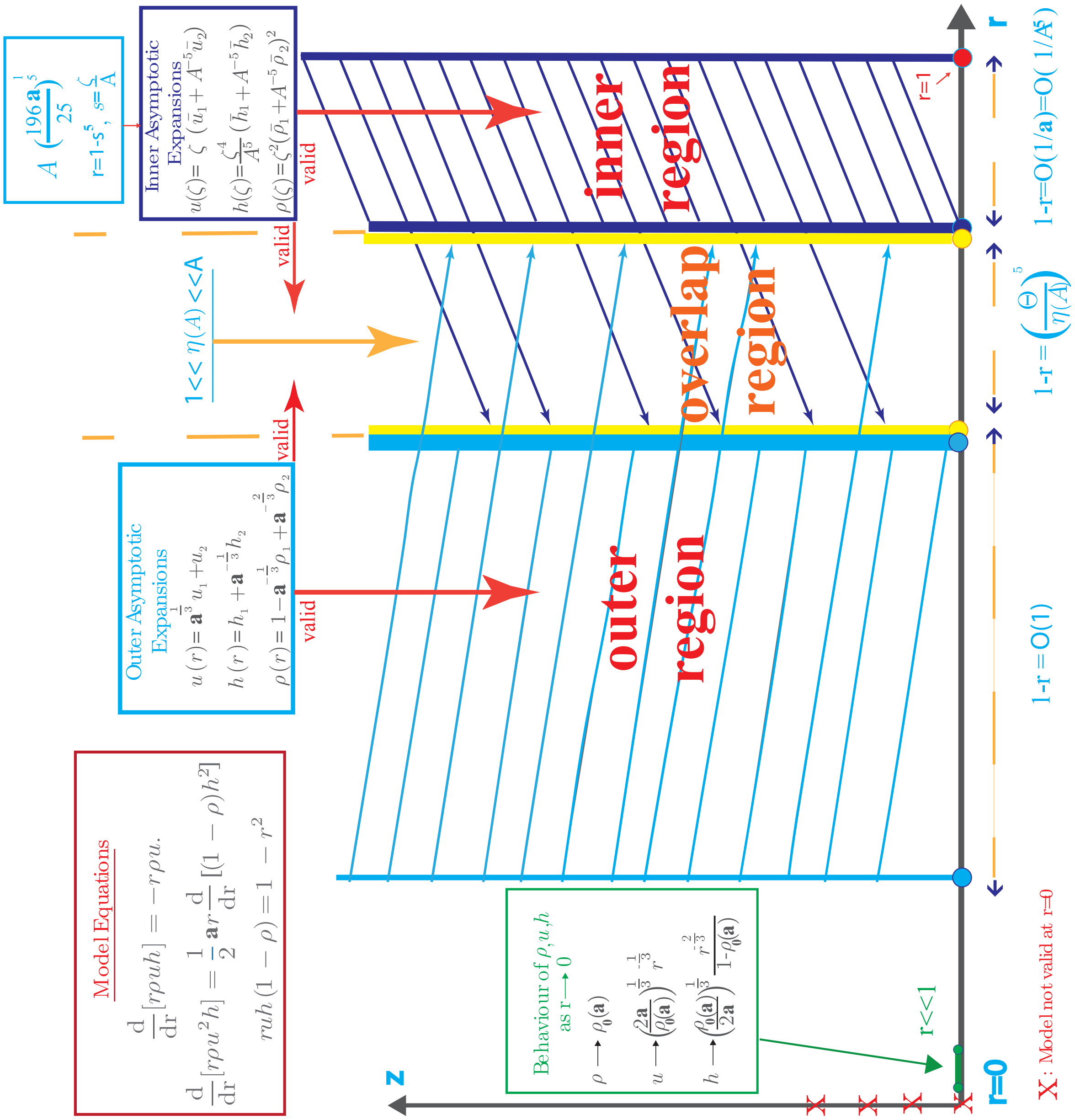

Figure 3.8: Schematic diagram of the asymptotic structure for large Richardson number.

part. The 'common part' is a result of re-expansion of either outer or inner solution in the overlap region. The overlap region can be defined in terms of the original independent variable as

$$1 - r = \left(\frac{\Theta}{\eta(A)}\right)^5, \tag{3.110}$$

or in terms of the stretched independent variable as

$$s = \frac{\Theta}{\eta} \quad \text{or} \quad \zeta = \frac{\Theta A}{\eta}, \tag{3.111}$$

where $\Theta = \mathcal{O}(1)$, and $1 \ll \eta \ll A$. Once the overlap region is established we proceed with the introduction of the intermediate independent variable Θ into outer or inner asymptotic expansions, followed by re-expansions for $\eta \gg 1$ or $\eta \ll A$, equivalently. The result of either re-expansion would result to the common part.

Looking back at the procedure followed for obtaining the matching conditions to first order approximation, the limit $\zeta \to \infty$ was studied. That limiting procedure is no different mathematically, from expressing the inner asymptotic expansions via the intermediate independent variable Θ, and re-expanding, while keeping in mind that $\Theta = \mathcal{O}(1)$ and $A \gg \eta$. To see that let us consider the inner asymptotic expansions for u, i.e. $u(\zeta, 1/A) \sim \zeta(\bar{u}_1 + A^{-5}\bar{u}_2)$. For the leading order term $\bar{u}_1$ an approximation was found to be given as $\bar{u}_{1\mathrm{app}} = U_1 \bar{u}_{1\mathrm{rat}}$, where

$$U_1(\zeta) = 1 - z + \left(\frac{5}{14}\right)^{\frac{2}{3}} z\,\zeta^{\frac{2}{3}} \text{ and } \bar{u}_{1\mathrm{rat}} = 1 + \frac{(0.97796 - 1.0764\,z + 0.33330\,z^2)\,z\,(1-z)}{1 - 2.6042\,z + 2.5885\,z^2 - 0.98384\,z^3}.$$

Introducing the overlap variable Θ into U_1 while recalling that $z = \zeta/(\zeta+1)$ to get

$$U_1 = 1 - \frac{\frac{\Theta A}{\eta}}{\frac{\Theta A}{\eta} + 1} + \left(\frac{5}{14}\right)^{\frac{2}{3}} \frac{\frac{\Theta A}{\eta}}{\frac{\Theta A}{\eta} + 1} \zeta^{\frac{2}{3}}. \tag{3.112}$$

Re-expanding the z term for $\eta \ll A$ or $\eta/A \ll 1$

$$z = \frac{\frac{\Theta A}{\eta}}{\frac{\Theta A}{\eta} + 1} = \frac{1}{1 + \frac{\eta}{\Theta A}} \sim 1 - \frac{\eta}{\Theta A} + \mathcal{O}\left(\left(\frac{\eta}{\Theta A}\right)^2\right) + \cdots. \tag{3.113}$$

Thus U_1 and $\bar{u}_{1\mathrm{rat}}$ can be found to be given to leading order as

$$U_1 \sim \left(\frac{5}{14}\right)^{\frac{2}{3}} \left(\frac{\Theta A}{\eta}\right)^{\frac{2}{3}} \text{ and } \bar{u}_{1\mathrm{rat}} \sim 1. \tag{3.114}$$

Thus the leading order term for the inner expansion can be written as

$$\zeta \bar{u}_1 \approx \zeta U_1 \bar{u}_{1\mathrm{rat}} \sim \left(\frac{5}{14}\right)^{\frac{2}{3}} A^{\frac{5}{3}} \left(\frac{\Theta}{\eta}\right)^{\frac{5}{3}} = \mathbf{a}^{\frac{1}{3}} (1-r)^{\frac{1}{3}}. \tag{3.115}$$

Repeating the same procedure to second order to obtain that

$$A^{-5}\zeta\bar{u}_2 \approx A^{-5}\zeta U_2\bar{u}_{2\text{rat}} \sim \frac{7}{24}\mathbf{a}^{\frac{1}{3}}(1-r)^{\frac{4}{3}}. \tag{3.116}$$

Thus re-expansion of the inner asymptotic solution via the intermediate variable resulted in nothing other than the matching condition to first order with the outer solution for u obtained in equation (3.60a). To obtain the matching condition for u to second order resolving to the outer asymptotic equations was necessary where local analysis was performed at $r = 1$ or, more accurately, after the introduction of a new independent variable ξ as $\xi^3 = 1 - r$, local analysis was carried around $\xi = 0$. Once more this is an equivalent procedure to rewriting the outer asymptotic expansions in terms of the intermediate variable Θ and re-expanding for $\eta \gg 1$. For the outer asymptotic expansions for u (i.e . $u(r) \sim \mathbf{a}^{\frac{1}{3}}u_1 + u_2$) to leading order an approximation was found to be given as

$$u_{1\text{apr}} = \xi\left(1 + \frac{(0.00753 + 0.23197\,\xi - 0.15742\,\xi^2)\,\xi^2}{1 - 0.97077\,\xi - 0.00568\,\xi^2}\right)$$

Now ξ in terms of the independent intermediate variable is written as

$$\xi = \left(\frac{\Theta}{\eta}\right)^{\frac{5}{3}} \tag{3.117}$$

Thus it is straightforward to see that

$$u_{1\text{apr}} \sim \xi = \left(\frac{\Theta}{\eta}\right)^{\frac{5}{3}} = (1-r)^{\frac{1}{3}} \text{ for } \eta \gg 1. \tag{3.118}$$

The above result is the common part of inner and outer asymptotic expansions to leading order. To obtain the common part to second order the same procedure need to be applied to the second order term u_2, which easily leads to the result given in equation (3.100) i.e $u_2 \sim 8/9$.

It is thus clear that the common part of inner and outer asymptotic expansions had already been obtained, in the process of finding the matching conditions. Therefore introduction of intermediate variable and re-expansion of inner or outer asymptotic expansions is unnecessary, whereas the matching conditions to leading and second order can safely be presumed to constitute the common part. In that way the uniformly valid composite solutions for the dependent variable u is given as

$$u_{\text{uva}} = u_{\text{inner}} + u_{\text{outer}} - \frac{8}{9} - \mathbf{a}^{\frac{1}{3}}\left((1-r)^{\frac{1}{3}} + \frac{7}{24}(1-r)^{\frac{4}{3}}\right) \tag{3.119a}$$

while for h

$$h_{\text{uva}} = h_{\text{inner}} + h_{\text{outer}} - \frac{3}{4}(1-r) - \frac{51}{224}(1-r)^2 - \mathbf{a}^{-\frac{1}{3}}\frac{8}{9}(1-r)^{\frac{2}{3}}. \tag{3.119b}$$

Finally, a uniformly valid asymptotic expansion for ρ can be easily obtained, by solving the original algebraic model equation explicitly for ρ, and introducing the composite solutions for u and h, to get

$$\rho_{\text{uva}} \sim 1 - \frac{1-r^2}{r u_{\text{uva}} h_{\text{uva}}}. \tag{3.120}$$

3.7.1 Behaviour of the global approximations

The qualitative behaviour of the global approximations can be investigated when compared to the numerical solution for large varying values of Richardson number $\mathbf{a}$. In Figures 3.9, 3.10 and 3.11 a comparison of the composite solution for u, h and ρ is presented equivalently w.r.t the numerical solution while $\mathbf{a} = 2, 2^7, 10^i$ where $i = 3, 4 \ldots 6$. Overall the accuracy of the uniform approximations built on for large values of $\mathbf{a}$ is rather satisfying over the domain of interest $r \in [1\,, 0.1]$. To quantify this, in Figures 3.12, 3.13, presentation of relative and absolute error of the approximation is given, while in Table 3.3 maximum and minimum values of relative and absolute error is given for the approximations for different values of $\mathbf{a}$.

	$\lvert u-u_{\text{uva}}\rvert$		$\lvert h-h_{\text{uva}}\rvert$		$\lvert \rho-\rho_{\text{uva}}\rvert$	
a	max	min	max	min	max	min
2	3.2791e-01	7.9698e-03	3.0969e-03	3.7171e-05	9.6612e-02	9.4762e-04
128	2.2993e-01	7.1008e-03	7.7751e-04	2.6902e-05	3.4830e-02	2.1428e-04
10^3	2.4191e-01	8.6443e-03	4.8058e-04	9.1370e-06	1.4367e-02	1.0189e-04
10^4	3.1259e-01	6.6132e-03	6.0314e-04	1.3720e-05	4.7290e-03	3.1219e-05
10^5	5.0019e-01	5.3149e-03	6.7819e-04	1.1485e-05	1.4815e-03	2.9740e-05
10^6	8.5832e-01	2.4580e-02	6.9640e-04	1.9391e-07	2.6713e-04	1.2296e-06
10^7	1.1972e+00	4.5682e-04	7.1656e-04	5.0636e-08	8.1403e-05	1.0194e-08
10^8	3.1641e+00	3.5382e-03	7.1559e-04	8.0099e-09	2.9753e-05	1.9559e-06

	$\frac{\lvert u-u_{\text{uva}}\rvert}{\lvert u\rvert}$		$\frac{\lvert h-h_{\text{uva}}\rvert}{\lvert h\rvert}$		$\frac{\lvert \rho-\rho_{\text{uva}}\rvert}{\lvert \rho\rvert}$	
a	*max*	*min*	*max*	*min*	*max*	*min*
2	7.6897e-02	8.2515e-03	1.0397e-01	1.4413e-04	1.0040e+00	4.6925e-03
128	1.9682e-02	3.0060e-03	5.2063e-02	1.4880e-04	1.0647e-01	3.8651e-04
10^3	1.1332e-02	2.0461e-03	3.1435e-02	6.4988e-05	2.7282e-02	1.4108e-04
10^4	7.1145e-03	8.0598e-04	1.7296e-02	1.1469e-04	6.5851e-03	3.6687e-05
10^5	5.3907e-03	3.4391e-04	9.4924e-03	1.0634e-04	1.7648e-03	3.2552e-05
10^6	4.3353e-03	7.1574e-04	4.1216e-03	2.8066e-06	2.8999e-04	1.2929e-06
10^7	2.8130e-03	2.3059e-06	4.1225e-03	3.9802e-06	8.2375e-05	1.0512e-08
10^8	4.9494e-03	3.8481e-06	4.1303e-03	1.8678e-06	2.9941e-05	1.9671e-06

Table 3.3: Max-Min values of relative and absolute error for the approximations while $r \in [0.1,\, 0.97]$.

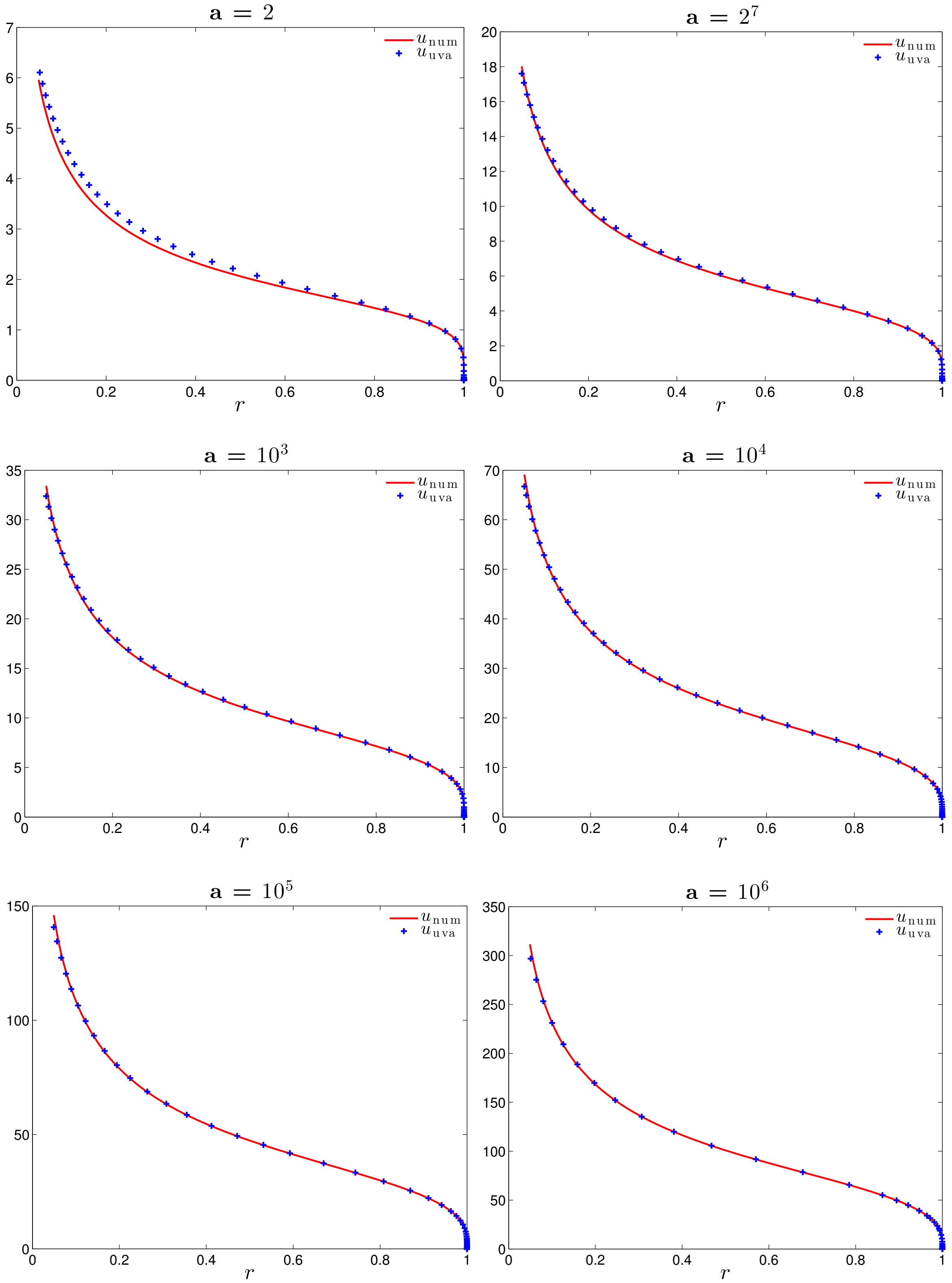

Figure 3.9: Behaviour of the uniform valid composite for u when compared to the numerical one, for large values of Richardson number.

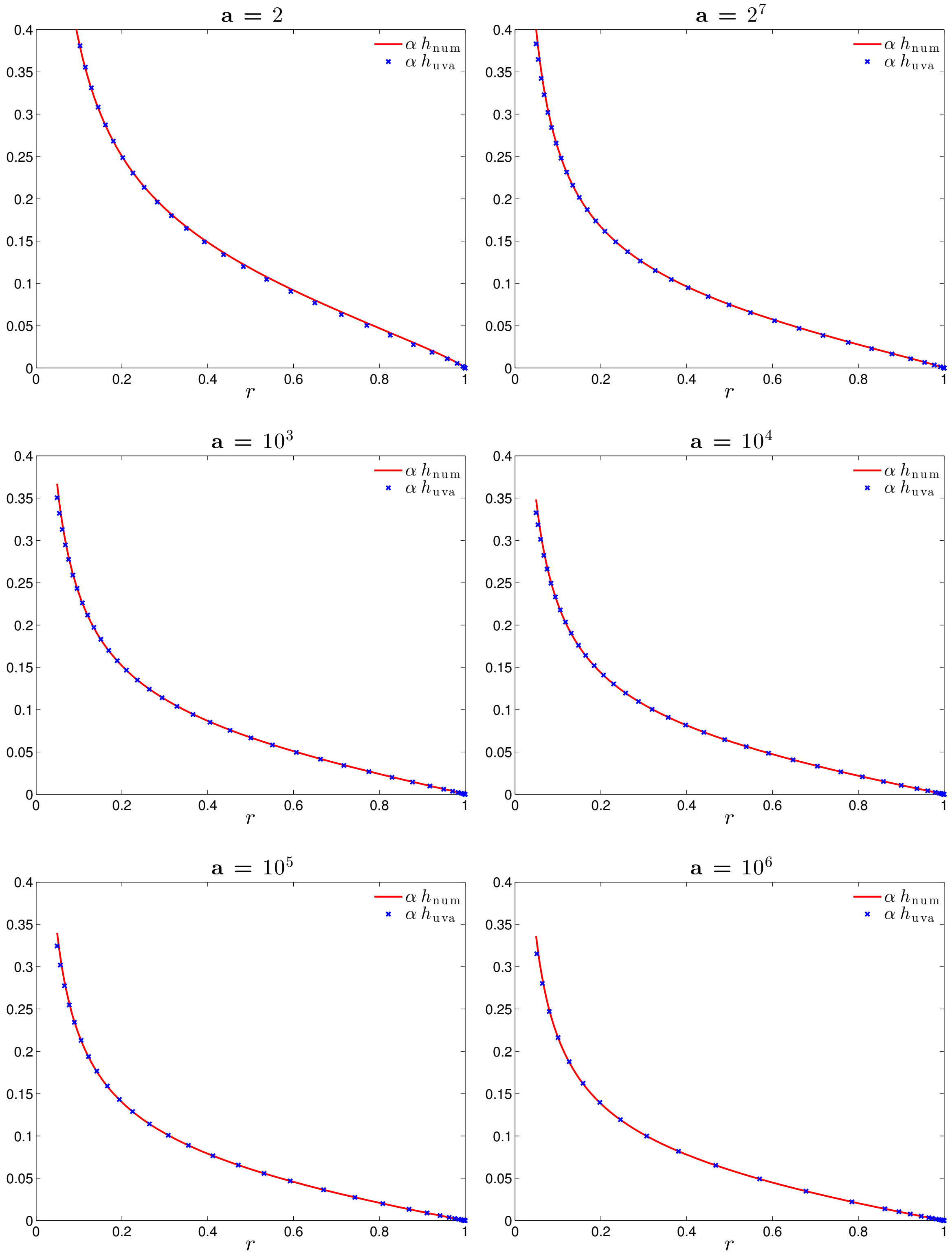

Figure 3.10: Behaviour of the uniform valid composite for αh when compared to the numerical one, for large values of Richardson number.

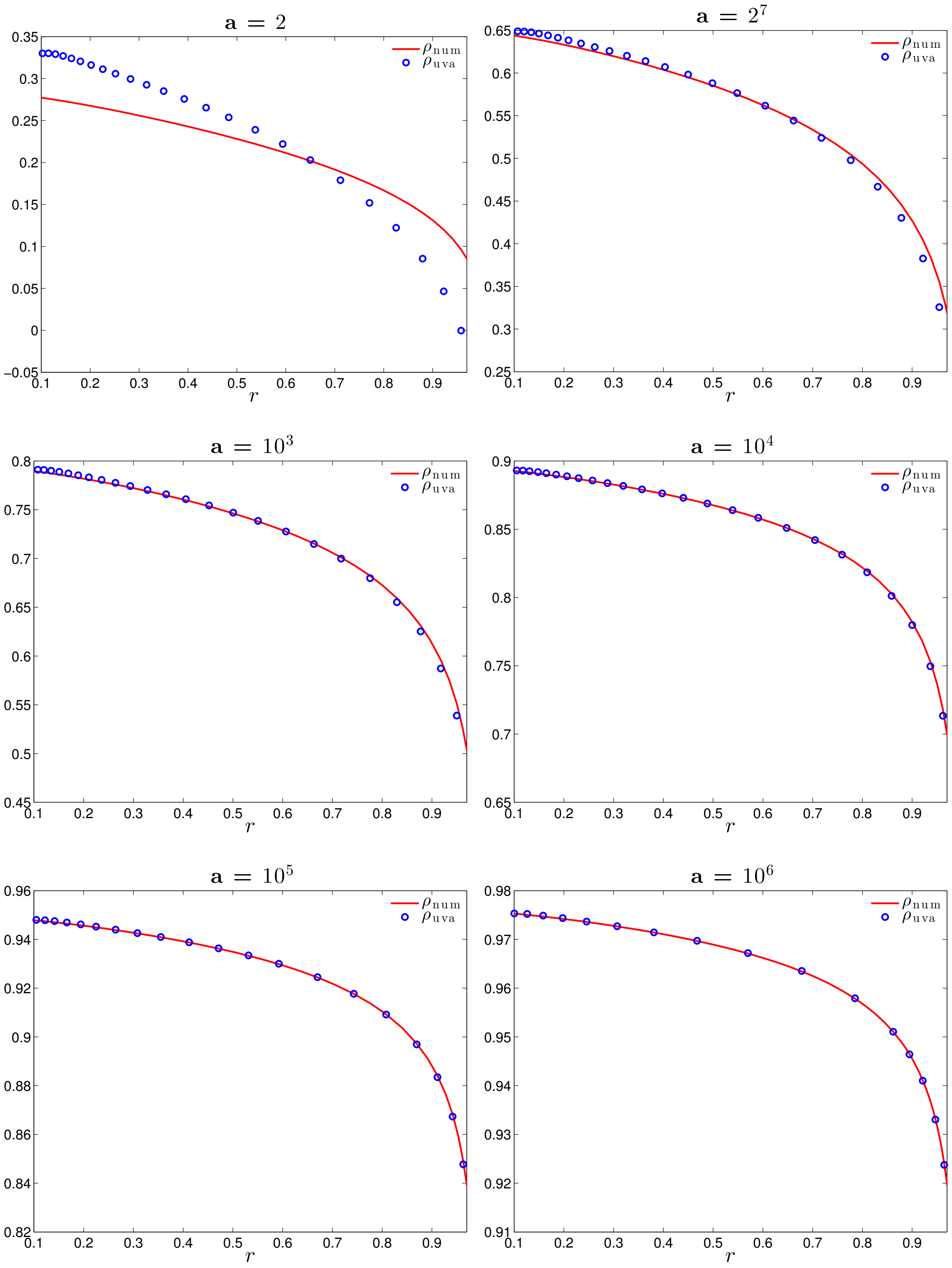

Figure 3.11: Behaviour of the uniform valid composite for ρ when compared to the numerical one, for large values of Richardson number. Note that $r \in [0.1,\ 0.97]$

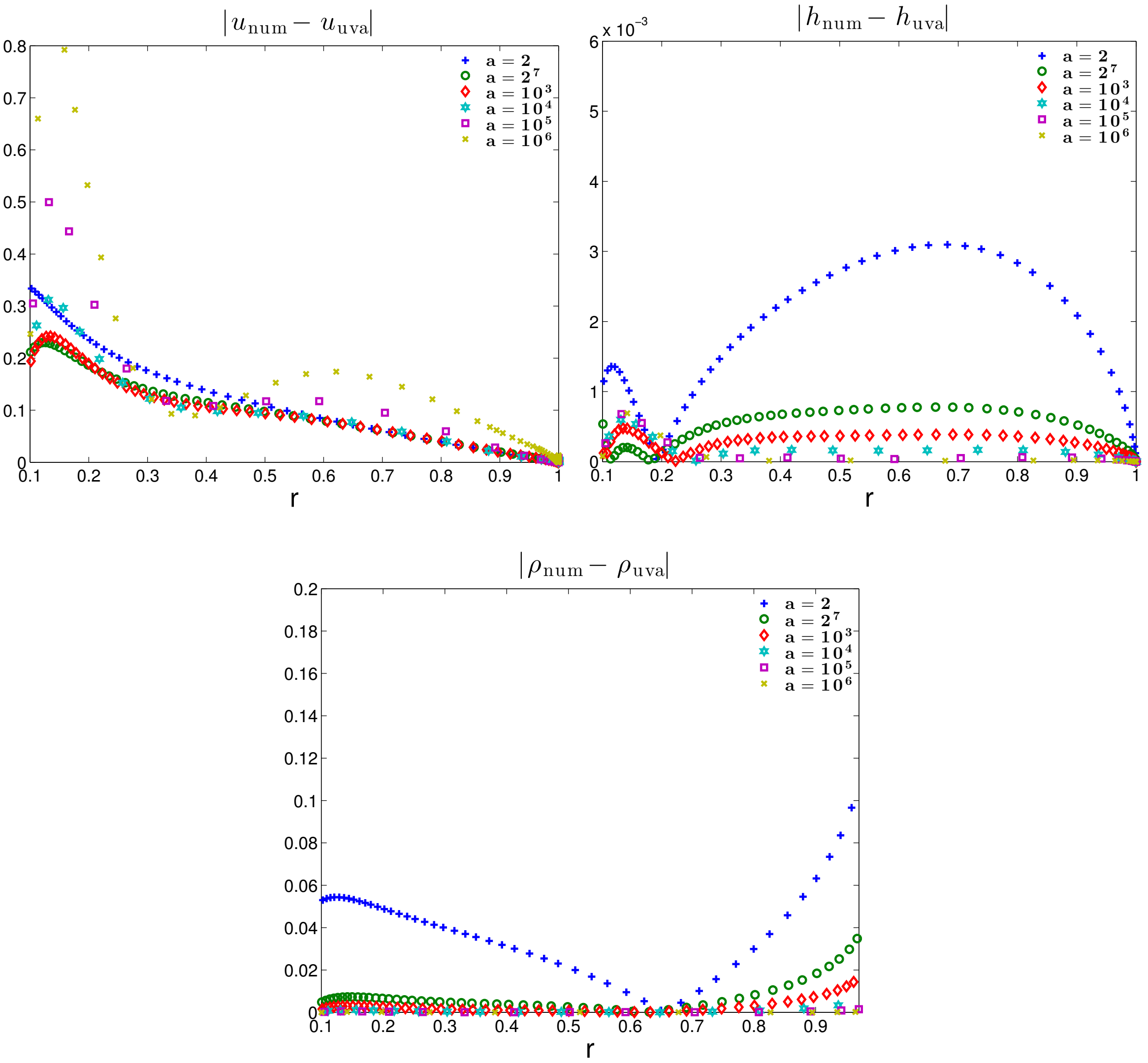

Figure 3.12: Absolute error for u,h and ρ, for different values of **a**. The absolute error for ρ is plotted for $r \in [0.1\,0.97]$, since $\rho_{\rm uva}$ is singular at $r = 1$.

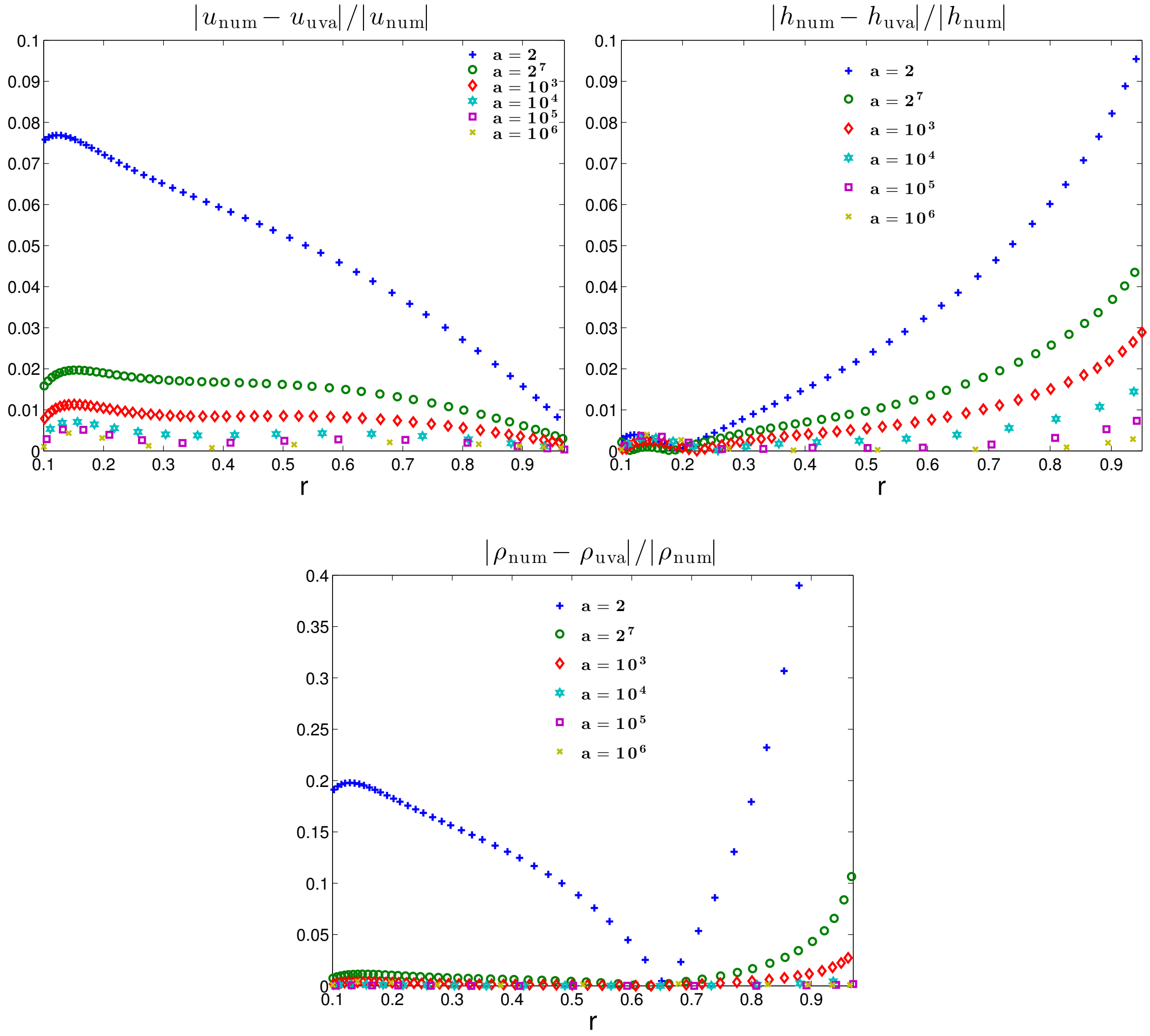

Figure 3.13: Relative error for u,h and ρ for different values $\mathbf{a}$. Relative error in all cases is plotted for $r \in [0.1\, 0.97]$ skipping numerical errors caused by dividing by zero around $r = 1$.

3.8 Summary

Over the last two chapters efforts were concentrated on the development of a theoretical model (termed as horizontal plume) for the description of the gross properties of horizontal buoyant attached currents, present above large are fires, as well as with its solution. The model was obtained after the application of the conservation principles of mass, momentum and energy, in addition to the assumptions of top hat formalism and an entrainment hypothesis, as analytically presented in Chapter 2. The resulting model equations were found to be given in their dimensionless form as

$$\frac{\mathrm{d}}{\mathrm{d}r}[r\rho uh] = -r\sqrt{\rho}u,$$

$$\frac{\mathrm{d}}{\mathrm{d}r}[r\rho u^2 h] = \frac{1}{2}\,\mathbf{a}r\frac{\mathrm{d}}{\mathrm{d}r}\left[(1-\rho)h^2\right],$$

$$ruh(1-\rho) = 1 - r^2,$$

subject to initial conditions (ICs) given as

$$\rho(1) = u(1) = h(1) = 0.$$

Furthermore the dimensionless parameter $\mathbf{a}$, present in the governing equations and termed as the Richardson number for the horizontal flow, was shown to be proportional to the radius of the circular area considered. Since the focus is on describing the flow above large area fires, this implies that $\mathbf{a}$ has to be treated as a large parameter.

In Chapter 3 the focus was directed towards the solution of the horizontal plume equations. Since an exact closed form solution does not exist for the DAE, a numerical as well as an asymptotic study in the limit $\mathbf{a} \to \infty$ was carried out. In what concerns the numerical solution, due to a singularity exhibited at $r = 1$, local analysis had to be performed for the approximation of the solution at that point, before initiation of the numerical integration. Regarding the asymptotic study in the limit $\mathbf{a} \to \infty$, the problem was treated as a singular perturbation problem, since a boundary layer of thickness $\mathcal{O}(1/\mathbf{a})$ was shown to be located in the neighbourhood of $r = 1$. Second order inner and outer asymptotic expansions were obtained, and a second order uniform valid semi-analytical approximation was constructed. Closing, the numerical and the semi-analytical approximations were shown to be in excellent agreement for values of $\mathbf{a}$ ranging from 10^2 to 10^6.

Chapter 4

Heated Horizontal Circular Plates

4.1 Prologue

In the following two chapters we diverge from the work done so far in order to revisit a classic problem, that of laminar natural convection above heated horizontal surfaces, or indirect natural convection after borrowing the terminology of [80]. Reasons behind this deviation arose naturally whilst still in the course of closing the theoretical model for the horizontal plume. Clearly it is the same physical mechanism that drives boundary layer flow. Absence of a buoyancy component along the surface means that the flow is accelerated by a buoyancy induced pressure gradient [69]. The fluid being lighter in the vicinity of the hot plate results in a reduced pressure gradient in the boundary layer and therefore a reduced pressure. The pressure drop along the plate direction translates to a negative transverse pressure gradient caused by a positive transverse temperature gradient (fluid heated by the plate) [36], [28],[80]. Further, as difficulties manifested throughout several attempts in modelling the region close to the centre of the circular plate, and thus the transition of the horizontal to vertical plume, an impression came on the scene that valuable lessons could be obtained after the study of the laminar limit. Finally, at the time, discussions were ongoing towards an experiment that would test the theoretical model of the horizontal plume model and assist in its improvement. The design of the 'hot plate' experiment offered the prospect for the laminar limit to be studied, so the task was pursued.

Historically the first analysis of a free convective flow adjacent to heated or cooled horizontal plates is due to Stewartson [89], going back as far as 1958. By considering an isothermal plate with one leading edge (the semi-infinite plate) thus removing a characteristic length, and adopting the Boussinesq approximation he derived the boundary layer equations for the flow and obtained similarity solutions. His conclusions though were erroneous due to a sign mistake in the transverse momentum equation. It took seven years for his analysis to be corrected by the work of Gill et al [28], that went on to include variable temperature (power law) along the plate, and to correctly conclude that boundary layer type flow only exists on a heated plate facing upwards or a cooled plate facing downwards. The self similar equations were studied in detail and accompanied by experiments by Rotem and Claaseen [74], where in addition the asymptotic cases of large and small Prandtl number was taken into consideration, and by Pera and Gebhart [67], where effects of small inclination were studied as a perturbation of the flow from the horizontal. In both cases a boundary layer flow near the edge of the plate was validated, using Schlieren photography in [74] and a Mach-Zehnder interferometer in [67] where in addition it was shown that separation occurs for local Grashof number $\mathrm{Gr}_{\mathrm{x}}^{1/3} > 80$ for a horizontal plate, while it was observed that separation is delayed when the plate is inclined.

Patterns of free convection above horizontal heated plates of different shape were studied in the experiment carried out by Husar and Sparrow [35], with the aid of electrochemical flow visualisation technique. They found that in the case of a square, a rectangle, or an equilateral triangle plate, the flow field has a partitioned character and that among partitions the flow can be considered independent. The partition of the flow field happens to almost correspond to the bisectors of the angles along which there is no flow, Figure 4.1. The origins of the partition can be explained as fluid 'simultaneously' leaving the different edges of the plate and moving inwards in parallel paths normal to the edge. Now as opposing streams approach the bisectors their paths become wavy and meandering to a vertical buoyant plume having as line source the bisectors. When changing the geometry of the plate to circular they found that the character of the flow is slightly different. Now there are no partition lines while the paths of the fluid, which is accelerating towards the centre, are convergent rather than parallel. The central region of the plate is dominated by a buoyant plume. It can be argued though that their conclusion w.r.t circular plates can be viewed differently, i.e. the flow is *partitioned* into two concentric regions, the outer being dominated by indirect natural convection (attached flow) and the inner by an axisymmetric buoyant plume, while the radius of the inner region must somehow be dependent on the Grashof number of the flow. Adopting this viewpoint resembles our plume theoretical model.

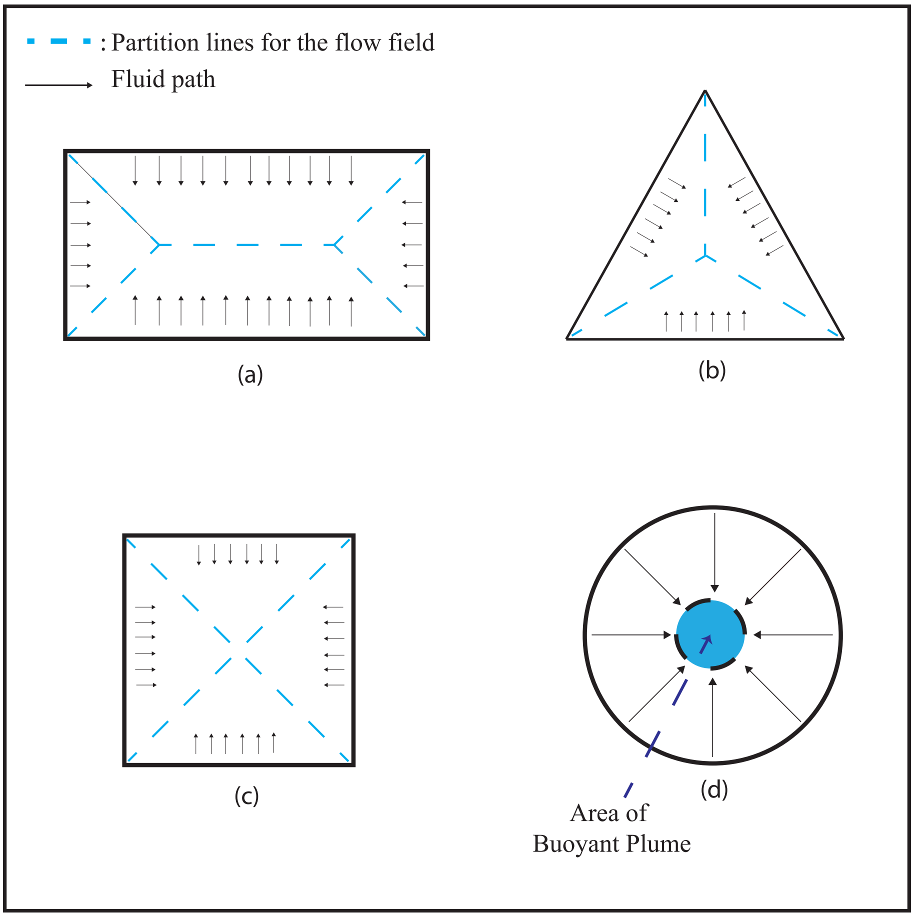

Figure 4.1: Synopsis of the experiment of [35] using heated plates of different geometry. Parallel paths normal to the edges of inward moving fluid is observed for (a), (b) and (c) with convergent paths for (d). Vertical buoyant currents result above the bisectors, or in the concentric region of the circular plate.

A more recent study of the flow field above rectangular plates (water used as the test fluid) is due to Kitamura and Kimura [48]. Their results showed that the flow field can be divided into four regions, starting with a laminar boundary layer located at the edge of the plate followed by a lengthy streaky transitional flow region which is marked with a three dimensional separation of heated fluid and the attachment of cold fluid downstream of the separation. A region where turbulence has fully dominated follows, while as the centerline of the plate is approached the final distinctive region is uncovered, that of collision. In investigating turbulence transition phenomena above horizontal plates, Kitamura et al [47] carried out an unsteady 3D numerical simulation of the full Navier-Stokes equations coupled with the energy equation under the Boussinesq approximation accompanied by an experiment. Computations uncovered that the undertaking of transition to turbulence happens in the following manner. A laminar boundary layer is located at the vicinity of the edge of the plate while downstream and due to unstable stratification a vertical exchange of hot and cold fluid takes place with the appearance of longitudinal vortices. Vortices become irregular as they now grow larger further downstream and consequently parts of them breakup and separate from the surface. Moving on and the vortices are fully distorted and turbulence is dominating. Experimental results supported the above conclusions.

Drawn in by the peculiar flow patterns above circular disks shown in [35], Kitamura and Kimura [49] carried out an experiment on the convection of air and water induced by isothermally upward-facing horizontal heated disks. Focusing initially on the visualisation of the flow field (dye for water, smoke for air) above the disks, it was found that for Rayleigh numbers (length scale taken to be the diameter D) smaller than $8 \times 10^5 - 10^6$ for water and $(1-2) \times 10^6$ for air, the flow remains laminar all over the plate and separates at the centre of the plate giving rise to a buoyant plume. On the other hand, exceeding of the above stated values results in separation and the onset of turbulence taking place at distance $r_s < D/2$. Visualisations showed that when critical values of Rayleigh number are surpassed, filaments are formed at distance r_s from the circumference of the disk which detach in a three dimensional manner and rise towards the centre of the plate, Figure 4.2. They found that the radial distance and the peripheral pitches of separation are independent of the diameter and that there is a monotonic decrease with the temperature scale defined as the temperature of the plate minus the ambient. Further they observed that these lengths can be predicted. Therefore there must be a regularity in the separation, using Rayleigh numbers having as length scales r_s and p_θ. In what concerns the onset of turbulence, responsibility is attributed once more to longitudinal vortices having axis parallel to the flow direction.

A rather detailed analysis for heated semi-infinite plates is given by Jones [38]. By treating small inclination of $\mathcal{O}(\mathrm{Gr}^{-1/5})$ positive[1] and negative and as a perturbation to the horizontal, he went on to obtain series solutions valid at the edge of the leading

---

[1] Positive inclination meaning that the leading edge is at the lowest point

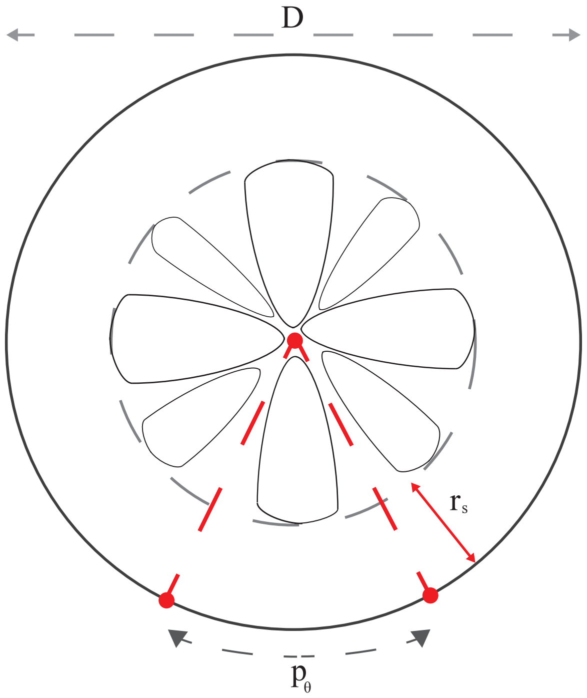

Figure 4.2: Structure of the flow for Rayleigh number above critical values as observed by [49]. The diameter of the plate is D, r_s is the mean radial distance of the separation, $p_\theta = 2\pi D/n$ is the peripheral pitches of separation, while n is the total number of separations.

edge of the plate and far away from it (only for positive inclination). Further, he allowed departures from similarity by numerically solving the non similar PDEs. His results show that for negative inclination, separation of the flow occurs which is not accompanied by a singularity in the solution of the equations, while flow reversal along the plate develops after the separation point. For the case of positive inclination, the flow far away from the leading edge attains the behaviour of classic free convection. Ackroyd [2] revisited the problem of the semi-infinite near horizontal plate, only he discarded the Boussinesq approximation for the inclusion of variable fluid property effects in the formulation. His motivation was based on poor agreements of correlations involving the Nusselt and Grashof (equivalently Rayleigh) number, between theoretical predictions and experiments, mainly after the mass transfer experiment of [29]. First order boundary layer theory predicts the heat transfer rates to be $\mathrm{Nu} \propto \mathrm{Gr}^{1/5}$, while most experimental results conclude to $\mathrm{Nu} \propto \mathrm{Gr}^{1/4}$. In his analysis he showed that the introduction of variable properties alters the constant of proportionality and thus improves the predictions of boundary layer theory. He further went on to show that stress work effects and the influence of pressure on density are second order effects with still little significance at such orders.

The first analytical study of natural convection above isothermal circular discs is due to Zakerullah and Ackroyd [101]. Under the same philosophy as in [2], variable fluid properties were assumed and series solutions valid near the edge of the plate were obtained. Merkin [56] went on to extend their analysis by solving numerically the full boundary layer equations (making the Boussinesq approximation) marching from the edge of the disk and approaching almost the centre of the disk and providing a detailed analysis for the flow in the region of the centre of the disk. The same analysis was repeated by Merkin [57], but this time imposing constant heat flux rather than constant temperature at the disk. Recently, Siddiqa and Hossain [86] studied the effect of thermal radiation q_r on a boundary layer flow of liquid metal above a heated circular disk. In their analysis the Rosseland diffusion approximation (thick radiation limit) was used in the energy equation.

Closing the prologue, for the next two chapters the focus lies on isothermal circular discs, starting with the solution of the boundary layer equations using variable fluid properties, followed by the full numerical solution of the Navier-Stokes equations coupled with the energy equation. The parting ends with a chapter dedicated to the semi-infinite plate using variable fluid properties, i.e. following Ackroyd [2], but providing the numerical solution of the boundary layer equations.

4.2 Introduction

Attention in this chapter is directed towards the study of boundary layer flow above a uniformly heated circular disc of radius a. On the disk constant temperature T_w is imposed such that ($T_\mathrm{w} > T_\infty$), with T_∞ being the ambient temperature, while the flow is assumed to be steady and laminar. The analysis is based on variable fluid properties, so that the density ρ and the fluid transport properties, i.e. viscosity μ and the thermal conductivity κ, are all functions of temperature T. In addition, secondary thermodynamic properties like the specific heat capacity $\mathrm{c_p}$ and the Prandtl number Pr are assumed constant. Specifically a linear law[2] is used for viscosity and

---

[2] The more accurate Sutherland's formula [98] for the law of viscosity was not used in order not to over complicate analytical calculations.

conductivity given as

$$\frac{\mu}{\mu_\mathrm{r}} = C\frac{T}{T_\mathrm{r}} \quad \text{and} \quad \frac{\kappa}{\kappa_r} = C\frac{T}{T_\mathrm{r}}, \tag{4.1}$$

with the subscript r corresponding to a reference point where the properties are evaluated. The reference point is assumed to be located within the ambient (∞) so that $T_\mathrm{r} = T_\infty$, $\kappa_r = \kappa_\infty$ and $\mu_\mathrm{r} = \mu_\infty$. Furthermore the constant C is the Chapman-Rubesin constant [80],[25],[98] given as

$$C = \frac{\rho_\mathrm{w}\mu_\mathrm{w}}{\rho_\infty\mu_\infty}. \tag{4.2}$$

The constant C is assumed here to be unity apart from when it is used for the viscosity-temperature relation, valid for gases. The above problem has previously been studied by [101], thus based on the foundations of their work, here we are trying to extend it. Specifically on adopting the above assumptions, it will be shown that an additional parameter (Prandtl number being present as usual) will be introduced in the non-dimensional, non-similar boundary layer equations. Variable fluid properties are solely responsible for the presence of the newly introduced parameter, defined as $\lambda_\mathrm{T} = (T_\mathrm{w} - T_\infty)/T_\infty$, so that setting $\lambda_\mathrm{T} = 0$ is equivalent to making the Boussinesq approximation. A detailed analysis of the effect that λ has on the flow will be carried out, accompanied by a brief study of the effect of the Prandtl number. Analytically a fourth order series approximation valid at the circumference of the disk will be obtained for $\lambda = 0, 1, \ldots, 4$ while the Prandtl number considered will be 0.1, 0.72, 1, 5 and 10. Most importantly, the numerical solution of the full boundary layer equations will be given using a finite difference scheme (Keller Box Method) and a commercial finite element package COMSOL Multiphysics 3.5a.

The governing equations for an axisymmetric flow [80], are listed below as

$$\frac{\partial}{\partial r}(r\rho u) + \frac{\partial}{\partial z}(r\rho w) = 0, \tag{4.3a}$$

$$\rho\left(u\frac{\partial u}{\partial r} + w\frac{\partial u}{\partial z}\right) = f_r - \frac{\partial P}{\partial r} + \frac{1}{r}\frac{\partial(r\tau_{rr})}{\partial r} + \frac{\partial \tau_{rz}}{\partial z}, \tag{4.3b}$$

$$\rho\left(u\frac{\partial w}{\partial r} + w\frac{\partial w}{\partial z}\right) = f_z - \frac{\partial P}{\partial z} + \frac{1}{r}\frac{\partial(r\tau_{zr})}{\partial r} + \frac{\partial \tau_{zz}}{\partial z}, \tag{4.3c}$$

$$\rho c_p\left(u\frac{\partial T}{\partial r} + w\frac{\partial T}{\partial z}\right) = \frac{1}{r}\frac{\partial}{\partial r}\left(kr\frac{\partial T}{\partial r}\right) + \frac{\partial}{\partial z}\left(k\frac{\partial T}{\partial z}\right). \tag{4.3d}$$

The system of equations is closed with the ideal gas law i.e

$$\rho T = \rho_\infty T_\infty. \tag{4.3e}$$

Viscous stresses are given as

$$\tau_{rr} = 2\mu\frac{\partial u}{\partial r}, \quad \tau_{zz} = 2\mu\frac{\partial w}{\partial z} \quad \text{and} \quad \tau_{rz} = \tau_{zr} = \mu\left(\frac{\partial u}{\partial z} + \frac{\partial w}{\partial r}\right), \tag{4.3f}$$

while it should be pointed that pressure work and dissipation effects have been neglected from the energy equation [1] [36].

The only external field considered here is that of gravity so that the radial component of the body force is $f_r = 0$. Furthermore by breaking the pressure into hydrostatic (p_∞) and dynamic (p) i.e.

$$P = p_\infty + p \quad \text{and noting that} \quad \nabla p_\infty = \rho_\infty \mathbf{g}, \tag{4.4a}$$

then in vector form we can write

$$\mathbf{f} - \nabla P = \rho\mathbf{g} - \nabla\left(p_\infty + p\right) = (\rho - \rho_\infty)\mathbf{g} - \nabla p. \tag{4.4b}$$

The z-component of (4.4b) is then given as

$$f_z - \frac{\partial P}{\partial z} = (\rho_\infty - \rho)g - \frac{\partial p}{\partial z}. \tag{4.4c}$$

In this way the equations (4.3b) and (4.3c) change to

$$\rho\left(u\frac{\partial u}{\partial r} + w\frac{\partial u}{\partial z}\right) = -\frac{\partial p}{\partial r} + \frac{1}{r}\frac{\partial(r\tau_{rr})}{\partial r} + \frac{\partial \tau_{rz}}{\partial z}, \tag{4.5}$$

$$\rho\left(u\frac{\partial w}{\partial r} + w\frac{\partial w}{\partial z}\right) = (\rho_\infty - \rho)g - \frac{\partial p}{\partial z} + \frac{1}{r}\frac{\partial(r\tau_{zr})}{\partial r} + \frac{\partial \tau_{zz}}{\partial z}. \tag{4.6}$$

Equations (4.3e), (4.3a), (4.3d), (4.5) and (4.6) constitute the governing set of equations which will be nondimensionalised with the introduction of the following scalings

$$x = a\dot{x}, \quad y = a\dot{y}, \quad \rho = \rho_\infty\dot{\rho}, \quad u = \frac{\nu_\infty}{a}\dot{u}, \quad w = \frac{\nu_\infty}{a}\dot{w}, \quad k = k_\infty\dot{k}, \quad \mu = \mu_\infty\dot{\mu},$$

$$\theta = \frac{T - T_\infty}{T_\mathrm{w} - T_\infty}, \quad \Pi = \frac{pL^2}{\rho_\infty \nu^2} \quad \text{and} \quad \lambda_\mathrm{T} = \frac{T_\mathrm{w} - T_\infty}{T_\infty}. \tag{4.7}$$

Fluid properties having as a subscript ∞ correspond to ambient properties, so that ν_∞ and μ_∞ refer to the kinematic and dynamic viscosity respectively, while κ_∞ is the thermal conductivity, and ρ_∞, T_∞ the ambient density and temperature. Further since there is no characteristic velocity scale, simple dimensional arguments of the main physical parameters of the problem can lead to a velocity scale given as ν_∞/a.

Introduction of the nondimensional parameters into the governing equations will result in the continuity equation given as

$$\frac{\partial}{\partial \dot{r}}\left(\dot{r}\dot{\rho}\dot{u}\right) + \frac{\partial}{\partial \dot{z}}\left(\dot{r}\dot{\rho}\dot{w}\right) = 0, \tag{4.8a}$$

whilst momentum and energy equations change to

$$\dot{\rho}\left(\dot{u}\frac{\partial \dot{u}}{\partial \dot{r}} + \dot{w}\frac{\partial \dot{u}}{\partial \dot{z}}\right) = -\frac{\partial \Pi}{\partial \dot{r}} + \frac{1}{\dot{r}}\frac{\partial}{\partial \dot{r}}\left(\dot{r}\dot{\tau}_{rr}\right) + \frac{\partial}{\partial \dot{z}}\left(\dot{\tau}_{rz}\right), \tag{4.8b}$$

$$\dot{\rho}\left(\dot{u}\frac{\partial \dot{w}}{\partial \dot{r}} + \dot{w}\frac{\partial \dot{w}}{\partial \dot{z}}\right) = -\frac{\partial \Pi}{\partial \dot{z}} + \frac{a^3\left(1-\dot{\rho}\right)g}{\nu_\infty^2} + \frac{1}{\dot{r}}\frac{\partial}{\partial \dot{r}}\left(\dot{r}\dot{\tau}_{zr}\right) + \frac{\partial}{\partial \dot{z}}\left(\dot{\tau}_{zz}\right), \tag{4.8c}$$

$$\dot{\rho}\left(\dot{u}\frac{\partial \theta}{\partial r} + \dot{w}\frac{\partial \theta}{\partial \dot{z}}\right) = \frac{\kappa_\infty}{\rho_\infty \mathrm{c_p} \nu_\infty}\left(\frac{1}{\dot{r}}\frac{\partial}{\partial \dot{r}}\left(\dot{r}\dot{\kappa}\frac{\partial \theta}{\partial r}\right) + \frac{\partial}{\partial \dot{z}}\left(\dot{\kappa}\frac{\partial \theta}{\partial \dot{z}}\right)\right). \tag{4.8d}$$

Finally the ideal gas law now reads as

$$1-\dot{\rho} = \frac{\dot{\rho}\theta\left(T_w - T_\infty\right)}{T_\infty} = \dot{\rho}\theta\lambda_{\mathrm{T}}. \tag{4.8e}$$

The main similarity parameters for free convective flows are the Grashof [3] and Prandtl numbers defined as[4]

$$\mathrm{Gr} = \frac{ga^3\left(T_w - T_\infty\right)}{\nu_\infty^2 T_\infty} = \frac{ga^3\lambda_{\mathrm{T}}}{\nu_\infty^2}, \quad \frac{1}{\mathrm{Pr}} = \frac{\kappa_\infty}{\rho_\infty \mathrm{c_p}\nu_\infty}. \tag{4.9}$$

Unveiling of the above similarity parameters in equations (4.8) and dropping the dots provides the final form of the nondimensional equations, given as

$$\frac{\partial}{\partial r}\left(r\rho u\right) + \frac{\partial}{\partial z}\left(r\rho w\right) = 0, \tag{4.10a}$$

$$\rho\left(u\frac{\partial u}{\partial r} + w\frac{\partial u}{\partial z}\right) = -\frac{\partial \Pi}{\partial r} + \frac{1}{r}\frac{\partial}{\partial r}\left(r\tau_{rr}\right) + \frac{\partial}{\partial z}\left(\tau_{rz}\right), \tag{4.10b}$$

$$\rho\left(u\frac{\partial w}{\partial r} + w\frac{\partial w}{\partial z}\right) = -\frac{\partial \Pi}{\partial z} + \mathrm{Gr}\rho\theta + \frac{1}{r}\frac{\partial}{\partial r}\left(r\tau_{zr}\right) + \frac{\partial}{\partial z}\left(\tau_{zz}\right), \tag{4.10c}$$

$$\rho\left(u\frac{\partial \theta}{\partial r} + w\frac{\partial \theta}{\partial z}\right) = \frac{1}{\mathrm{Pr}}\left(\frac{1}{r}\frac{\partial}{\partial r}\left(r\kappa\frac{\partial \theta}{\partial r}\right) + \frac{\partial}{\partial z}\left(\kappa\frac{\partial \theta}{\partial z}\right)\right). \tag{4.10d}$$

---

[3] Quite often Rayleigh number is used instead

[4] Here the gas expansion coefficient $\beta = \frac{1}{T_\infty}$ [25] has already been included in the Grashof number definition

4.2.1 The boundary layer equations

The nondimensional set of equations can be treated as a singular perturbation problem as $\mathrm{Gr} \to \infty$; therefore following [89], we start by introducing the following set of stretched variables

$$z = \epsilon \hat{z}, \quad u = \epsilon^{-2}\hat{u}, \quad w = \epsilon^{-1}\hat{w}, \quad \Pi = \epsilon^{-4}\hat{\Pi}, \quad \text{where} \quad \epsilon = \mathrm{Gr}^{-1/5} \tag{4.11}$$

into the governing equations, so by keeping the leading order terms, the first order boundary layer approximation equations are obtained as

$$\frac{\partial}{\partial r}(r\rho\hat{u}) + \frac{\partial}{\partial \hat{z}}(r\rho\hat{w}) = 0, \tag{4.12a}$$

$$\rho\left(\hat{u}\frac{\partial \hat{u}}{\partial r} + \hat{w}\frac{\partial \hat{u}}{\partial \hat{z}}\right) = -\frac{\partial \hat{\Pi}}{\partial r} + \frac{\partial}{\partial \hat{z}}\left(\mu\frac{\partial \hat{u}}{\partial \hat{z}}\right) + \mathcal{O}(\epsilon^2), \tag{4.12b}$$

$$\frac{\partial \hat{\Pi}}{\partial \hat{z}} = \rho\vartheta + \mathcal{O}(\epsilon^2), \tag{4.12c}$$

$$\rho\left(\hat{u}\frac{\partial \vartheta}{\partial r} + \hat{w}\frac{\partial \vartheta}{\partial \hat{z}}\right) = \frac{1}{\mathrm{Pr}}\frac{\partial}{\partial \hat{z}}\left(\kappa\frac{\partial \vartheta}{\partial \hat{z}}\right) + \mathcal{O}(\epsilon^2). \tag{4.12d}$$

The above parabolic partial differential equations are to be solved subject to the following boundary conditions

$$\begin{gathered}\hat{u} = \hat{w} = 0 \text{ and } \vartheta = 1, \text{ on } \hat{z} = 0 \text{ while } r \in (0\,,1], \\ \hat{u}, \hat{w}, \vartheta \to 0 \text{ as } \hat{z} \to \infty, \\ \hat{u} = \hat{w} = \vartheta = 0 \text{ at } r = 1 \text{ and } \hat{z} > 0.\end{gathered} \tag{4.12e}$$

At this point we shall introduce the following coordinate system, given in Figure 4.3, based on the transformation $r \to 1 - r$. In this way the edge of the plate corresponds to $r = 0$, while the centre of the plate is now located at $r = 1$. Further, note that the velocity vector in the nondimensional coordinate system $(r, \hat{z})$ was given as $\mathbf{u} = \hat{u}\mathbf{e}_r + \hat{w}\mathbf{e}_{\hat{z}}$, then for the above described transformation the velocity vector is given as $\mathbf{u} = \hat{u}\mathbf{e}_{1-r} + \hat{w}\mathbf{e}_{\hat{z}} = -\hat{u}\mathbf{e}_r + \hat{w}\mathbf{e}_{\hat{z}}$.

In doing so boundary layer equations for the momentum and energy remain unchanged as well as the boundary conditions. The only change corresponds to the mass

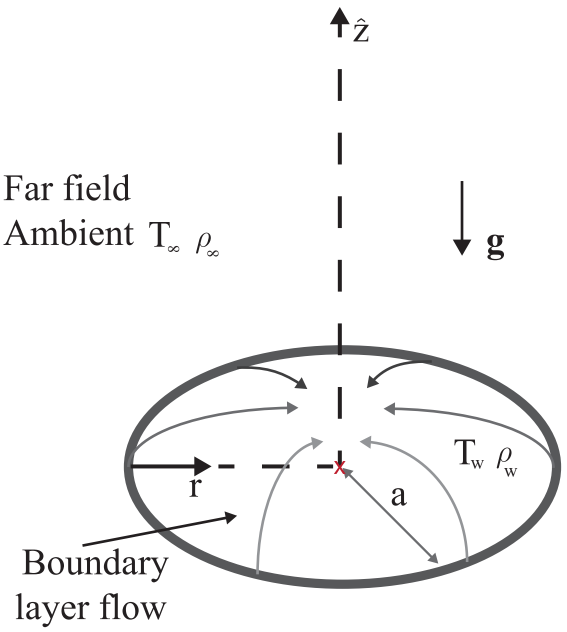

Figure 4.3: The coordinate system for the boundary layer equations.

continuity equations which is now listed as

$$\frac{\partial}{\partial r}\big((1-r)\rho\hat{u}\big)+\frac{\partial}{\partial\hat{z}}\big((1-r)\rho\hat{w}\big)=0. \tag{4.13}$$

The boundary layer equations (4.12b),(4.12c),(4.12d) and (4.13), will occupy us for the rest of this chapter.

Moving on with the introduction of a stream function that satisfies the continuity equation i.e.

$$(1-r)\rho\hat{u}=\frac{\partial\Psi}{\partial\hat{z}},\ \text{and}\ -(1-r)\rho\hat{w}=\frac{\partial\Psi}{\partial r}, \tag{4.14}$$

and similarity transformations for the independent variables based on the Dorodnitsyn-Howarth transformation [90],[31] [79] (in order to remove the density from the formal equations) given as

$$\zeta=r,\ \text{and}\ \eta=(Cr)^{-2/5}\int_0^{\hat{z}}\rho d\tilde{z}. \tag{4.15}$$

In addition for the mapping $(r\,,z)\to(\zeta\,,\eta)$ the formal transformations will be given as

$$\frac{\partial}{\partial r}=\frac{\partial}{\partial\zeta}+\frac{\partial\eta}{\partial r}\frac{\partial}{\partial\eta}\ \text{ and }\ \frac{\partial}{\partial\hat{z}}=\rho(Cr)^{-2/5}\frac{\partial}{\partial\eta}. \tag{4.16}$$

Furthermore the dependent variables are transformed as

$$\Psi(r,z)=(Cr)^{3/5}f(\zeta,\eta),\quad \hat{\Pi}(r,z)=(Cr)^{2/5}g(\zeta,\eta)\quad\text{and}\quad\vartheta(r,z)=\vartheta(\zeta,\eta), \tag{4.17}$$

with C being the Chapman variable. Applying the above transformations into r-momentum boundary layer equation (4.12b) we obtain for the l.h.s

$$\rho\Big(\hat{u}\frac{\partial \hat{u}}{\partial r}+\hat{w}\frac{\partial \hat{u}}{\partial \hat{z}}\Big)=\rho\Bigg[\frac{\tfrac{1}{5}C(Cr)^{-3/5}(1-r)+(Cr)^{2/5}}{(1-r)^3}f_\eta^2+\frac{(Cr)^{2/5}}{(1-r)^2}f_\eta f_{\eta\zeta}- \\ -\frac{3}{5}\frac{C(Cr)^{-3/5}}{(1-r)^2}ff_{\eta\eta}-\frac{(Cr)^{2/5}}{(1-r)^2}f_\zeta f_{\eta\eta}\Bigg],$$

whilst the r.h.s is given as

$$-\frac{\partial \hat{\Pi}}{\partial r}+\frac{\partial}{\partial \hat{z}}\left(\mu\frac{\partial \hat{u}}{\partial \hat{z}}\right)=\left[-\Big(\frac{2}{5}C(Cr)^{-3/5}g+(Cr)^{2/5}g_\zeta+\frac{\partial \eta}{\partial r}(Cr)^{2/5}g_\eta\Big)+\rho\frac{(Cr)^{-3/5}}{1-r}\frac{\partial}{\partial \eta}\big[\mu\rho f_{\eta\eta}\big]\right].$$

After collecting and simplifying the above terms the transformed r-momentum equation writes as

$$(1-\zeta)^2\Big[\frac{\mu\rho}{C}f_{\eta\eta}\Big]_\eta+\frac{3}{5}(1-\zeta)ff_{\eta\eta}-\frac{1}{5}f_\eta^2-\frac{4}{5}\zeta f_\eta^2=\zeta(1-\zeta)\Big(f_{\eta\zeta}f_\eta-f_{\eta\eta}f_\zeta\Big)+ \\ +\frac{1}{\rho}(1-\zeta)^3\Big[\frac{2}{5}g+\zeta g_\zeta+\zeta\frac{\partial \eta}{\partial r}g_\eta\Big]. \quad (4.18a)$$

Meanwhile the $\hat{z}$-momentum boundary layer equation, after the introduction of the similarity variables changes to

$$\vartheta=\frac{\partial g}{\partial \eta}. \quad (4.18b)$$

Finally, the energy equation is given as

$$(1-\zeta)\frac{1}{\mathrm{Pr}}\Big[\frac{\kappa\rho}{C}\vartheta_\eta\Big]_\eta=\zeta\Big(f_\eta\vartheta_\zeta-f_\zeta\vartheta_\eta\Big)-\frac{3}{5}f\vartheta_\eta. \quad (4.18c)$$

A problem that needs addressing appears in the r.h.s of equation (4.18a) by means of the term $(\partial\eta/\partial r)$, since an explicit expression of that term is required if it is to make any progress. One way to proceed is to start by writing the transformations of the independent variables in matrix-vector form, i.e.

$$\begin{bmatrix}\dfrac{\partial}{\partial r}\\ \dfrac{\partial}{\partial \hat{z}}\end{bmatrix}=\mathbf{Q}\begin{bmatrix}\dfrac{\partial}{\partial \zeta}\\ \dfrac{\partial}{\partial \eta}\end{bmatrix}\quad\text{where } \mathbf{Q}=\begin{bmatrix}\dfrac{\partial \zeta}{\partial r} & \dfrac{\partial \eta}{\partial r}\\ \\ \dfrac{\partial \zeta}{\partial \hat{z}} & \dfrac{\partial \eta}{\partial \hat{z}}\end{bmatrix}. \quad (4.19)$$

Similarly the inverse transformation, i.e. $(\zeta\,,\eta)\rightarrow(r\,,\hat{z})$, is given as

$$\begin{bmatrix}\dfrac{\partial}{\partial \zeta}\\ \dfrac{\partial}{\partial \eta}\end{bmatrix}=\mathbf{R}\begin{bmatrix}\dfrac{\partial}{\partial r}\\ \dfrac{\partial}{\partial \hat{z}}\end{bmatrix}\quad\text{where } \mathbf{R}=\begin{bmatrix}\dfrac{\partial r}{\partial \zeta} & \dfrac{\partial \hat{z}}{\partial \zeta}\\ \\ \dfrac{\partial r}{\partial \eta} & \dfrac{\partial \hat{z}}{\partial \eta}\end{bmatrix}. \quad (4.20)$$

Clearly $\mathbf{R} = \mathbf{Q}^{-1}$ while the inverse of $\mathbf{Q}$ is given as

$$\mathbf{Q}^{-1} = \begin{bmatrix} 1 & -\dfrac{1}{(Cr)^{-2/5}\rho}\dfrac{\partial \eta}{\partial r} \\ & \\ 0 & \dfrac{1}{(Cr)^{-2/5}\rho}. \end{bmatrix}. \tag{4.21}$$

Therefore the following must hold

$$\begin{bmatrix} \dfrac{\partial r}{\partial \zeta} & \dfrac{\partial \hat{z}}{\partial \zeta} \\ & \\ \dfrac{\partial r}{\partial \eta} & \dfrac{\partial \hat{z}}{\partial \eta} \end{bmatrix} = \begin{bmatrix} 1 & -\dfrac{1}{(Cr)^{-2/5}\rho}\dfrac{\partial \eta}{\partial r} \\ & \\ 0 & \dfrac{1}{(Cr)^{-2/5}\rho}. \end{bmatrix}. \tag{4.22}$$

From the above we can obtain the inverse Dorodnitsyn-Howarth transformation as

$$\hat{z} = (Cr)^{2/5} \int_0^{\eta} \frac{1}{\rho} \mathrm{d}\tilde{\eta}, \tag{4.23}$$

in addition to

$$\frac{\partial \eta}{\partial r} = -(Cr)^{-2/5} \rho \frac{\partial z}{\partial \zeta}. \tag{4.24}$$

It is not hard now, using (4.23) (4.24), to obtain

$$\frac{\partial \eta}{\partial r} = \rho \Big(-\frac{2}{5\zeta} \int_0^{\eta} \frac{1}{\rho} \, d\tilde{\eta} + \int_0^{\eta} \frac{1}{\rho^2} \frac{\partial \rho}{\partial \zeta} \, d\tilde{\eta} \Big). \tag{4.25}$$

Turning attention to the terms including the highest derivatives in the momentum and energy equation, the fractions including the fluid properties can easily be simplified by recalling the linear law for viscosity and thermal conductivity (4.1) which is now expressed in terms of density (using the ideal gas law) in non dimensional form as

$$\mu = C\,\frac{1}{\rho}, \quad \kappa = C\,\frac{1}{\rho} \quad \text{and} \quad \frac{1}{\rho} = 1 + \lambda_{\mathrm{T}} \vartheta = 1 + \lambda_{\mathrm{T}} g_{\eta}. \tag{4.26}$$

Utilising the above to obtain the final form of the nonsimilar governing equations

$$\begin{aligned} (1-\zeta)^2 f_{\eta\eta\eta} + \frac{3}{5}(1-\zeta) f f_{\eta\eta} - \frac{1}{5} f_{\eta}^2 - \frac{4}{5} \zeta f_{\eta}^2 = \zeta(1-\zeta)\Big(f_{\eta\zeta} f_{\eta} - f_{\eta\eta} f_{\zeta} \Big) + \\ + \frac{1}{\rho}(1-\zeta)^3 \Big[\frac{2}{5} g + \zeta g_{\zeta} \Big] - (1-\zeta)^3 \left(\frac{2}{5} \int_0^{\eta} \frac{1}{\rho} \, d\tilde{\eta} - \zeta \int_0^{\eta} \frac{1}{\rho^2} \frac{\partial \rho}{\partial \zeta} \, d\tilde{\eta} \right) g_{\eta}, \end{aligned} \tag{4.27a}$$

$$g_{\eta} = \vartheta, \tag{4.27b}$$

$$(1-\zeta)\frac{1}{\mathrm{Pr}}g_{\eta\eta\eta}+\frac{3}{5}fg_{\eta\eta}=\zeta\Big(f_{\eta}g_{\eta\zeta}-f_{\zeta}g_{\eta\eta}\Big). \tag{4.27c}$$

The above coupled system of PIDEs, is to be solved subject to the following boundary conditions

$$f(0,\zeta)=f_{\eta}(0,\zeta)=0,\ \ \vartheta(0,\zeta)=g_{\eta}(0,\zeta)=1\ \text{ and} \tag{4.27d}$$

$$f_{\eta}(\eta,\zeta)=\vartheta(\eta,\zeta)=g_{\eta}(\eta,\zeta)=g(\eta,\zeta)=0\ \text{ as }\ \eta\to\infty.$$

4.3 Series solutions valid for $\zeta \to 0$

Setting $\zeta = 0$ in equations (4.27) results in the similarity equations describing the flow above the horizontal semi-infinite plate. Similarity equations can be viewed as a leading order approximation of the flow at the edge of the circular plate, thus allowing departures from similarity power series of the form

$$f(\zeta\,,\eta)\approx\sum_{i=0}^{n}\zeta^{i}f_{i}(\eta),\ \ g(\zeta\,,\eta)\approx\sum_{i=0}^{n}\zeta^{i}G_{i}(\eta),\ \text{ and }\ \Theta(\zeta\,,\eta)\approx\sum_{i=0}^{n}\zeta^{i}\Theta_{i}(\eta) \tag{4.28a}$$

will be assumed valid for small values of ζ. In addition, the density is also approximated as

$$\frac{1}{\rho}\approx1+\lambda_{\mathrm{T}}\sum_{i=0}^{n}\zeta^{i}\Theta_{i}(\eta)=1+\lambda_{\mathrm{T}}\sum_{i=0}^{n}\zeta^{i}G_{i}' \tag{4.28b}$$

where the prime notation corresponds to differentiation w.r.t η, while $n = 3$. Application of the series expansion into the governing equations results in the following set of equations

- $\mathcal{O}(1)$

$$f_0'''+\frac{3}{5}f_0f_0''+\frac{2}{5}\left(\eta-\lambda_{\mathrm{T}}G_0\left(0\right)\right)G_0'-\frac{1}{5}\left(f_0'\right)^2-\frac{2}{5}G_0=0, \tag{4.29a}$$

$$\frac{1}{\mathrm{Pr}}G_0'''+\frac{3}{5}f_0G_0''=0, \tag{4.29b}$$

- $\mathcal{O}(\zeta)$

$$f_1'''+\frac{1}{5}\left(8f_1+3f_0\right)f_0''+\frac{3}{5}f_0f_1''+\frac{1}{5}\Big(\lambda_{\mathrm{T}}\big(2G_0(0)-7G_1(0)\big)-2\eta\Big)G_0'-\frac{6}{5}\left(f_0'\right)^2-\frac{7}{5}f_0'f_1'+$$
$$+\frac{2}{5}\Big(\eta-\lambda_{\mathrm{T}}G_0(0)\Big)G_1'-\frac{7}{5}G_1+\frac{2}{5}G_0=0, \tag{4.29c}$$

$$\frac{1}{\mathrm{Pr}}G_1'''+\frac{1}{5}\left(3f_0+8f_1\right)G_0''+\frac{3}{5}f_0G_1''-f_0'G_1'=0, \tag{4.29d}$$

- $\mathcal{O}(\zeta^2)$

$$\begin{aligned} f_2''' + \frac{1}{5}\Big(3f_0 + 8f_1 + 13f_2\Big) f_0'' + \frac{1}{5}\Big(3f_0 + 8f_1\Big) f_1'' + \frac{3}{5} f_0 f_2'' - \frac{11}{5}\left(f_0'\right)^2 - \frac{6}{5}\left(f_1'\right)^2 - \\ - \frac{1}{5}\Big(17f_1' + 12f_2'\Big) f_0' + \frac{\lambda_{\mathrm{T}}}{5}\Big(7G_1(0) - 12G_2(0)\Big) G_0' + \frac{1}{5}\Big(\lambda_{\mathrm{T}}\big(2G_0(0) - 7G_1(0)\big) - 2\eta\Big) G_1' + \\ + \frac{2}{5}\Big(\eta - \lambda_{\mathrm{T}} G_0(0)\Big) G_2' + \frac{7}{5} G_1 - \frac{12}{5} G_2 = 0, \end{aligned} \tag{4.29e}$$

$$\frac{1}{\mathrm{Pr}} G_2''' + \frac{1}{5}\left(3f_0 + 8f_1 + 13f_2\right) G_0'' + \frac{1}{5}\left(3f_0 + 8f_1\right) G_1'' + \frac{3}{5} f_0 G_2'' - \left(f_0' + f_1'\right) G_1' - 2 f_0' G_2' = 0, \tag{4.29f}$$

- $\mathcal{O}(\zeta^3)$

$$\begin{aligned} f_3''' + \frac{1}{5}\Big(3f_0 + 8f_1 + 13f_2 + 18f_3\Big) f_0'' + \frac{1}{5}\Big(3f_0 + 8f_1 + 13f_2 + \Big) f_1'' + \frac{1}{5}\Big(8f_1 + 3f_0\Big) f_2'' + \\ + \frac{3}{5} f_0 f_3'' - \frac{16}{5}\left(f_0'\right)^2 - \frac{1}{5}\Big(27f_1' + 22f_2' + 17f_3'\Big) f_0' - \frac{17}{5} f_1' f_2' - \frac{11}{5}\left(f_1'\right)^2 + \\ + \frac{\lambda_{\mathrm{T}}}{5}\Big(12G_2(0) - 17G_3(0)\Big) G_0' + \frac{\lambda_{\mathrm{T}}}{5}\Big(7G_1(0) - 12G_2(0)\Big) G_1' + \\ + \frac{1}{5}\Big(\lambda_{\mathrm{T}}\big(2G_0(0) - 7G_1(0)\big) - 2\eta\Big) G_2' + \frac{2}{5}\Big(\eta - \lambda_{\mathrm{T}} G_0(0)\Big) G_3' + \frac{12}{5} G_2 - \frac{17}{5} G_3 = 0, \end{aligned} \tag{4.29g}$$

$$\begin{aligned} \frac{1}{\mathrm{Pr}} G_3' + \frac{1}{5}\left(3f_0 + 8f_1 + 13f_2 + 8f_3\right) G_0'' + \frac{1}{5}\left(3f_0 + 8f_1 + 13f_2\right) G_1'' + \frac{1}{5}\left(3f_0 + 8f_1\right) G_2'' + \\ + \frac{3}{5} f_0 G_3'' - \left(f_0' + f_1' + f_2'\right) G_1' - 2\left(f_0' + f_1'\right) G_2' - 3 f_0' G_3' = 0, \end{aligned} \tag{4.29h}$$

while the boundary conditions are now given by

$$\begin{aligned} & f_i(0) = f_i'(0) = 0, \;\; G_0'(0) = 1 \;\text{ while }\; G_{i+1}'(0) = 0, \;\text{ and} \\ & f_i'(\eta) \to 0, \;\; G_i(\eta) = G_i'(\eta) \to 0 \;\text{ as }\; \eta \to \infty, \;\text{ for }\; i = 0 \ldots n. \end{aligned} \tag{4.30}$$

It must be noted that on invoking the Boussinesq approximation $\lambda_{\mathrm{T}} = 0$ for the leading order term equations (self similar), the semi-infinite plate equations given in [89] are recovered.

4.3.1 Numerical solution

This section is dedicated to the numerical solution of equations (4.29) subject to BCs (4.30) using the shooting method. The shooting method is a numerical technique for solving boundary value problems (BVPs) by treating them as initial value ones (IVPs). Analytically the ‘shooting’ procedure is initiated by making a guess for the missing ICs and calling a standard numerical scheme for the solution of an IVP, disregarding for the time being the BCs. Once the numerical solution of the IVP is available, a test is imposed on the solution in order to check whether it satisfies the boundary conditions to desired tolerance. If the tolerance criterion is satisfied the procedure terminates, otherwise the initial guesses for the ICs are updated and the procedure is repeated until fulfilment of the tolerance criterion.

In dealing with eight third order differential equations (4.29), the first step in order to implement the shooting method is order reduction of the DEs to one. Introduction of new dependent variables u_i and v_i such that[5]

$$f_k^{(j)} = u_{3k+j},\ G_k^{(j)} = v_{3k+j},\ \text{where } k = 0 \dots 3 \text{ and } j = 0 \dots 2, \tag{4.31}$$

while

$$\frac{\mathrm{d}u_{3i}}{\mathrm{d}\eta} = u_{3i+1},\ \frac{\mathrm{d}u_{3i+1}}{\mathrm{d}\eta} = u_{3i+2} \text{ and } \frac{\mathrm{d}v_{3i}}{\mathrm{d}\eta} = v_{3i+1},\ \frac{\mathrm{d}v_{3i+1}}{\mathrm{d}\eta} = v_{3i+2},\ \text{for } i = 0 \dots 3. \tag{4.32}$$

Now order reduction has led to a system of twenty four coupled first order DEs for the solution of which twenty four ICs are required. Looking back to equation (4.30) only twelve from the twenty four constraints are available (at $\eta = 0$) which implies that twelve initial guesses are necessary. Specifically the known ICs are given in terms of the newly introduced variables as

$$\begin{gathered} u_{3i}(0) = 0,\ u_{3i+1}(0) = 0,\ \text{for } i = 0 \dots 3 \text{ and} \\ v_1(0) = 1,\ v_{3i+1}(0) = 0,\ \text{where now } i = 1 \dots 3. \end{gathered} \tag{4.33}$$

For the remaining variables the following initial guesses are assumed

$$u_{3i+2}(0) = \alpha_i,\ v_{3i}(0) = \beta_i,\ v_{3i+2}(0) = \gamma_i \text{ and } i = 0 \dots 3. \tag{4.34}$$

A further difficulty that needs resolving is the appearance of terms $v_{3i}(0)$ directly into the DE’s for which, as mentioned, there is no prior knowledge. A way to overcome that problem numerically is by treating constants $v_{3i}(0)$ as new variables that simply

---

[5] Notation $^{(j)}$ denotes differentiation with respect to η.

need to obey four additional differential equations subject to ICs given by the guesses (i.e. $v_{3i}(0) = \beta_i$). Analytically we shall introduce

$$\frac{\mathrm{d}q_i}{\mathrm{d}\eta} = 0 \text{ subject to } q_i(0) = \beta_i \text{ for } i = 0 \ldots 3. \tag{4.35}$$

Equation (4.32) presents only sixteen of the twenty four available DEs resulting from order reduction of equations (4.29), the remaining ones are listed below

$$\frac{1}{Pr}\frac{\mathrm{d}v_2}{\mathrm{d}\eta} + \frac{3}{5}\,v_2 u_0 = 0, \tag{4.36a}$$

$$\frac{1}{Pr}\frac{\mathrm{d}v_5}{\mathrm{d}\eta} + \frac{1}{5}\,(3\,u_0 + 8\,u_3)\,v_2 + \frac{3}{5}\,u_0 v_5 - u_1 v_4 = 0, \tag{4.36b}$$

$$\begin{aligned}\frac{1}{Pr}\frac{\mathrm{d}v_8}{\mathrm{d}\eta} + \frac{1}{5}\,(8u_3 + 13u_6 + 3\,u_0)\,v_2 + \frac{1}{5}\,(3u_0 + 8u_3)\,v_5 + {}&\\ + \frac{3}{5}u_0 v_8 - (u_1 + u_4)\,v_4 - 2u_1 v_7 = 0,&\end{aligned} \tag{4.36c}$$

$$\begin{aligned}\frac{1}{Pr}\frac{\mathrm{d}v_{11}}{\mathrm{d}\eta} + \frac{1}{5}\,(18u_9 + 13u_6 + 8u_3 + 3u_0)\,v_2 + \frac{1}{5}\,(8u_3 + 13u_6 + 3u_0)\,v_5 + {}&\\ + \frac{1}{5}\,(3u_0 + 8u_3)\,v_8 + \frac{3}{5}u_0 v_{11} - (u_1 + u_4 + u_7)\,v_4 - {}&\\ - 2\,(u_1 + u_4)\,v_7 - 3u_1 v_{10} = 0,&\end{aligned} \tag{4.36d}$$

$$\frac{\mathrm{d}u_2}{\mathrm{d}\eta} + \frac{3}{5}u_2 u_0 - \frac{1}{5}u_1^2 + \frac{2}{5}\,(\eta - \lambda_{\mathrm{T}} q_1)\,v_1 - \frac{2}{5}v = 0, \tag{4.36e}$$

$$\begin{aligned}\frac{\mathrm{d}u_5}{\mathrm{d}\eta} + \frac{1}{5}\,(3u_0 + 8u_3)\,u_2 + \frac{3}{5}u_0 u_5 + \frac{1}{5}\Big(\lambda_{\mathrm{T}}(2q_1 - 7\lambda_{\mathrm{T}} q_2) - 2\eta\Big)v_1 + \frac{2}{5}\,(\eta - \lambda_{\mathrm{T}} q_1)\,v_4 - {}&\\ - \frac{6}{5}u_1^2 - \frac{7}{5}u_1 u_4 + \frac{2}{5}v_0 - \frac{7}{5}v_3, = 0&\end{aligned} \tag{4.36f}$$

$$\begin{aligned}\frac{\mathrm{d}u_8}{\mathrm{d}\eta} + \frac{1}{5}\,(8u_3 + 13u_6 + 3u_0)\,u_2 + \frac{1}{5}\,(3u + 8u_3)\,u_5 + \frac{3}{5}u_0 u_8 - \frac{1}{5}\,(17u_4 + 12u_7)\,u_1 - {}&\\ - \frac{11}{5}\,u_1^2 - \frac{6}{5}\,u_4^2 + \frac{\lambda}{5}\,(7q_2 - 12q_3)\,v_1 + \frac{1}{5}\,\Big(2\lambda_{\mathrm{T}}(q_1 - 7q_2) - 2\eta\Big)v_4 + {}&\\ + \frac{2}{5}\,(\eta - \lambda_{\mathrm{T}} q_1)\,v_7 + \frac{7}{5}v_3 - \frac{12}{5}v_6 = 0,&\end{aligned} \tag{4.36g}$$

$$\begin{aligned}\frac{\mathrm{d}u_{11}}{\mathrm{d}\eta} + \frac{1}{5}\,(18u_9 + 13u_6 + 8u_3 + 3u_0)\,u_2 + \frac{1}{5}\,(8u_3 + 13u_6 + 3u_0)\,u_5 + {}&\\ + \frac{1}{5}\,(3u_0 + 8u_3)\,u_8 + \frac{3}{5}\,u_0 u_{11} - \frac{1}{5}\,(17\,u_{10} + 22\,u_7 + 27\,u_4)\,u_1 - \frac{17}{5}\,u_4 u_7 - \frac{16}{5}u_1^2 - \frac{11}{5}\,u_4^2 + {}&\\ + \frac{\lambda_{\mathrm{T}}}{5}\,(12q_3 - 17q_4)\,v_1 + \frac{\lambda_{\mathrm{T}}}{5}\,(7q_2 - 12q_3)\,v_4 + \frac{1}{5}\,\Big(2\lambda_{\mathrm{T}}(2q_1 - 7q_2) - 2\eta\Big)v_7 + \frac{2}{5}\,(\eta - \lambda_{\mathrm{T}} q_1)\,v_{10} + {}&\\ + \frac{12}{5}\,v_6 - \frac{17}{5}\,v_9 = 0.&\end{aligned} \tag{4.36h}$$

We are now at a stage where the shooting technique can be applied. The original system of eight third order equations (4.29) has been transformed to twenty eight first order DEs (i.e.(4.32), (4.35), and (4.36)), for which only twenty four ICs are required. Taking into account that only twelve are available (4.33) and the remaining twelve are guessed (4.34), an iterative procedure is initiated until the numerical solution obtained satisfies the BCs given by

$$u_{3i+1}(\infty) = 0,\ v_{3i}(\infty) = 0 \text{ and } v_{3i+1}(\infty) = 0 \text{ for } i = 0 \ldots 3. \tag{4.37}$$

to desired accuracy, which in our study was set to ten decimal digits.

The numerical scheme is implemented in **Maple** using *ShootLib* [55]. The BCs are imposed on $\eta = 10$, while computations are carried for $\lambda_{\mathrm{T}} \in [0,\, 4]$ and $\mathrm{Pr} = 0.72$, representing air. Furthermore, extensive numeric tables for the computed initial conditions $G_i(0)$, $\Theta_i'(0)$ and $f_i''(0)$, for $i = 0 \ldots 3$ and $\lambda_{\mathrm{T}} = 0, 0.1, 0.2, \ldots, 4$ are given in **Appendix A**. In addition a study for the effect of Prandtl number on the equations is carried out. Constant fluid properties are assumed i.e. $\lambda_{\mathrm{T}} = 0$, while Prandtl number is varied as $\mathrm{Pr} = 0.05, 0.1, 0.72, 1, 6, 10$. In each instance, the far field BCs were applied at different “large” values of η so as to accommodate the thickening or the thinning of the thermal layer as Prandtl number increases or decreases respectively.

4.3.2 Results and conclusions

The parameter λ_{T} introduced in the formulation of the problem, by discarding the Boussinesq approximation and including variable fluid effects, seems to have a large effect on the velocity distribution, though somehow the thermal layer remains almost unaffected. In Figure 4.4, the leading order approximation of the velocity function is seen to increase significantly with λ_{T} while, for the second order term, the effect is reversed. Third and fourth order approximations are almost equivalent and of small magnitude. The thermal layer is observed to be perturbed as λ_{T} is increased in Figure 4.5. The thinning observed to leading order is also demonstrated in the next order approximations, which are similar while there is a damping as the orders are increased. The thinning of the thermal layer results in a reduced negative pressure function in all approximations, as shown in the curves in Figure 4.6. It should be expected that the strong effect of λ_{T} on the velocity, would affect the laminar stability.

Directing attention now on the effect of Prandtl number to the flow, from the curves shown in Figure 4.7, it can be observed that the leading order term of the velocity function decreases with increasing Prandtl number. The second order term shows the opposite behaviour, while third and fourth order contributions are almost identical and of smaller magnitude, encompassing both behaviours as η varies. For the temperature function Figure 4.8, the leading order approximation indicates the thinning of the thermal layer, with increasing Prandtl number. The next three order approximations are all similar and of the same order, accompanied by a slight decrease in amplitude, as the order of the approximation is increased. The thinning of the thermal layer to leading order as Prandtl increases, is the reason for a decreased pressure gradient shown in Figure 4.9. The trend is repeated in higher order terms as the negative pressure function decreases by increasing the Prandtl number.

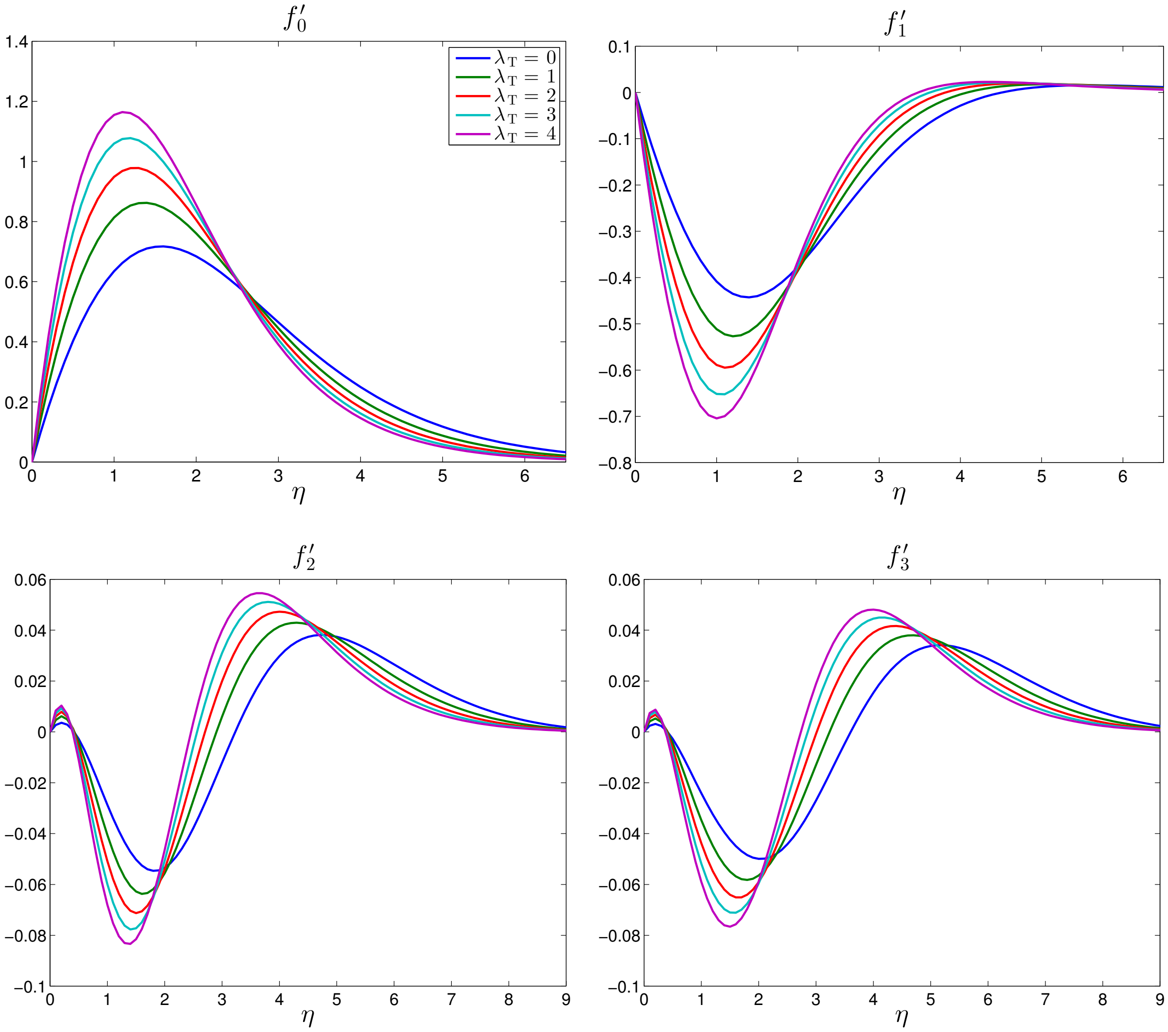

Figure 4.4: Effect of λ_T on the velocity function approximations while $\mathrm{Pr} = 0.72$.

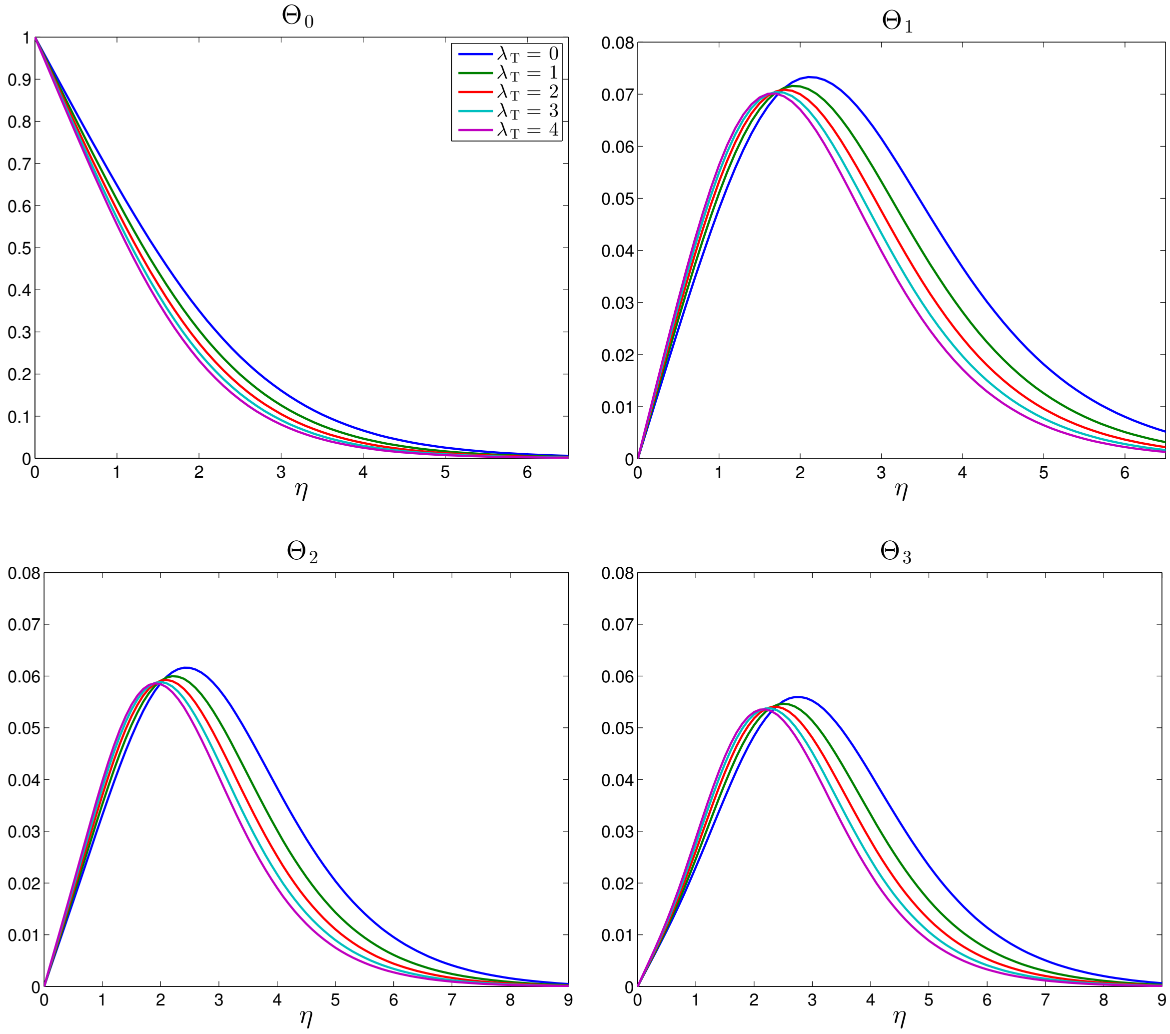

Figure 4.5: Effect of λ_T on the temperature function approximations while $\Pr = 0.72$.

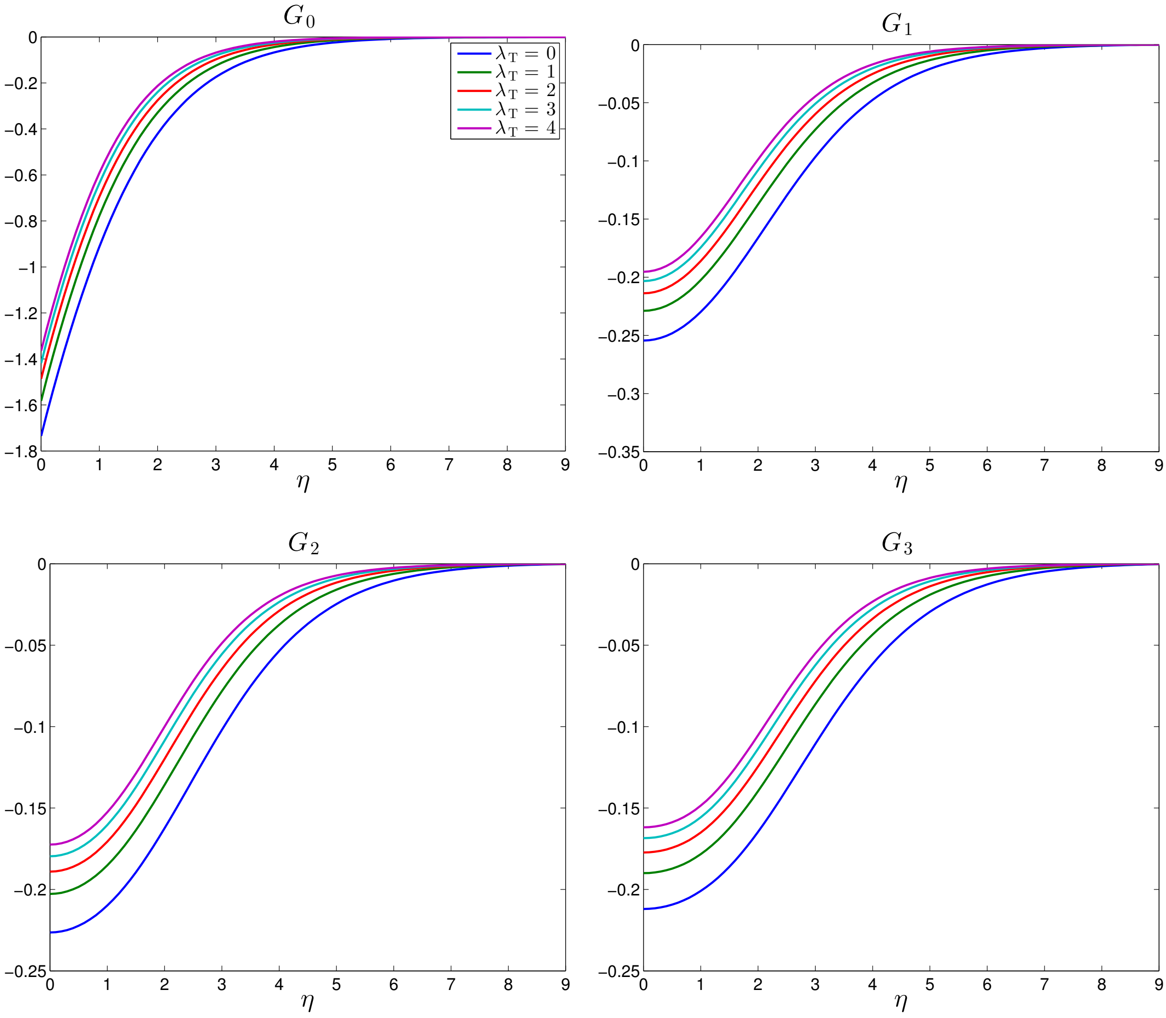

Figure 4.6: Effect of λ_T on the pressure function approximations while $\mathrm{Pr} = 0.72$.

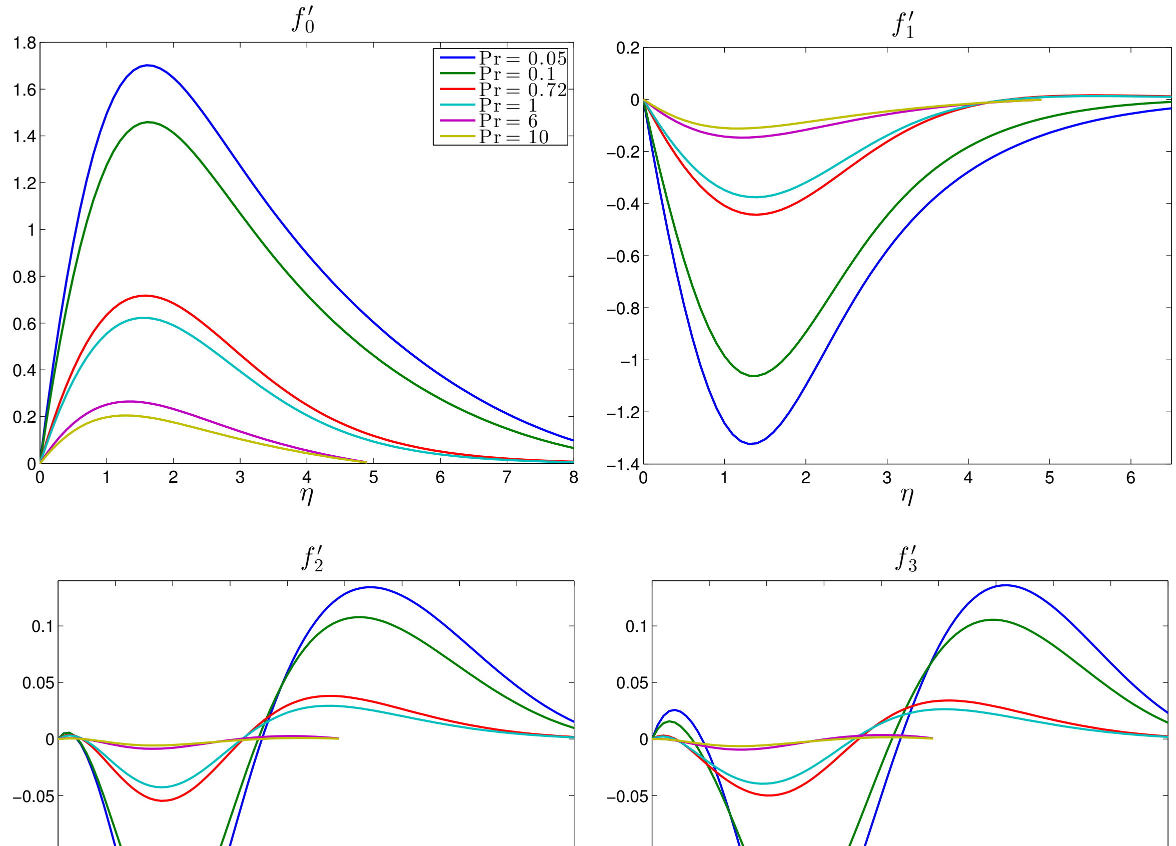

Figure 4.7: Effect of Pr on the velocity function approximations while $\lambda_{\mathrm{T}} = 0$.

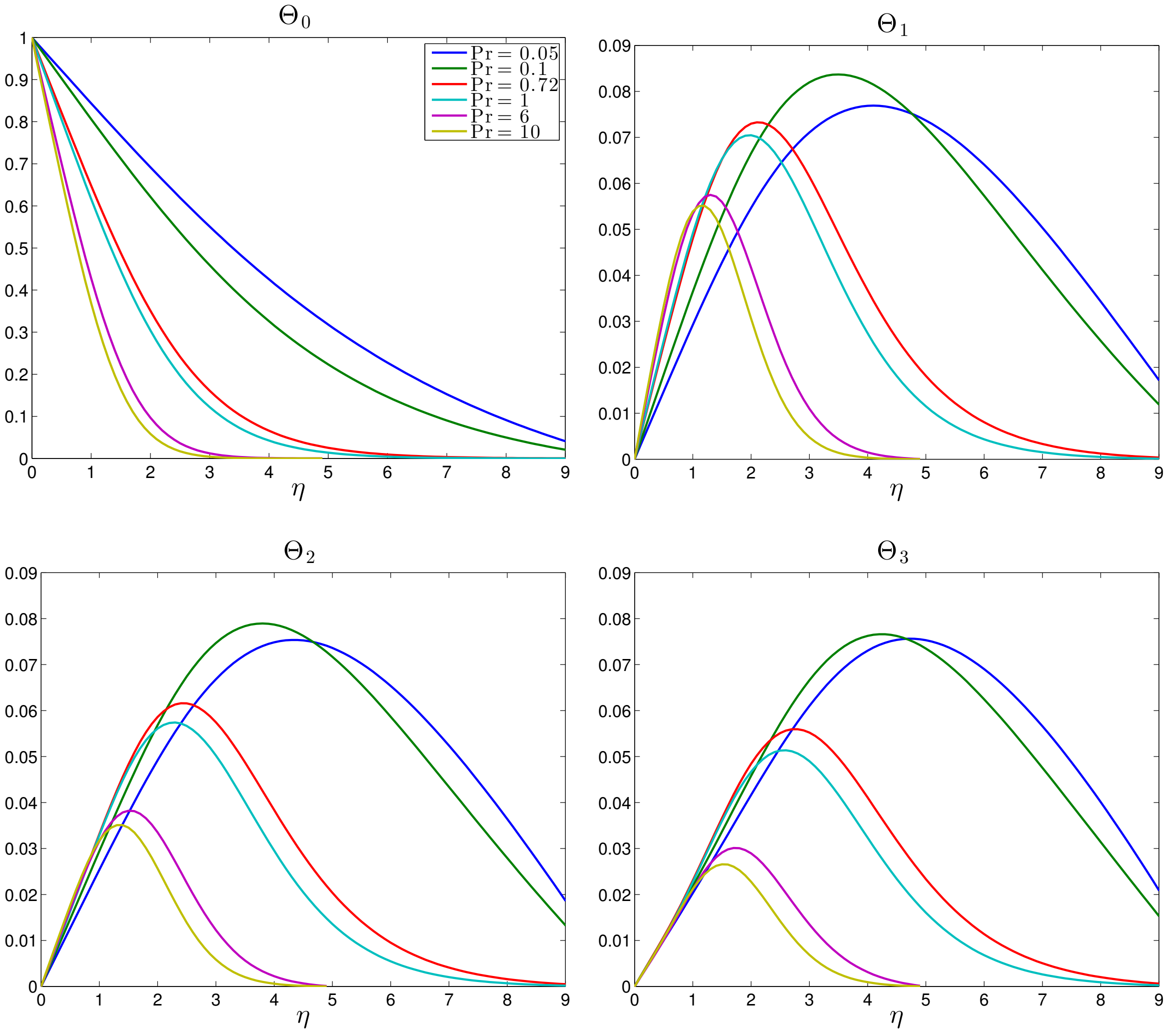

Figure 4.8: Effect of Pr on the temperature function approximations while $\lambda_{\mathrm{T}} = 0$.

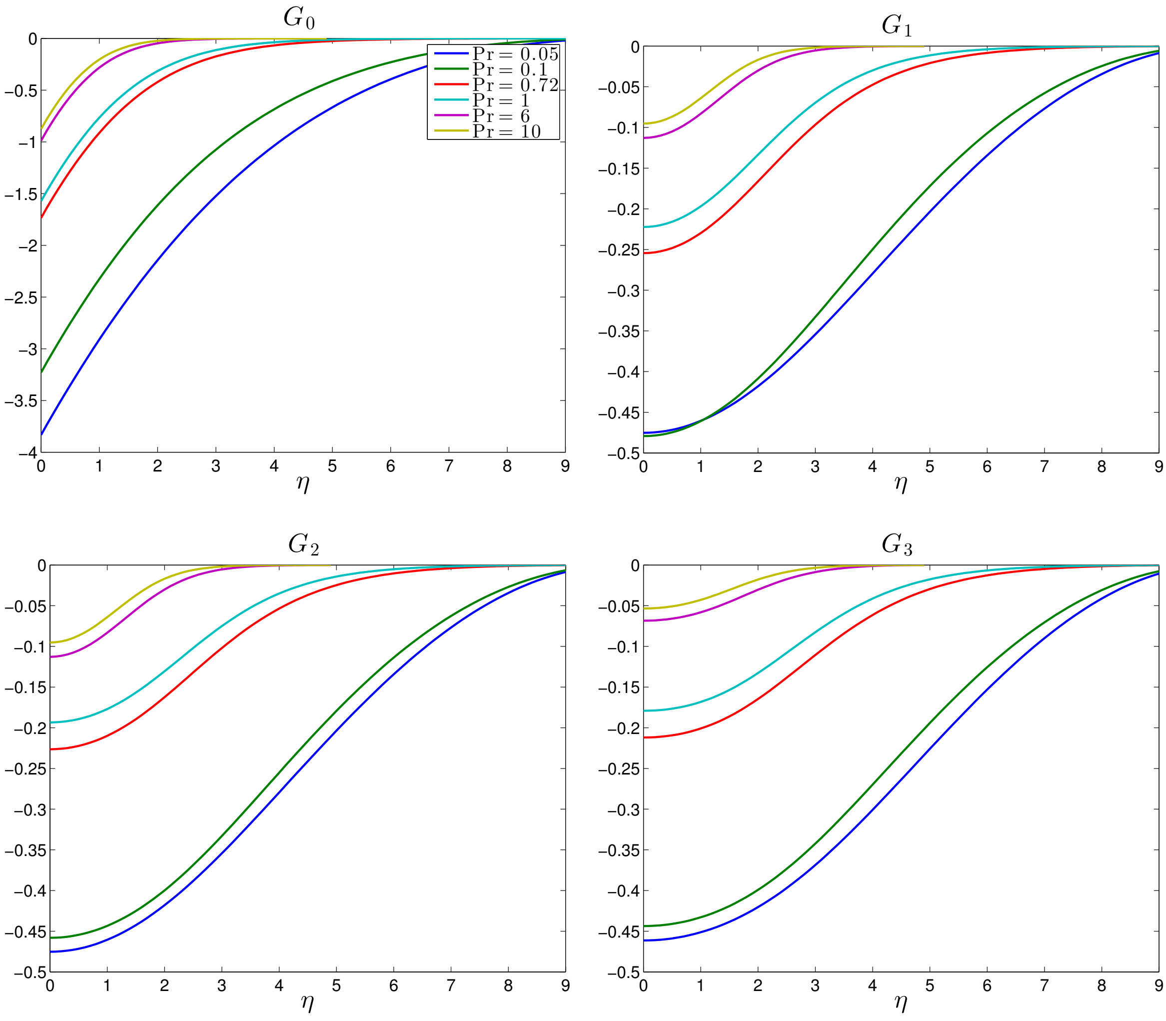

Figure 4.9: Effect of Pr on the pressure function approximations while $\lambda_{\mathrm{T}} = 0$.

4.4 Numerical formulation of the nonsimilar PDEs - The Keller Box method

Having obtained solutions valid at the edge of the disk, i.e. $\zeta \ll 1$, in this section validity of the solution is extended for every value of ζ by obtaining the full numerical solution of the nonsimilar PDEs (4.27). The chosen method for the solution of the nonsimilar integro-partial differential equations is the Keller Box finite difference scheme. The Keller Box (due to Keller) [41],[42],[43] or simply the Box method, is an implicit method of second order accuracy in both directions. It allows nonuniform meshing and, moreover, an improved accuracy by two orders when Richardson extrapolation is used.

The method overall consists of four steps; reduction of the order of the given PDEs to one, application of a difference scheme based on central differences, linearisation using Newton's method and finally numerical solution of a linear system of equations, for which the coefficient matrix has a block tridiagonal structure. The method is adequate for solving parabolic differential equations and has been used extensively in laminar [44] and turbulent boundary layer flows [45], flows with separation [14], and multiphase flows [85] . For the interested reader, a detailed description of the method can be found in the excellent textbook of Cebeci and Bradshaw [12], where the main focus lies on heat transfer problems as well as in [16] where attention is directed toward turbulent boundary layers. Helpful texts where found to be the more general [15],[13] and [64].

Returning to the system of the nonsimilar coupled integro-differential equations (4.27), order reduction to one is necessary in order to apply the Box method. For this reason the additional functions $u(\zeta,\eta)$, $v(\zeta,\eta)$, $l(\zeta,\eta)$ are introduced such that

$$f_\eta = u,\; u_\eta = v \,\text{and}\, \vartheta_\eta = l. \tag{4.38}$$

In this way the transformed r-momentum and energy equations change to

$$\begin{aligned}(1-\zeta)^2 v_\eta + \frac{3}{5}(1-\zeta) f v - \frac{1}{5}u^2 - \frac{4}{5}\zeta u^2 &= \zeta(1-\zeta)\Big(u_\zeta u - v f_\zeta\Big) + \\ + \frac{1}{\rho}(1-\zeta)^3\Big[\frac{2}{5}g + \zeta g_\zeta\Big] - (1-\zeta)^3\zeta&\left(\frac{2}{5\zeta}\int_0^\eta \frac{1}{\rho}\,d\tilde{\eta} - \int_0^\eta \frac{1}{\rho^2}\frac{\partial\rho}{\partial\zeta}\,d\tilde{\eta}\right)\vartheta, \end{aligned} \tag{4.39}$$

$$(1-\zeta)\frac{1}{\mathrm{Pr}}l_\eta + \frac{3}{5}fl = \zeta\Big(u\vartheta_\zeta - f_\zeta l\Big). \tag{4.40}$$

Equation (4.39) is still a partial integro-differential equation, therefore a direct application of a standard numerical technique including the Box method is not straightforward. On a general note many physical problems are described by nonclassical (sometimes termed as nonstandard), parabolic or hyperbolic initial-boundary value problems [23]. What differentiates a standard from a nonclassical initial-boundary value problem, is the appearance of a dependent unknown function or its first spatial derivative in an integral term over the spatial domain. Depending on the appearance of the integral term, one could generically classify these problems into four categories; boundary value problems with nonlocal initial conditions, boundary value problems with nonlocal boundary conditions [19], partial integro-differential equations (PIDEs) where the integral term is now present within the equations, while the final category can be considered the one that includes an integral term in both boundaries and equation.

Due to the presence of the integral term, it is natural to expect that standard numerical techniques would tend to be more complicated to implement or even would have to be modified in order to accommodate the integral term. That would raise additional questions towards stability and accuracy. So whenever possible, it is desirable to reformulate a nonclassical initial boundary value problem to a standard one. A general review on the reformulation of certain category of nonclassical problems is given in [23].

Luckily, reformulation of the partial integro-differential equation (4.39), to standard form is straightforward. Starting with the introduction of two additional functions $b(\zeta,\eta)$ and $c(\zeta,\eta)$ given as

$$b(\zeta,\eta) = \int_0^\eta \frac{1}{\rho}\,d\tilde{\eta} \text{ and } c(\zeta,\eta) = \int_0^\eta \frac{1}{\rho^2}\frac{\partial\rho}{\partial\zeta}\,d\tilde{\eta}, \tag{4.41}$$

then further proceeding by recalling that $\rho(1+\lambda_{\mathrm{T}}\vartheta)=1$, so that equation (4.41) can be written as

$$b(\zeta,\eta) = \int_0^\eta (1+\lambda_{\mathrm{T}}\vartheta)\,d\tilde{\eta} \text{ and } c(\zeta,\eta) = -\int_0^\eta \lambda_{\mathrm{T}}\vartheta_\zeta\,d\tilde{\eta}. \tag{4.42}$$

Differentiation of equations (4.42) w.r.t η results in the final system of eight coupled first order PDEs which is listed below

$$f_\eta = u, \tag{4.43a}$$

$$u_\eta = v, \tag{4.43b}$$

$$g_\eta = \vartheta, \tag{4.43c}$$

$$\vartheta_\eta = l, \tag{4.43d}$$

$$b_\eta = 1 + \lambda_{\mathrm{T}}\vartheta, \tag{4.43e}$$

$$c_\eta = -\lambda_{\mathrm{T}}\vartheta_\zeta, \tag{4.43f}$$

$$(1-\zeta)\frac{1}{\mathrm{Pr}}l_\eta + \frac{3}{5}fl = \zeta\Big(u\vartheta_\zeta - f_\zeta l\Big), \tag{4.43g}$$

$$\begin{aligned}(1-\zeta)^2 v_\eta + \frac{3}{5}(1-\zeta)fv - \frac{1}{5}u^2 - \frac{4}{5}\zeta u^2 = \zeta(1-\zeta)\Big(u_\zeta u - vf_\zeta\Big)+ \\ + (1-\zeta)^3(1+\lambda_{\mathrm{T}}\vartheta)\Big[\frac{2}{5}g + \zeta g_\zeta\Big] - (1-\zeta)^3\left(\frac{2}{5}b - \zeta c\right)\vartheta,\end{aligned} \tag{4.43h}$$

subject to the following boundary conditions

$$f(\zeta,0) = u(\zeta,0) = b(\zeta,0) = c(\zeta,0) = 0, \text{ and } \vartheta(\zeta,0) = 1, \ \text{ and} \tag{4.44}$$

$$u(\zeta,\infty) = \vartheta(\zeta,\infty) = g(\zeta,\infty) = 0.$$

The price paid for the reformulation is the increase of the number of unknowns by two, but this is outweighed by the fact that the numerical scheme can directly be applied.

4.4.1 The difference scheme

Consider an arbitrary rectangular net of points (ζ_n, η_j) given in Figure 4.10. The nonuniform grid and its intermediate points are created as

$$\begin{aligned}&\zeta_0 = 0,\ \zeta_n = \zeta_{n-1} + \kappa_n,\ \text{ for } n = 1..N \text{ and } \zeta_{n-\frac{1}{2}} = \frac{1}{2}(\zeta_n + \zeta_{n-1}),\\ &\eta_0 = 0,\ \eta_j = \eta_{j-1} + h_j,\ \text{ for } j = 1..J \text{ for and } \eta_{j-\frac{1}{2}} = \frac{1}{2}(\eta_j + \eta_{j-1}).\end{aligned} \tag{4.45}$$

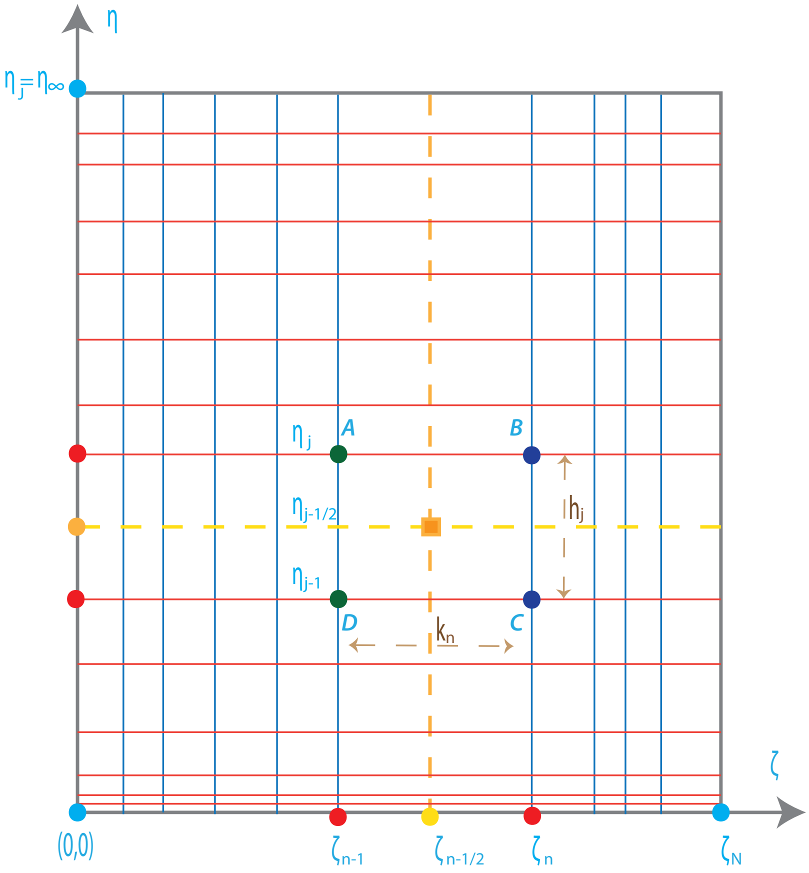

Figure 4.10: Grid for the Box finite difference scheme.

Given a function F, it will be approximated by the net function F_j^n at each point (ζ_n, η_j). In addition the notation used throughout for the averages of the net function, say F_j^n, is listed below

$$F_{j-\frac{1}{2}}^{n} = \frac{1}{2}(F_j^n + F_{j-1}^n), \;\; F_{j-\frac{1}{2}}^{n-1} = \frac{1}{2}(F_j^{n-1} + F_{j-1}^{n-1}), \;\; F_j^{n-\frac{1}{2}} = \frac{1}{2}(F_j^n + F_j^{n-1})$$
$$F_{j-1}^{n-\frac{1}{2}} = \frac{1}{2}(F_{j-1}^n + F_{j-1}^{n-1}), \;\; a_n = \frac{\zeta_{n-\frac{1}{2}}}{k_n} \text{ and } m_n = 1 - a_n k_n, \tag{4.46}$$

while nonlinear terms arising, say F^2, will be averaged as

$$(F^2)_{j-\frac{1}{2}}^{n-\frac{1}{2}} = \frac{1}{4}\left(F_j^n F_j^n + F_{j-1}^n F_{j-1}^n + F_j^{n-} F_j^{n-1} + F_{j-1}^{n-1} F_{j-1}^{n-1}\right). \tag{4.47}$$

Alternative averages could be used for the non linear terms, provided that the information is gathered from no more than the four points of the net rectangle. The stated form of averaging is optimal in terms of computations [44], and it will be pursued in what follows.

Central differences are used for the derivatives, so the ODEs, namely (4.43a), (4.43b), (4.43c), (4.43d) and (4.43e), will be averaged at the midpoint $(\zeta_n, \eta_{j-1/2})$ of the line segment BC, while the remaining PDEs, i.e. (4.43g), (4.43e) and (4.43h), will be averaged at the midpoint $(\zeta_{n-1/2}, \eta_{j-1/2})$ of the net rectangle $ABCD$. Starting with ODEs, the above described procedure results in

$$f_j^n - f_{j-1}^n = \frac{1}{2} h_j \left(u_j^n + u_{j-1}^n\right) = h_j u_{j-\frac{1}{2}}^n, \tag{4.48a}$$

$$u_j^n - u_{j-1}^n = \frac{1}{2} h_j \left(v_j^n + v_{j-1}^n\right) = h_j v_{j-\frac{1}{2}}^n, \tag{4.48b}$$

$$g_j^n - g_{j-1}^n = \frac{1}{2} h_j \left(\vartheta_j^n + \vartheta_{j-1}^n\right) = h_j \vartheta_{j-\frac{1}{2}}^n, \tag{4.48c}$$

$$\vartheta_j^n - \vartheta_{j-1}^n = \frac{1}{2} h_j \left(l_j^n + l_{j-1}^n\right) = h_j l_{j-\frac{1}{2}}^n, \tag{4.48d}$$

$$b_j^n - b_{j-1}^n = \frac{1}{2} h_j \left(2 + \lambda_{\mathrm{T}}\, \vartheta_j^n + \lambda_{\mathrm{T}}\, \vartheta_{j-1}^n\right) = h_j \left(1 + \lambda_{\mathrm{T}} \vartheta_{j-\frac{1}{2}}^n\right). \tag{4.48e}$$

For the PDEs we obtain

$$\begin{aligned} &\frac{m_n \left(l_j^n - l_{j-1}^n\right)}{\Pr\, h_j} + \left(a_n + \frac{3}{5}\right) (lf)_{j-\frac{1}{2}}^n + \\ &+ a_n \left(u_{j-\frac{1}{2}}^n \vartheta_{j-\frac{1}{2}}^{n-1} - u_{j-\frac{1}{2}}^{n-1} \vartheta_{j-\frac{1}{2}}^n - l_{j-\frac{1}{2}}^n f_{j-\frac{1}{2}}^{n-1} + l_{j-\frac{1}{2}}^{n-1} f_{j-\frac{1}{2}}^n\right) - (u\vartheta)_{j-\frac{1}{2}}^n = [R_5]_{j-\frac{1}{2}}^{n-1}, \end{aligned} \tag{4.49a}$$

$$\frac{c_j^n - c_{j-1}^n}{h_j} + \frac{2 a_n \lambda_{\mathrm{T}}}{1 - m_n} \vartheta_{j-\frac{1}{2}} = [R_7]_{j-\frac{1}{2}}^{n-1}, \tag{4.49b}$$

$$\begin{aligned} &(c\vartheta)_{j-\frac{1}{2}}^n {m_n}^4 + \Bigg(\left(a_n - \frac{1}{5}\right) \lambda_{\mathrm{T}} \vartheta_{j-\frac{1}{2}}^n g_{j-\frac{1}{2}}^{n-1} - \left(\frac{1}{5} + a_n\right) \left(\lambda_{\mathrm{T}} \vartheta_{j-\frac{1}{2}} g_{j-\frac{1}{2}}^n + \lambda_{\mathrm{T}} (g\vartheta)_{j-\frac{1}{2}}^n + 2 g_{j-\frac{1}{2}}^n\right) + \\ &+ \frac{2}{5} (b\vartheta)_{\mathrm{J}-\frac{1}{2}}^n - (c\vartheta)_{j-\frac{1}{2}}^n \Bigg) {m_n}^3 + \frac{\left(v_j^n - v_{j-1}^n\right)}{h_j} m_n^2 + \Bigg(a_n \left(v_{j-\frac{1}{2}}^{n-1} f_{j-\frac{1}{2}}^n - v_{j-\frac{1}{2}}^n f_{j-\frac{1}{2}}^{n-1}\right) + \\ &+ \left(\frac{3}{5} + a_n\right) (fv)_{j-\frac{1}{2}}^n + \left(\frac{4}{5} - a_n\right) (u^2)_{j-\frac{1}{2}}^n \Bigg) m_n - (u^2)_{j-\frac{1}{2}}^n = [R_8]_{j-\frac{1}{2}}^{n-1}, \end{aligned} \tag{4.49c}$$

where

$$[R_5]_{j-\frac{1}{2}}^{n-1} = \left(a_n - \frac{3}{5}\right) (fl)_{j-\frac{1}{2}} - \frac{m_n \left(l_j - l_{j-1}\right)}{\Pr h_j} - a_n (u\vartheta)_{j-\frac{1}{2}}, \tag{4.50a}$$

$$[R_7]_{j-\frac{1}{2}}^{n-1} = \left[\frac{2 a_n \lambda_{\mathrm{T}}}{1 - m_n} \vartheta_{j-\frac{1}{2}} - \frac{c_j - c_{j-1}}{h_j}\right]^{n-1}, \tag{4.50b}$$

$$
\begin{aligned}
[R_8]^{n-1}_{j-\frac{1}{2}} = \Bigg[&- (c\vartheta)_{j-\frac{1}{2}}\, m_n^4 + \Bigg(\left(\frac{1}{5} - a_n\right) \left(\lambda_{\mathrm{T}}\ (g\vartheta)_{j-\frac{1}{2}} + 2g_{j-\frac{1}{2}}\right) - \frac{2}{5}\,(b\vartheta)_{j-\frac{1}{2}} + \\
&+(c\vartheta)_{j-\frac{1}{2}} \Bigg) m_n^3 - \frac{v_j - v_{j-1}}{h_j} m_n^2 + \Bigg(\left(a_n - \frac{3}{5}\right)(fv)_{j-\frac{1}{2}} - \left(a_n + \frac{4}{5}\right)\left(u^2\right)_{j-\frac{1}{2}} \Bigg) m_n + \left(u^2\right)_{j-\frac{1}{2}} \Bigg]^{n-1}.
\end{aligned}
\tag{4.50c}
$$

Finally the boundary conditions now will be given as

$$
f_0^n = 0,\ u_0^n \ = 0\ \vartheta_0^n = 1,\ b_0^n = 0,\ c_0^n = 0\ u_J^n = 0,\ \vartheta_J^n = 0 \text{ and } g_J^n = 0. \tag{4.51}
$$

4.4.2 Solution of the difference equations

The task of solving the nonlinear difference scheme is undertaken in this section. We begin by revisiting the grid given in Figure 4.10, where we assume that at a given ζ-station namely ζ_{n-1}, the values of the net functions f_j^{n-1}, u_j^{n-1}, $v_j^{n-1} g_j^{n-1}$, ϑ_j^{n-1}, l_j^{n-1}, b_j^{n-1}, c_j^{n-1} are known $\forall j \in [0, J]$. The difference equations then form a nonlinear algebraic system of $8J + 8$ unknowns, f_j^n, u_j^n, v_j^n, g_j^n, ϑ_j^n, l_j^n, b_j^n, c_j^n between $n-1$ and n, ζ-stations. The solution of the nonlinear system will be obtained by means of Newton's method, through the process described below.

Firstly it is customary to rewrite the unknowns in a more compact form, so the following notation will be adopted

$$
f_j^n, u_j^n, v_j^{n,} g_j^n, \vartheta_j^n, l_j^n, b_j^n, c_j^n \equiv f_j, u_j, v_j, g_j, \vartheta_j, l_j, b_j, c_j. \tag{4.52}
$$

For Newton's method, the iterates are denoted as

$$
\{f_j^{\{i\}}, u_j^{\{i\}}, v_j^{\{i\},} g_j^{\{i\}}, \vartheta_j^{\{i\}}, l_j^{\{i\}}, b_j^{\{i\}}, c_j^{\{i\}}\} \text{ with } i = 0, 1 \ldots, \tag{4.53}
$$

while higher iterates are obtained as

$$
\begin{aligned}
&f_j^{\{i+1\}} = f_j^{\{i\}} + \delta f_j^{\{i\}}, u_j^{\{i+1\}} = u_j^{\{i\}} + \delta u_j^{\{i\}}, v_j^{\{i+1\}} = v_j^{\{i\}} + \delta v_j^{\{i\}}, \\
&g_j^{\{i+1\}} = g_j^{\{i\}} + \delta g_j^{\{i\}}, \vartheta_j^{\{i+1\}} = \vartheta_j^{\{i\}} + \delta \vartheta_j^{\{i\}}, l_j^{\{i+1\}} = l_j^{\{i\}} + \delta l_j^{\{i\}}, \\
&b_j^{\{i+1\}} = b_j^{\{i\}} + \delta b_j^{\{i\}},\ c_j^{\{i+1\}} = c_j^{\{i\}} + \delta c_j^{\{i\}}.
\end{aligned}
\tag{4.54}
$$

In a similar fashion

$$
\begin{aligned}
&f_{j-1}^{\{i+1\}} = f_{j-1}^{\{i\}} + \delta f_{j-1}^{\{i\}}, u_{j-1}^{\{i+1\}} = u_{j-1}^{\{i\}} + \delta u_{j-1}^{\{i\}}, v_{j-1}^{\{i+1\}} = v_{j-1}^{\{i\}} + \delta v_{j-1}^{\{i\}}, \\
&g_{j-1}^{\{i+1\}} = g_{j-1}^{\{i\}} + \delta g_{j-1}^{\{i\}} \vartheta_{j-1}^{\{i+1\}} = \vartheta_{j-1}^{\{i\}} + \delta \vartheta_{j-1}^{\{i\}}, l_{j-1}^{\{i+1\}} = l_{j-1}^{\{i\}} + \delta l_{j-1}^{\{i\}}, \\
&b_{j-1}^{\{i+1\}} = b_{j-1}^{\{i\}} + \delta b_{j-1}^{\{i\}}, c_{j-1}^{\{i+1\}} = c_{j-1}^{\{i\}} + \delta c_{j-1}^{\{i\}}.
\end{aligned}
\tag{4.55}
$$

The procedure of the linearisation is direct and in two steps. It includes the substitution of the r.h.s of the higher iterates given in equation (4.54), in place of the net functions, and the neglect of quadratic or higher order terms of δ. The nonlinear algebraic equations transform to a linear algebraic system in terms of δf_j, δu_j, δv_j, δg_j, $\delta \vartheta_j$, δl_j, δb_j, δc_j[6]. In this way, equations (4.48a)–(4.48e) change to

$$\delta f_j - \delta f_{j-1} - \frac{1}{2} h_j \left(\delta u_j + \delta u_{j-1} \right) = (r_1)_j, \tag{4.56a}$$

$$\delta u_j - \delta u_{j-1} - \frac{1}{2} h_j \left(\delta v_j + \delta v_{j-1} \right) = (r_2)_j, \tag{4.56b}$$

$$\delta g_j - \delta g_{j-1} - \frac{1}{2} h_j \left(\delta \vartheta_j + \delta \vartheta_{j-1} \right) = (r_3)_j, \tag{4.56c}$$

$$\delta \vartheta_j - \delta \vartheta_{j-1} - \frac{1}{2} h_j \left(\delta l_j + \delta l_{j-1} \right) = (r_4)_j, \tag{4.56d}$$

$$\delta b_j - \delta b_{j-1} - \frac{1}{2} \lambda_{\mathrm{T}} h_j \left(\delta \vartheta_j + \delta \vartheta_{j-1} \right) = (r_6)_j. \tag{4.56e}$$

Equations (4.49a)–(4.49c) are now given as

$$\begin{split}(s_1)_j \delta l_j + (s_2)_j \delta l_{j-1} + (s_3)_j \delta \vartheta_j + (s_4)_j \delta \vartheta_{j-1} + (s_5)_j \delta u_j + \\ + (s_6)_j \delta u_{j-1} + (s_7)_j \delta f_j + (s_8)_j \delta f_{j-1} = (r_5)_j,\end{split} \tag{4.57a}$$

$$(\phi_1)_j \delta c_j + (\phi_2)_j \delta c_{j-1} + (\phi_3)_j \delta \vartheta_j + (\phi_4) \delta \vartheta_{j-1} = (r_7)_j, \tag{4.57b}$$

$$\begin{split}(\mu_1)_j \delta v_j + (\mu_2)_j \delta v_{j-1} + (\mu_3)_j \delta u_j + (\mu_4)_j \delta u_{j-1} + (\mu_5)_j \delta f_j + (\mu_6)_j \delta f_{j-1} + \\ + (\mu_7)_j \delta \vartheta_j + (\mu_8)_j \delta \vartheta_{j-1} + (\mu_9)_j \delta g_{j-1} + (\mu_{10})_j \delta g_{j-1} + (\mu_{11})_j \delta b_{j-1} + \\ + (\mu_{12})_j \delta b_{j-1} + (\mu_{13})_j \delta c_{j-1} + (\mu_{14})_j \delta c_{j-1} = (r_8)_j,\end{split} \tag{4.57c}$$

where

$$(r_1)_j = -f_j^{\{i\}} + f_{j-1}^{\{i\}} + \tfrac{1}{2} h_j u_{j-\frac{1}{2}}^{\{i\}}, \tag{4.58a}$$

$$(r_2)_j = -u_j^{\{i\}} + u_{j-1}^{\{i\}} + \tfrac{1}{2} h_j v_{j-\frac{1}{2}}^{\{i\}}, \tag{4.58b}$$

$$(r_3)_j = -p_j^{\{i\}} + p_{j-1}^{\{i\}} + \tfrac{1}{2} h_j \vartheta_{j-\frac{1}{2}}^{\{i\}}, \tag{4.58c}$$

$$(r_4)_j = -\vartheta_j^{\{i\}} + \vartheta_{j-1}^{\{i\}} + \tfrac{1}{2} h_j l_{j-\frac{1}{2}}^{\{i\}}, \tag{4.58d}$$

$$(r_6)_j = -b_j^{\{i\}} + b_{j-1}^{\{i\}} + h_j \left(1 + \lambda_{\mathrm{T}} \, \vartheta_{j-\frac{1}{2}}^{\{i\}} \right), \tag{4.58e}$$

---

[6] Superscript $\{i\}$, has been omitted from δ terms for compactness

$$\begin{aligned}(r_5)_j = [R_5]^{n-1}_{j-\frac{1}{2}} - \Bigg(&\mathrm{Pr}^{-1}\mathrm{m_n}\mathrm{h}_\mathrm{j}^{-1}(\mathrm{l}_\mathrm{j}^{\{\mathrm{i}\}} - \mathrm{l}_{\mathrm{j-1}}^{\{\mathrm{i}\}}) + (\mathrm{fl})^{\{\mathrm{i}\}}_{\mathrm{j}-\frac{1}{2}}\left(\mathrm{a_n} + \tfrac{3}{5}\right) - \mathrm{a_n}(\mathrm{u}\vartheta)^{\{\mathrm{i}\}}_{\mathrm{j}-\frac{1}{2}} + \\ &+a_n\left(u^{\{i\}}_{j-\frac{1}{2}}\vartheta^{n-1}_{j-\frac{1}{2}} - u^{n-1}_{j-\frac{1}{2}}\vartheta^{\{i\}}_{j-\frac{1}{2}} - l^{\{i\}}_{j-\frac{1}{2}}f^{n-1}_{j-\frac{1}{2}} + l^{n-1}_{j-\frac{1}{2}}f^{\{i\}}_{j-\frac{1}{2}}\right)\Bigg),\end{aligned} \tag{4.59a}$$

$$(r_7)_j = \frac{2\lambda_\mathrm{T}a_n\left(\vartheta^{n-1}_{j-\frac{1}{2}} - \vartheta^{\{i\}}_{j-\frac{1}{2}}\right)}{1-m_n} - h_j^{-1}(c_j^{n-1} - c_{j-1}^{n-1}) - h_j^{-1}(c_j^{\{i\}}, -c_{j-1}^{\{i\}}), \tag{4.59b}$$

$$\begin{aligned}(r_8)_j =&[R_8]^{n-1}_{j-\frac{1}{2}} - \\ &-\Bigg((c\vartheta)^{\{i\}}_{j-\frac{1}{2}}m_n^4 + \Big((a_n - \tfrac{1}{5})\lambda_\mathrm{T}\vartheta^{\{i\}}_{j-\frac{1}{2}}g^{n-1}_{j-\frac{1}{2}} - (\tfrac{1}{5} + a_n)\big(2\,g^{\{i\}}_{j-\frac{1}{2}} + \\ &+ \lambda_\mathrm{T}\,(p\vartheta)^{\{i\}}_{j-\frac{1}{2}} + \lambda_\mathrm{T}\vartheta^{n-1}_{j-\frac{1}{2}}g^{\{i\}}_{j-\frac{1}{2}}\big) + \tfrac{2}{5}\,(b\vartheta)^{\{i\}}_{j-\frac{1}{2}} - (c\vartheta)^{\{i\}}_{j-\frac{1}{2}}\Big)m_n^3 + \\ &+ h_j^{-1}(v_j^{\{i\}} - v_{j-1}^{\{i\}})m_n^2 + \Big(\tfrac{4}{5}\,(u^2)^{\{i\}}_{j-\frac{1}{2}} - a_nv^{\{i\}}_{j-\frac{1}{2}}f^{n-1}_{j-\frac{1}{2}} + a_nv^{n-1}_{j-\frac{1}{2}}f^{\{i\}}_{j-\frac{1}{2}} - \\ &-a_n(u^2)^{\{i\}}_{j-\frac{1}{2}} + (fv)^{\{i\}}_{j-\frac{1}{2}}\left(\tfrac{3}{5} + a_n\right)\Big)m_n - (u^2)^{\{i\}}_{j-\frac{1}{2}}\Bigg).\end{aligned} \tag{4.59c}$$

The coefficients of the linearised equations are given below. Starting with (4.57a)

$$(s_1)_j = \left(\tfrac{3}{10} + \tfrac{1}{2}\,a_n\right)f_j^{\{i\}} - \tfrac{1}{2}\,a_nf^{\{i\}}_{j-\frac{1}{2}} + \frac{m_n}{\mathrm{Pr}\ h_j}, \tag{4.60a}$$

$$(s_2)_j = \left(\tfrac{3}{10} + \tfrac{1}{2}\,a_n\right)f_{j-1}^{\{i\}} - \tfrac{1}{2}\,a_nf^{\{i\}}_{j-\frac{1}{2}} - \frac{m_n}{\mathrm{Pr}\ h_j}, \tag{4.60b}$$

$$(s_3)_j = -\tfrac{1}{2}\,a_nu^{n-1}_{j-\frac{1}{2}}, \tag{4.60c}$$

$$(s_4)_j = -\tfrac{1}{2}\,a_nu^{n-1}_{j-\frac{1}{2}}, \tag{4.60d}$$

$$(s_5)_j = \tfrac{1}{2}\,a_n\vartheta^{n-1}_{j-\frac{1}{2}}, \tag{4.60e}$$

$$(s_6)_j = (s_5)_j, \tag{4.60f}$$

$$(s_7)_j = \tfrac{1}{10}\,(3 + 5\,a_n)\,l_j^{\{i\}} + \tfrac{1}{2}\,a_nl^{n-1}_{j-\frac{1}{2}}, \tag{4.60g}$$

$$(s_8)_j = \tfrac{1}{10}\,(3 + 5\,a_n)\,l_{j-1}^{\{i\}} + \tfrac{1}{2}\,a_nl^{n-1}_{j-\frac{1}{2}}. \tag{4.60h}$$

For equation (4.57b) the following is obtained

$$(\phi_1)_j = h_j^{-1},\ (\phi_2)_j = -(\phi_1)_j,\ (\phi_3)_j = (\phi_4)_j = \frac{\lambda_\mathrm{T}a_n}{1-m_n}, \tag{4.61}$$

while for (4.57c)

$$(\mu_1)_j = \tfrac{1}{2}\,m_n\left(\tfrac{3}{5} + a_n\right)f_j^{\{i\}} - \tfrac{1}{2}\,a_nm_nf^{n-1}_{j-\frac{1}{2}} + \frac{m_n^2}{h_j}, \tag{4.62a}$$

$$(\mu_2)_j = \tfrac{1}{2}\, m_n \left(\tfrac{3}{5} + a_n\right) f^{\{i\}}_{j-1} - \tfrac{1}{2}\, a_n m_n f^{n-1}_{j-\frac{1}{2}} - \frac{m_n^2}{h_j}, \tag{4.62b}$$

$$(\mu_3)_j = \left(-1 + \tfrac{4}{5}\, m_n - a_n m_n\right) u^{\{i\}}_j, \tag{4.62c}$$

$$(\mu_4)_j = \left(-1 + \tfrac{4}{5}\, m_n - a_n m_n\right) u^{\{i\}}_{j-1}, \tag{4.62d}$$

$$(\mu_5)_j = \tfrac{1}{2}\, \left(\left(v^{n-1}_{j-\frac{1}{2}} + v^{\{i\}}_j\right) a_n + \tfrac{3}{5}\, v^{\{i\}}_j\right) m_n, \tag{4.62e}$$

$$(\mu_6)_j = \tfrac{1}{2}\, \left(\left(v^{n-1}_{j-\frac{1}{2}} + v^{\{i\}}_{j-1}\right) a_n + \tfrac{3}{5}\, v^{\{i\}}_{j-1}\right) m_n, \tag{4.62f}$$

$$(\mu_7)_j = -\tfrac{1}{2} \left((1 - m_n)\, c^{\{i\}}_j + \left((\tfrac{1}{5} + a_n) g^{\{i\}}_j + (\tfrac{1}{5} - a_n) g^{n-1}_{j-\frac{1}{2}}\right) \lambda_{\mathrm{T}} - \tfrac{2}{5} b^{\{i\}}_j\right) m_n^3, \tag{4.62g}$$

$$(\mu_8)_j = -\tfrac{1}{2} \left((1 - m_n)\, c^{\{i\}}_{j-1} + \left((\tfrac{1}{5} + a_n) g^{\{i\}}_{j-1} + (\tfrac{1}{5} - a_n) g^{n-1}_{j-\frac{1}{2}}\right) \lambda_{\mathrm{T}} - \tfrac{2}{5}\, b^{\{i\}}_{j-1}\right) m_n^3, \tag{4.62h}$$

$$(\mu_9)_j = -\tfrac{1}{2}\, \left(2 + \left(\vartheta^{\{i\}}_j + \vartheta^{n-1}_{j-\frac{1}{2}}\right) \lambda_{\mathrm{T}}\right) \left(\tfrac{1}{5} + a_n\right) m_n^3, \tag{4.62i}$$

$$(\mu_{10})_j = -\tfrac{1}{2}\, \left(2 + \left(\vartheta^{\{i\}}_{j-1} + \vartheta^{n-1}_{j-\frac{1}{2}}\right) \lambda_{\mathrm{T}}\right) \left(\tfrac{1}{5} + a_n\right) m_n^3, \tag{4.62j}$$

$$(\mu_{11})_j = \tfrac{1}{5}\, \vartheta^{\{i\}}_j m_n^3, \tag{4.62k}$$

$$(\mu_{12})_j = \tfrac{1}{5}\, \vartheta^{\{i\}}_{j-1} m_n^3, \tag{4.62l}$$

$$(\mu_{13})_j = -\tfrac{1}{2}\, (1 - m_n)\, \vartheta^{\{i\}}_j m_n^3, \tag{4.62m}$$

$$(\mu_{14})_j = -\tfrac{1}{2}\, (1 - m_n)\, \vartheta^{\{i\}}_{j-1} m_n^3. \tag{4.62n}$$

Finally, the boundary conditions listed in equation (4.51) change to

$$\delta f_0 = 0,\ \ \delta u_0 = 0,\ \delta\vartheta_0 = 0,\ \delta b_0 = 0,\ \ \delta c_0 = 0,\ \ \delta u_J = 0,\ \delta\vartheta_J = 0 \,\text{and}\, \delta g_J = 0. \tag{4.63}$$

Having derived the linear system, the next step is to proceed with its solution. In rewriting the algebraic equations in matrix-vector form, two points are worthwhile mentioning. Firstly, the coefficient matrix obtained in the Box method is of tridiagonal form, as it is in another popular implicit finite difference method, that of Crank-Nicolson. The difference being that in the Box method, entries are blocks of size $q \times q$ rather than scalars, with q being the number of unknowns.

Further another important thing to notice is that at ζ_0 (i.e. $\zeta = 0$) it can be observed from the system of PDEs (4.43a)–(4.43h), that the number of dependent variables is reduced from eight to seven. Analogously, by setting $\zeta_{n-1/2} = 0$, or equivalently $a_n = 0$ and $m_n = 1$, the same conclusion can be recovered. This is because the newly introduced variable $c(\zeta, \eta)$, due to the reformulation of the integro-differential equation to standard form, ceases to appear. It is therefore inevitable that a special treatment must be given at the origin (solution of the similarity ODEs system) in order to avoid a singular matrix before marching downstream. That will become clearer once the linearised problem is formulated into matrix-vector form. Once the construction of the block tridiagonal matrix is complete, the solution of the system is computed and the iterates are updated, until the fulfilment of a convergence criterion. Once convergence criterion is satisfied, a shift is made downstream, where the same procedure is repeated, until $\zeta = \zeta_N$.

4.4.3 The case of $\zeta = 0$

The linear algebraic system needs to be solved from $n = 0 \dots N$. As already mentioned the case of $n = 0$ or $\zeta = 0$, which physically represent the edge of the plate, requires a special treatment. By neglecting the dependence on ζ, the system of PDEs transforms to a system of ODEs, the solution of which was already obtained in the previous section using the shooting technique. For completeness we shall assume no prior knowledge of the solution at the edge, and the Box method will be used to obtain it. Once the solution is known at $n = 0$ then we shall proceed to $n = 1$ where the current solution is used as an initial guess. But before doing so, due to the nature of the problem, for the construction of the coefficient matrix two distinctive cases need to be considered, these being $\zeta = 0$ and $\zeta \neq 0$.

The reformulation of the integro-differential equation to a standard first order system requires the introduction of two functions representing the integrals. At the edge of the plate equation (4.43h) becomes

$$v_\eta + \tfrac{3}{5} f v - \tfrac{1}{5} u^2 = \tfrac{2}{5}\Big((1 + \lambda_{\mathrm{T}}\vartheta)g - b\vartheta\Big). \tag{4.64}$$

So the ODE is independent of the variable c, additionally (4.49b) plays no role in the coupled system, and is neglected. Therefore the unknowns are reduced to seven i.e. f, u, v, g, ϑ, l, b. The difference scheme used so far does not need altering, so that the linearised equations and coefficients computed can safely be used. Simply, $n = 0$ implies that $a_n = 0$ and $m_n = 1$ so that the difference scheme for the ODEs is recovered. In addition, (4.43f) is not included in the construction of the blocks consisting of the block tridiagonal coefficient matrix. The linear algebraic system given in equation (4.56) and (4.57) is written in Matrix-vector form as

$$\mathbf{M}^0 \boldsymbol{\delta}^0 = \mathbf{r}^0 \text{ valid for } n = 0 \,\text{and}\, \forall j \tag{4.65}$$

Where $\mathbf{M^0}$ is the block tridiagonal given as

$$\mathbf{M}^0 = \begin{bmatrix} \mathbf{A}_0 & \mathbf{C}_0 & & & & & & \\ \mathbf{B}_1 & \mathbf{A}_1 & \mathbf{C}_1 & & & & & \\ & \ddots & \ddots & \ddots & & & & \\ & & \mathbf{B}_j & \mathbf{A}_j & \mathbf{C}_j & & & \\ & & & \ddots & \ddots & \ddots & & \\ & & & & \mathbf{B}_{J-1} & \mathbf{A}_{J-1} & \mathbf{C}_{J-1} & \\ & & & & & \mathbf{B}_J & \mathbf{A}_J & \end{bmatrix}, \tag{4.66}$$

where

$$\mathbf{A}_0^0 = \begin{bmatrix} 1 & 0 & 0 & 0 & 0 & 0 & 0 \\ 0 & 1 & 0 & 0 & 0 & 0 & 0 \\ 0 & 0 & 0 & 0 & 1 & 0 & 0 \\ 0 & 0 & 0 & 0 & 0 & 1 & 0 \\ 0 & -1 & \frac{h_1}{2} & 0 & 0 & 0 & 0 \\ 0 & 0 & 0 & -1 & \frac{h_1}{2} & 0 & 0 \\ 0 & 0 & 0 & 0 & 0 & -1 & -\frac{h_1}{2} \end{bmatrix} \tag{4.67}$$

$$\mathbf{A}_j^0 = \begin{bmatrix} 1 & -\frac{h_j}{2} & 0 & 0 & 0 & 0 & 0 \\ 0 & 0 & 0 & 0 & 1 & -\frac{\lambda_{\mathrm{T}} h_j}{2} & 0 \\ (s_7)_j & (s_5)_j & 0 & 0 & 0 & (s_3)_j & (s_1)_j \\ (\mu_5)_j & (\mu_3)_j & (\mu_1)_j & (\mu_9)_j & (\mu_{11})_j & (\mu_7)_j & 0 \\ 0 & -1 & -\frac{h_{j+1}}{2} & 0 & 0 & 0 & 0 \\ 0 & 0 & 0 & -1 & 0 & -\frac{h_{j+1}}{2} & 0 \\ 0 & 0 & 0 & 0 & 0 & -1 & -\frac{h_{j+1}}{2} \end{bmatrix} \text{ for } 1 \le j \le J-1 \tag{4.68}$$

$$\mathbf{A}_J^0 = \begin{bmatrix} 1 & -\dfrac{h_J}{2} & 0 & 0 & 0 & 0 & 0 \\ 0 & 0 & 0 & 0 & 1 & -\dfrac{\lambda_{\mathrm{T}} h_J}{2} & 0 \\ (s_7)_J & (s_5)_J & 0 & 0 & 0 & (s_3)_J & (s_1)_J \\ (\mu_5)_J & (\mu_3)_J & (\mu_1)_J & (\mu_9)_J & (\mu_{11})_J & (\mu_7)_J & 0 \\ 0 & 1 & 0 & 0 & 0 & 0 & 0 \\ 0 & 0 & 0 & 1 & 0 & 0 & 0 \\ 0 & 0 & 0 & 0 & 0 & 1 & 0 \end{bmatrix} \tag{4.69}$$

$$\mathbf{C}_j^0 = \begin{bmatrix} 0 & 0 & 0 & 0 & 0 & 0 & 0 & 0 \\ 0 & 0 & 0 & 0 & 0 & 0 & 0 & 0 \\ 0 & 0 & 0 & 0 & 0 & 0 & 0 & 0 \\ 0 & 0 & 0 & 0 & 0 & 0 & 0 & 0 \\ 0 & 0 & 0 & 0 & 0 & 0 & 0 & 0 \\ 0 & 1 & -\dfrac{h_{j+1}}{2} & 0 & 0 & 0 & 0 & 0 \\ 0 & 0 & 0 & 1 & 0 & 0 & -\dfrac{h_{j+1}}{2} & 0 \\ 0 & 0 & 0 & 0 & 0 & 0 & 1 & -\dfrac{h_{j+1}}{2} \end{bmatrix} \quad \text{for } 0 \le j \le J-1 \tag{4.70}$$

and

$$\mathbf{B}_j^0 = \begin{bmatrix} -1 & -\dfrac{h_j}{2} & 0 & 0 & 0 & 0 & 0 & 0 \\ 0 & 0 & 0 & 0 & -1 & 0 & -\dfrac{\lambda_{\mathrm{T}} h_j}{2} & 0 \\ 0 & 0 & 0 & 0 & 0 & (\phi_2)_j & (\phi_4)_j & 0 \\ (s_8)_j & (s_6)_j & 0 & 0 & 0 & 0 & (s_4)_j & (s_2)_j \\ (\mu_6)_j & (\mu_4)_j & (\mu_2)_j & (\mu_{10})_j & (\mu_{12})_j & (\mu_{14})_j & (\mu_8)_j & 0 \\ 0 & 0 & 0 & 0 & 0 & 0 & 0 & 0 \\ 0 & 0 & 0 & 0 & 0 & 0 & 0 & 0 \\ 0 & 0 & 0 & 0 & 0 & 0 & 0 & 0 \end{bmatrix} \quad \text{for } 1 \le j \le J. \tag{4.71}$$

The vectors $\boldsymbol{\delta}$ and $\mathbf{r}$ for each value of j are given as

$$\boldsymbol{\delta}_j^0 = \begin{bmatrix} \delta f_j \\ \delta u_j \\ \delta v_j \\ \delta g_j \\ \delta b_j \\ \delta \vartheta_j \\ \delta l_j \end{bmatrix} \text{ for } 0 \le j \le J, \tag{4.72}$$

and

$$\mathbf{r}_0^0 = \begin{bmatrix} 0 \\ 0 \\ 0 \\ 0 \\ (r_2)_1 \\ (r_3)_1 \\ (r_4)_1 \end{bmatrix}, \ \mathbf{r}_j^0 = \begin{bmatrix} (r_1)_j \\ (r_6)_j \\ (r_5)_j \\ (r_8)_j \\ (r_2)_{j+1} \\ (r_3)_{j+1} \\ (r_4)_{j+1} \end{bmatrix} \text{for}\, 1 \le j \le J-1, \text{ and}\, \mathbf{r}_J^0 = \begin{bmatrix} (r_1)_J \\ (r_6)_J \\ (r_5)_J \\ (r_8)_J \\ 0 \\ 0 \\ 0 \end{bmatrix}. \tag{4.73}$$

4.4.4 The case of $\zeta \neq 0$

In the case that $n \neq 0$, the system of PDEs is recovered and the function c regains it's role. The procedure is the same, the linear algebraic system is written in a matrix vector form, with the difference being that tridiagonal elements of the coefficient matrix are blocks of size 8×8. Now the linear algebraic system that needs to be solved is given as

$$\mathbf{M}^n \boldsymbol{\delta}^n = \mathbf{r}^n \text{ valid for } n = 1 \ldots N \,\text{and}\, \forall j \tag{4.74}$$

Analytically the block elements of matrix $\mathbf{M}^n$ is given below

$$\mathbf{A}_0^n = \begin{bmatrix} 1 & 0 & 0 & 0 & 0 & 0 & 0 & 0 \\ 0 & 1 & 0 & 0 & 0 & 0 & 0 & 0 \\ 0 & 0 & 0 & 0 & 1 & 0 & 0 & 0 \\ 0 & 0 & 0 & 0 & 0 & 1 & 0 & 0 \\ 0 & 0 & 0 & 0 & 0 & 0 & 1 & 0 \\ 0 & -1 & -\dfrac{h_1}{2} & 0 & 0 & 0 & 0 & 0 \\ 0 & 0 & 0 & -1 & 0 & 0 & -\dfrac{h_1}{2} & 0 \\ 0 & 0 & 0 & 0 & 0 & 0 & -1 & -\dfrac{h_1}{2} \end{bmatrix} \tag{4.75}$$

$$\mathbf{A}_j^n = \begin{bmatrix} 1 & -\dfrac{h_j}{2} & 0 & 0 & 0 & 0 & 0 & 0 \\ 0 & 0 & 0 & 0 & 1 & 0 & -\dfrac{\lambda_{\mathrm{T}} h_j}{2} & 0 \\ 0 & 0 & 0 & 0 & 0 & (\phi_1)_j & (\phi_3)_j & 0 \\ (s_7)_j & (s_5)_j & 0 & 0 & 0 & 0 & (s_3)_j & (s_1)_j \\ (\mu_5)_j & (\mu_3)_j & (\mu_1)_j & (\mu_9)_j & (\mu_{11})_j & (\mu_{13})_j & (\mu_7)_j & 0 \\ 0 & -1 & \dfrac{h_{j+1}}{2} & 0 & 0 & 0 & 0 & 0 \\ 0 & 0 & 0 & -1 & 0 & 0 & -\dfrac{h_{j+1}}{2} & 0 \\ 0 & 0 & 0 & 0 & 0 & 0 & -1 & -\dfrac{h_{j+1}}{2} \end{bmatrix} \quad \text{for } 1 \leq j \leq J{-}1 \tag{4.76}$$

$$\mathbf{A}_J^n = \begin{bmatrix} 1 & -\dfrac{h_J}{2} & 0 & 0 & 0 & 0 & 0 & 0 \\ 0 & 0 & 0 & 0 & 1 & 0 & -\dfrac{\lambda_{\mathrm{T}} h_J}{2} & 0 \\ 0 & 0 & 0 & 0 & 0 & (\phi_1)_J & (\varphi_3)_J & 0 \\ (s_7)_J & (s_5)_J & 0 & 0 & 0 & 0 & (s_3)_J & (s_1)_J \\ (\mu_5)_J & (\mu_3)_J & (\mu_1)_J & (\mu_9)_J & (\mu_{11})_J & (\mu_{13})_J & (\mu_7)_J & 0 \\ 0 & 1 & 0 & 0 & 0 & 0 & 0 & 0 \\ 0 & 0 & 0 & 1 & 0 & 0 & 0 & 0 \\ 0 & 0 & 0 & 0 & 0 & 0 & 1 & 0 \end{bmatrix} \tag{4.77}$$

$$\mathbf{C}_j^n = \begin{bmatrix} 0 & 0 & 0 & 0 & 0 & 0 & 0 & 0 \\ 0 & 0 & 0 & 0 & 0 & 0 & 0 & 0 \\ 0 & 0 & 0 & 0 & 0 & 0 & 0 & 0 \\ 0 & 0 & 0 & 0 & 0 & 0 & 0 & 0 \\ 0 & 0 & 0 & 0 & 0 & 0 & 0 & 0 \\ 0 & 1 & -\dfrac{h_{j+1}}{2} & 0 & 0 & 0 & 0 & 0 \\ 0 & 0 & 0 & 1 & 0 & 0 & -\dfrac{h_{j+1}}{2} & 0 \\ 0 & 0 & 0 & 0 & 0 & 0 & 1 & -\dfrac{h_{j+1}}{2} \end{bmatrix} \quad \text{for } 0 \le j \le J-1 \tag{4.78}$$

$$\mathbf{B}_j^n = \begin{bmatrix} -1 & -\dfrac{h_j}{2} & 0 & 0 & 0 & 0 & 0 & 0 \\ 0 & 0 & 0 & 0 & -1 & 0 & -\dfrac{\lambda_{\mathrm{T}} h_j}{2} & 0 \\ 0 & 0 & 0 & 0 & 0 & (\phi_2)_j & (\phi_4)_j & 0 \\ (s_8)_j & (s_6)_j & 0 & 0 & 0 & 0 & (s_4)_j & (s_2)_j \\ (\mu_6)_j & (\mu_4)_j & (\mu_2)_j & (\mu_{10})_j & (\mu_{12})_j & (\mu_{14})_j & (\mu_8)_j & 0 \\ 0 & 0 & 0 & 0 & 0 & 0 & 0 & 0 \\ 0 & 0 & 0 & 0 & 0 & 0 & 0 & 0 \\ 0 & 0 & 0 & 0 & 0 & 0 & 0 & 0 \end{bmatrix} \quad \text{for } 1 \leq j \leq J. \tag{4.79}$$

Finally, the vectors $\boldsymbol{\delta}^n$ and $\mathbf{r}^n$ are given as

$$\boldsymbol{\delta}_j^n = \begin{bmatrix} \delta f_j \\ \delta u_j \\ \delta v_j \\ \delta g_j \\ \delta b_j \\ \delta c_j \\ \delta \theta_j \\ \delta l_j \end{bmatrix} \tag{4.80}$$

and

$$\mathbf{r}_0^n = \begin{bmatrix} 0 \\ 0 \\ 0 \\ 0 \\ 0 \\ (r_2)_j \\ (r_3)_j \\ (r_4)_j \end{bmatrix} \quad \mathbf{r}_j^n = \begin{bmatrix} (r_1)_j \\ (r_6)_j \\ (r_7)_j \\ (r_5)_j \\ (r_8)_j \\ (r_2)_{j+1} \\ (r_3)_{j+1} \\ (r_4)_{j+1} \end{bmatrix} \quad \text{for } 1 \le j \le J-1, \text{ and } \mathbf{r}_J^n = \begin{bmatrix} (r_1)_J \\ (r_6)_J \\ (r_7)_J \\ (r_5)_J \\ (r_8)_J \\ 0 \\ 0 \\ 0 \end{bmatrix}. \tag{4.81}$$

Finalising, a closer look at the general coefficient matrix $\mathbf{M^n}$, and its block elements of the main diagonal (i.e $\mathbf{A}_0^n$, $\mathbf{A}_j^n$,and $\mathbf{A}_J^n$), unveils the necessity for separate treatment of the case $\zeta = 0$. At $n = 0$ the blocks $\mathbf{A}_0^0$, $\mathbf{A}_j^0$ and $\mathbf{A}_J^0$ all become singular.

4.4.5 Further considerations

So far in our discussion we intentionally neglected to touch on two important topics of the solution process, namely, the convergence criterion and the initial profiles. Starting with the latter, since Newton's method is used, initial profiles are necessary for the station $\zeta = 0$ (the similar problem). The procedure followed was to set $\lambda_{\mathrm{T}} = 0$, therefore dealing with Boussinesq problem, and then provide the following initial profiles for u and ϑ

$$u_{\mathrm{in}} = \mathrm{Ni}(1-\mathrm{Ni})^2 \text{ and } \vartheta_{\mathrm{in}} = (1-\mathrm{Ni})^2, \text{ where } \mathrm{Ni} = \frac{\eta}{\eta_\infty}. \tag{4.82a}$$

From the definitions of f, v, g, l, b given in (4.43), it is a matter of integration or differentiation w.r.t η to find the remaining initial profiles, listed below

$$f_{\mathrm{in}} = \frac{\eta}{12}\mathrm{Ni}(6 - 8\mathrm{Ni} + 3\mathrm{Ni}^2), \tag{4.82b}$$

$$v_{\mathrm{in}} = \frac{1}{\eta_\infty}(1 - 4\mathrm{Ni} + 3\mathrm{Ni}^2), \tag{4.82c}$$

$$g_{\mathrm{in}} = -\frac{\eta_\infty}{3}(1-\mathrm{Ni})^3, \tag{4.82d}$$

$$b_{\mathrm{in}} = \eta + \lambda_{\mathrm{T}}\big(p_{\mathrm{in}} - p_{\mathrm{in}}(0)\big), \tag{4.82e}$$

and

$$l_{\text{in}} = -\frac{2}{\eta_\infty}(1 - \text{Ni}). \tag{4.82f}$$

Using the above profiles convergence for the coupled system of ODEs was obtained after a few iterations. The solution obtained for $\lambda_{\text{T}} = 0$ is used throughout as an initial guess at $\zeta = 0$, for different values of λ_{T}. Once the solution is obtained at $n = 0$, it is passed as an initial guess to the downstream $\zeta-$station ($n = 1$) with the additional initial profile for c, given as $c_{\text{in}} = 0$, and iteration takes place until convergence. The procedure is repeated as we march on until $n = N$.

In what concerns the convergence criterion, in boundary layer theory the greatest error usually appears in the wall shear $\tau_w = \mu(\partial u/\partial z)_{z=0}$ [16]. In terms of the transformed variables the wall shear parameter is analogous to $f_0'' = v_0$. It is therefore the commonly used criterion for laminar flows of this type, so iterations were set to terminate once

$$|v_0^{\{i\}}| < 10^{-5}. \tag{4.83}$$

Finally, the code was implemented in MATLAB. Sparse matrix structure was used for the block tridiagonal mass matrix $\mathbf{M}$, while for the solution of the linear system, MATLAB's built in backslash operator \ was used.

4.5 Finite element approach

In this section the numerical solution of the boundary layer equations (4.12) subject to BCs given in (4.30) will be obtained via a commercial CFD (Computational Fluid Dynamics) tool, namely COMSOL Multiphysics 3.5a. COMSOL Multiphysics is a powerful interactive environment for solving engineering and scientific problems based on PDEs, using the finite element method (FEM).

Initially it was contemplated that direct use of COMSOL is the wise way to go, considering the amount of work the finite difference code would require. As it became apparent, implementation of the nonsimilar PDEs (4.29) subject to BCs given in (4.30) using COMSOL's General PDEs mode was not as straightforward as it was initially thought. No problems were encountered when the size of the rectangular domain was set to be $[0\,, Z] \times [0\,, H]$ with $Z = 0.991$ and $H = 9$. Actually the code had no problem in converging, even when Z was set closer to the singularity, i.e. $Z = 0.998$, resulting though in an inaccurate solution.

For an optimal domain a requirement for H would be to lie somewhere in the region of twenty five to fifty. In this way the solution could fully capture the increasingly thickening boundary layer, as the singularity is approached. Problems started to appear when the size of H was increased in terms of convergence. Solution was obtained for $H = 10$, but stepping up this value turned out to be a difficult task. Numerous approaches were taken, from using different solvers and different meshing techniques, to introducing an artificial diffusion parameter, and parametrically starting from an isothermal flow, to name a few. All efforts turned out to be unsuccessful and the feeling we got, stated with scepticism, is that a finer mesh is required, and consequently unavailable computational resources, making the task unfeasible for us.

For the above stated reasons a different strategy was considered necessary. Inspired by Merkin [56] and his secondary similarity variable transformation given as $\eta = e^y - 1$, we return back to the boundary layer equations (4.12) and define a modified 'compressed' Dorodnitsyn-Howarth transformation for the independent variables given as

$$\zeta = r, \text{ and } Y = \ln\left[(Cr)^{-2/5}\int_0^z \rho d\tilde{z} + 1\right], \tag{4.84}$$

while the transformations for the dependent variables given in (5.17) remain unchanged.

The reasoning behind the introduction of transformation (4.84) is straightforward. Recall that the height of the domain corresponding to η was earlier defined as H, but now redefined as H_η. Once the nonsimilar PDEs using the modified Dorodnitsyn-Howarth transformation are obtained (i.e. in terms of ζ and Y), for computational considerations lets define the height of the domain required as H_Y. Now by comparing the standard and modified Dorodnitsyn-Howarth transformations it is not hard to see that $Y = \ln(\eta - 1)$ and thus $H_Y = \ln(H_\eta + 1)$. Thus for example in $(\zeta\,, \eta)$ coordinate system, a domain of height $H_\eta = 20$ is equivalent to $H_Y \approx 3.045$ in the $(\zeta\,, Y)$ domain. In this way it is believed that numerical instabilities appearing can be resolved, since the meshing process might turn out to be more efficient.

As a result, the boundary layer equations (4.12) are revisited but this time application of the modified Dorodnitsyn-Howarth transformation takes place. Now formal transformations are given as

$$\frac{\partial}{\partial r} = \frac{\partial}{\partial \zeta} + \frac{\partial Y}{\partial r}\frac{\partial}{\partial Y} \quad \text{and} \quad \frac{\partial}{\partial \hat{z}} = \rho e^{-Y}(Cr)^{-2/5}\frac{\partial}{\partial Y}, \tag{4.85a}$$

and in addition, by following the same procedure described earlier, the term $\partial Y/\partial r$ is evaluated as

$$\frac{\partial Y}{\partial r} = \rho e^{-Y}\Big(-\frac{2}{5\zeta}\int_0^Y e^Y \frac{1}{\rho}\, d\tilde{Y} + \int_0^Y e^Y \frac{1}{\rho^2}\frac{\partial \rho}{\partial \zeta}\, d\tilde{Y}\Big). \tag{4.85b}$$

Therefore the modified nonsimilar boundary layer equations are now given as

$$u_{YY} = 3u_Y - 2u + \frac{e^{3Y}(1-\zeta)}{\rho}\Big(\frac{2}{5}g + \zeta g_\zeta\Big) + e^{3Y}(1-\zeta)\Big(\zeta c - \frac{2}{5}b\Big)\vartheta + \frac{e^Y}{(1-\zeta)^2}\times$$

$$\times\Bigg(\frac{1}{5}u^2 + \frac{4}{5}\zeta u^2 + \zeta(1-\zeta)\Big(u u_\zeta - f_\zeta(u_Y - u)\Big) - \frac{3}{5}(1-\zeta) f\big(u_Y - u\big)\Bigg), \tag{4.86a}$$

$$g_Y = e^Y \vartheta, \tag{4.86b}$$

and

$$\vartheta_{YY} = \frac{e^Y \mathrm{Pr}}{1-\zeta}\Big[\zeta\left(u\vartheta_\zeta - f_\zeta \vartheta_Y\right) - \frac{3}{5} f \vartheta_Y\Big] + \vartheta_Y, \tag{4.86c}$$

where

$$u = f_Y,\; b = \int_0^Y e^Y \frac{1}{\rho}\, d\tilde{Y},\; c = \int_0^Y e^Y \frac{1}{\rho^2}\frac{\partial \rho}{\partial \zeta}\, d\tilde{Y}, \text{ and } \frac{1}{\rho} = 1 + \lambda_{\mathrm{T}}\vartheta. \tag{4.86d}$$

to be solved under the same boundary conditions listed in (4.44).

Once more the same difficulties appeared when the above stated equations were modelled in COMSOL. Convergence difficulties manifested, even though a solution was obtained for $H_Y = 3.3$ (equivalent to $H_\eta \approx 26$), regions of large error were present. Nevertheless a slight improvement was achieved, by obtaining a solution in a domain of height $H_Y = 2.5$, therefore all results presented in what will follow will be based on those simulations.

4.6 Behaviour of the different numerical methods

Having presented the numerical techniques to be used for the solution of the nonsimilar PIDEs, this section serves as an investigation of the correctness and the performance of the Box method code. An analytical examination of the behaviour of both methods when compared will be presented, furthermore some necessary supplementary details concerning the finite difference code are provided. Finally a detailed analysis for the flow under the Boussinesq approximation is given using both methods.

Having discussed in the previous section, the difficulties faced using a FEM solver, at this point it should be mentioned that even though the FEM method posed restrictions on the height of the domain, something that we did not experience when the Box method was employed ($H_\eta = 50$ was attempted without trouble), use of COMSOL was superior in terms of moving downstream and approaching the singularity in the $\zeta-$direction. Meaning that when Box Method was used and $\lambda_{\mathrm{T}} = 0, 1$[7] no problems whatsoever were encountered in moving from $\zeta = 0$ to $\zeta = 0.9$ uniformly with $\kappa_n = 0.1$. Moving though above 0.9, and trying to approach the singularity, appeared to be a harder task especially as the values of λ_{T} were increasing from zero. The uniform grid had to be abandoned and a time consuming step by step process, of trial and error had to be performed in order to obtain the correct spacing for the $\zeta-$nodes.

By using the Box method we succeeded in marching as far as $\zeta = 0.99$, for the case of $\lambda_{\mathrm{T}} = 0$, and $\mathrm{Pr} = 0.72$. The grid used was uniform in the η direction with $h_j = 0.01$ and $H_\eta = 26$, while the $\zeta-$ nodes were positioned at

$$\zeta_n = \Big[0, 0.1, 0.2, \ldots 0.9, 0.91, 0.92, 0.925, 0.930, \ldots, 0.945, 0.948, 0.9510, \ldots, 0.99\Big]. \tag{4.87}$$

Now changes in λ_{T} or Pr, require a change in the grid and because each case has to be treated uniquely, especially after $\zeta = 0.9$, for that we decided against trying to obtain solution as close to the singularity as for the Boussinesq case. For that it is considered reasonable to rely on COMSOL when describing effect on λ_{T} and Pr as the singularity is approached, unless the opposite is stated.

4.6.1 Comparison of the methods for $\lambda_{\mathrm{T}} = 0$ and $\mathrm{Pr} = 0.72$

Starting at the edge of the plate, numerical solution was obtained using three methods namely, the shooting method, the Box method and FEM. Excellent agreement can be observed in Figure 4.11, where the computed velocity, temperature and pressure

---

[7] For the cases that $\lambda_{\mathrm{T}} > 2$ the $\zeta-$nodes spacing, had to be decreased as 0.9 is approached.

profiles are plotted using the three techniques. Moving away from the leading edge and

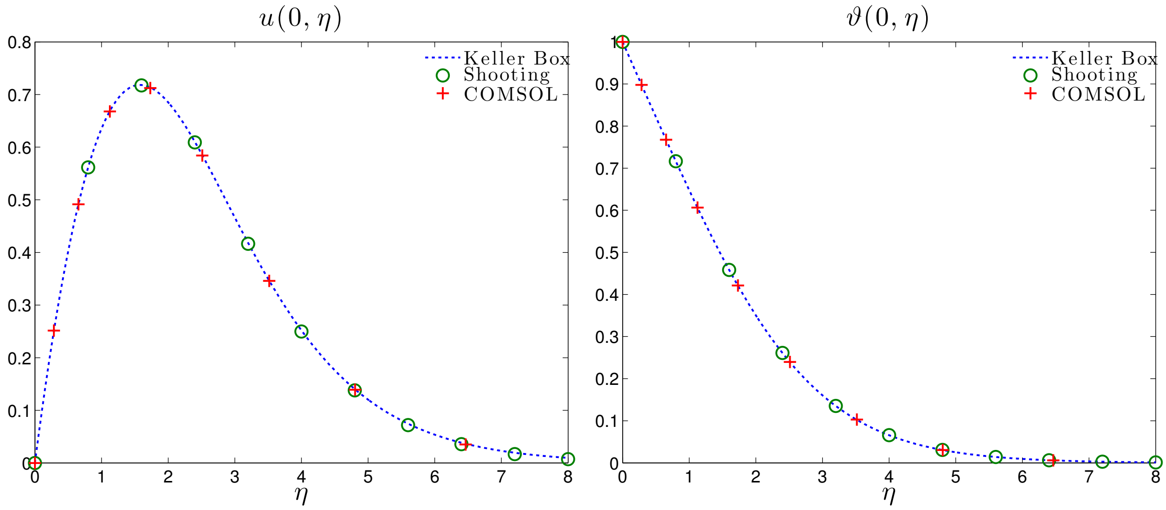

(a) Velocity function (b) Temperature function

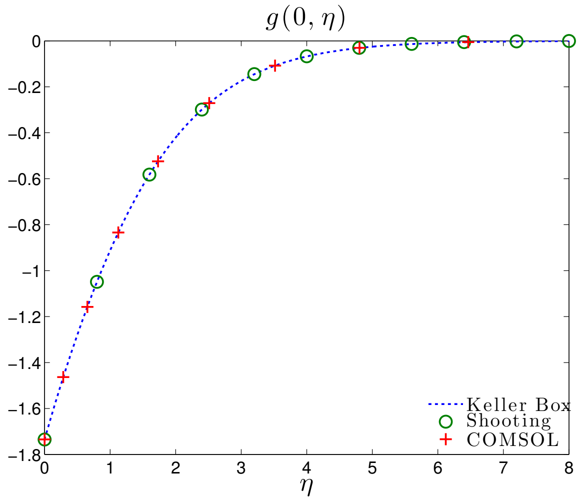

(c) Pressure function

Figure 4.11: Comparison of the numerical solution obtained at the leading edge of the disk, using Keller box, shooting method, and FEM.

proceeding towards the centre of the plate, it can be observed from Figures 4.12, and Figure 4.13 that the thermal layer (b) is rapidly increasing its thickness as the centre is approached, a growth that is accompanied with an increase in the negative pressure (c), and a significant drop in the velocity function (a). Numerical computations show good agreement apart from $\zeta = 0.99$, and particularly in the pressure function there is a significant deviation something that has to be attributed to the singularity at $r = 1$.

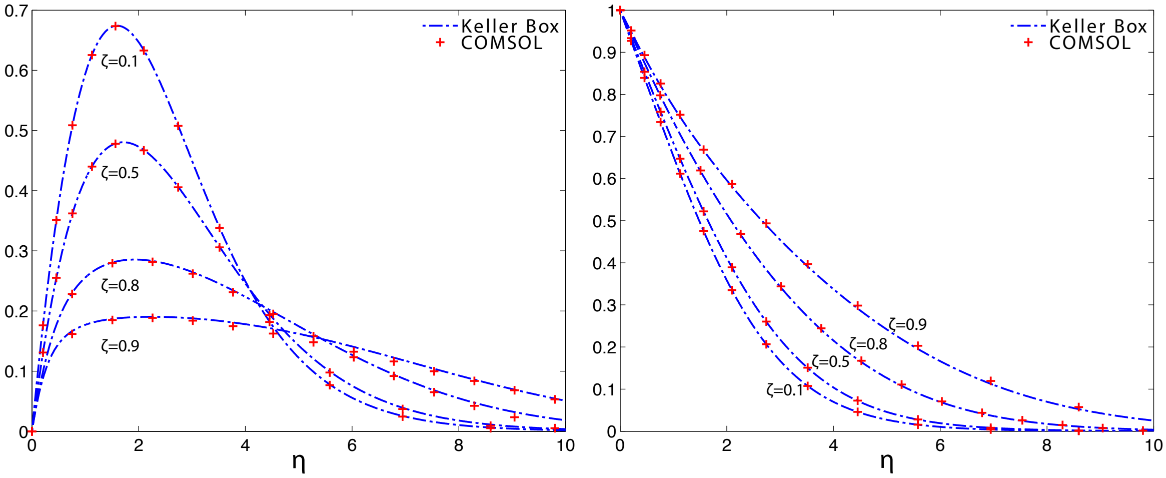

(a) Velocity function profiles u

(b) Temperature function profiles ϑ

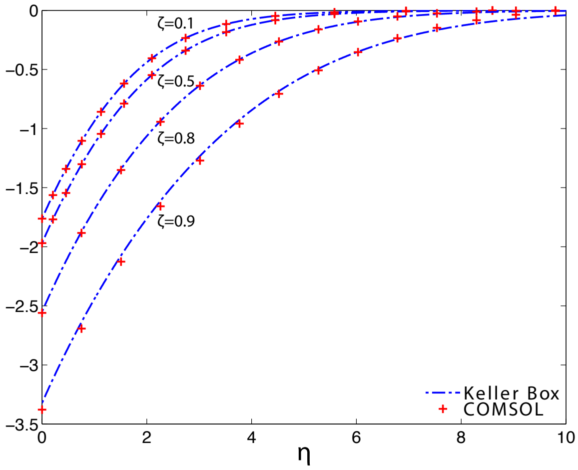

(c) Pressure function profiles g

Figure 4.12: Profiles for $\zeta = 0.1, 0.5, 0.8, 0.9$, obtained using Keller box, and FEM.

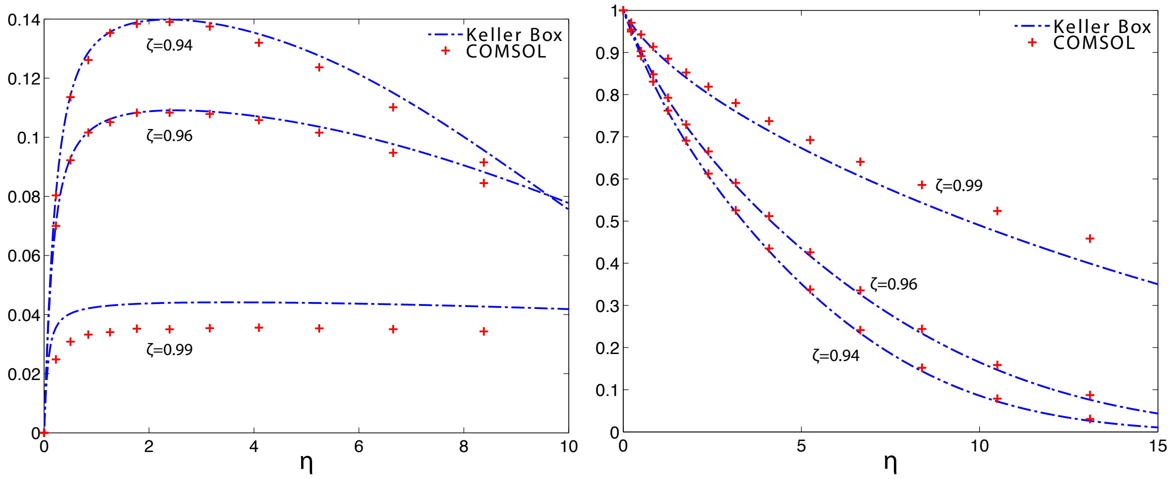

(a) Velocity function profiles u (b) Temperature function profiles ϑ

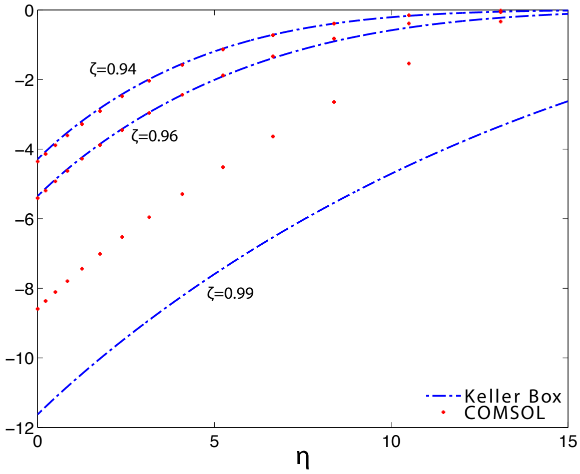

(c) Pressure function profiles g

Figure 4.13: Profiles for $\zeta = 0.94, 0.96, 0.99$, obtained using Keller box, and FEM.

4.6.2 Variable property effects

Introduction of variable fluid property effects by allowing λ_{T} to deviate from zero, results in an increase of the velocity function profiles with λ_{T}, as shown in Figure 4.14. This behaviour is retained as the velocity is decreasing, while moving towards the centre of the plate. On the other hand, an increase in λ_{T} results in slightly reduced temperature function profiles (Figure 4.15) and consequently in the negative pressure (Figure 4.16). As the centre of the plate is approached the variable property effects seem to have a negligible effect to the thickening thermal layer and the the negative pressure function. Overall it can be claimed that λ_{T} has significant effects mainly on the velocity profiles.

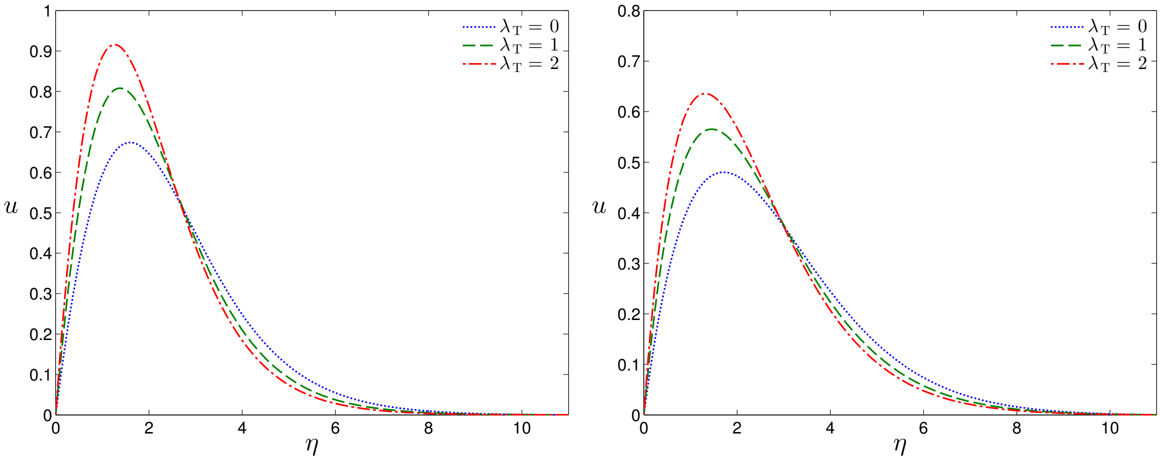

(a) $\zeta = 0.1$ (b) $\zeta = 0.5$

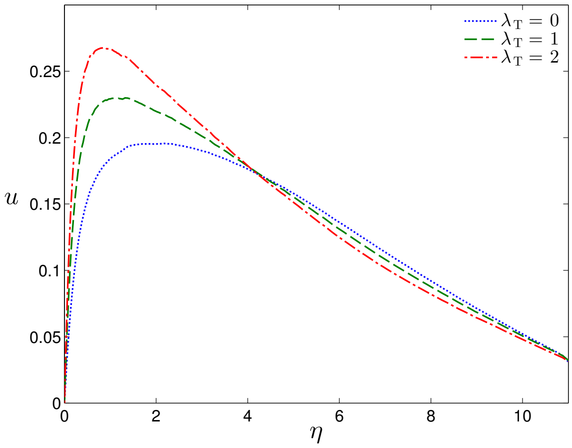

(c) $\zeta = 0.9$

Figure 4.14: Velocity function profiles u at $\zeta = 0.1, 0.5, 0.9$, for different values of λ_{T}, while $\mathrm{Pr} = 0.72$.

In what concerns the heat transfer Q, in nondimensional variables $(\zeta, \hat{z})$ is given

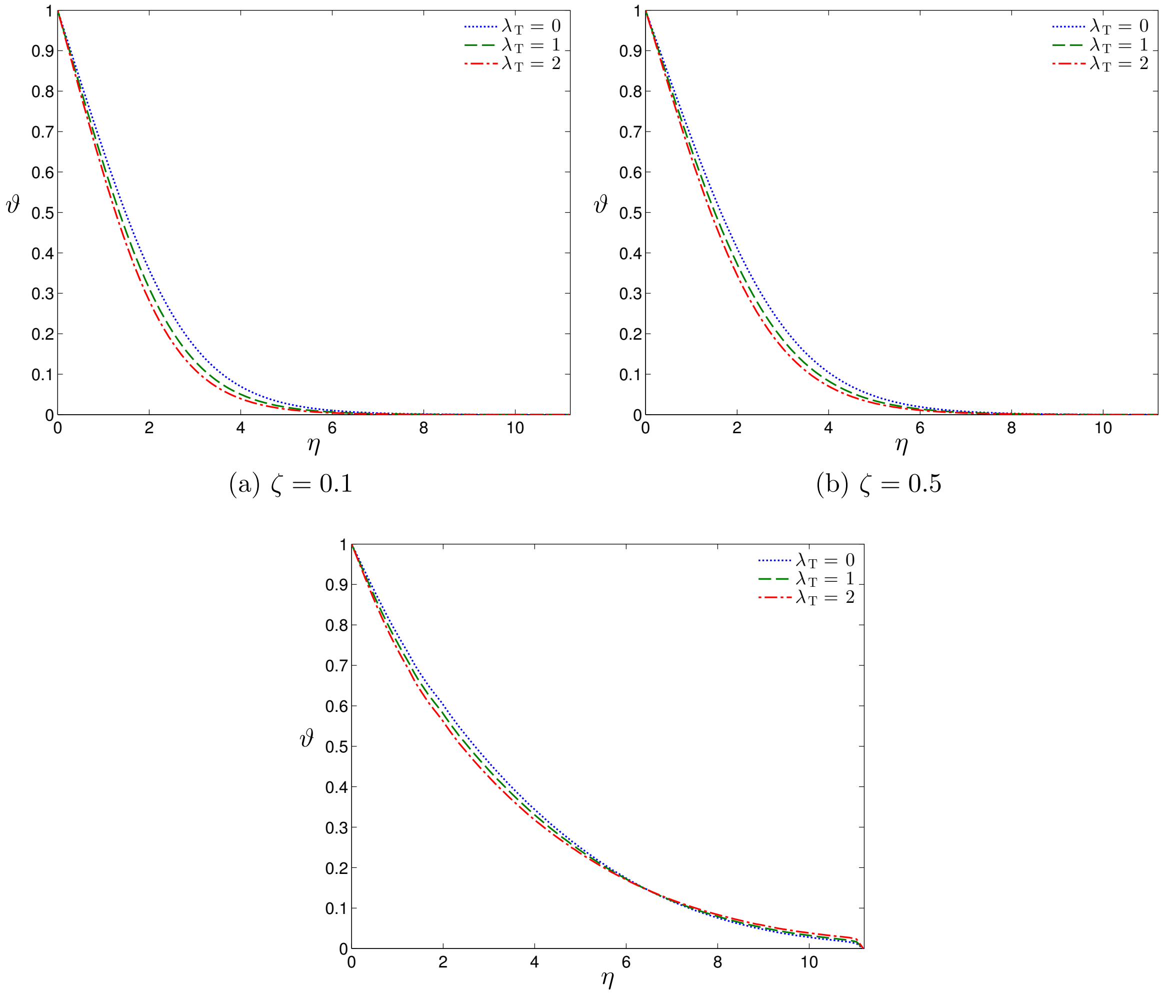

(a) $\zeta = 0.1$

(b) $\zeta = 0.5$

(c) $\zeta = 0.9$

Figure 4.15: Temperature function profiles ϑ at $\zeta = 0.1, 0.5, 0.9$, for different values of λ_{T}, while $\mathrm{Pr} = 0.72$.

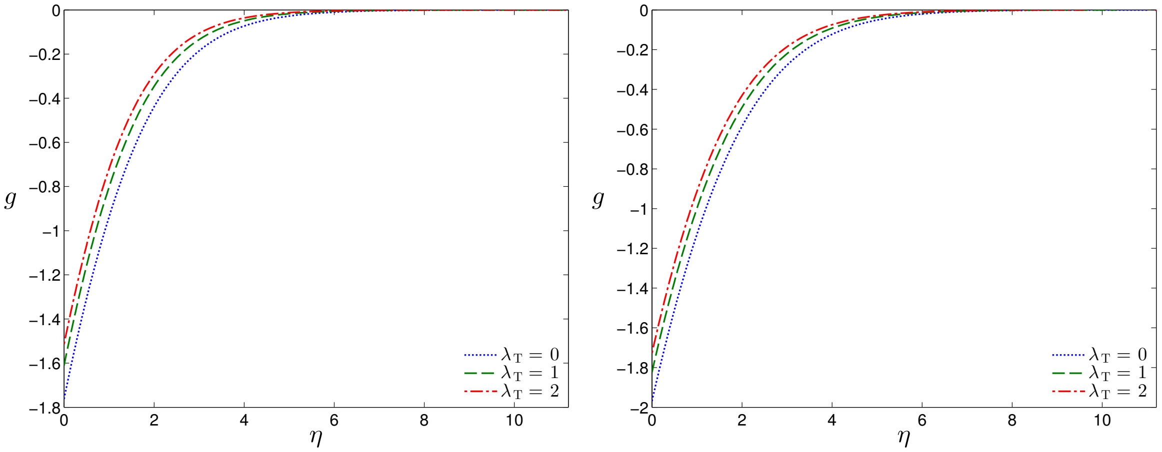

(a) $\zeta = 0.1$ (b) $\zeta = 0.5$

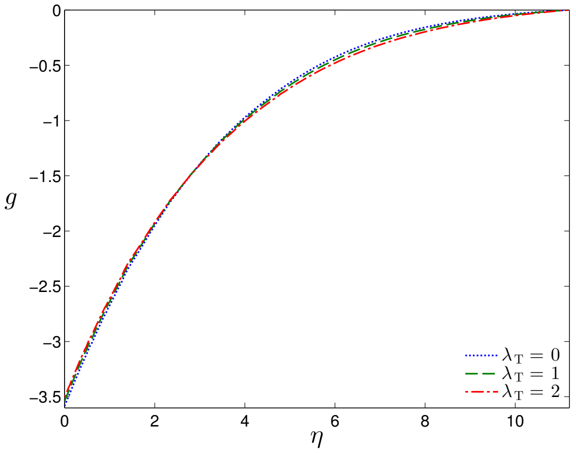

(c) $\zeta = 0.9$

Figure 4.16: Pressure function profiles g at $\zeta = 0.1, 0.5, 0.9$, for different values of λ_{T}, while $\mathrm{Pr} = 0.72$.

as

$$Q = -\frac{\partial \vartheta}{\partial \hat{z}}\Big|_{\hat{z}=0} = -\rho (Cr)^{-2/5}\frac{\partial \vartheta}{\partial \hat{\eta}}\Big|_{\eta=0}. \tag{4.88}$$

As it can be observed in Figure 4.17, computations indicate a reduced heat transfer with increasing λ_{T}, in addition to $Q \to 0$ as $\zeta \to 1$. Finally for the skin friction i.e.

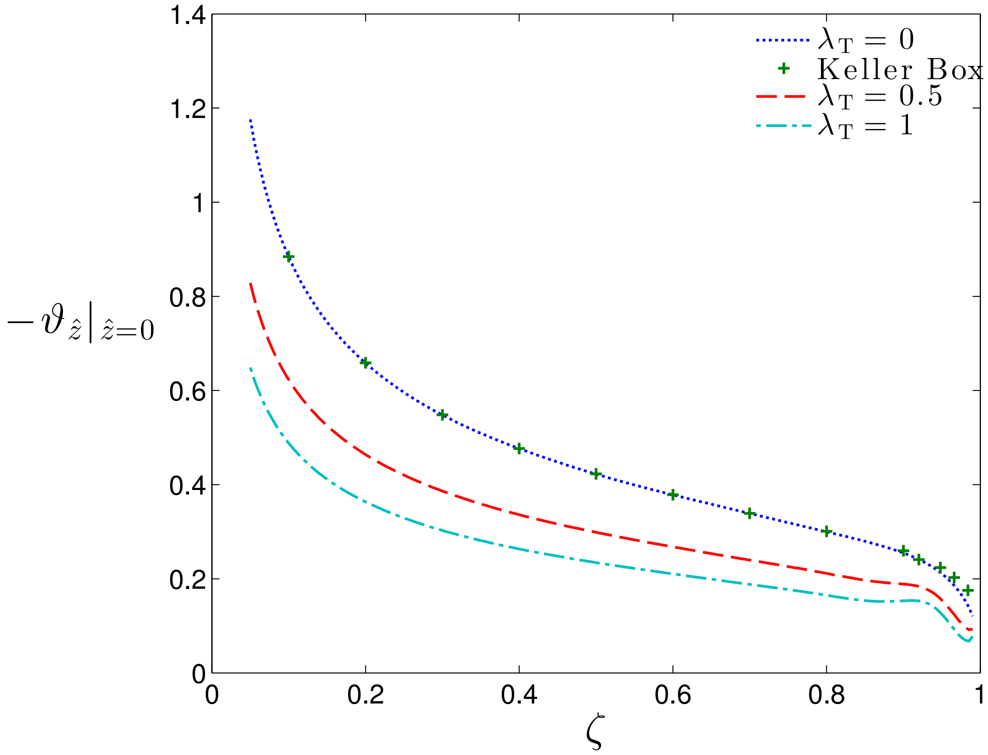

Figure 4.17: Variation of heat transfer with r for different values of λ_{T} while Pr=0.72 and $C = 1$.

$$\frac{\partial \hat{u}}{\partial \hat{z}}\Big|_{\hat{z}=0} = \rho\frac{(Cr)^{-1/5}}{1-r}\frac{\partial^2 f}{\partial \eta^2}\Big|_{\eta=0} = \rho\frac{(Cr)^{-1/5}}{1-r}\frac{\partial u}{\partial \eta}\Big|_{\eta=0}, \tag{4.89}$$

from Figure 4.18 it can be observed that an increase in λ_{T} results in a reduction of the skin friction along the plate while a rapid increase is detected as $\zeta \to 1$ in all cases.

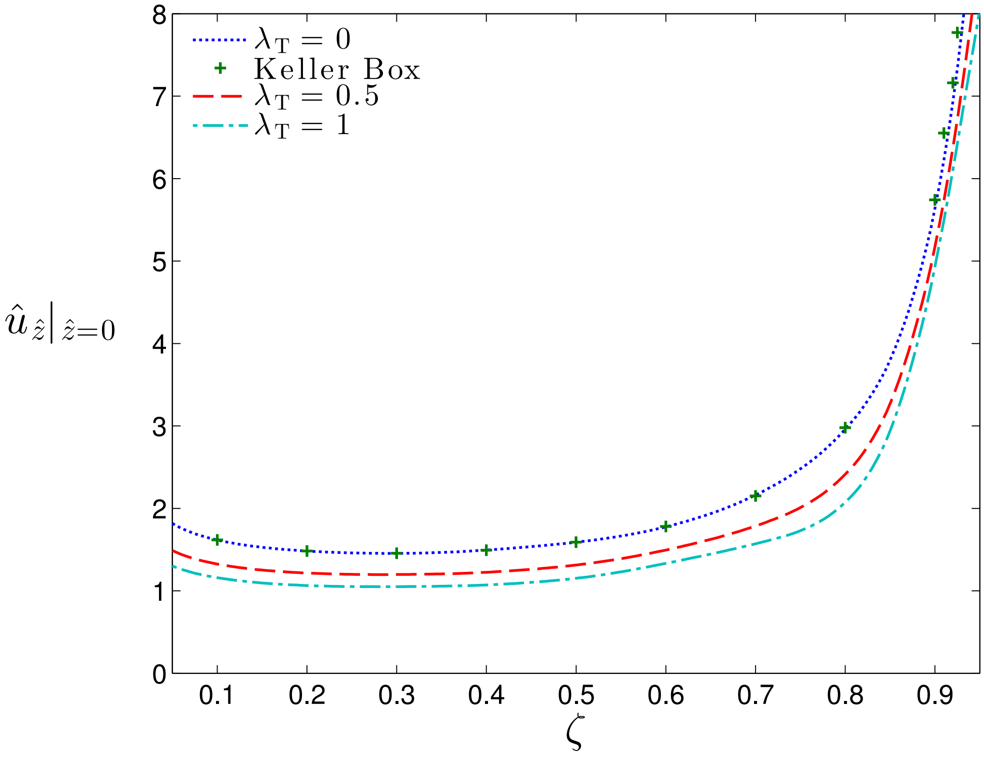

Figure 4.18: Variation of the skin friction coefficient with ζ for different values of λ_T, while Pr=0.72.

4.6.3 Varying the Prandtl number Pr

Turning attention on the effect of Pr to the flow, the Boussinesq approximation is now adopted (i.e. $\lambda_{\mathrm{T}} = 0$) and computations are carried for $\mathrm{Pr} = 0.01, 0.05, 0.1, 0.72, 6, 10$. As clearly demonstrated in Figure 4.19, there is a velocity function increase with a decreasing Prandtl number. In addition reduction of the Pr results in a thicker thermal layer which translates to larger negative pressure as seen in Figures 4.20 and 4.21 . Moving downstream and as the centre of the plate is approached the deceleration appears to be more intense for smaller values of Pr, while the temperature profiles at $\zeta = 0.9$ indicate a significantly thicker thermal layer for $\mathrm{Pr} = \mathcal{O}(10^{-2})$.

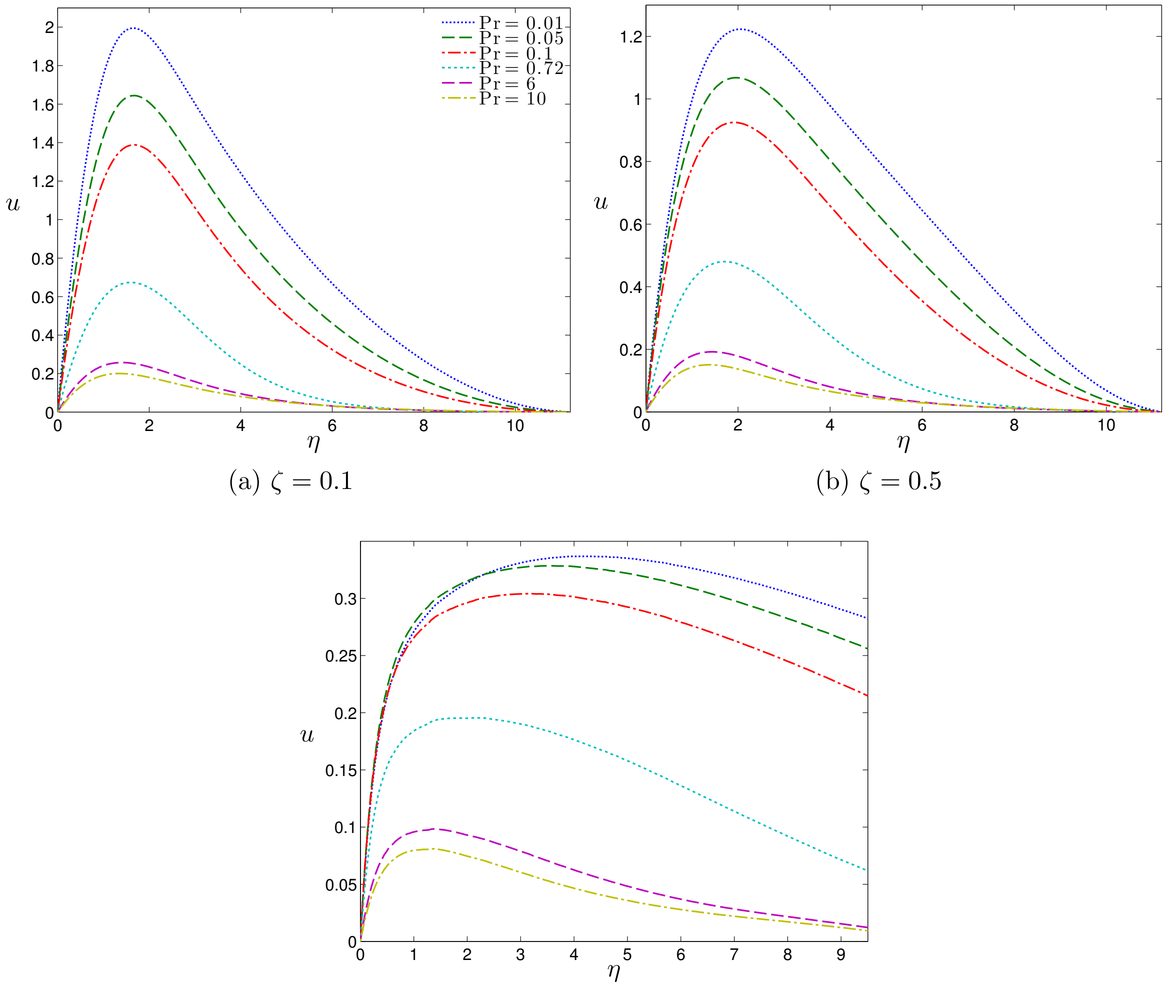

(a) $\zeta = 0.1$

(b) $\zeta = 0.5$

(c) $\zeta = 0.9$

Figure 4.19: Velocity function profiles u at $\zeta = 0.1, 0.5, 0.9$, for $\lambda_{\mathrm{T}} = 0$ while $\mathrm{Pr} = 0.01, 0.05, 0.1, 0.72, 6, 10$.

Concluding , computations of heat transfer as shown in Figure 4.22, indicate that the heat transfer rates are reduced monotonically with decreasing Pr, while for the

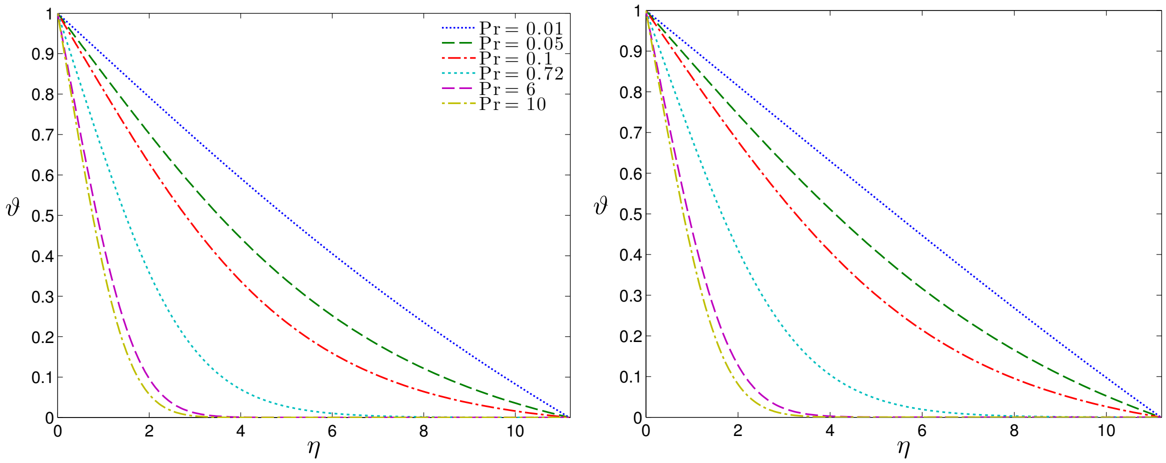

(a) $\zeta = 0.1$ (b) $\zeta = 0.5$

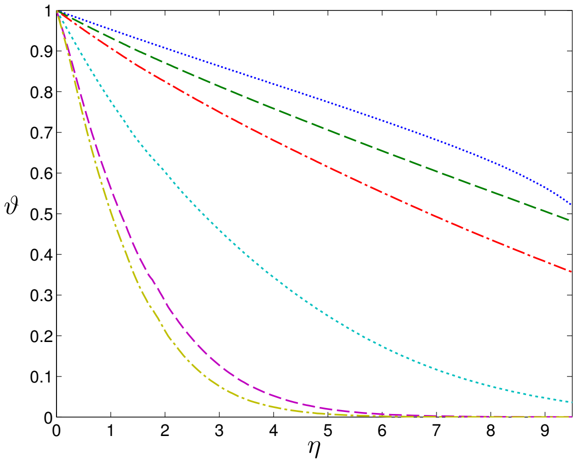

(c) $\zeta = 0.9$

Figure 4.20: Temperature function profiles u at $\zeta = 0.1, 0.5, 0.9$, for $\lambda_{\mathrm{T}} = 0$ while $\mathrm{Pr} = 0.01, 0.05, 0.1, 0.72, 6, 10$.

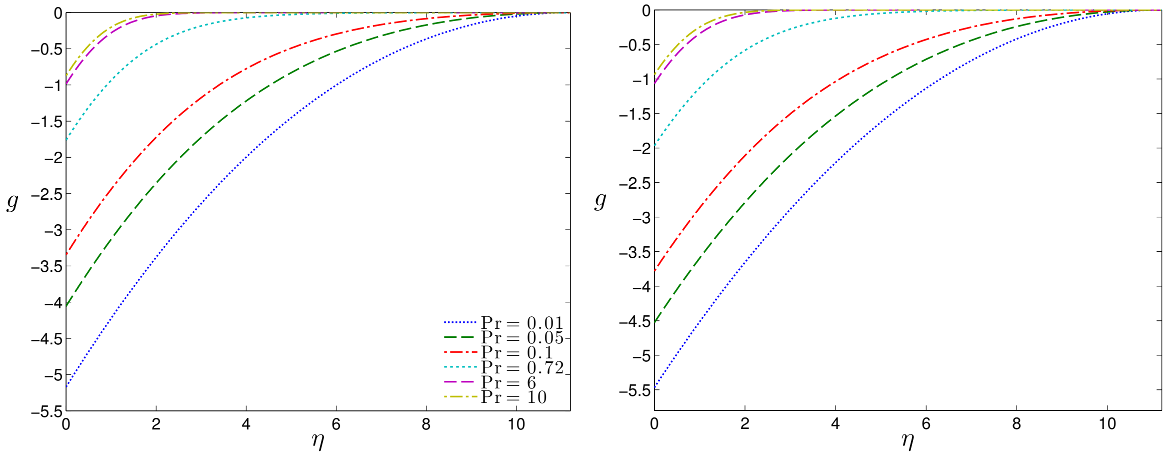

(a) $\zeta = 0.1$ (b) $\zeta = 0.5$

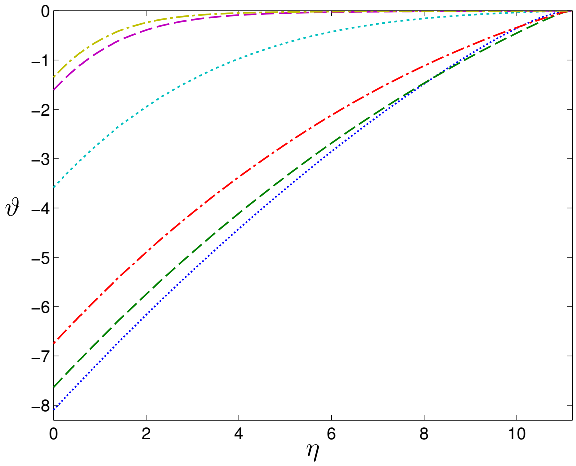

(c) $\zeta = 0.9$

Figure 4.21: Temperature function profiles u at $\zeta = 0.1, 0.5, 0.9$, for $\lambda_{\mathrm{T}} = 0$ while $\mathrm{Pr} = 0.01, 0.05, 0.1, 0.72, 6, 10$.

skin friction results demonstrated in Figure 4.23 indicate an opposite behaviour, since the skin friction increases with a decreasing value assigned to Pr.

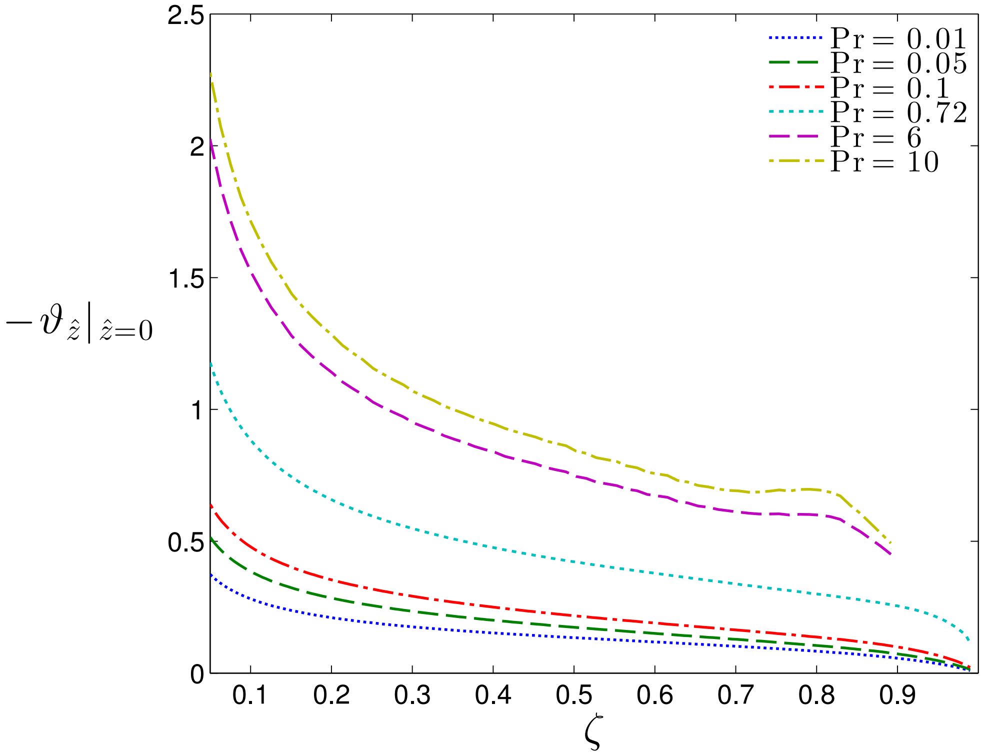

Figure 4.22: Variation of heat transfer with ζ for different values of Pr, while λ_{T}=0 and $C = 1$.

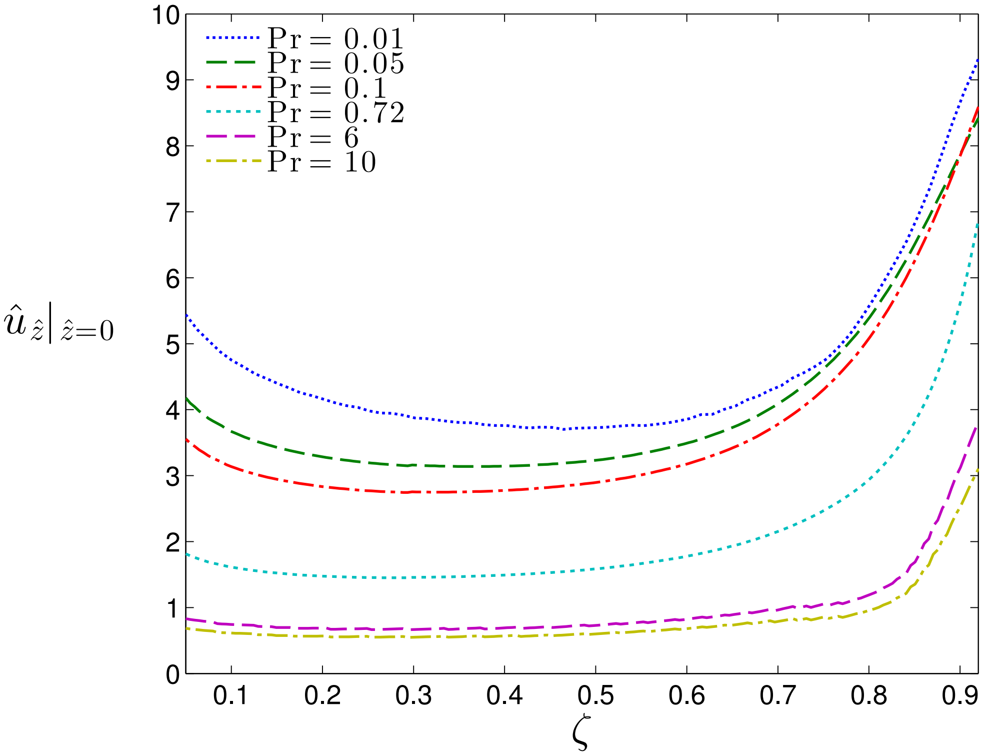

Figure 4.23: Variation of the skin friction coefficient with ζ for different values of Pr, while λ_{T}=0 and $C = 1$.

4.7 Summary

Attention in this chapter was directed towards the study of the boundary layer flow above a uniformly heated circular disc of radius a. Allowances were made for variable fluid properties and a linear law for the thermal conductivity and the viscosity was assumed. Inclusion of variable fluid properties within the formulation resulted in the presence of an additional dimensionless parameter, λ_{T}, within the set of equations. This newly introduced parameter also enabled the study of the Boussinesq approximation limit, by simply setting $\lambda_{\mathrm{T}} = 0$. An analytic study concerning the significance of variable fluid properties (by varying the parameter λ_{T}), as well as the influence of the Prandtl number (under the Boussinesq approximation) on the flow, was presented. Firstly, fourth order series approximations valid at the edge of the circular disc were obtained, followed by the numerical solution of the governing PIDEs. A finite difference scheme was developed for the solution of the PIDEs using the Keller-Box method. In addition a 'compressed' Dorodnitsyn-Howarth transformation was defined for the Boundary layer equations, and the numerical solution was obtained via FEM using COMSOL Multiphysics 3.5a.

It was shown that the introduction of variable fluid properties had a significant effect on the velocity function, but a perturbation effect on the thermal layer and consequently on the pressure function. In particular, it was observed that an increase in the value of λ_{T} led to a noteworthy increase of the velocity function and a thinning of the thermal layer, accompanied by a reduced negative pressure gradient. Moving towards the centre of the disc and the same behaviour was exhibited w.r.t λ_{T}, only now the velocity decreased, while the thickness of the thermal layer and the negative pressure function increased as the centre of the disc was approached. Furthermore, heat transfer and skin friction decreased with an increasing λ_{T}.

Finally, when the Boussinesq approximation was invoked ($\lambda_{\mathrm{T}} = 0$), and the study concentrated on the effect of Pr on the flow, the following behaviour was observed. A decrease in the velocity profiles, a thinning on the thermal layer and a decrease on the negative pressure function with an increase in the value of Pr. Closing, higher heat transfer rates were observed for increasing values of Pr, while the opposite behaviour was exhibited for the skin friction.

Chapter 5

Study of Laminar Natural Convection Above Inclined to Horizontal Plates

5.1 Introduction

In this chapter, the first order boundary layer analysis of laminar natural convection above a uniformly heated horizontal and slightly inclined semi-infinite plate is revisited. Based on the work of Ackroyd [2], variable fluid properties are introduced in the formulation, while a fourth order series approximation based on a small inclination angle $\gamma = \mathcal{O}(\mathrm{Gr}^{-1/5})$, valid near the edge of the plate is obtained. With the angle positive implying that the leading edge is positioned at the lowest point of the semi-infinite heated plate, we further allow departures from similarity and a numerical solution is obtained in regions where the series solution ceases to be valid. Both positive $\sigma > 0$ and negative $\sigma < 0$ inclinations are considered as previously explored by Jones [38]. The difference here being the inclusion of variable property effects, as well as a study for the effect of Prandtl number when the Boussinesq approximation is applied.

As was demonstrated in Chapter 4, usage of variable fluid properties resulted in the appearance of an additional nondimensional parameter, namely λ_{T}, in the boundary layer equations. Since the same assumptions are made here w.r.t the density, the fluid transport properties and the secondary thermodynamic properties, the parameter λ_{T}

naturally arises in the formulation. It will be shown that when the inclination is negative and $\lambda_{\mathrm{T}} = 0$ we obtain the separation point x_s followed by flow reversal, firstly revealed by [38]. When departing from the Boussinesq approximation, i.e. $\lambda_{\mathrm{T}} > 0$, it will be shown that the separation point moves downstream as the value of λ_{T} is increased. In addition the effect of the Prandtl number as well as the constant parameter of inclination σ, to the position of the separation point when $\lambda_{\mathrm{T}} = 0$, is also considered. Finally when the inclination to horizontal is positive, the effect of λ_{T} and σ is studied by numerically solving the PDE's for large values of x.

5.2 Formulation

A Cartesian coordinate system is used with the origin positioned at the leading edge with x measuring along the plate and y being normal to it as shown in Figure 5.1. Again the plate is kept at a higher temperature than the environment and once more the suffix w corresponds to properties on the plate, while suffix ∞ corresponds to ambient properties.

Proceeding with the introduction of the governing equations for the flow, starting with the the ideal gas law, the continuity and the momentum equations are given as

$$\rho T = \rho_\infty T_\infty, \tag{5.1a}$$

$$\frac{\partial}{\partial x}(\rho u) + \frac{\partial}{\partial y}(\rho v) = 0, \tag{5.1b}$$

$$\frac{\partial}{\partial x}\left(\rho u^2\right) + \frac{\partial}{\partial y}(\rho u v) = f_x - \frac{\partial P}{\partial x} + \frac{\partial}{\partial x}(\tau_{xx}) + \frac{\partial}{\partial y}(\tau_{xy}), \tag{5.1c}$$

$$\frac{\partial}{\partial x}(\rho u v) + \frac{\partial}{\partial y}\left(\rho v^2\right) = f_y - \frac{\partial P}{\partial y} + \frac{\partial}{\partial x}(\tau_{yx}) + \frac{\partial}{\partial y}(\tau_{yy}), \tag{5.1d}$$

where

$$\tau_{xx} = 2\mu\frac{\partial u}{\partial x}, \ \tau_{yy} = 2\mu\frac{\partial v}{\partial y}, \ \text{and } \tau_{xy} = \tau_{yx} = \mu\left(\frac{\partial u}{\partial y} + \frac{\partial v}{\partial x}\right). \tag{5.1e}$$

Finally the energy equation writes as

$$\frac{\partial}{\partial x}(\rho c_p u T) + \frac{\partial}{\partial y}(\rho c_p v T) = \frac{\partial}{\partial x}\left(\kappa\frac{\partial T}{\partial x}\right) + \frac{\partial}{\partial y}\left(\kappa\frac{\partial T}{\partial y}\right). \tag{5.1f}$$

Breaking the pressure into hydrostatic (p_∞) and dynamic (p) parts, i.e. $P = p_\infty + p$, and noting that $\nabla p_\infty = \rho_\infty \mathbf{g}$, then in vector form we can write

$$\mathbf{f} - \nabla P = \rho\mathbf{g} - \nabla\left(p_\infty + p\right) = (\rho - \rho_\infty)\mathbf{g} - \nabla p,$$

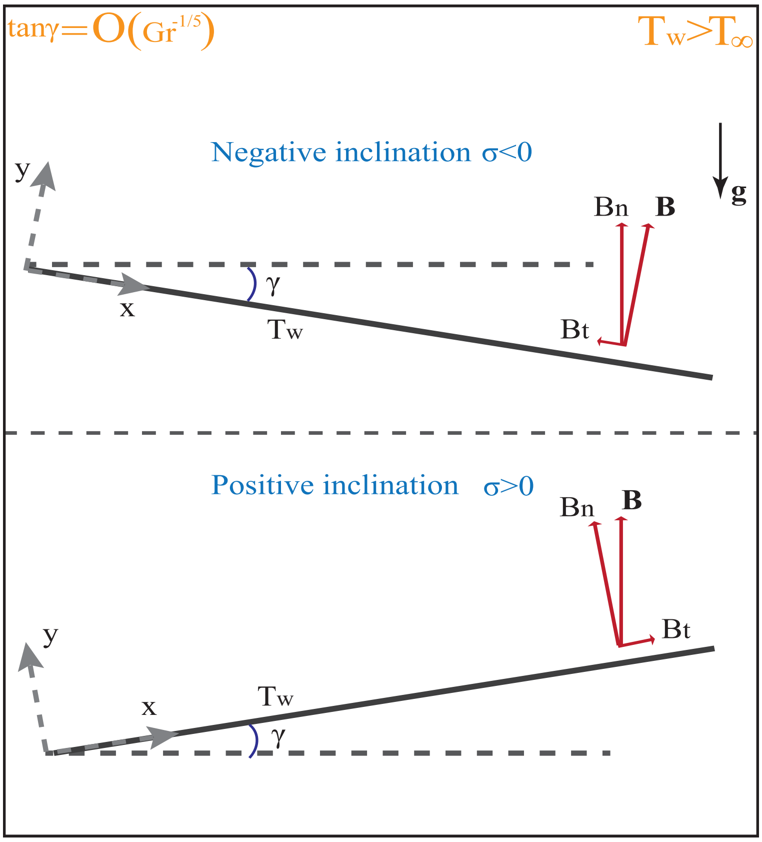

Figure 5.1: Coordinate systems for negative and positive inclination.The angle of inclination γ, $\mathbf{B}$ is the buoyancy force i.e. $(\mathbf{g}(\rho-\rho_\infty))$ and σ the inclination parameter.

having x and y components given as

$$f_x - \frac{\partial P}{\partial x} = (\rho_\infty - \rho)g_x - \frac{\partial p}{\partial x} \quad \text{and} \quad f_y - \frac{\partial P}{\partial y} = (\rho_\infty - \rho)g_y - \frac{\partial p}{\partial y} \tag{5.1g}$$

where $g_x = g\sin\gamma$ and $g_y = g\cos\gamma$.

The governing equations will now be nondimensionalised using the following scalings

$$x = L\dot{x}, \quad y = L\dot{y}, \quad \rho = \rho_\infty\dot{\rho}, \quad u = \frac{\nu_\infty}{L}\dot{u}, \quad v = \frac{\nu_\infty}{L}\dot{v}, \quad \kappa = \kappa_\infty\dot{k}, \quad \mu = \mu_\infty\dot{\mu},$$
$$\theta = \frac{T - T_\infty}{T_w - T_\infty}, \quad \text{and} \quad \Pi = \frac{pL^2}{\rho_\infty \nu_\infty^2}. \tag{5.2}$$

Introducing the above nondimensional parameters into the governing set of equations, the ideal gas law now changes to

$$1 - \dot{\rho} = \frac{\dot{\rho}\theta\,(T_w - T_\infty)}{T_\infty}, \tag{5.3}$$

while the continuity and momentum equations are now given as

$$\frac{\partial}{\partial\dot{x}}\left(\dot{\rho}\dot{u}\right) + \frac{\partial}{\partial\dot{y}}\left(\dot{\rho}\dot{v}\right) = 0, \tag{5.4}$$

$$\frac{\partial}{\partial \dot{x}}\left(\dot{\rho}\dot{u}^2\right)+\frac{\partial}{\partial \dot{y}}\left(\dot{\rho}\dot{u}\dot{v}\right)=-\frac{\partial \Pi}{\partial \dot{x}}+\frac{L^3\left(1-\dot{\rho}\right)g\sin\gamma}{\nu^2}+\frac{\partial}{\partial \dot{x}}\left(\dot{\tau}_{xx}\right)+\frac{\partial}{\partial \dot{y}}\left(\dot{\tau}_{xy}\right), \tag{5.5}$$

$$\frac{\partial}{\partial \dot{x}}\left(\dot{\rho}\dot{u}\dot{v}\right)+\frac{\partial}{\partial \dot{y}}\left(\dot{\rho}\dot{v}^2\right)=-\frac{\partial \Pi}{\partial \dot{y}}+\frac{L^3\left(1-\dot{\rho}\right)g\cos\gamma}{\nu^2}+\frac{\partial}{\partial \dot{x}}\left(\dot{\tau}_{yx}\right)+\frac{\partial}{\partial \dot{y}}\left(\dot{\tau}_{yy}\right). \tag{5.6}$$

Defining the Grashof number as

$$\mathrm{Gr}=\frac{gL^3\left(T_w-T_\infty\right)\cos\gamma}{\nu^2 T_\infty}, \tag{5.7}$$

then with the aid of equation (5.3), the momentum equations after dropping the dots change to

$$\frac{\partial}{\partial x}\left(\rho u^2\right)+\frac{\partial}{\partial y}\left(\rho uv\right)=-\frac{\partial \Pi}{\partial x}+\mathrm{Gr}\rho\theta\tan\gamma+\frac{\partial}{\partial x}\left(\tau_{xx}\right)+\frac{\partial}{\partial y}\left(\tau_{xy}\right) \tag{5.8}$$

$$\frac{\partial}{\partial x}\left(\rho uv\right)+\frac{\partial}{\partial y}\left(\rho v^2\right)=-\frac{\partial \Pi}{\partial y}+\mathrm{Gr}\rho\theta+\frac{\partial}{\partial x}\left(\tau_{yx}\right)+\frac{\partial}{\partial y}\left(\tau_{yy}\right) \tag{5.9}$$

Turning attention to the energy equation, by noticing that the term T appears only within derivatives, it can thus be changed to $T-T_\infty$. In doing so, and after the introduction of the nondimensional scalings, the nondimensional energy equation (after dropping dots) is given as

$$\rho u\frac{\partial \theta}{\partial x}+\rho u\frac{\partial \theta}{\partial y}=\frac{1}{\mathrm{Pr}}\left(\frac{\partial}{\partial x}\left(\kappa\frac{\partial \theta}{\partial x}\right)+\frac{\partial}{\partial y}\left(\kappa\frac{\partial \theta}{\partial y}\right)\right), \tag{5.10}$$

and the Prandtl number Pr is defined as

$$\frac{1}{\mathrm{Pr}}=\frac{\kappa_\infty}{\rho_\infty \mathrm{c_p}\nu_\infty}. \tag{5.11}$$

The above equations are to be solved subject to the following boundary conditions

$$u=v=0 \quad \text{and} \quad \theta=1, \quad \text{on} \quad y=0 \quad \text{while } x>0,$$

$$u,\ \theta,\ \Pi\to 0 \text{ as } y\to\infty, \tag{5.12}$$

$$u=\Pi=\theta=0 \quad \text{at} \quad x=0, \quad \text{and} \quad y>0.$$

5.2.1 The boundary layer equations

For a large Grashof number and when the plate is horizontal i.e ($\gamma = 0$), the above problem can be treated as a singular perturbation problem and be reduced to a self similar form as was firstly shown by Stewartson [89]. In our formulation following [38] and [67], we shall assume small inclinations to the horizontal such that $\tan\gamma = \mathcal{O}(\epsilon)$, where $\epsilon = \mathrm{Gr}^{-1/5}$. This will enable us to use the same similarity variables as [89] and then depart from the horizontal self similar solutions by expanding in terms of the perturbation parameter ϵ, so that inclination effects can be included. The above will become clear once the boundary layer equations are obtained.

In treating the problem as a boundary layer one, in the limit $\mathrm{Gr} \to \infty$, following [74] we begin by introducing the following stretched variables

$$y = \epsilon\hat{y},\ u = \epsilon^{-2}\hat{u},\ v = \epsilon^{-1}\hat{v},\ \Pi = \epsilon^{-4}\hat{\Pi},\ \text{where } \epsilon = \mathrm{Gr}^{-1/5}, \tag{5.13a}$$

into the governing equations. Thus keeping leading order terms as $\mathrm{Gr} \to \infty$ results in the following set of equations

$$\frac{\partial}{\partial x}(\rho\hat{u}) + \frac{\partial}{\partial\hat{y}}(\rho\hat{v}) = 0, \tag{5.13b}$$

$$\frac{\partial}{\partial x}\left(\rho\hat{u}^2\right) + \frac{\partial}{\partial\hat{y}}(\rho\hat{u}\hat{v}) = -\frac{\partial\hat{\Pi}}{\partial x} + \epsilon^{-1}\rho\theta\tan\gamma + \frac{\partial}{\partial\hat{y}}\left(\mu\frac{\partial\hat{u}}{\partial\hat{y}}\right) + \mathcal{O}(\epsilon^2), \tag{5.13c}$$

$$-\frac{\partial\hat{\Pi}}{\partial\hat{y}} + \rho\theta + \mathcal{O}(\epsilon^2) = 0, \tag{5.13d}$$

$$\rho\hat{u}\frac{\partial\theta}{\partial x} + \rho\hat{u}\frac{\partial\theta}{\partial\hat{y}} = +\frac{1}{\mathrm{Pr}}\frac{\partial}{\partial\hat{y}}\left(\kappa\frac{\partial\theta}{\partial\hat{y}}\right) + \mathcal{O}(\epsilon^2). \tag{5.13e}$$

Focusing on equation (5.13c), it can be observed that the term $\epsilon^{-1}\rho\theta\tan\gamma$ has been retained. The reason for doing so is that we require that the buoyancy force has to be of the same order as the induced pressure gradient. In order to achieve this a necessary constraint needs to be imposed on the angle of inclination i.e. $\tan\gamma = \mathcal{O}(\epsilon)$, so that

$$\epsilon^{-1}\rho\theta\tan\gamma = \sigma\rho\theta$$

with σ being an $\mathcal{O}(1)$ constant which we shall term the inclination parameter. A positive or negative value assigned to σ implies a positive or negative inclination respectively. Therefore the x-momentum equation is now written as

$$\frac{\partial}{\partial x}\left(\rho\hat{u}^2\right)+\frac{\partial}{\partial\hat{y}}\left(\rho\hat{u}\hat{v}\right)=-\frac{\partial\hat{\Pi}}{\partial x}+\sigma\rho\theta+\frac{\partial}{\partial\hat{y}}\left(\mu\frac{\partial\hat{u}}{\partial\hat{y}}\right)+\mathcal{O}(\epsilon^2). \tag{5.14}$$

Having obtained the boundary layer equations we shall now proceed by introducing the stream function Ψ, so that

$$\rho\hat{u}=\frac{\partial\Psi}{\partial\hat{y}} \quad \text{and} \quad \rho\hat{v}=-\frac{\partial\Psi}{\partial x}. \tag{5.15}$$

In addition, similarity transformations for the independent variables based on the Dorodnitsyn-Howarth transformation are given as [90],[31],[2],

$$\xi = x \text{ and } \eta=(Cx)^{-2/5}\int_0^{\hat{y}}\rho d\tilde{y}. \tag{5.16}$$

Furthermore, for the dependent variables the transformations read as

$$\Psi(x,\hat{y})=(Cx)^{3/5}f(\xi,\,\eta),\ \hat{\Pi}(x,\hat{y})=(Cx)^{2/5}G(\xi,\,\eta) \text{ and } \theta(x,\hat{y})=\Theta(\xi,\,\eta), \tag{5.17}$$

where C is the Chapman variable taken to be unity everywhere, unless it is to be used in the viscosity temperature relation.

For the mapping $(x,\,y)\rightarrow(\xi,\,\eta)$ the formal transformations are given as

$$\frac{\partial}{\partial x}=\frac{\partial}{\partial\xi}+\frac{\partial\eta}{\partial x}\frac{\partial}{\partial\eta} \quad \text{and} \quad \frac{\partial}{\partial\hat{y}}=\rho(Cx)^{-2/5}\frac{\partial}{\partial\eta}. \tag{5.18}$$

Applying the above stated transformations into the x-momentum equation (5.14), the convective term changes to

$$\rho\Big(\hat{u}\frac{\partial\hat{u}}{\partial x}+\hat{v}\frac{\partial\hat{u}}{\partial\hat{y}}\Big)=\rho\left[(Cx)^{-4/5}\Big[\Psi_\eta\Psi_{\eta\xi}-\Psi_\xi\Psi_{\eta\eta}\Big]-\frac{2}{5}(Cx)^{-9/5}C\Psi_\eta^2\right]=$$

$$=\rho\left[\frac{3}{5}C(Cx)^{-3/5}f_\eta^2+(Cx)^{2/5}f_\eta f_{\eta\xi}-\frac{3}{5}C(Cx)^{-3/5}ff_{\eta\eta}-(Cx)^{2/5}f_\xi f_{\eta\eta}-\frac{2}{5}C(Cx)^{-3/5}f_\eta^2\right],$$

while for the r.h.s term

$$-\frac{\partial\hat{\Pi}}{\partial x}+\sigma\rho\theta+\frac{\partial}{\partial\hat{y}}\left(\mu\frac{\partial\hat{u}}{\partial\hat{y}}\right)=-\Bigg[\frac{2}{5}C(Cx)^{-3/5}G+(Cx)^{2/5}\Big[G_\xi+\frac{\partial\eta}{\partial x}G_\eta\Big]+$$

$$+\sigma\rho\Theta+(Cx)^{-3/5}\rho\Big[\mu\rho f_{\eta\eta}\Big]_\eta\Bigg].$$

Collecting and simplifying the above terms, the transformed x-momentum boundary layer equation takes the following form

$$\left[\frac{\mu\rho}{C} f_{\eta\eta}\right]_\eta - \frac{1}{5} f_\eta^2 + \frac{3}{5} f f_{\eta\eta} - \frac{2}{5\rho}\Big(G + \frac{5\xi}{2} G_\xi + \frac{5\xi}{2}\frac{\partial\eta}{\partial x} G_\eta\Big) + \sigma C^{-2/5}\xi^{3/5}\Theta = \xi\Big(f_{\eta\xi} f_\eta - f_{\eta\eta} f_\xi\Big), \tag{5.19}$$

while for the y-momentum boundary layer equation, introduction of the similarity variables results in

$$\Theta = \frac{\partial G}{\partial \eta}. \tag{5.20}$$

Finally introducing the stream function into the energy equation gives

$$\Psi_\eta \Theta_\xi - \Psi_\xi \Theta_\eta = \frac{1}{\mathrm{Pr}}(Cx)^{-2/5}\Big[\kappa\rho\Theta_\eta\Big]_\eta$$

or

$$\frac{1}{\mathrm{Pr}}\left[\frac{\kappa\rho}{C}\Theta_\eta\right]_\eta = \xi\Big(f_\eta\Theta_\xi - f_\xi\Theta_\eta\Big) - \frac{3}{5} f\Theta_\eta. \tag{5.21}$$

Once more the term $\partial\eta/\partial x$ appears in the x-momentum equation, as a result of the employment of the Dorodnitsyn- Howarth transformation. By noticing that its inverse transformation can be obtained as

$$\hat{y} = (Cx)^{2/5}\int_0^\eta \frac{1}{\rho}\, d\tilde{\eta}, \tag{5.22}$$

and that

$$\frac{\partial \hat{y}}{\partial \xi} = -\frac{(Cx)^{2/5}}{\rho}\frac{\partial\eta}{\partial x}, \tag{5.23}$$

then a simple combination of the last two expressions will result in an explicit expression for $\partial\eta/\partial x$, given as follows

$$\frac{\partial\eta}{\partial x} = \rho\Big(-\frac{2}{5\xi}\int_0^\eta \frac{1}{\rho}\, d\tilde{\eta} + \int_0^\eta \frac{1}{\rho^2}\frac{\partial\rho}{\partial\xi}\, d\tilde{\eta}\Big). \tag{5.24}$$

Furthermore, the highest derivatives in x-momentum and energy, nonsimilar boundary layer equations include the fractions $\mu\rho/C$ and $\kappa\rho/C$. As was mentioned earlier, no deviation is made from Chapter 4 w.r.t the laws for viscosity and thermal conductivity. Therefore in nondimensional form, the chosen laws for fluid properties are given as

$$\mu = C\left(1 + \Theta\lambda_{\mathrm{T}}\right), \quad \kappa = C\left(1 + \Theta\lambda_{\mathrm{T}}\right), \quad \rho\big(1 + \Theta\lambda_{\mathrm{T}}\big) = 1, \text{ and } \lambda_{\mathrm{T}} = \frac{T_{\mathrm{w}} - T_\infty}{T_\infty}. \tag{5.25}$$

Adaptation of the above laws introduces a simplification into the governing equations since the fractions change to unity. Therefore the final form of the governing equations, after the introduction of (5.24) into the x-momentum equation, and the order increase of the energy equation, after using the y-momentum equation, follows as

$$f_{\eta\eta\eta} - \frac{1}{5}f_\eta^2 + \frac{3}{5}f f_{\eta\eta} - \frac{2}{5\rho}\left(G + \frac{5\xi}{2}G_\xi\right) + \left(\frac{2}{5}\int_0^\eta \frac{1}{\rho}\,d\tilde{\eta} - \xi\int_0^\eta \frac{1}{\rho^2}\frac{\partial\rho}{\partial\xi}\,d\tilde{\eta}\right)G_\eta + \\ + \sigma\, C^{-2/5}\,\xi^{3/5}G_\eta = \xi\Big(f_{\eta\xi}f_\eta - f_{\eta\eta}f_\xi\Big), \quad (5.26a)$$

$$\frac{1}{\mathrm{Pr}}G_{\eta\eta\eta} + \frac{3}{5}fG_{\eta\eta} = \xi\Big(f_\eta G_{\eta\xi} - f_\xi G_{\eta\eta}\Big), \quad (5.26b)$$

with $G_\eta = \Theta$. The resulting two third order, coupled system of PIDEs is to be solved subject to the BCs given below

$$f(0,\xi) = f_\eta(0,\xi) = 0,\ \ \Theta(0,\xi) = G_\eta(0,\xi) = 1,\ \text{ for }\ \xi > 0\ \text{ and} \quad (5.26c)$$

$$f_\eta(\eta,\xi) = \Theta(\eta,\xi) = G_\eta(\eta,\xi) = G(\eta,\xi) = 0\ \text{ as }\ \eta \to \infty.$$

5.2.2 Series solutions valid for $\xi \ll 1$

Setting $\xi = 0$ in equations (5.26) and $\lambda_{\mathrm{T}} = 0$ results in Stewartson's similarity equations describing the flow above a horizontal semi-infinite plate. It must be recalled that the same equations were obtained when the flow above a disk was studied, as a leading order approximation valid at the circumference of the disk. This implies that curvature effects are negligible to leading order. Allowing departures from similarity so as to include inclination effects, power series of the form

$$f(\xi\,,\eta) \approx \sum_{i=0}^{n}\beta^i f_i(\eta),\ \ G(\xi\,,\eta) \approx \sum_{i=0}^{n}\beta^i G_i(\eta),\ \text{ and }\ \Theta(\xi\,,\eta) \approx \sum_{i=0}^{n}\beta^i\Theta_i(\eta), \quad (5.27a)$$

with $\beta = \sigma\,\xi^{3/5}/C^{2/5}$ will be assumed valid for $\xi \ll 1$. In addition, the density is also approximated as

$$\frac{1}{\rho} \approx 1 + \lambda_{\mathrm{T}}\sum_{i=0}^{n}\beta^i\Theta_i(\eta) = 1 + \lambda_{\mathrm{T}}\sum_{i=0}^{n}\beta^i G_i', \quad (5.27b)$$

where the prime notation corresponds to differentiation w.r.t η, while $n = 3$. Applying the above expansions into equations (5.26a)–(5.26b), and collecting terms of $\mathcal{O}(1)$, $\mathcal{O}(\beta)$, $\mathcal{O}(\beta^2)$ and $\mathcal{O}(\beta^3)$ equivalently, the following four sets of coupled differential equations is obtained

- To leading order $\mathcal{O}(1)$

$$\frac{1}{\mathrm{Pr}}G_0''' + \frac{3}{5}f_0G_0'' = 0, \tag{5.28a}$$

$$f_0''' + \frac{3}{5}f_0''f_0 - \frac{1}{5}\left(f_0'\right)^2 + \frac{2}{5}\left(\eta - \lambda_{\mathrm{T}}G_0(0)\right)G_0' - \frac{2}{5}G_0 = 0, \tag{5.28b}$$

- $\mathcal{O}(\beta)$

$$\begin{aligned} f_1''' + \frac{6}{5}f_1f_0'' + \frac{3}{5}f_0f_1'' + \left(1 - \lambda_{\mathrm{T}}G_1(0)\right)G_0' + \\ + \frac{2}{5}\left(\eta - \lambda_{\mathrm{T}}G_0(0)\right)G_1' - f_0'f_1' - G_1 = 0, \end{aligned} \tag{5.28c}$$

$$\frac{1}{\mathrm{Pr}}G_1''' - \frac{3}{5}f_0'G_1' + \frac{6}{5}f_1G_0'' + \frac{3}{5}f_0G_1'' = 0, \tag{5.28d}$$

$\mathcal{O}(\beta^2)$

$$\begin{aligned} f_2''' - \frac{4}{5}\left(f_1'\right)^2 + \frac{9}{5}f_2f_0'' + \frac{6}{5}f_1f_1'' + \frac{3}{5}f_0f_2'' + \left(1 - \lambda_{\mathrm{T}}G_1(0)\right)G_1' + \\ + \frac{2}{5}\left(\eta - \lambda_{\mathrm{T}}G_0(0)\right)G_2' - \frac{8}{5}\left(G_0'\lambda_{\mathrm{T}}G_2(0) + G_2 + f_0'f_2'\right) = 0, \end{aligned} \tag{5.28e}$$

$$\frac{1}{\mathrm{Pr}}G_2''' + \frac{9}{5}f_2G_0'' - \frac{6}{5}f_0'G_2' - \frac{3}{5}f_1'G_1' + \frac{6}{5}f_1G_1'' + \frac{3}{5}f_0G_2'' = 0, \tag{5.28f}$$

- $\mathcal{O}(\beta^3)$

$$\begin{aligned} f_3''' + \frac{12}{5}f_3f_0'' + \frac{9}{5}f_2f_1'' + \frac{6}{5}f_1f_2'' + \frac{3}{5}f_0f_3'' - \frac{8}{5}G_1'\lambda_{\mathrm{T}}G_2(0) + \left(1 - \lambda_{\mathrm{T}}G_1(0)\right)G_2' + \\ + \frac{2}{5}\left(\eta - \lambda_{\mathrm{T}}G_0(0)\right)G_3' - \frac{11}{5}\left(G_3 + G_0'\lambda_{\mathrm{T}}G_3(0) + f_1'f_2' + f_0'f_3'\right) = 0, \end{aligned} \tag{5.28g}$$

$$\frac{1}{\mathrm{Pr}}G_3''' + \frac{3}{5}f_0G_3'' + \frac{12}{5}f_3G_0'' + \frac{9}{5}f_2G_1'' + \frac{6}{5}f_1G_2'' - \frac{3}{5}f_2'G_1' - \frac{9}{5}f_0'G_3' - \frac{6}{5}f_1'G_2' = 0. \tag{5.28h}$$

The above systems of coupled differential equations is to be solved subject to the BCs listed below

$$\begin{aligned} f_i(0) = f_i'(0) = 0,\ G_0'(0) = 1 \text{ while } G_{i+1}'(0) = 0, \text{ and} \\ f_i'(\eta) \to 0,\ \ G_i(\eta) = G_i'(\eta) \to 0 \text{ as } \eta \to \infty, \text{ for } i = 0 \ldots n. \end{aligned} \tag{5.29}$$

5.2.3 Numerical solution for the series approximations

In this section the numerical solution of equations (5.28) subject to BCs (5.29) using the shooting method is given. Exactly the same numerical procedure is applied here, as the one analytically described in **Section 4.3.1**, the only difference being that equations (4.36) are now different. For this reason we opt not get into a detailed description, as the reader can always refer to **Section 4.3.1**. Once more the numerical scheme is implemented in **Maple** [55] using *ShootLib*. The far field BCs are imposed at $\eta = 10$, while computations are carried for $\lambda_{\mathrm{T}} \in [0,\ 4]$ and $Pr = 0.72$, representing air. Furthermore, extensive numerical tables for the computed initial conditions $G_i(0)$, $\Theta_i'(0)$ and $f_i''(0)$, for $i = 0, 1, \ldots, 3$ and $\lambda_{\mathrm{T}} = 0, 0.1, \ldots, 4$, are given in **Appendix B**.

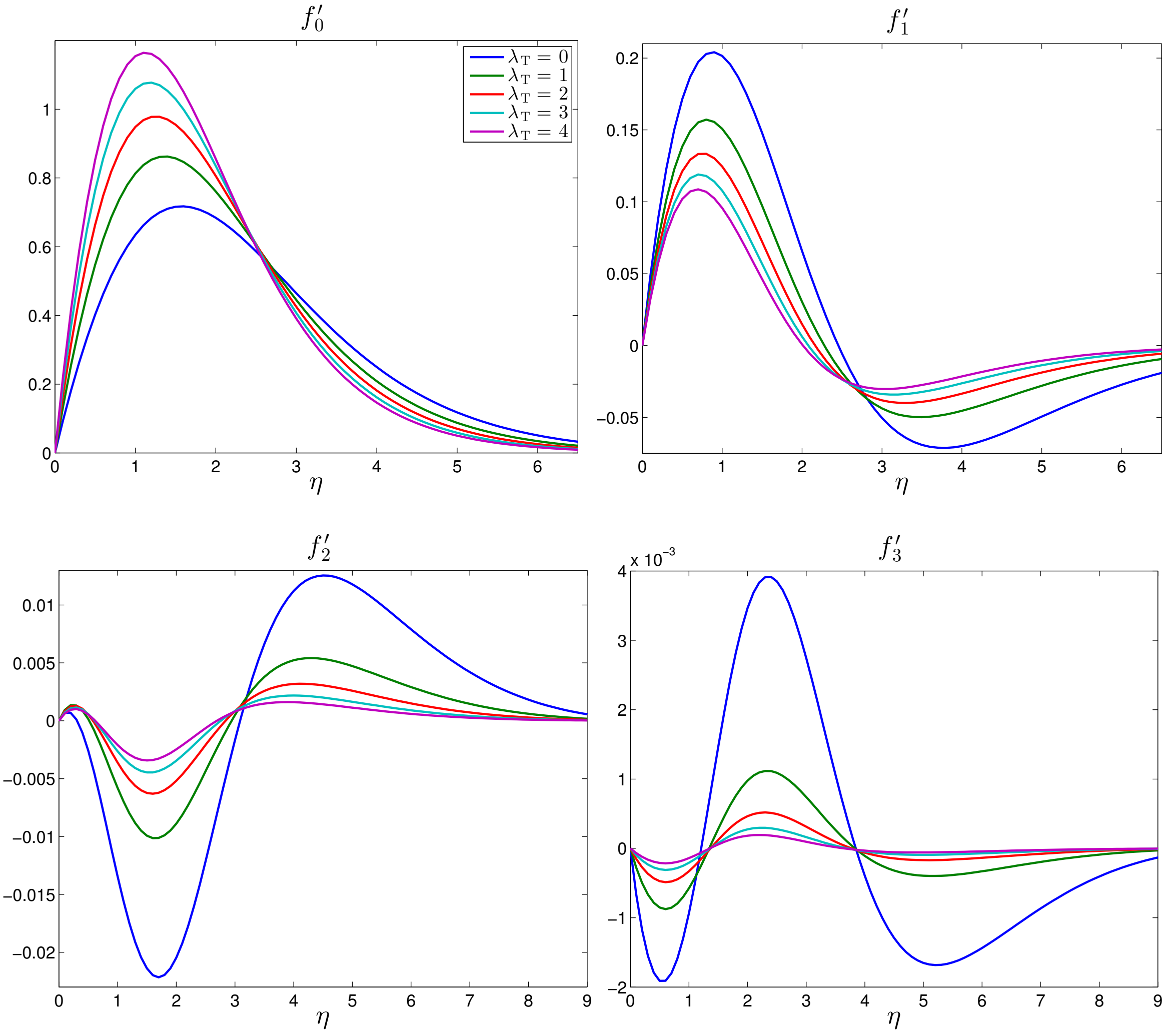

Figure 5.2: Effect of λ_{T} on the velocity function approximations Pr $= 0.72$.

From the numerical solutions presented in Figures 5.2, 5.3 and 5.4 it is clear that third and fourth order approximations are of small magnitude and will have a small contribution on the general solution. Regarding the effect of λ_{T}, it can be observed that as the value of λ_{T} increases, the magnitude of inclination effects are reduced, so that λ_{T} acts as a damping parameter on the inclination. The concluding remark is that the effect of inclination is stronger on the velocity and pressure functions, i.e. $\mathcal{O}(10^{-1})$, but of smaller strength in the temperature function since contribution is of

$\mathcal{O}(10^{-2})$.

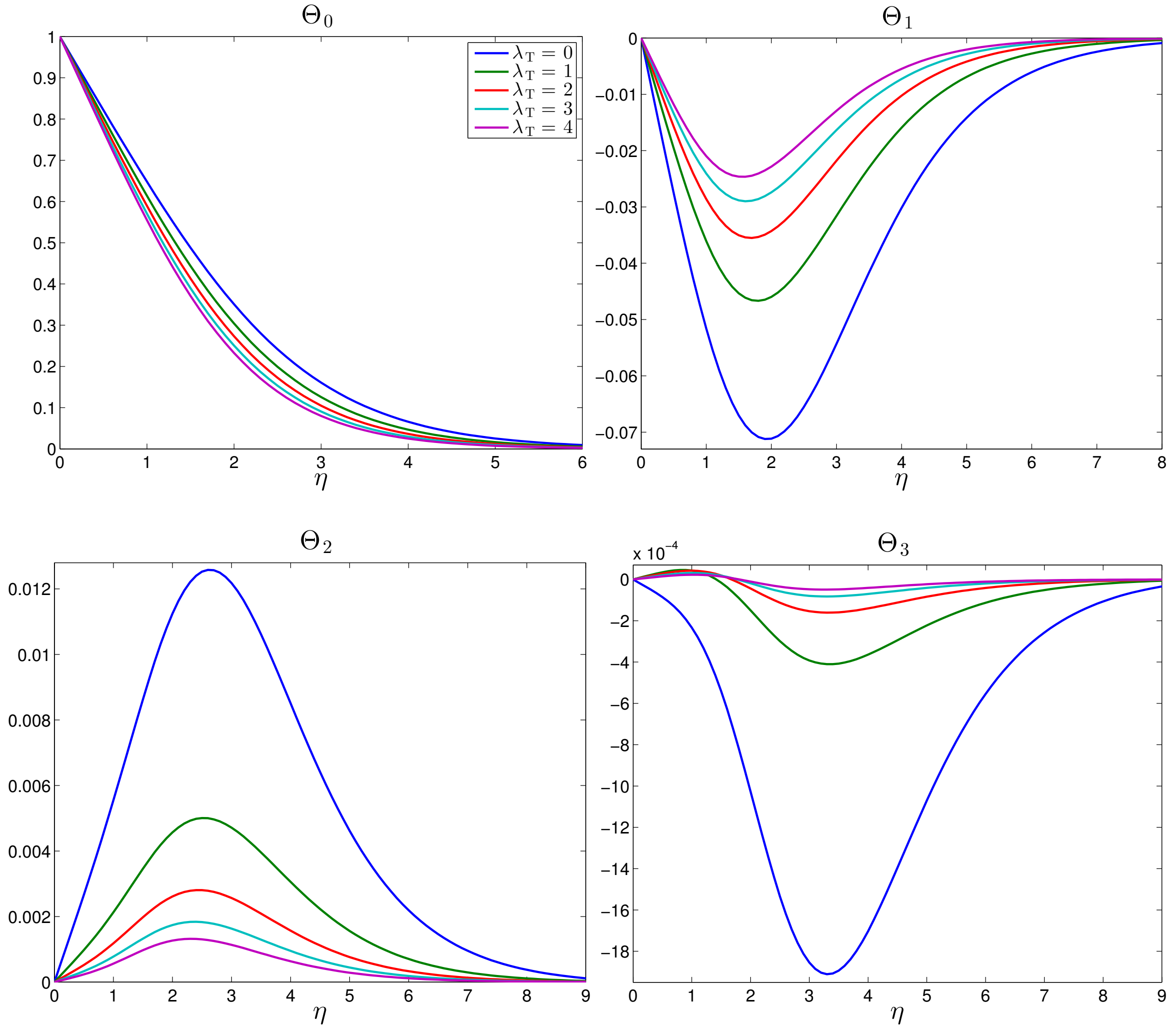

Figure 5.3: Effect of λ_T on the temperature function approximations $\Pr = 0.72$.

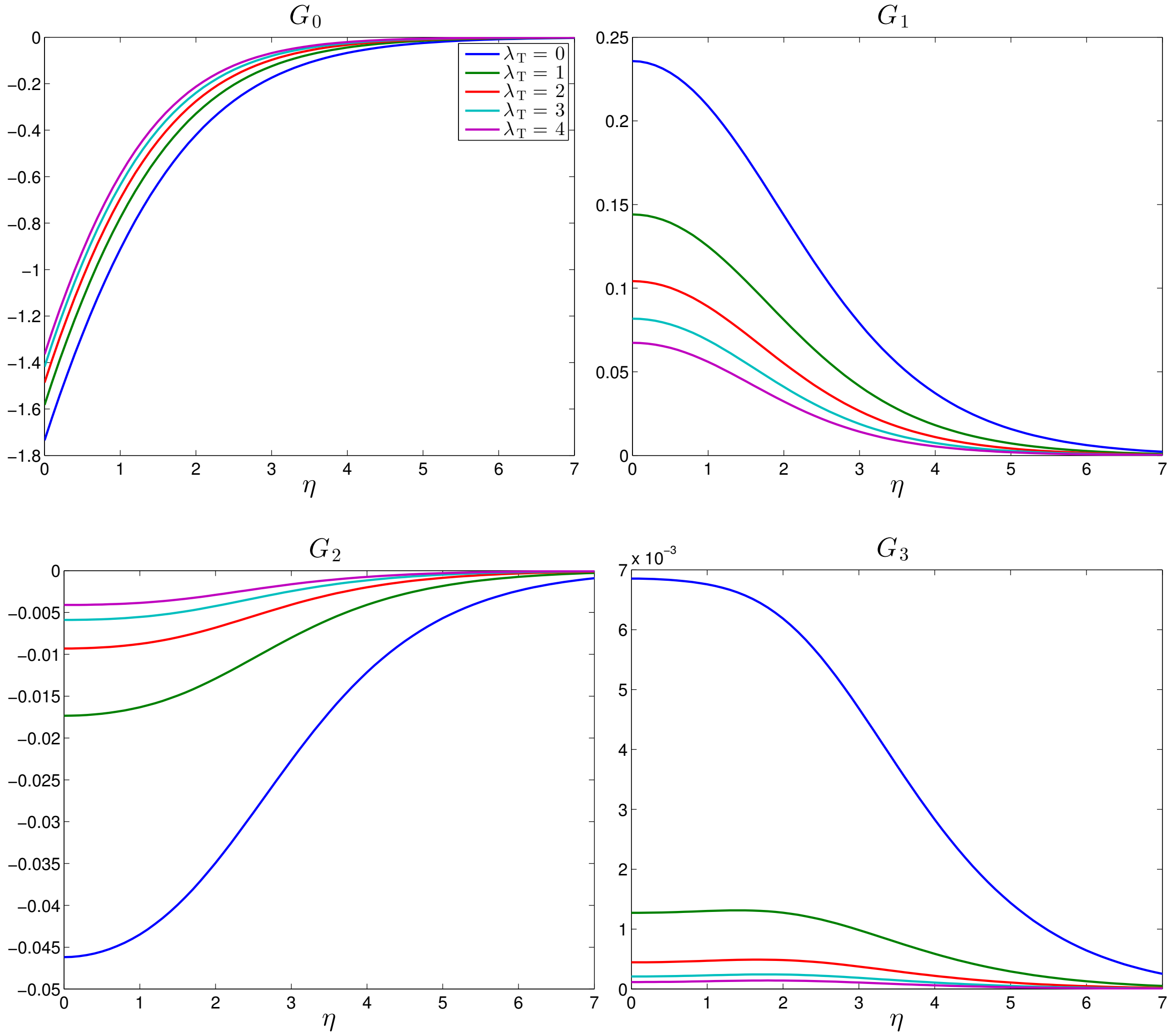

Figure 5.4: Effect of λ_T on the pressure function approximations $\mathrm{Pr} = 0.72$.

5.3 Negative inclination

Having obtained series solutions valid for $\xi \ll 1$, we shall now proceed in our analysis and obtain solutions valid for $\xi = \mathcal{O}(1)$ by numerically solving the PIDEs given in equation (5.26). The case of negative inclination is studied first ($\sigma < 0$). When the inclination is negative it can be seen from the diagram given in Figure 5.1 that the tangential buoyancy force component is opposing the motion, so it is expected that the flow will eventually separate.

In our analysis we shall begin by assigning $\sigma = -1$ and $\lambda_{\mathrm{T}} = 0$, so as to follow Jones. In doing so, recovery of the position of the separation point is achieved, which comes to an agreement with the position obtained by Jones in his analysis. We shall then proceed by departing from the Boussinesq approximation and vary the parameter λ_{T}, studying the position of the separation point. The next step in our analysis will correspond to the position of the separation point for different values of Pr, and the section will conclude by studying the effect of slightly perturbing the parameter of inclination σ.

The numerical solution of PIDEs (5.26) is achieved with the aid of COMSOL Multiphysics 3.5a, using the General PDE Mode. Three different computational domains D_A ,D_B and D_C were used, in all cases having rectangular shape, and each one suitable for different limiting values of λ_{T} and Pr. Attention was placed on the choice of the size of the domain and the meshing. For example, in dealing with the Boussinesq case a domain of size $[0, 4] \times [0, 15.5]$ is suitable since the separation point is located at around 3.7. Furthermore, care must be taken when the size of the domain is altered while its suitability for given parameters has to be examined ,so that convergence difficulties or even oscillations for the skin friction parameter can be avoided. The sizes of the three different computational domains starting with D_A which was set to be $[0, 4] \times [0, 15.5]$, D_B $[0, 8] \times [0, 15.5]$,while the larger one D_C was set to $[0, 21.5] \times [0, 20]$, with the small and intermediate domains being suitable for small and intermediate values of λ_{T} and intermediate and large values of Pr. The size of the domains and the meshing of their subdomain were chosen carefully under the criterion that for an intermediate value of λ_{T} for which two different domains are suitable for converging to a solution, the same solution is obtained.

5.3.1 From Boussinesq approximation to variable fluid properties

Starting with $\lambda_{\mathrm{T}} = 0$ and $\sigma = -1$, Jones' formulation is recovered. Numerical solution for Pr $= 0.72$ indicated that the separation point is located at $x_s = \xi = 3.705$, a result that comes to an agreement with the one Jones obtained, i.e. ($x_s = 3.704$). The domain D_B was utilised for the computations, therefore solutions were obtained for values of ξ ranging from zero to eight. In Figure 5.5, profiles of the velocity (a) temperature (b), and pressure (c) functions, are plotted for different values of ξ.

Keeping in mind that separation takes place at $\xi = 3.705$, flow reversal is evident at $\xi = 4$ but can clearly be observed at $\xi = 6$ and $\xi = 8$. Velocity is decreasing until the separation point, while after separation velocity function profiles are translated downstream, with the ones further down including an escalated effect of flow reversal. A thickening thermal layer as we move downstream is accompanied by an increase in the pressure.

Introducing variable fluid properties so that $\lambda_{\mathrm{T}} > 0$, results in the separation point moving downstream. Computations were carried out for $\lambda_{\mathrm{T}} = 0, 0.1, 0.2, \ldots 1.9, 2$, while the Prandtl number was kept fixed at Pr $= 0.72$ and $\sigma = -1$. The position of the separation point for selected values of λ_{T} is given in Table 5.1. The complete extent of our analysis is given in Figure 5.6, where in addition to the separation points obtained via numerical solution (marked with +), a simple curve is fitted in the least-squares sense (the blue dashed line). The following function was found suitable

λ_{T}	0	0.1	0.2	0.5	0.7	1	1.5	1.8	2
x_s	3.705	4.242	4.850	6.827	8.358	10.858	15.671	18.934	21.254

Table 5.1: Position of the separation point x_s, for different values λ_{T} while Pr $= 0.72$ and $\sigma = -1$.

$$x_s = x_{s_0} + A\,\lambda_{\mathrm{T}}^{B}, \quad \text{where} \quad A = 7.224, \quad B = 1.265 \quad \text{and} \quad x_{s_0} = 3.705. \tag{5.30}$$

The above can be relaxed and a value of $B = 5/4$ will roughly give the same approximation.

Moving downstream from the leading edge, and allowing departures from the Boussinesq approximation then, as can clearly be seen in Figure 5.7, velocity increases

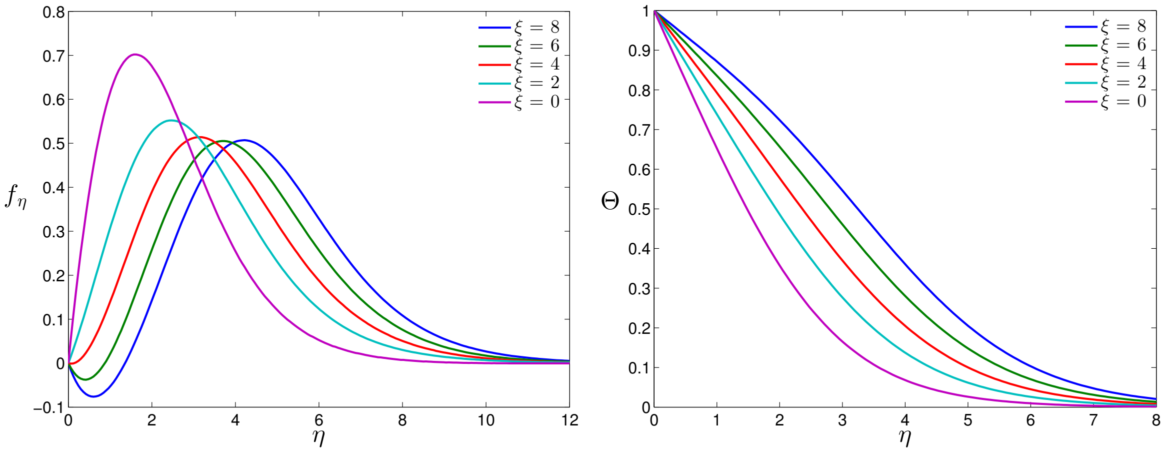

(a) Velocity function profiles f_η (b) Temperature function profiles Θ

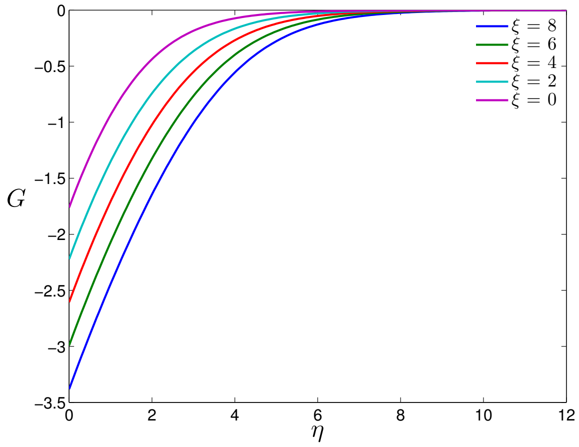

(c) Pressure function profiles G

Figure 5.5: Profiles for $\xi = 0, 2, 4, 6, 8$, while $\lambda_{\mathrm{T}} = 0$, $\mathrm{Pr} = 0.72$ and $\sigma = -1$.

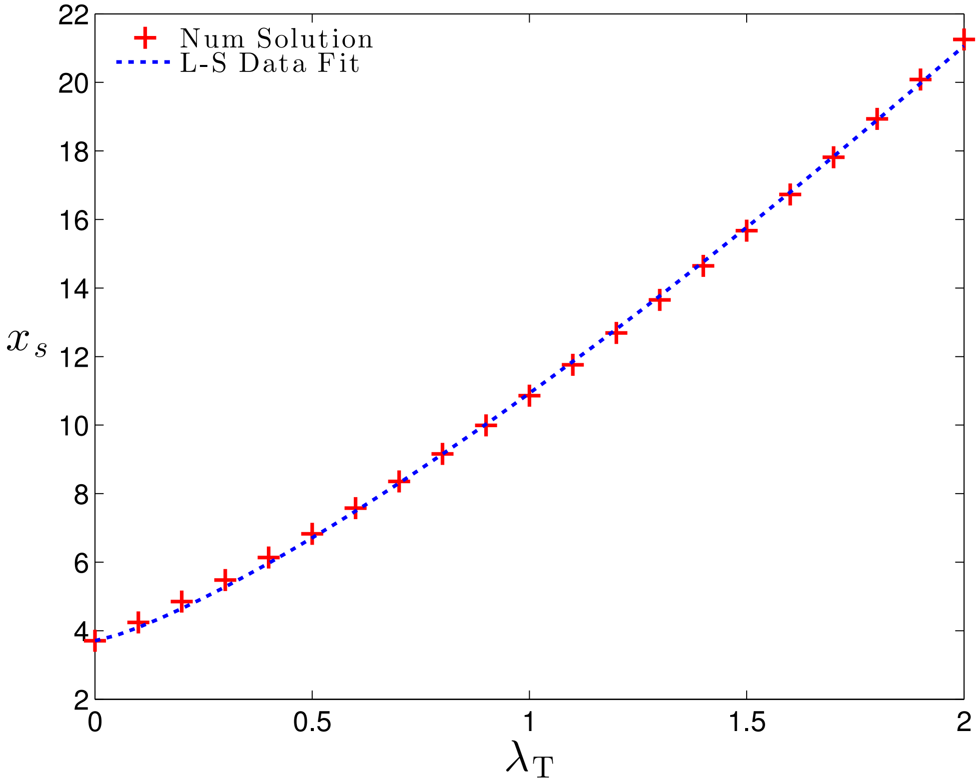

Figure 5.6: Separation point as a function of λ_{T}, while Pr=0.72 and σ=-1. Crosses correspond to actual numerical solutions.

with λ_{T}. At $\xi = 1$ and when $\lambda_{\mathrm{T}} = 0.5$, there is a more significant increase in velocity than when the Boussinesq approximation is used. Further downstream at $\xi = 5$, for the particular cases of $\lambda_{\mathrm{T}} = 0, 0.1$, separation has already taken place, with the difference being that when $\lambda_{\mathrm{T}} = 0$, the flow reversal is stronger since the separation takes place earlier. The velocity profile for $\lambda_{\mathrm{T}} = 0.5$ indicates a deceleration since there is a velocity drop from $\xi = 1$ to $\xi = 5$, as expected. Finally at $\xi = 8$, separation has taken place for all the cases presented, with the difference being that the same levels of flow reversal are obtained further downstream for $\lambda_{\mathrm{T}} > 0$. Reflecting on the effects that an increase of λ_{T} has on the thermal layer, the behaviour shown by the series approximations is verified. There is a slight thinning of the thermal layer as the value of λ_{T} increases, which can be observed at $\xi = 1$ in Figure 5.8. As ξ increases, shown by the profiles at $\xi = 5$ and $\xi = 8$, the thermal layer can be observed to thicken for any value of λ_{T}. Still though, when variable fluid properties are included the thermal layer is thinner for all values of ξ. Finally in what concerns the pressure function, Figure 5.9 indicates that at $\xi = 1$ it can be seen that the negative pressure is increasing towards zero with increasing λ_{T}, a trend that is verified at $\xi = 5$ and $\xi = 8$. Moving

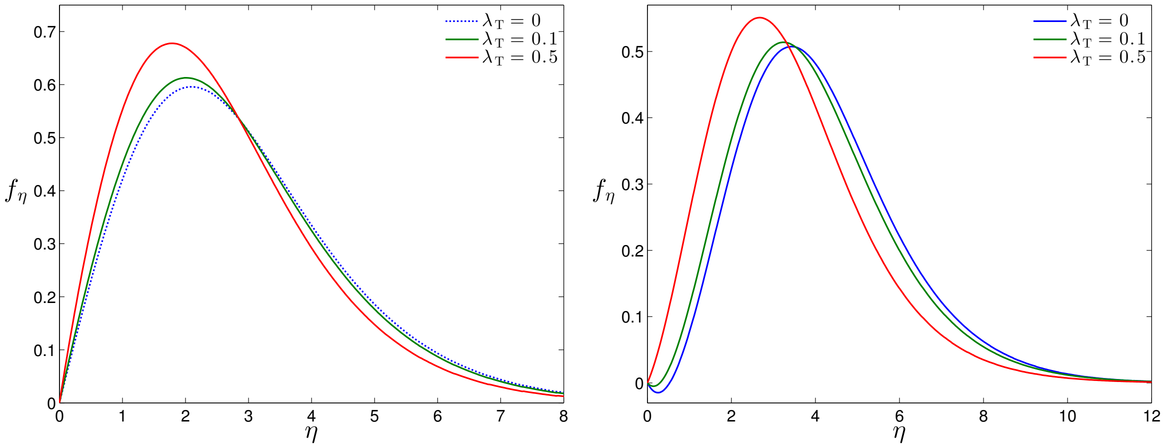

(a) $\xi = 1$ (b) $\xi = 5$

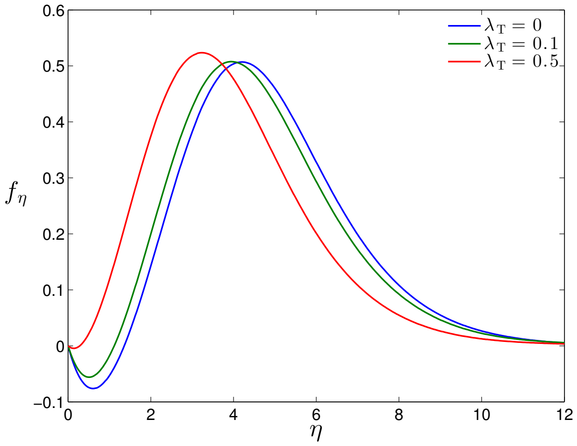

(c) $\xi = 8$

Figure 5.7: Velocity function profiles at different distances from the leading edge of the plate, for different values of λ_T. Computations were carried for $\mathrm{Pr} = 0.72$ and $\sigma = -1$.

downstream results in a reduced pressure gradient for all values of λ_T.

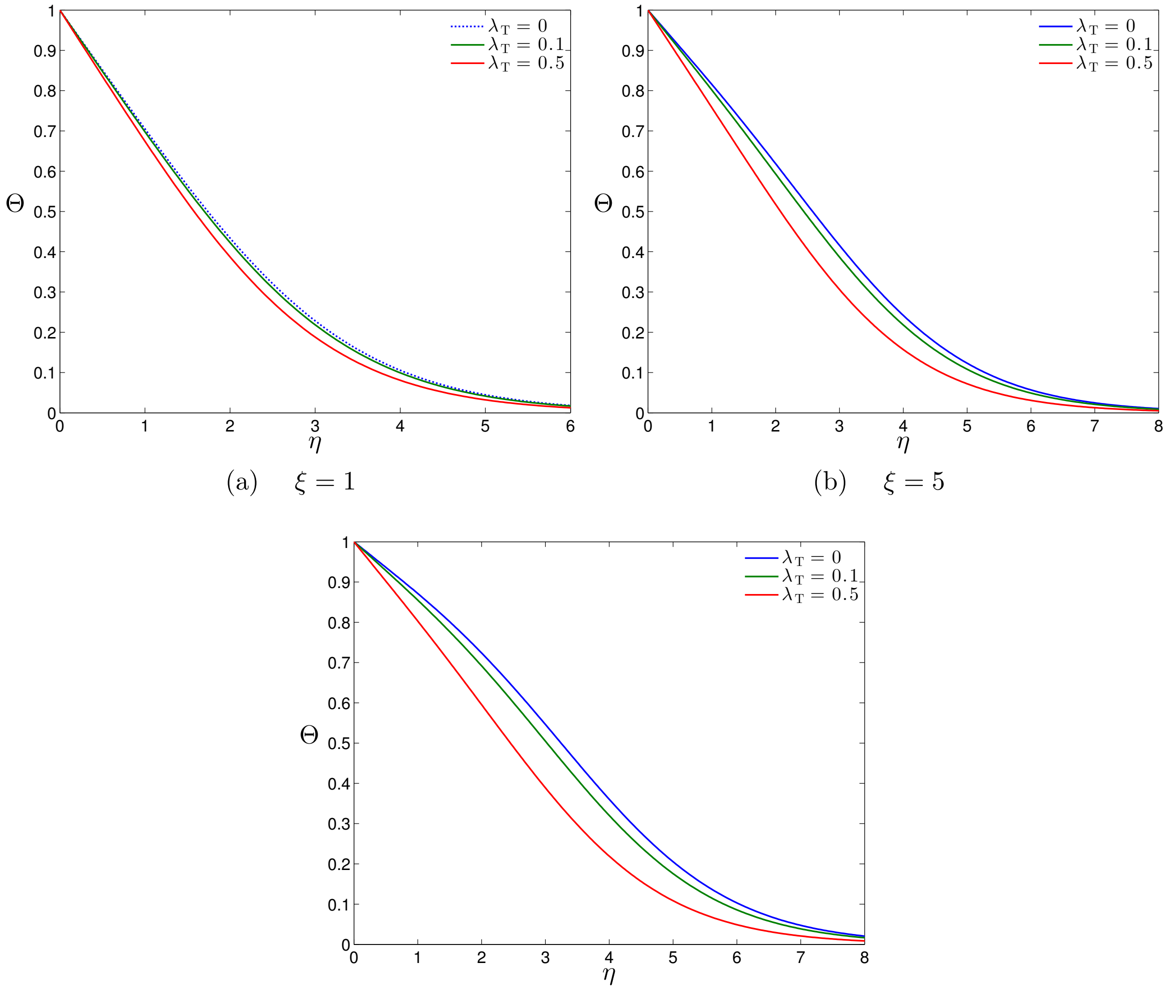

(a) $\xi = 1$

(b) $\xi = 5$

(c) $\xi = 8$

Figure 5.8: Temperature function profiles at different distances from the leading edge of the plate for different values of λ_T. Computations were carried for $\mathrm{Pr} = 0.72$ and $\sigma = -1$.

The heat transfer coefficient in nondimensional variables x and $\hat{y}$ is given as

$$-\frac{\partial \Theta}{\partial \hat{y}}\Big|_{\hat{y}=0} = -\rho (C\xi)^{-2/5} \frac{\partial \Theta}{\partial \eta}\Big|_{\eta=0}. \tag{5.31}$$

Variable property effects on heat transfer, can be observed in Figure 5.10. High heat transfer rates are seen in the neighbourhood of the leading edge, while an increase in the value of λ_T results in lower heat transfer rates to the plate. Meanwhile the skin friction i.e.

$$\frac{\partial \hat{u}}{\partial \hat{y}}\Big|_{\hat{y}=0} = \rho (C\xi)^{-1/5} \frac{\partial^2 f}{\partial \eta^2}\Big|_{\eta=0} \tag{5.32}$$

and its variation with x, for different values of λ_T is given in Figure 5.11. Furthermore the variation of the pressure function at $\eta = 0$ with ξ is given in Figure 5.12. The

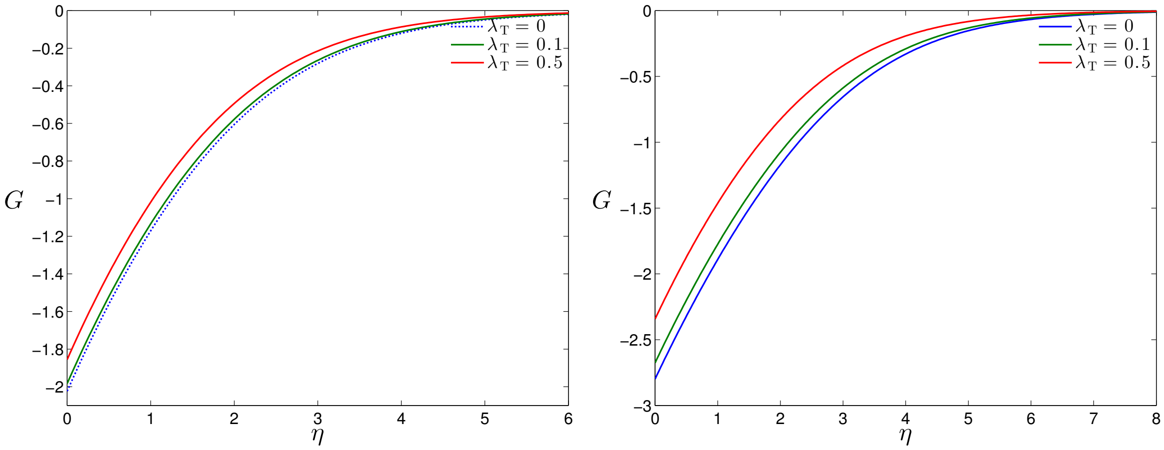

(a) $\xi = 1$ (b) $\xi = 5$

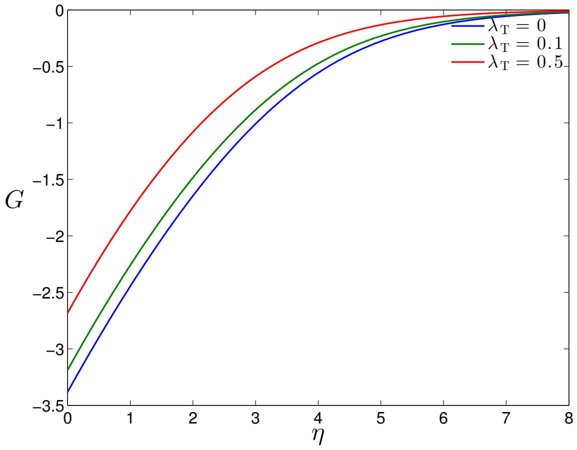

(c) $\xi = 8$

Figure 5.9: Pressure function profiles at different distances from the leading edge of the plate, for different values of λ_T. Computations were carried for $\Pr = 0.72$ and $\sigma = -1$

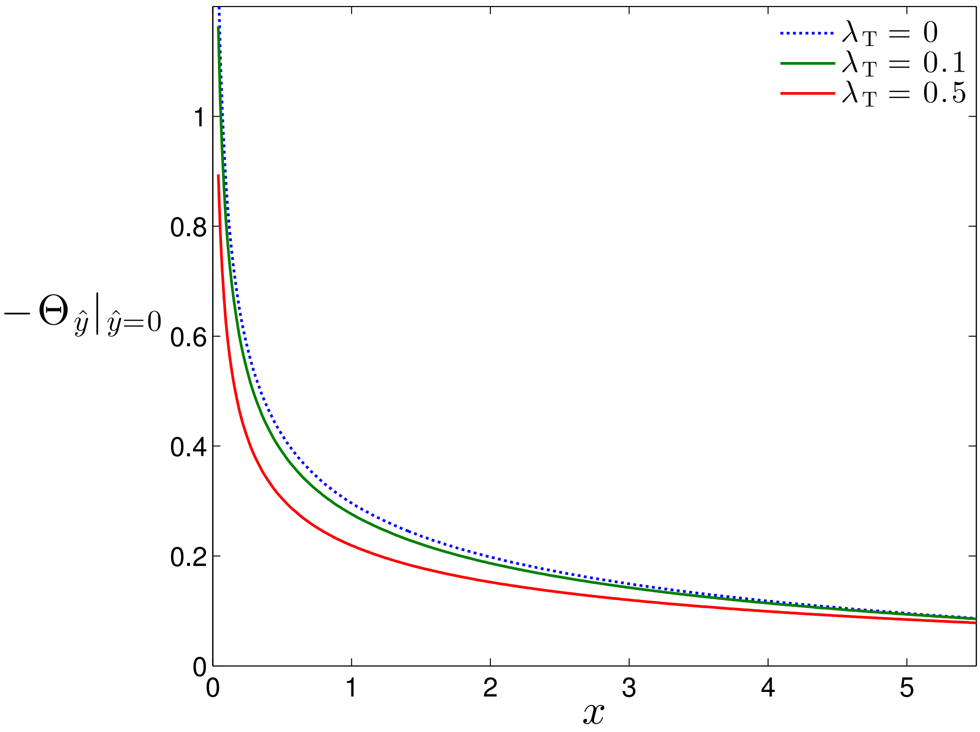

Figure 5.10: Variation of heat transfer with x for different values of λ_T while Pr=0.72, C=1, σ=−1.

study concludes with a presentation of surface plots for the horizontal component of velocity $\hat{u}$, the velocity function f_y, the the temperature function gradient Θ_η all given in Figure 5.13

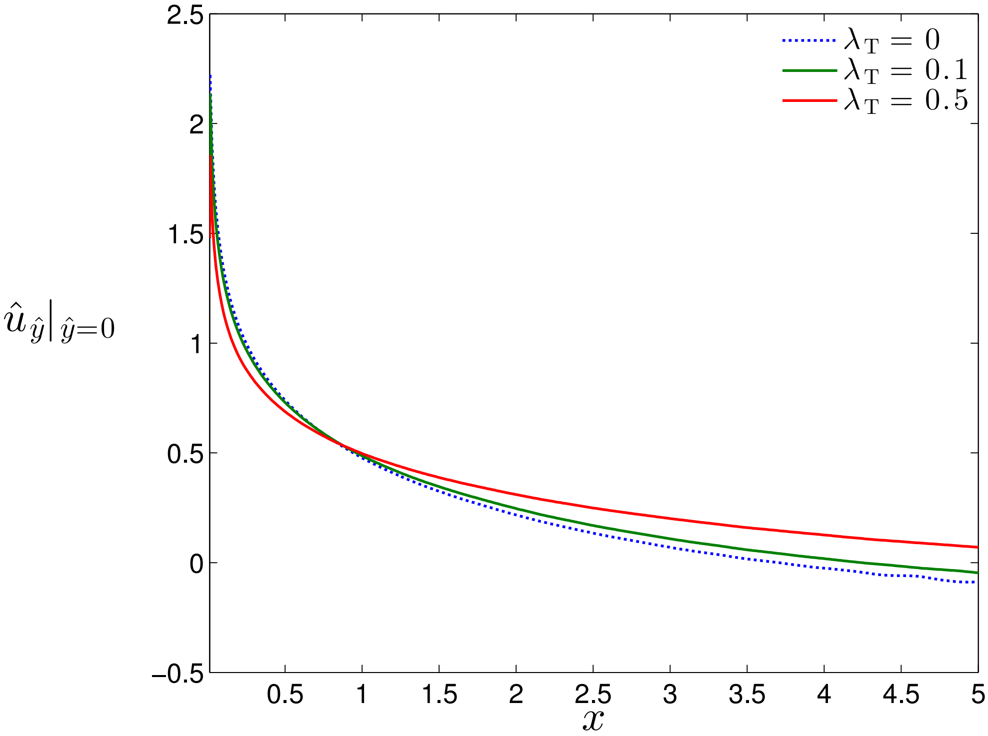

Figure 5.11: Variation of the skin friction with x for different values of λ_{T}, while Pr=0.72, C=1, σ=−1.

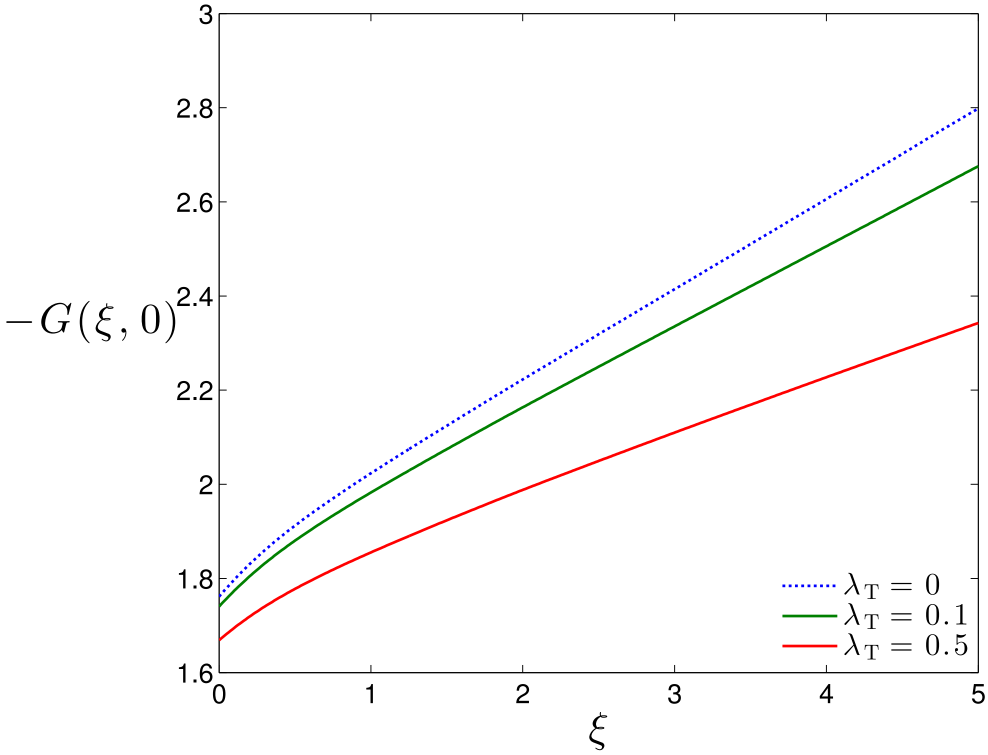

Figure 5.12: Variation of pressure function with ξ for different values of λ_{T} while Pr=0.72, C=1, σ=−1.

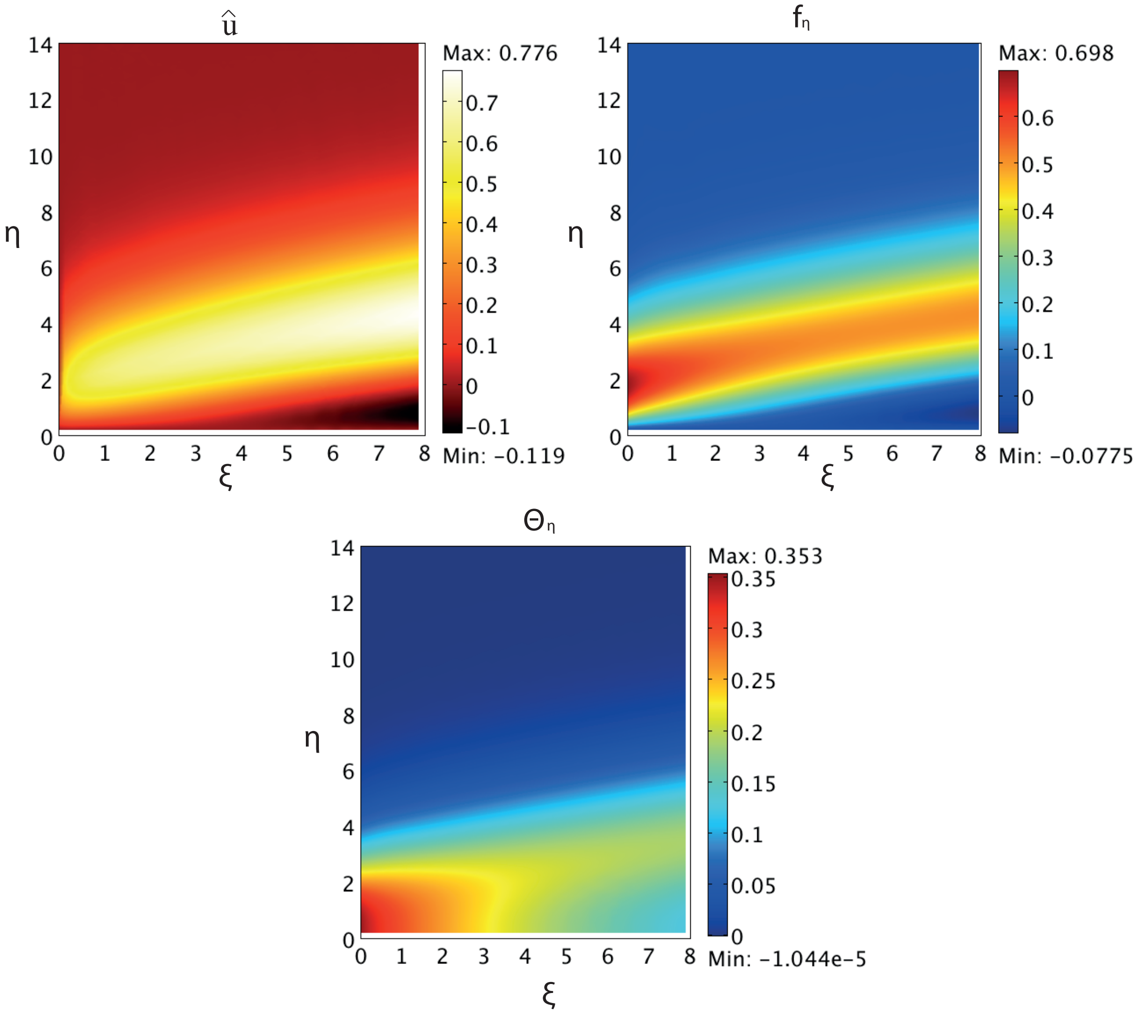

Figure 5.13: Surface plots while $\lambda_{\mathrm{T}} = 0$, Pr=0.72 and $\sigma = -1$, for the horizontal component of velocity $\hat{u}$, the velocity parameter function f_η and the temperature function gradient $-\Theta_\eta$.

5.3.2 Changing the Prandtl number

Turning attention to the effect of Prandtl number on the flow, extensive computations were carried out by varying the Prandtl number and obtaining the position of the separation point x_s under the Boussinesq approximation. A few computed positions are listed below in Table 5.2.

Pr	0.05	0.1	0.5	0.72	1	5	7	10
x_s	12.306	8.914	4.290	3.705	3.241	1.790	1.593	1.399

Table 5.2: Position of the separation point x_s, for different values of Prandtl number Pr while $\lambda_{\mathrm{T}} = 0$ and $\sigma = -1$.

The full range of the separation points obtained for different values of the Prandtl number is given in Figure 5.14, denoted with red circles. In addition, a curve-fitting to the data in a least-squares sense was performed (the blue dashed line in Figure 5.14). For the nonlinear fit, a function of the following form was chosen

$$x_s = A + B_1 e^{-C_1 \mathrm{Pr}} + B_2 e^{-C_2 \mathrm{Pr}}, \tag{5.33a}$$

where the values of the constants were computed as

$$A = 1.569, \quad B_1 = 3.873, \quad C_1 = 0.735, \quad B_2 = 11.784, \quad C_2 = 10.751. \tag{5.33b}$$

The effect that an increasing Prandtl number has on the flow parameters can be seen in in Figures 5.15, 5.16 and 5.17. At $\xi = 1$ where the flow remains attached for all cases the general trend expected from the similarity analysis are manifested, so that an increase in Pr results in a drop in the velocity, a thinning of the thermal layer and a drop in the pressure gradient. In Figure 5.15 the station $\xi = 2$, is past the separation points for $\mathrm{Pr} = 7, 10$ and flow reversal is evident, while there is a velocity drop as we move downstream. The profiles for the temperature function in Figure 5.16 at $\xi = 1$ show the expected behaviour of a thinner thermal layer, for larger values of Pr, which tend to thicken downstream. Interestingly at $\xi = 4$, i.e. far from the separation point for $\mathrm{Pr} = 7, 10$, the thermal boundary layer is now thicker from the one that the flow is still attached i.e ($\mathrm{Pr} = 1$). The pressure function is increasing downstream. Finally the plots for the skin friction and heat transfer rates for different values of Pr are given in Figures 5.18 and 5.19. It can be observed that the skin friction is decreasing with an increasing Pr number and concerning the heat transfer, an increase is observed with an increasing Pr.

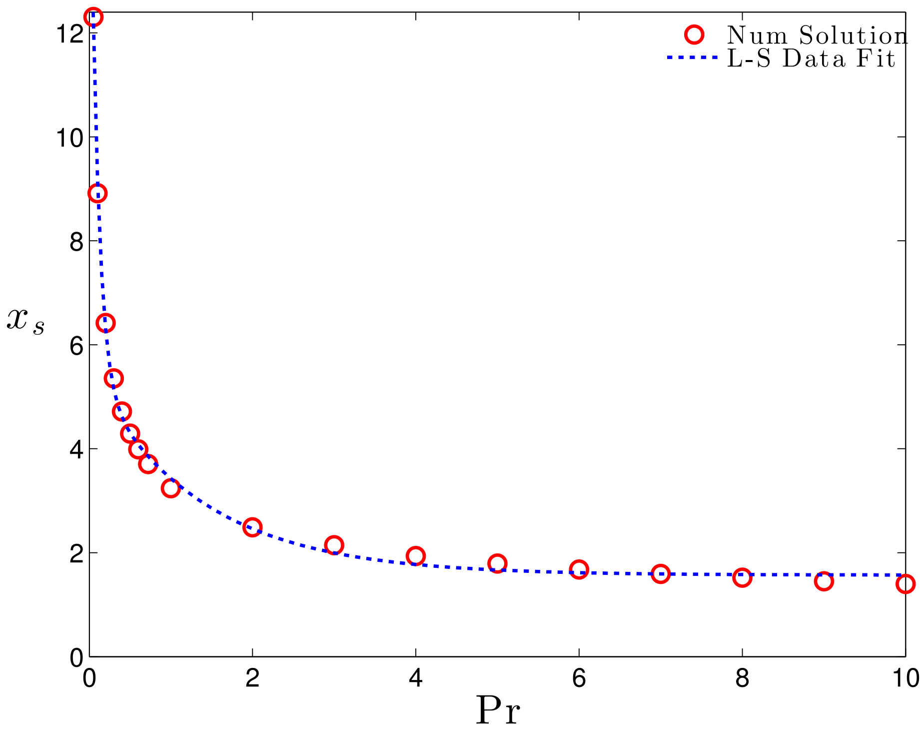

Figure 5.14: Separation point as a function of Prandtl number, while λ_T=0. Circles correspond to actual numerical solutions obtained by varying Prandtl number.

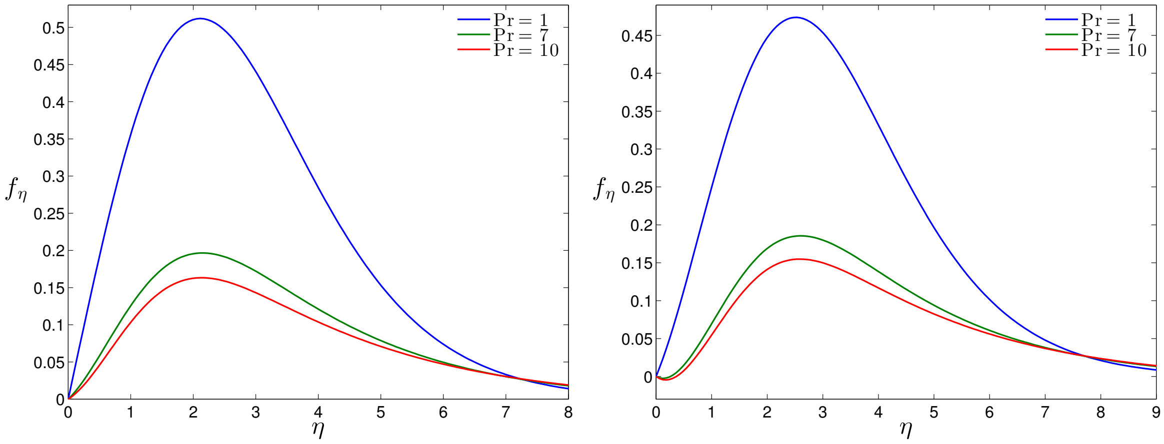

(a) $\xi = 1$ (b) $\xi = 2$

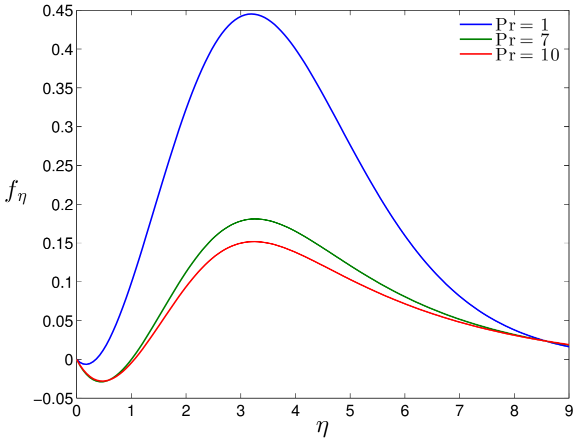

(c) $\xi = 4$

Figure 5.15: Velocity function profiles at different distances from the leading edge of the plate, for different values of λ_T. Computations were carried for $\Pr = 0.72$ and $\sigma = -1$.

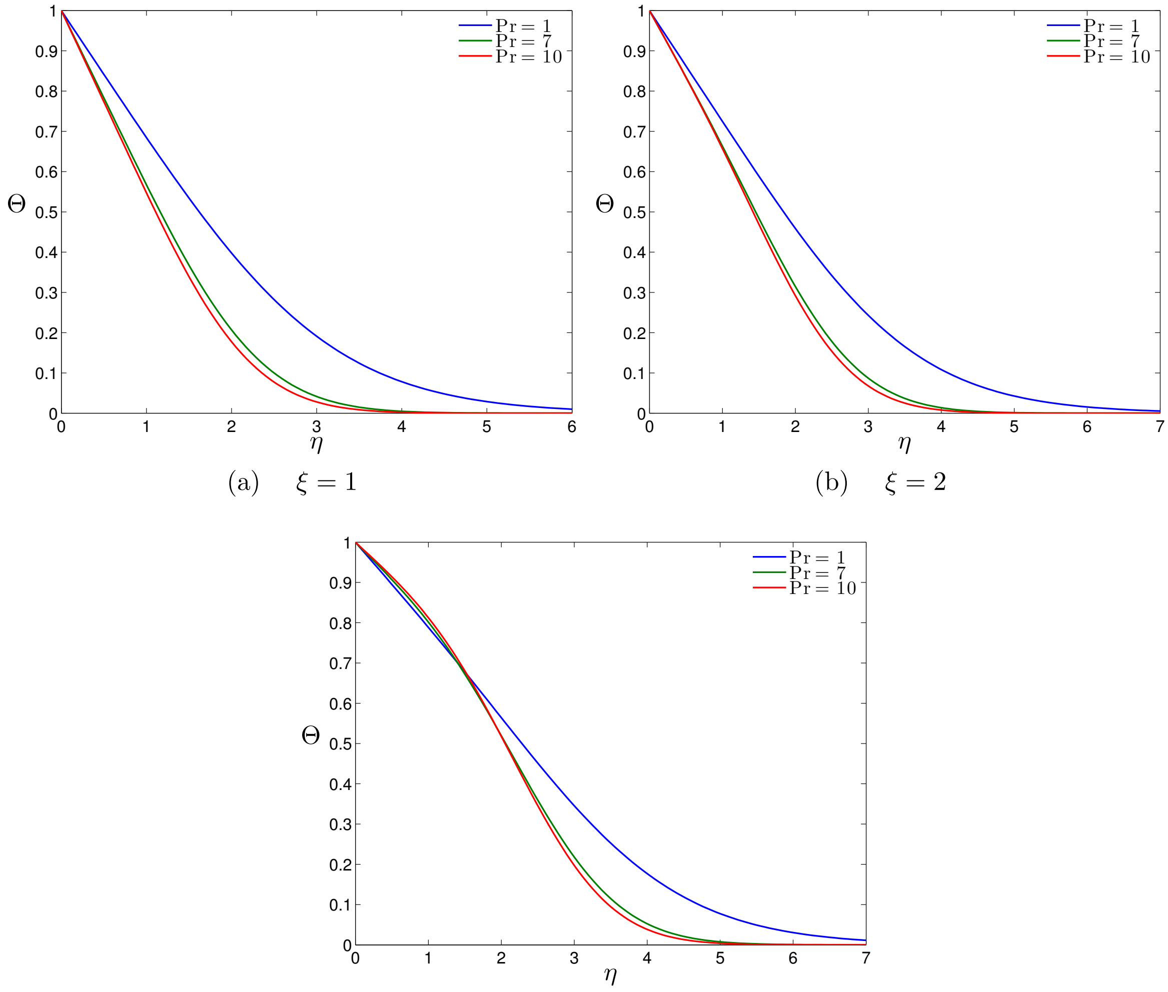

(a) $\xi = 1$

(b) $\xi = 2$

(c) $\xi = 4$

Figure 5.16: Temperature function profiles at different distances from the leading edge of the plate, for different values of Pr. Computations were carried for $\lambda_{\mathrm{T}} = 0$ and $\sigma = -1$.

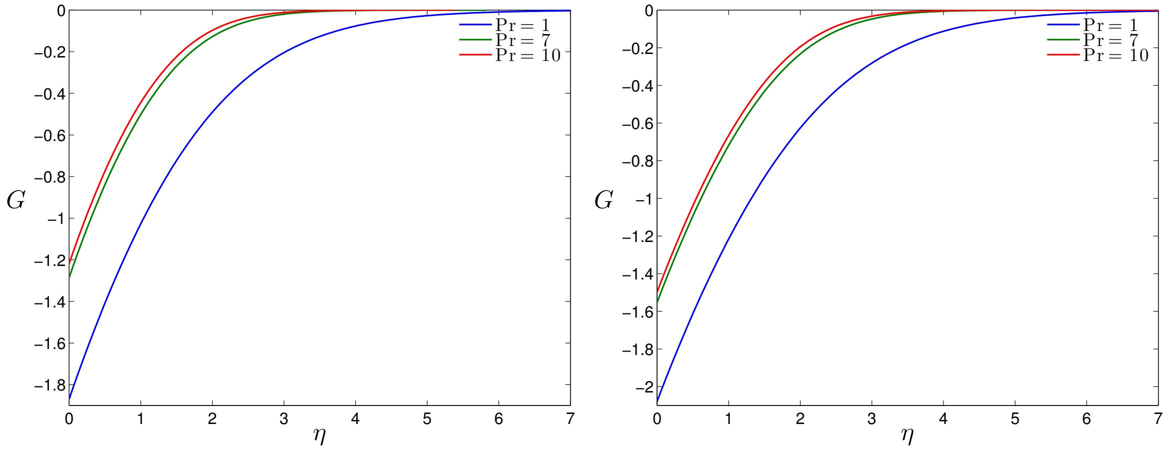

(a) $\xi = 1$ (b) $\xi = 2$

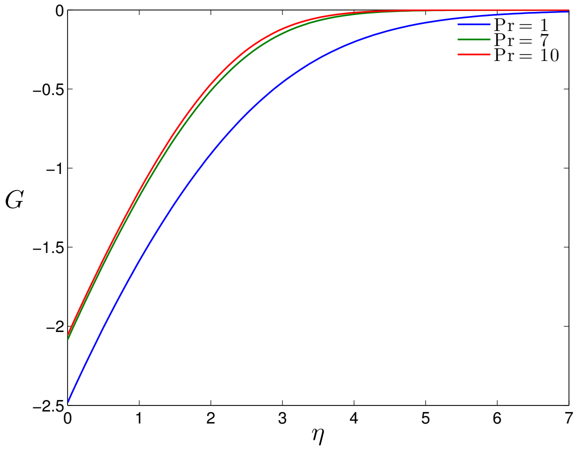

(c) $\xi = 4$

Figure 5.17: Pressure function profiles at different distances from the leading edge of the plate, for different values of Pr. Computations were carried for $\lambda_{\mathrm{T}} = 0$ and $\sigma = -1$

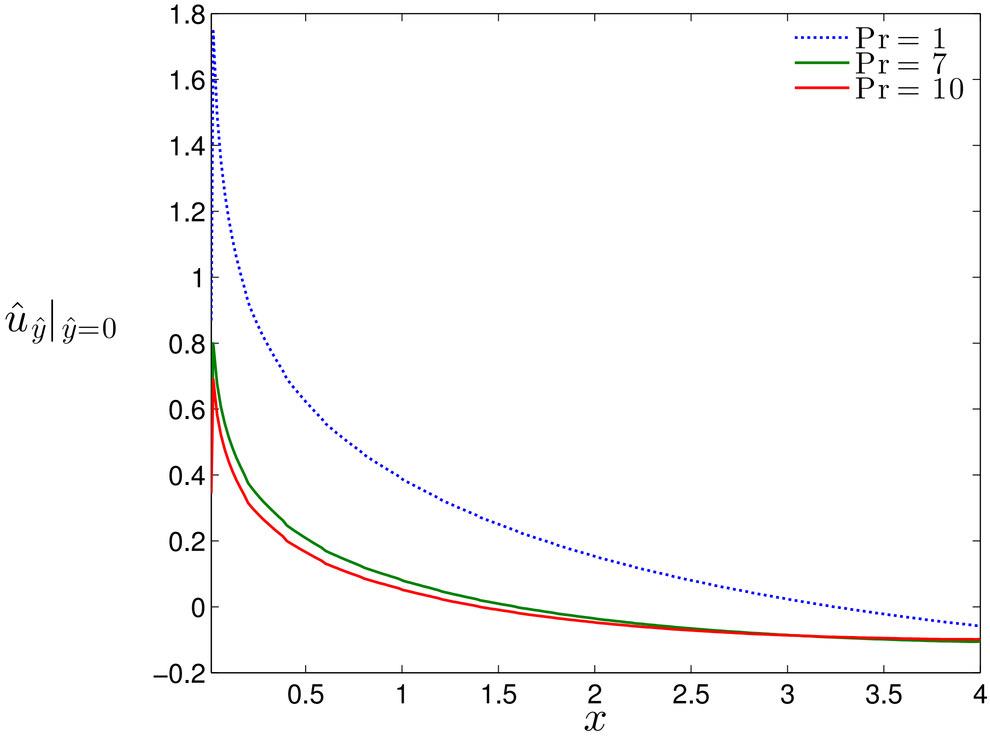

Figure 5.18: Variation of the skin friction with x for different values of Pr, while λ_{T}=0, C=1, σ=−1.

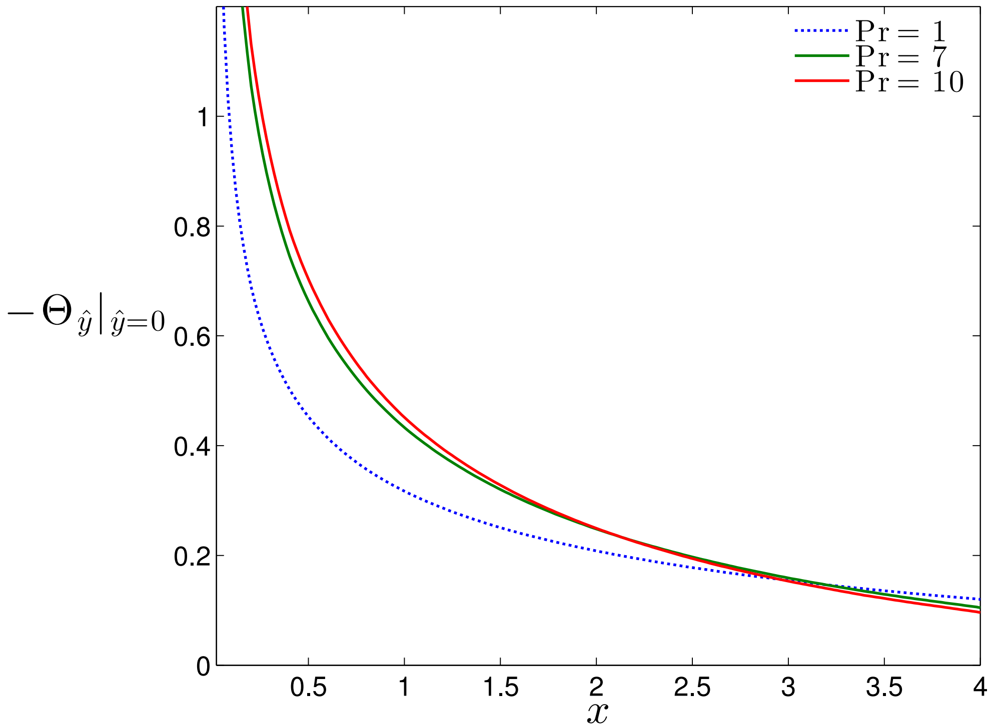

Figure 5.19: Variation of heat transfer function with x for different values of Pr, while λ_{T}=0, C=1, σ=−1.

5.3.3 Varying the inclination parameter σ

In this final part of the section dedicated to negative inclination ($\sigma < 0$) a brief investigation has been carried out related to the behaviour of the flow parameters with altering the inclination parameter σ. A decrease of σ implies larger negative inclination whereas an increase in the value of σ indicates a reduction in the angle of inclination. A reduction of the angle of negative inclination means that the plate is moving towards being horizontal, thus it should be expected that the separation point is moved downstream. The opposite result should be demonstrated when the negative inclination is increased.

In the analysis that follows, the Prandtl number is set to $\mathrm{Pr} = 0.72$ while $\lambda_{\mathrm{T}} = 0$ and the parameter of inclination varies as $\sigma = -1.2, -1.1, -1, -0.9, -0.8$. Table 7.1 presents the separation points for these values of σ. A decrease in the inclination parameter and therefore a larger negative inclination results in the separation point moving closer to the leading edge. The opposite effect is shown when the angle of inclination parameter is increased.

σ	-1.2	-1.1	-1	- 0.9	-0.8
x_s	2.722	3.155	3.705	4.400	5.353

Table 5.3: Position of the separation point x_s, for different values of σ while $\lambda_{\mathrm{T}} = 0$ and $\mathrm{Pr} = 0.72$.

In what concerns the flow parameters shown in Figure 5.20, the effect of varying inclination on the velocity function is presented. Clearly smaller negative inclination results in higher velocities since weaker buoyant forces oppose the flow. Profiles shown at $\xi = 4$, indicate that flow reversal is present for $\sigma = -1, -1.2$, being stronger for larger inclination. For the case where $\sigma = -0.8$ the flow is still attached. Focusing on the temperature function, in Figure 5.21, profiles at $\xi = 1$ indicate a thinning of the thermal layer with decreasing the inclination but the effects are not as strong as the ones observed for the velocity function. As the separation point is being approached the differences are magnified. The section concludes with a presentation of the variation of the heat transfer and skin friction with x given in Figure 5.23. Higher heat transfer rates are shown for smaller negative inclination.

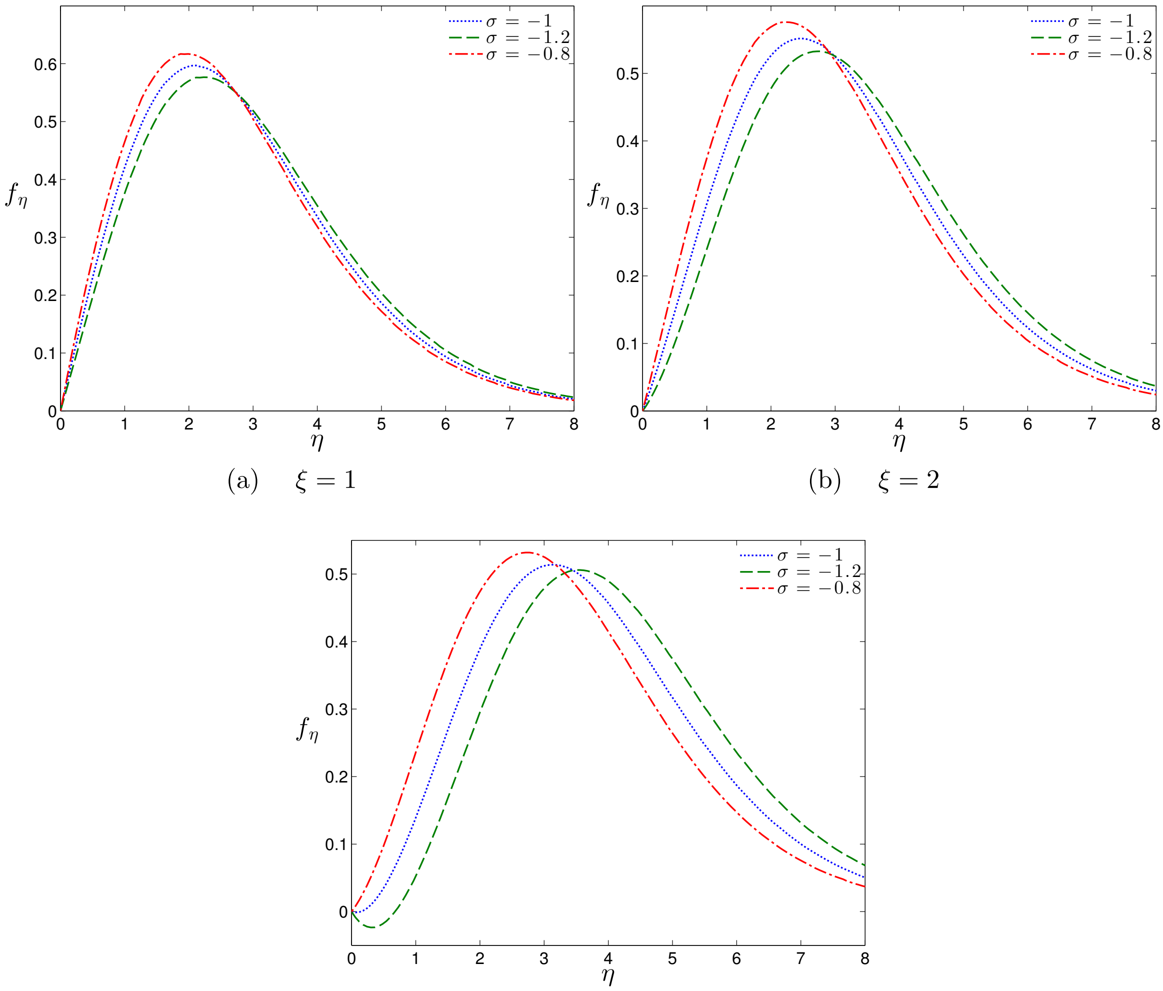

(a) $\xi = 1$

(b) $\xi = 2$

(c) $\xi = 4$

Figure 5.20: Velocity function profiles at different distances from the leading edge of the plate, for different values of σ. Computations were carried for $\mathrm{Pr} = 0.72$ and $\lambda_\mathrm{T} = 0$.

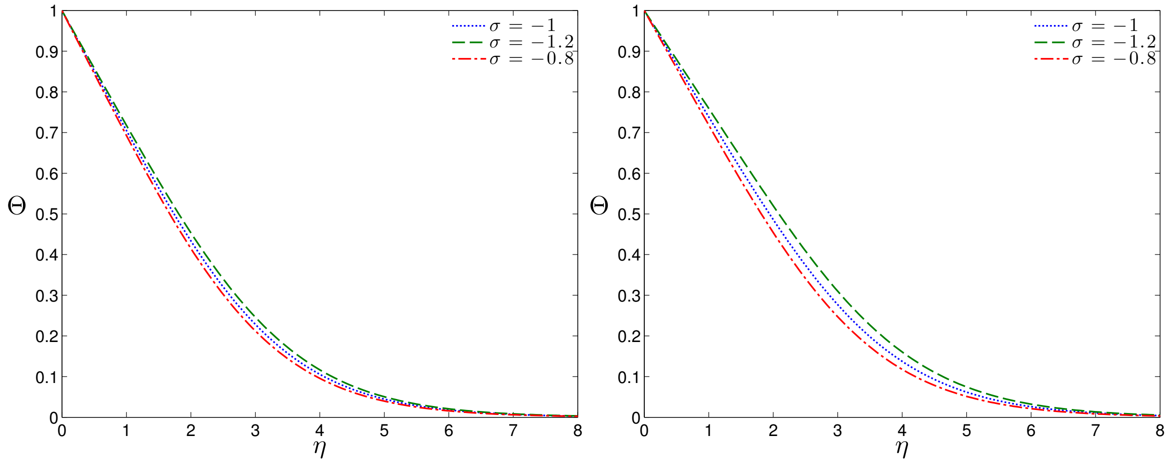

(a) $\xi = 1$ (b) $\xi = 2$

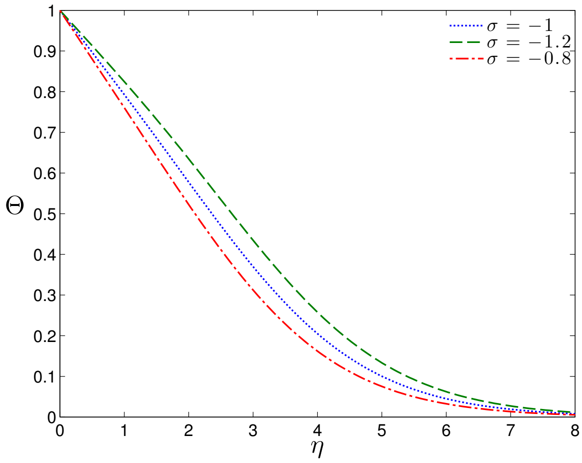

(c) $\xi = 4$

Figure 5.21: Temperature function profiles at different distances from the leading edge of the plate, for different values of σ. Computations were carried for $\lambda_{\mathrm{T}} = 0$ and $\mathrm{Pr} = 0.72$.

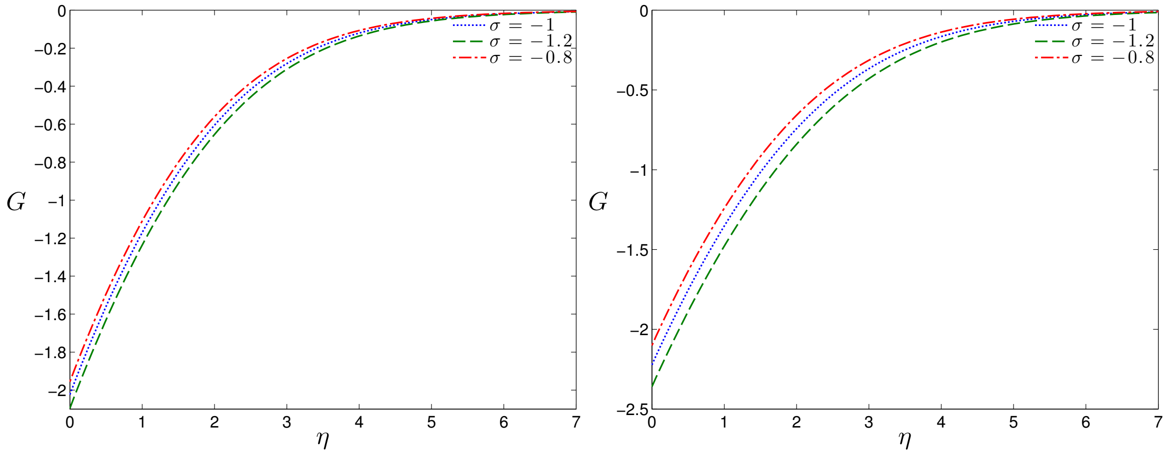

(a) $\xi = 1$ (b) $\xi = 2$

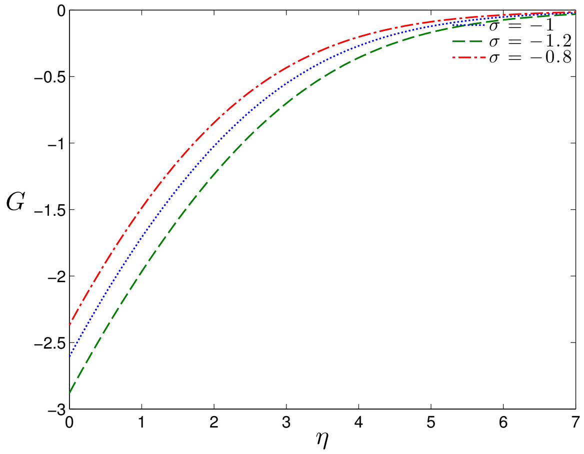

(c) $\xi = 4$

Figure 5.22: Pressure function profiles at different distances from the leading edge of the plate, for different values of σ. Computations were carried for $\lambda_{\mathrm{T}} = 0$ and $\mathrm{Pr} = 0.72$

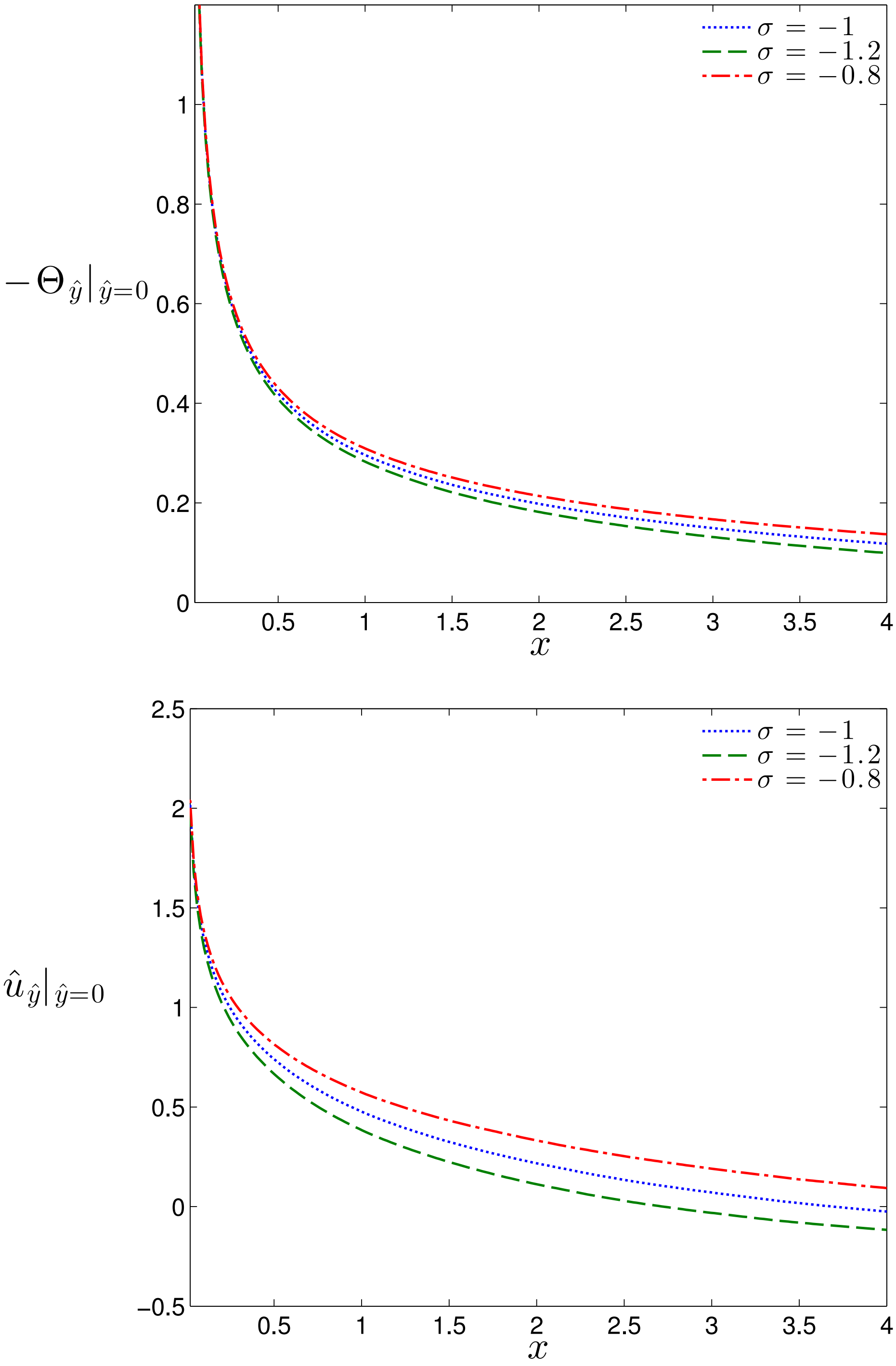

Figure 5.23: Variation of heat transfer and skin friction for different values of the inclination parameter σ.

5.4 Positive inclination

This section is devoted to a discussion on the effects of positive inclination $\sigma > 0$ on the flow. When the inclination to horizontal is positive, then buoyancy forces sustain the flow rather than opposing it (Figure 5.1). It is therefore expected that the flow will be accelerating along the semi-infinite plate. Jones [38] in his analysis showed that, since at large distances from the leading edge of the plate the flow is primarily influenced by the buoyancy force component parallel to it, eventually it should be described by the classic free convection solution up a vertical flat heated plate. For that he went on to divide the flow field into two regions, with the first region being valid in the neighbourhood of the leading edge ($\xi = \mathcal{O}(1)$), while the second is valid for larger values of ξ and as $\xi \to \infty$. For the region next to the leading edge, the nonsimilarity boundary layer equations derived from the transformations (5.16) and (5.17) are valid. For the region far from the leading edge, the similarity transformations for the boundary layer equations are the ones for a heated vertical plate which in our case should be given as

$$\xi = x, \quad \eta = (Cx)^{-1/4} \int_0^{\hat{y}} \rho d\tilde{y},$$

$$\Psi(x, \hat{y}) = (Cx)^{3/4} f(\xi,\, \eta),\ \hat{\Pi}(x, \hat{y}) = (Cx)^{1/4} G(\xi,\, \eta) \text{ and } \theta(x, \hat{y}) = \Theta(\xi,\, \eta) \qquad (5.34)$$

where C is the Chapman variable. Application of the above transformations into the boundary layer results in a different set of PIDEs which is valid in the far field. Numerically Jones tackled the problem by solving the standard equations from $\xi = 0 \to 1$, while at $\xi = 1$ a changeover of the equations takes place and the numerical process was continued downstream. Computations terminated once there is a close agreement between the skin friction and the heat transfer at the plate, obtained by the numerical solution of the PDEs and the asymptotic series solution valid far from the leading edge of the plate.

A different approach is based on the work of Hunt and Wilks [34]. By providing a continuous set of transformation in the variable x, which takes into account both similarity regimes, the switch between two different set of equations becomes unnecessary and the problem can be tackled numerically by integrating just one set of equations valid in the neighbourhood of the leading edge and far downstream. A detailed presentation is given in the textbook of Pop and Ingham [69], where the following continuous transformations are used (here altered to include variable density)

$$\xi = x \text{ and } \eta = (Cx)^{-2/5}(1+Cx)^{3/20}\int_0^{\hat{y}} \rho d\tilde{y}.$$

$$\Psi(x,\hat{y}) = (Cx)^{3/5} f(\xi,\,\eta)(1+Cx)^{3/20}, \quad \hat{\Pi}(x,\hat{y}) = (Cx)^{2/5}(1+Cx)^{-3/2} G(\xi,\,\eta)$$
$$\text{and} \quad \theta(x,\hat{y}) = \Theta(\xi,\,\eta). \tag{5.35}$$

By considering the simplified, Boussinesq similarity transformation for the independent variable i.e. $\eta = x^{-2/5}(1+x)^{3/20}\hat{y}$, a truncated power series in x as $x \to 0$ and $x \to \infty$ for the term $x^{-2/5}(1+x)^{3/20}$ result in

$$\begin{aligned} &x^{-2/5} + \frac{3}{20}x^{3/5} - \frac{51}{800}x^{8/5} + \mathcal{O}\left(x^{13/5}\right) \quad \text{as} \quad x \to 0 \\ &x^{-1/4} + \frac{3}{20}x^{-5/4} - \frac{51}{800}x^{-9/4} + \mathcal{O}\left(x^{-13/4}\right) \quad \text{as} \quad x \to \infty. \end{aligned} \tag{5.36}$$

It is clear that to leading order, the Boussinesq similarity transformations for the independent variable are obtained, i.e $\eta = x^{-2/5}\hat{y}$ and $\eta = x^{-1/4}\hat{y}$, each one valid in the two distinguished similarity regimes. Similarly the same principle applies to the dependent variable transformations.

Application of the above continuous transformations into the boundary layer equations results in a new set of equations as given in [69], valid in both regimes. Interestingly [69] go on using the nonsimilarity equations resulting from the above continuous transformations and consider negative inclination, in particular $\sigma = -1$. Under the Boussinesq approximation a parametric study is performed where the parameter is the Prandtl number and the position of the separation point x_s is recovered. The results [69] show an agreement with the results presented earlier to one decimal digit for Pr=10, 5 , 2, 1, and 0.5. Though results presented for Pr = 0.3 and Pr = 0.1 deviate significantly especially for the latter case. Analytically they obtain $x_s = 5.263$ for Pr = 0.3 and $x_s = 7.671$ for Pr = 0.1. Instead our computations result in $x_s = 5.352$ and $x_s = 8.914$, respectively. Clearly as Pr is decreasing and the position of the separation point is moving further downstream, results obtained from nonsimilarity equations derived by continuous transformations and the ones based on the neighbourhood of the leading edge regime will deviate significantly. Jones in his analysis, when considering negative inclination, forced no changeover in the equations since the boundary layer separates from the plate and does not approach a similarity form as

$x \to \infty$. Furthermore, as shown earlier, the truncated series usage of continuous transformations imply that as x is increasing, the classic free convection scales dominate over the indirect ones. Therefore the need to march further downstream numerically in order to obtain the separation point due to the decreased value of Prandtl number results in stronger effects of classic free convection, which subsequently influence the solution; hence the deviation. We thus believe that for the case of negative inclination the similarity transformations used i.e (5.16) and (5.17) are appropriate, and the positions of separation points obtained for different Prandtl numbers should be trustworthy.

In our analysis no attempt is made in obtaining the classic free convection solution far from the leading edge. Instead the focus lies in the region close to the leading edge, where the transformations (5.16) and (5.17) are valid. For that region, variable property and inclination effects are studied, while the section concludes with an investigation concerning the strength of the induced pressure gradient term $\partial\hat{\Pi}/\partial x$, responsible for the indirect drive of the motion when compared with the tangential component of the buoyancy force (i.e direct drive).

5.4.1 Effect of λ_{T} on the flow

Once more, computations were carried out in COMSOL Multiphysics 3.5a using the General PDE Mode, while the results presented here were obtained using a rectangular domain D_{+}, of size $[0, 10] \times [0, 15]$. No difficulties arose when the width of the domain was increased. Actually a numerical solution was obtained for a domain having width of 200. Computations were performed for values of λ_{T} varying as $\lambda_{\mathrm{T}} = 0, 0.1, 0.2, \ldots, 2$, along with the parameters $\mathrm{Pr} = 0.72$ and $\sigma = 1$.

Results presented are based on the the same assigned values to the variable property parameter λ_{T}, as the ones used when the inclination was negative i.e.($\lambda_{\mathrm{T}} = 0, 0.1, 0.5$). Concentrating in the neighbourhood of the leading edge, profiles for velocity, temperature and pressure function are given at $\xi = 0.1$ $\xi = 0.5$ and $\xi = 1$. It can be observed in Figure 5.24 that an increase of λ_{T} results in an increase in velocity, while the velocity is increasing as we move away from the leading edge. Furthermore by revisiting Figure 5.7, it can be observed that at $\xi = 1$, variable property effects on velocity are weaker when the inclination is positive.

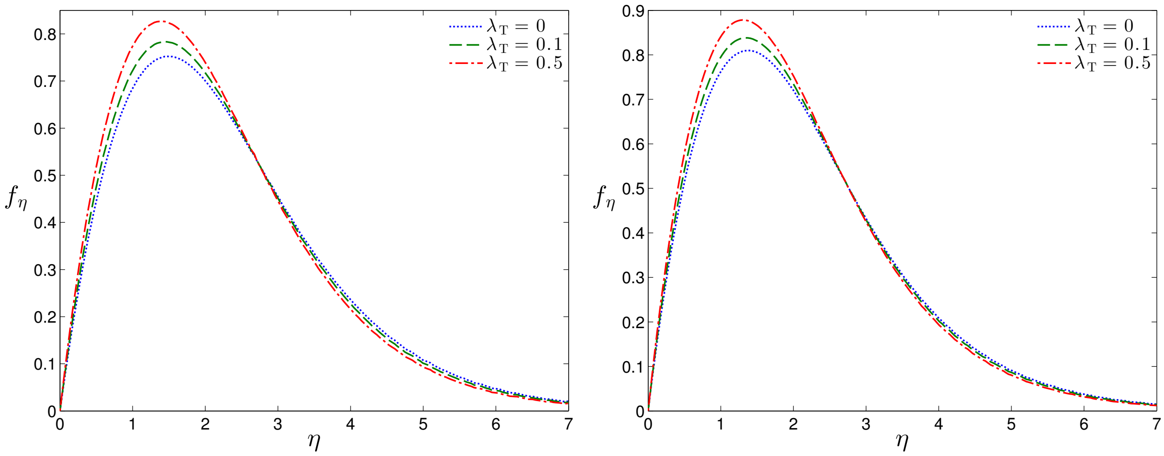

(a) $\xi = 0.1$ (b) $\xi = 0.5$

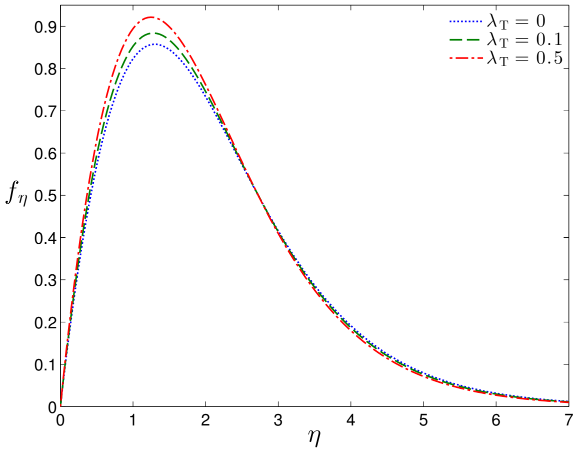

(c) $\xi = 1$

Figure 5.24: Velocity function profiles at different distances from the leading edge of the plate, for different values of λ_{T}. Computations were carried for $\mathrm{Pr} = 0.72$ and $\sigma = 1$.

Reflecting on the effects that an increase of λ_T has on the thermal layer, Figure 5.25 indicates a perturbation effect resulting in a slightly thinner thermal layer with an increasing λ_T. The thermal layer is thinning as the leading edge is left behind while effects of variable property almost diminish at $\xi = 1$. Once more variable property effects are weaker when the inclination is positive (see Figure 5.8). Finally in what concerns the pressure function, curves in Figure 5.26 indicate that the negative pressure is decreasing with an increasing λ_T, while the negative pressure is decreasing further downstream. Again at $\xi = 1$, a comparison with Figure 5.9 indicates that variable property effects are weaker when the inclination is positive.

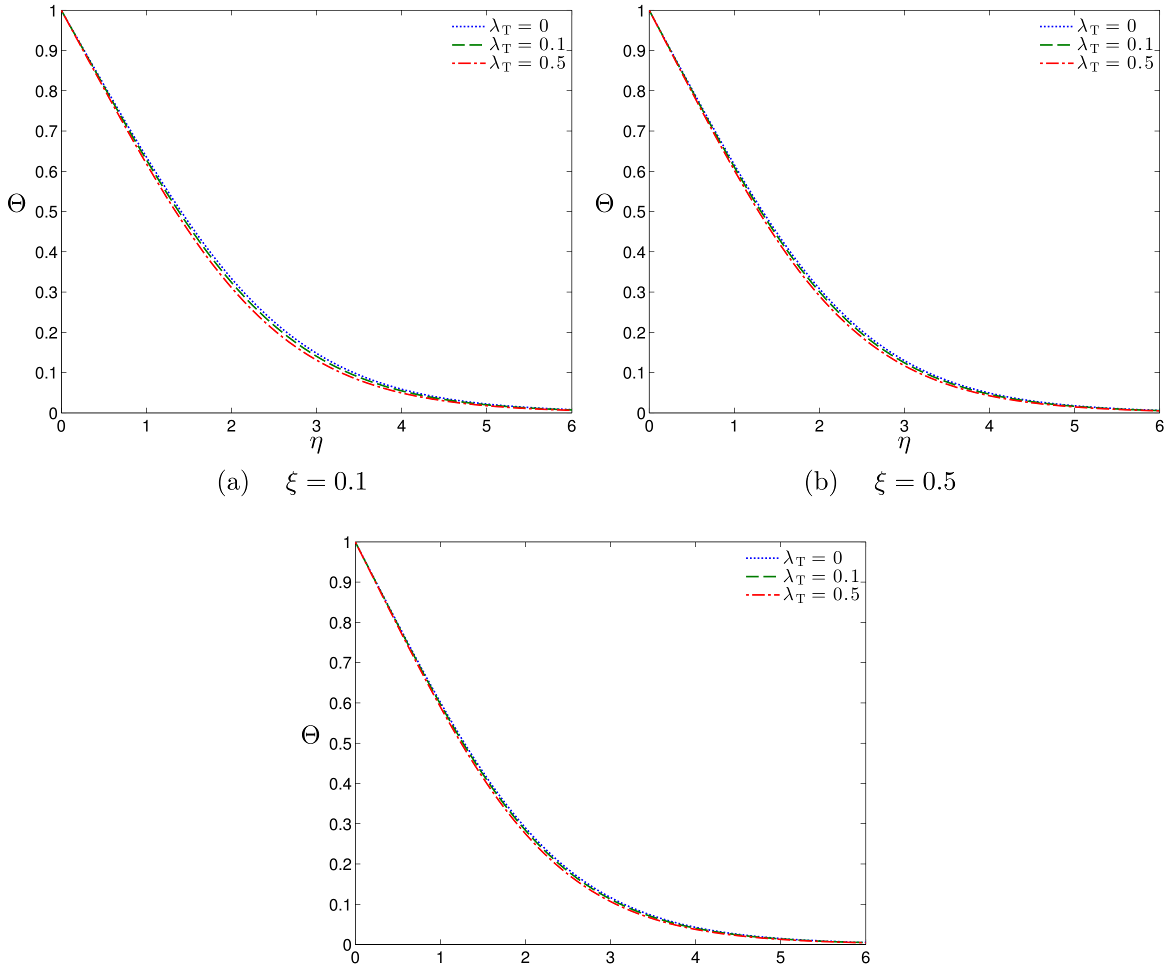

(a) $\xi = 0.1$

(b) $\xi = 0.5$

(c) $\xi = 1$

Figure 5.25: Temperature function profiles at different distances from the leading edge of the plate for different values of λ_T. Computations were carried for Pr = 0.72 and $\sigma = 1$.

Turning attention to heat transfer and skin friction at the plate it is observed that variable property effects are more notable. Figure 5.27 indicates that when the

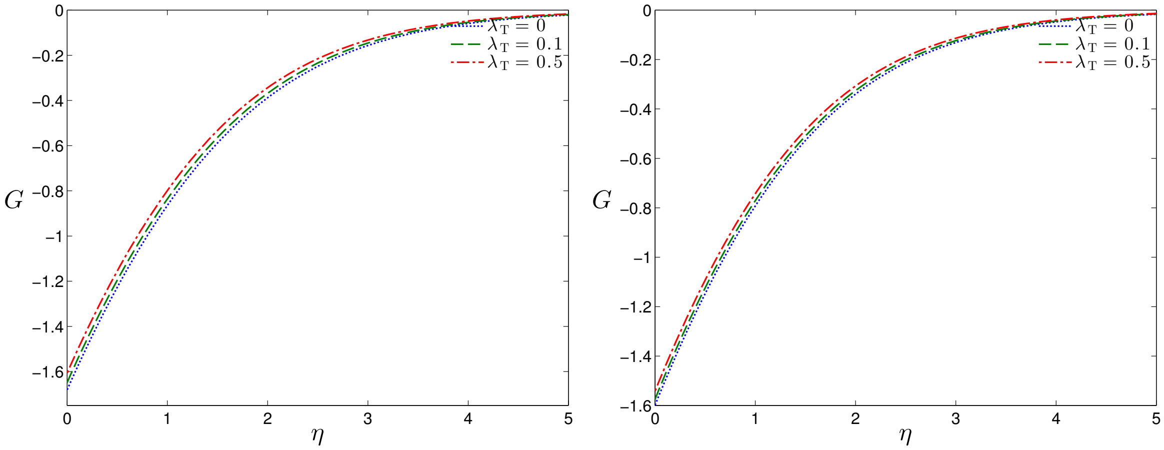

(a) $\xi = 0.1$ (b) $\xi = 0.5$

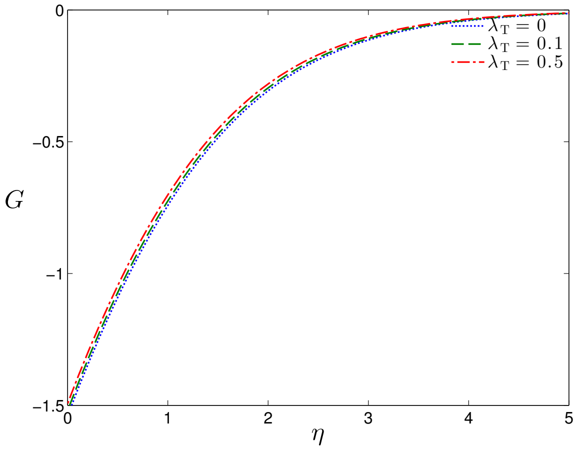

(c) $\xi = 1$

Figure 5.26: Pressure function profiles at different distances from the leading edge of the plate, for different values of λ_{T}. Computations were carried for $\mathrm{Pr} = 0.72$ and $\sigma = 1$.

Boussinesq approximation is adopted, higher heat transfer rates and skin friction are observed. So that an increase in λ_{T}, results in a reduced heat transfer rate and lower skin friction.

Concluding, it is found that when the inclination is positive, variable property effects are shown to have a weaker effect on flow properties especially on the pressure and temperature functions. Only the velocity function seems to be altered significantly, even so to a lesser degree than was observed when the inclination was set to negative. Skin friction and heat transfer rates are shown to be affected significantly. Moving downstream, in contrary to negative inclination, and as expected, the increasing velocity is accompanied by a thinning of the thermal layer and a reduced negative pressure.

5.4.2 Changing the inclination parameter σ

In this section the inclination effects are considered. In a similar fashion, the inclination parameter varies as $\sigma = 1.2, 1, 0.8$, with a reduced value of σ implying that the plate tends to the horizontal, while for the computations, Prandtl number and the variable property parameter are set to $\mathrm{Pr} = 0.72$ and $\lambda_{\mathrm{T}} = 0$ respectively. Computations show that for the particular cases of the inclination parameter stated above, changes reflected on the temperature and pressure functions were insignificant even though velocity did show some alteration, which is in contrast to when the inclination was negative. It must be pointed out though that the heat transfer rates and skin friction show a noteworthy deviation. For that reason a further variation on the inclination parameter was considered necessary for presentation purposes. Therefore results presented for velocity temperature and pressure function are based on the values $\sigma = 0.5, 1, 1.5$. Starting with the velocity function in Figure 5.28, as is expected an increased inclination results in higher velocities with a downstream accelerating flow, while the growth in the curves indicates that the larger the inclination the higher is the acceleration. Regarding the temperature function profiles, inclination seems to have a milder effect, while the higher the inclination the thinner the thermal layer is. Furthermore departures from the leading edge result in a thinning of the thermal layer as seen in Figure 5.29. Finally the pressure function profiles given in Figure 5.30, indicate that the pressure function, in a similar manner to the temperature, seems to

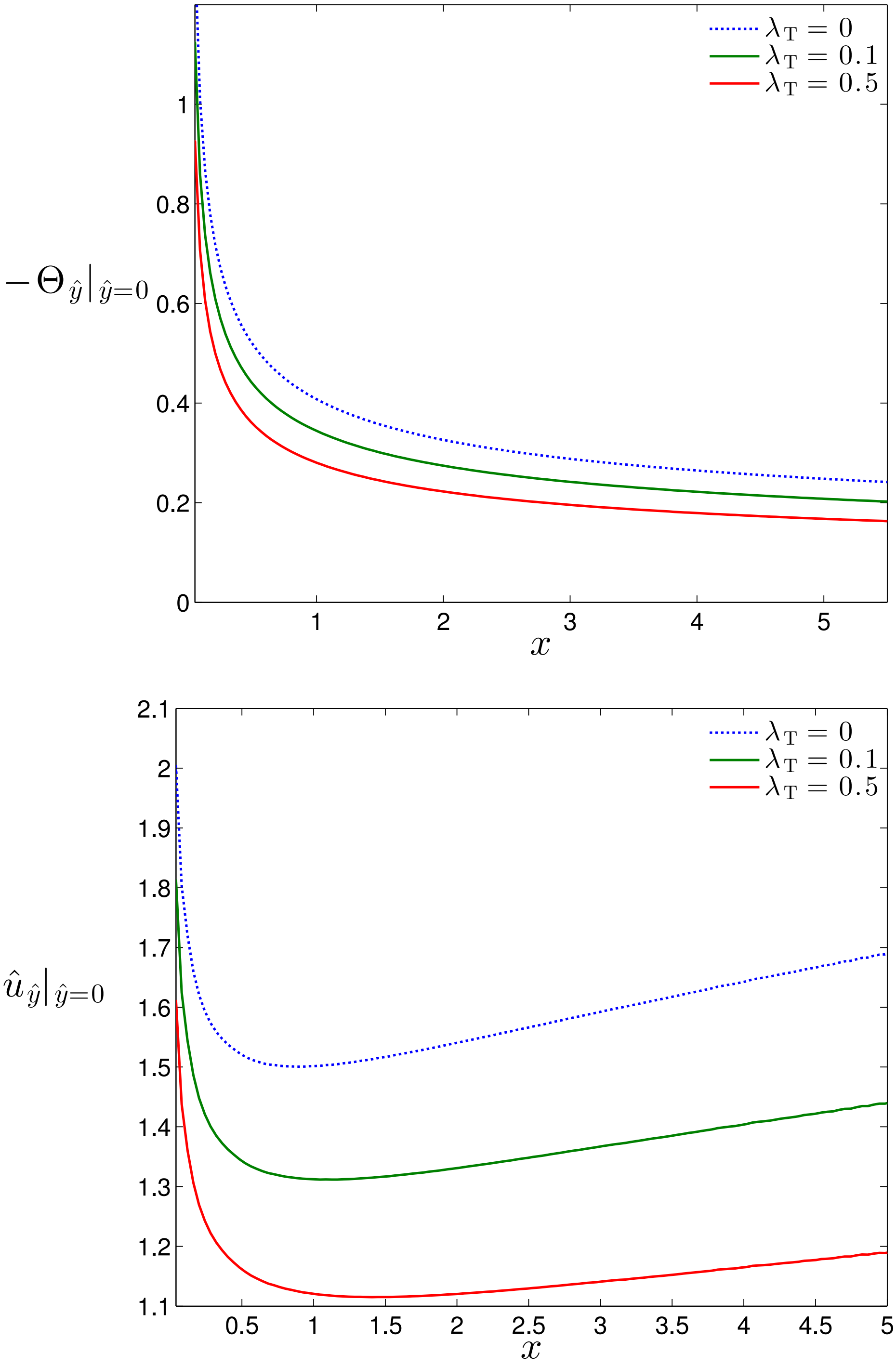

Figure 5.27: Variation of heat transfer and skin friction for different values of λ_{T}.

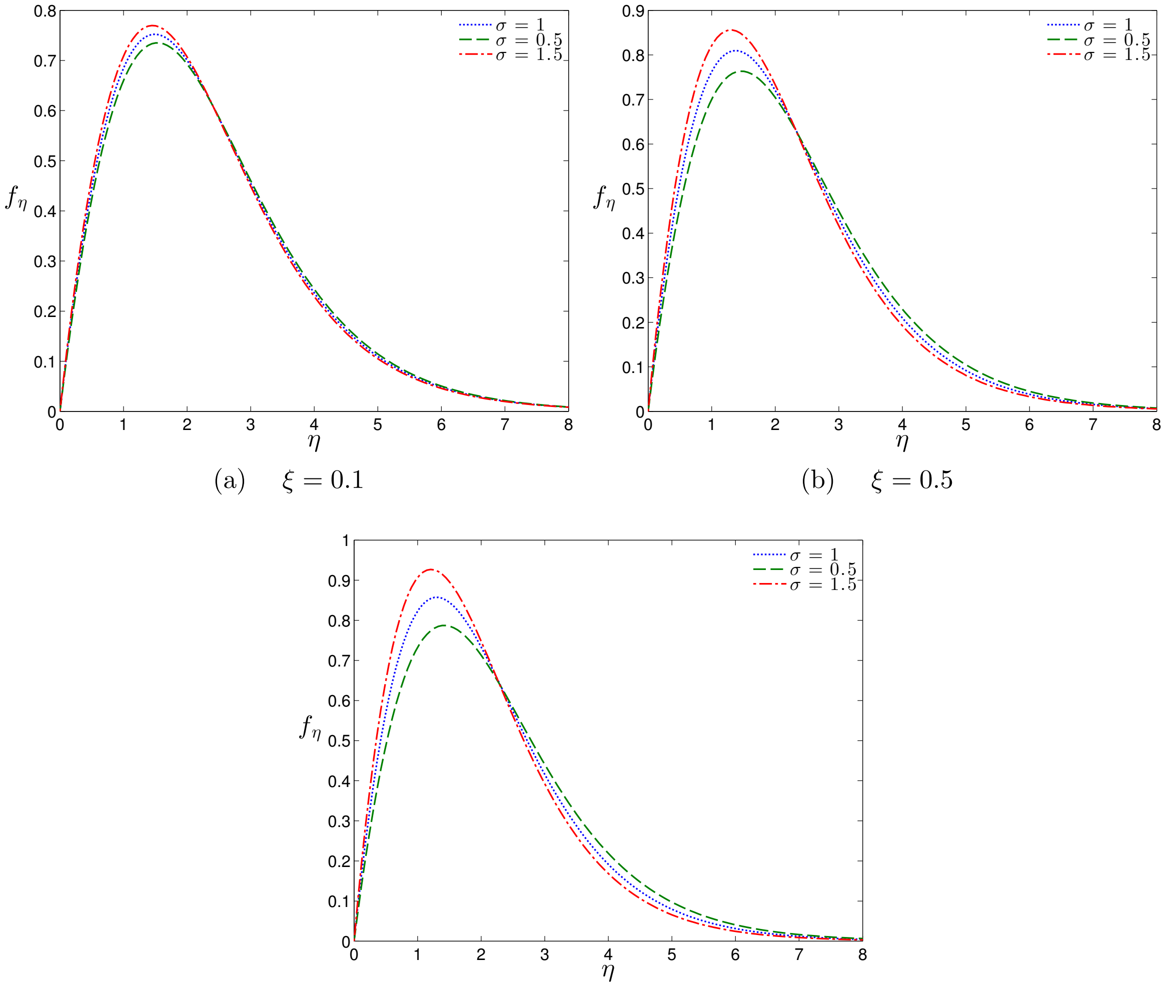

(a) $\xi = 0.1$

(b) $\xi = 0.5$

(c) $\xi = 1$

Figure 5.28: Velocity function profiles at different distances from the leading edge of the plate, for different values of σ. Computations were carried for $\mathrm{Pr} = 0.72$ and $\lambda_{\mathrm{T}} = 0$.

be almost unmoved by the inclination effects especially near the leading edge. The higher the inclination parameter is the smaller the negative pressure function is. The magnitude of the pressure function is decreasing downstream as the thermal layer is thinning and the velocity is increasing.

As mentioned earlier, even though relatively small deviations in the inclination parameter from $\sigma = 1$ disturb the flow field parameters fairly weakly, the skin friction and the heat transfer demonstrate a more notable variation. The section concludes with a presentation of this variation, for different values of σ, given in Figure 5.31. As can be observed, higher heat transfer rates are obtained at greater inclination, a behaviour that is also exhibited for the skin friction.

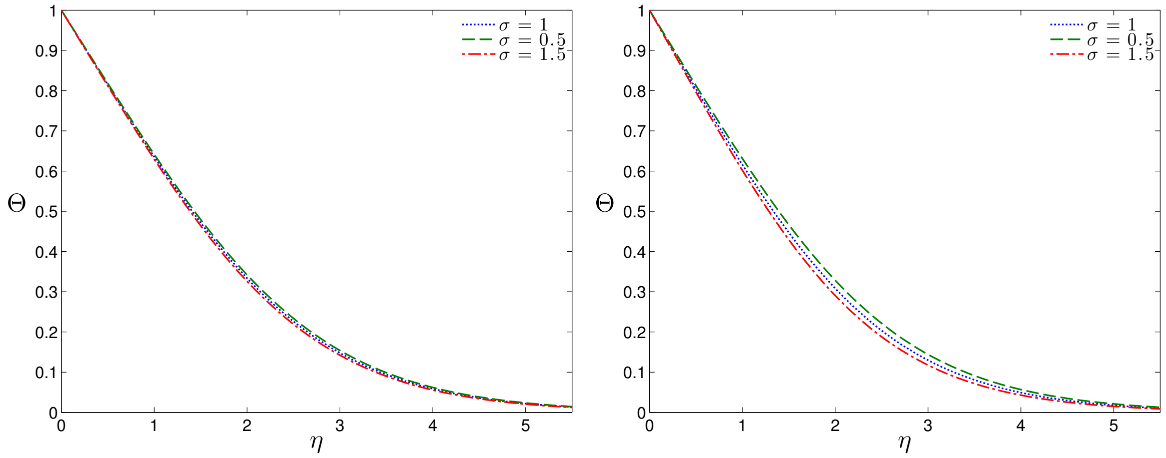

(a) $\xi = 0.1$ (b) $\xi = 0.5$

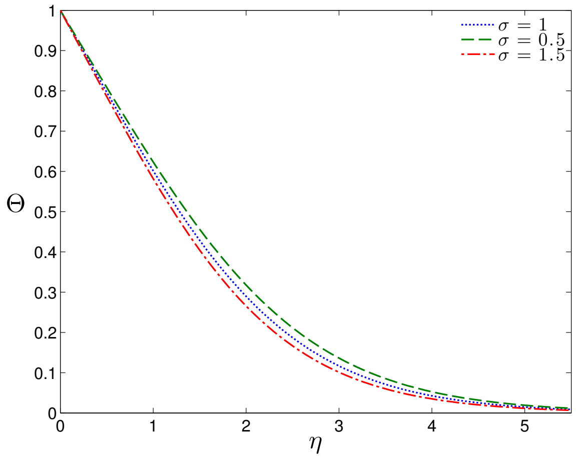

(c) $\xi = 1$

Figure 5.29: Temperature function profiles at different distances from the leading edge of the plate, for different values of σ. Computations were carried for $\lambda_{\mathrm{T}} = 0$ and $\mathrm{Pr} = 0.72$.

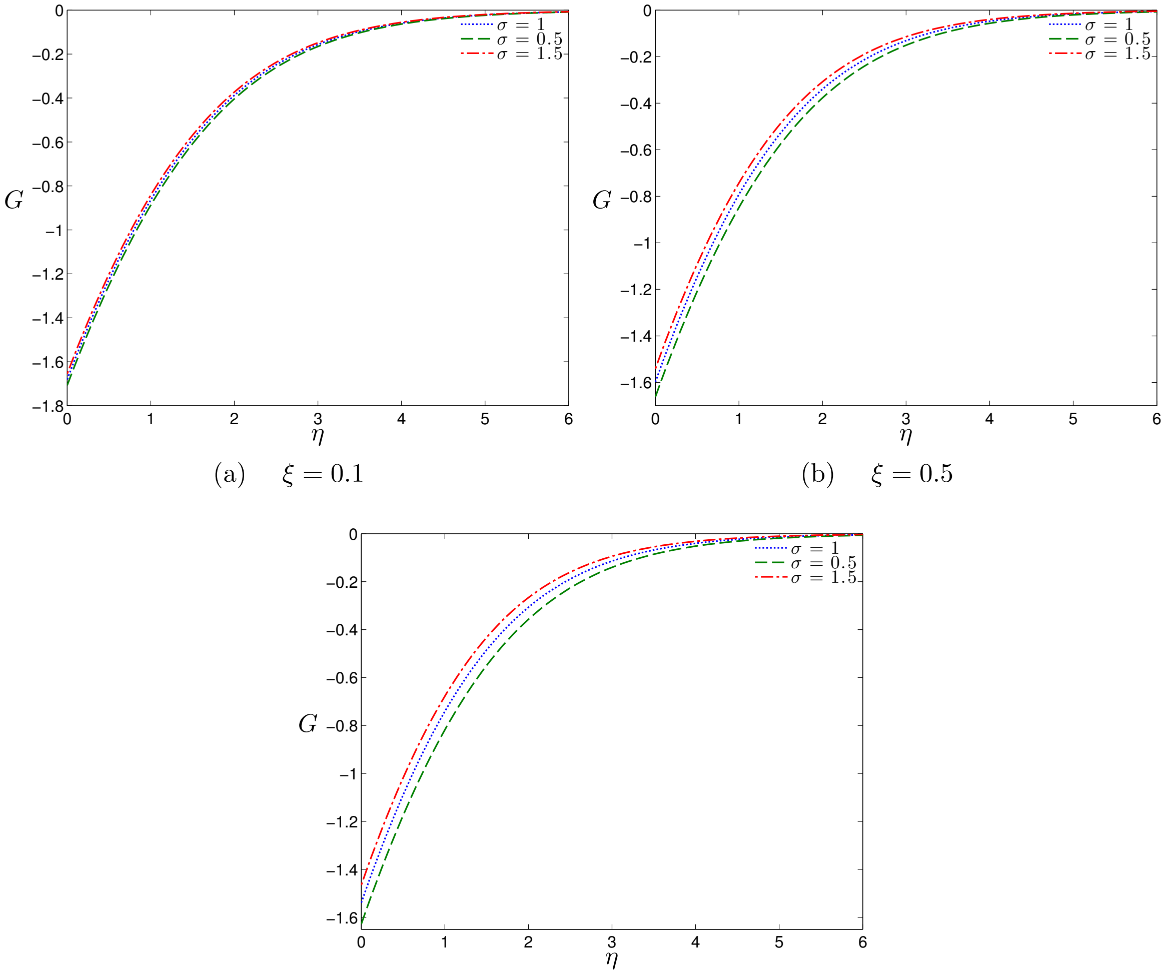

(a) $\xi = 0.1$

(b) $\xi = 0.5$

(c) $\xi = 1$

Figure 5.30: Pressure function profiles at different distances from the leading edge of the plate, for different values of σ. Computations were carried for $\lambda_{\mathrm{T}} = 0$ and $\mathrm{Pr} = 0.72$

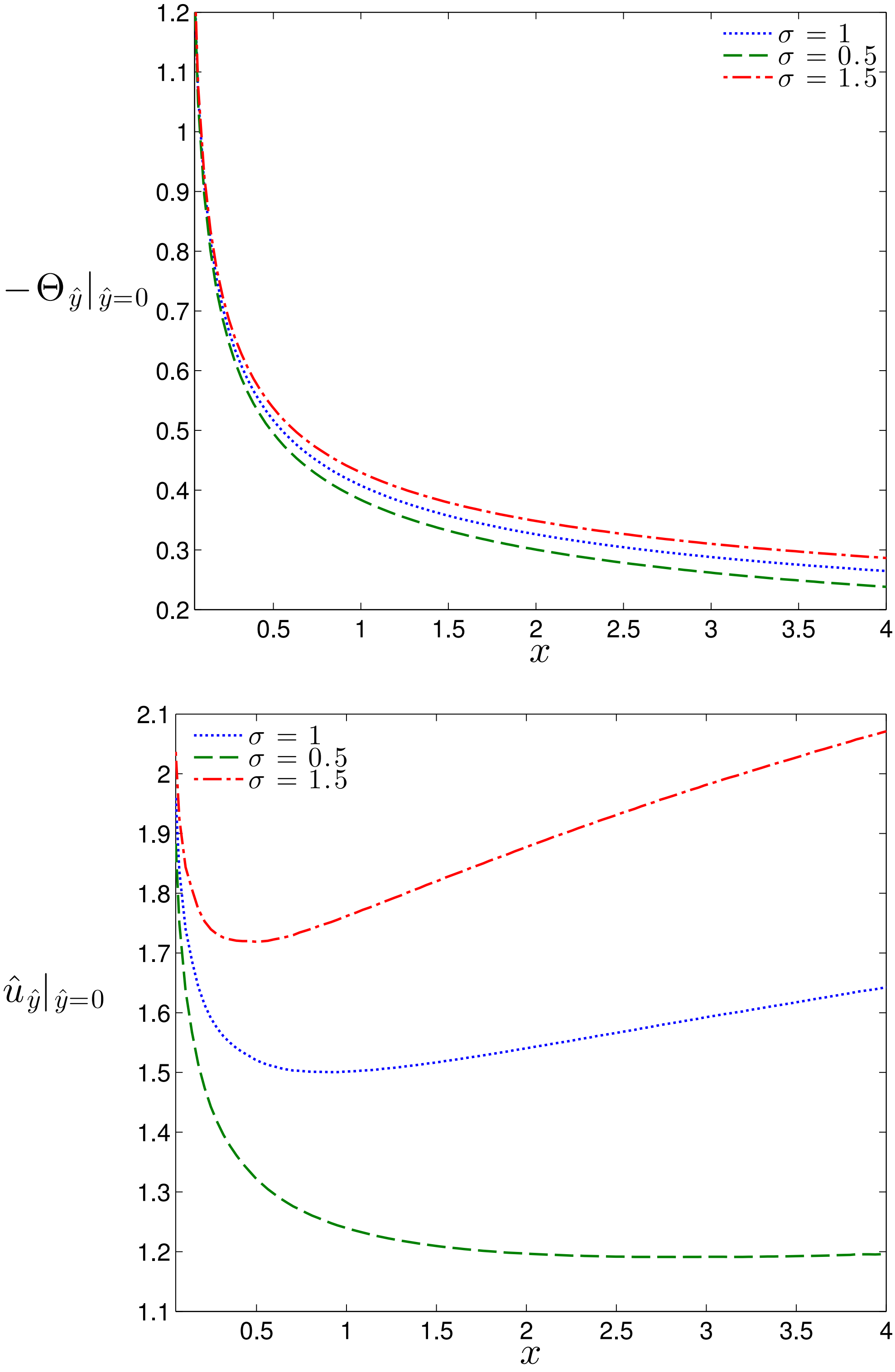

Figure 5.31: Variation of heat transfer and skin friction for different values of the inclination parameter σ.

5.5 The driving of the motion

The chapter is finalised with an investigation concerning the indirect pressure gradient $-\partial\hat{\Pi}/\partial x$ term, and its significance when compared with the tangential component of the buoyancy force. Analytically by computing numerically the radial pressure gradient in the region close to the the leading edge (i.e. $\xi = \mathcal{O}(1)$), an order of magnitude study can be established when the comparisons are made with the tangential component of buoyancy so that the region of actual influence can be determined. Computations are carried out for $\mathrm{Pr} = 0.72$, while λ_{T} varies as $\lambda_{\mathrm{T}} = 0, 0.1, \ldots, 0.5$.

The pressure gradient along the surface of the plate is evaluated in terms of the similarity transformations as

$$\frac{\partial\hat{\Pi}}{\partial x} = \frac{2C}{5}\,(C\xi)^{-3/5}G + (C\,\xi)^{2/5}G_{\xi} + \frac{\partial\eta}{\partial x}(C\,\xi)^{2/5}G_{\eta}. \tag{5.37}$$

Recalling that

$$\frac{\partial\eta}{\partial x} = \rho\Big(-\frac{2}{5\xi}\int_0^{\eta}\frac{1}{\rho}\,d\tilde{\eta} + \int_0^{\eta}\frac{1}{\rho^2}\frac{\partial\rho}{\partial\xi}\,d\tilde{\eta}\Big),$$

then the negative pressure gradient takes the following form

$$\frac{\partial\hat{\Pi}}{\partial x} = \frac{2C}{5}\,(C\xi)^{-3/5}G + (C\,\xi)^{2/5}G_{\xi} + \rho(C\,\xi)^{2/5}\Big(-\frac{2}{5\xi}\int_0^{\eta}\frac{1}{\rho}\,d\tilde{\eta} + \int_0^{\eta}\frac{1}{\rho^2}\frac{\partial\rho}{\partial\xi}\,d\tilde{\eta}\Big)\Theta. \tag{5.38}$$

where C, the Chapman constant, is taken to be unity within the computations. For the tangential component of the buoyancy force things are far more simple i.e.

$$\epsilon^{-1}\rho\theta\tan\gamma = \sigma\rho\Theta. \tag{5.39}$$

Constructing now the horizontal driving force mechanism as

$$\begin{aligned}-\frac{\partial\hat{\Pi}}{\partial x} + \epsilon^{-1}\rho\theta\tan\gamma = -\Big(\frac{2}{5}\,\xi^{-3/5}\,G + \xi^{2/5}G_{\xi}\Big) + \\ +\rho\Theta\left[\sigma + \Big(\frac{2}{5\xi}\int_0^{\eta}\frac{1}{\rho}\,d\tilde{\eta} - \int_0^{\eta}\frac{1}{\rho^2}\frac{\partial\rho}{\partial\xi}\,d\tilde{\eta}\Big)\right].\end{aligned} \tag{5.40}$$

Because the pressure gradient is negative i.e. $\partial\hat{\Pi}/\partial x < 0$, then $-\partial\hat{\Pi}/\partial x > 0$, so that when inclination is positive $\sigma > 0$ or negative $\sigma < 0$, the tangential buoyancy term is assisting or opposing the flow respectively. Contour plots of the pressure gradient $\partial\hat{\Pi}/\partial x$ and the tangential component of buoyancy $\sigma\rho\Theta$, for $\lambda_{\mathrm{T}} = 0$ and $\lambda_{\mathrm{T}} = 0.5$, while $\sigma = 1$ and $\mathrm{Pr} = 0.72$ are given in Figure 5.32. In addition contour plots for the combined term $\partial\hat{\Pi}/\partial + \sigma\rho\Theta$, is given in Figure 5.33 It can be observed that

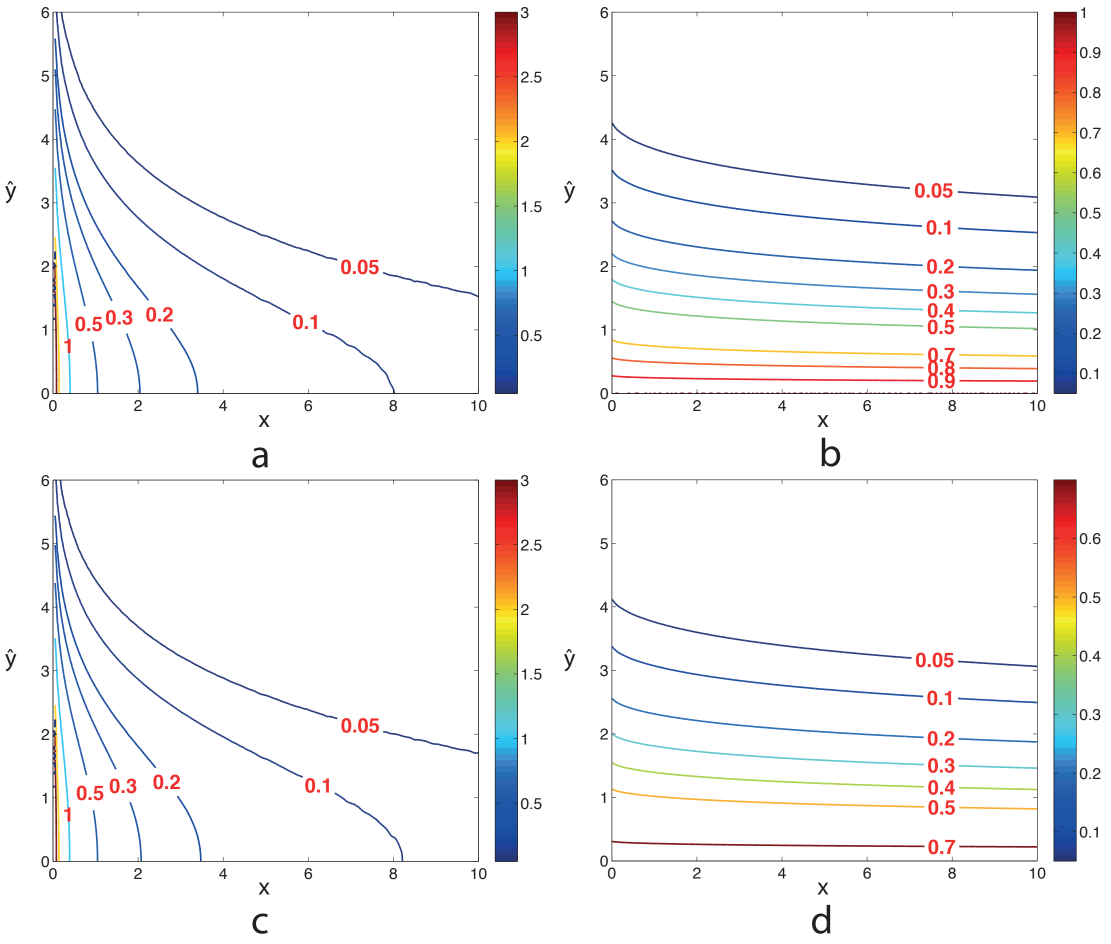

Figure 5.32: (**a**): Contour plot for the pressure gradient $-\partial\hat{\Pi}/\partial x$ for $\lambda_{\mathrm{T}} = 0$, (**b**): Contour plot for the tangential component of buoyancy $\sigma\rho\theta$, for $\lambda_{\mathrm{T}} = 0$, (**c**): $\partial\hat{\Pi}/\partial x$ for $\lambda_{\mathrm{T}} = 0.5$, (**d**): $\sigma\rho\theta$ for $\lambda_{\mathrm{T}} = 0.5$, all having $\sigma = 1$ and $\mathrm{Pr} = 0.72$.

the negative pressure gradient term is dominant over the tangential component of the buoyancy force in the region close to the leading edge of the plate. At around $x = 1$, the pressure gradient drops an order of magnitude (i.e. $\mathcal{O}(10^{-1})$), while further downstream at around $x = 8$ it drops an order once more, so that the buoyancy force can safely be assumed to drive the flow. Finally when departures from the Boussinesq approximation are assumed, the negative pressure gradient seems to get a slightly enhanced influence (as can clearly be seen at contour line 0.1), which is increasing with λ_{T}. The buoyancy term, as naturally expected, is stronger under the Boussinesq approximation.

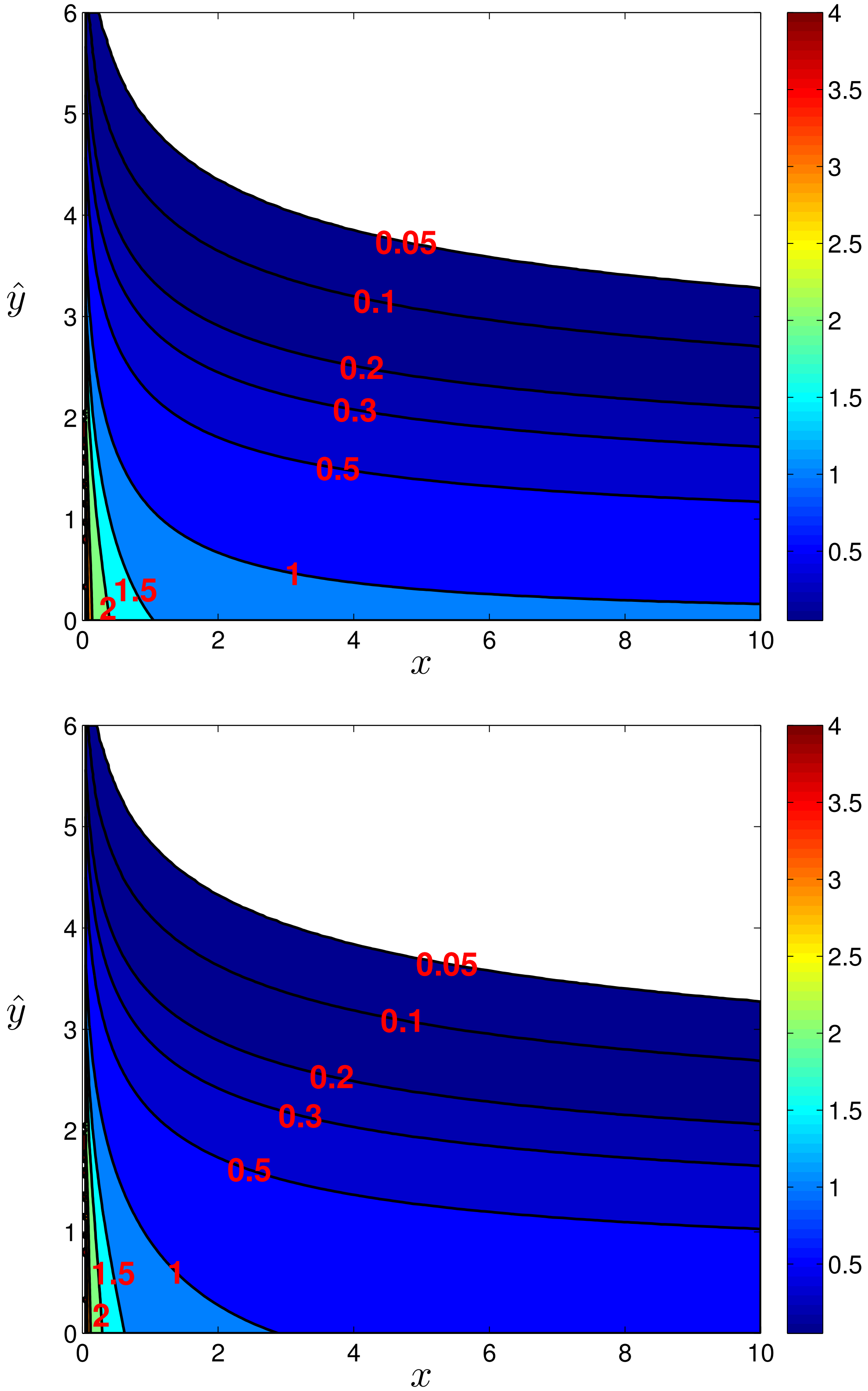

Figure 5.33: Contour plots for $-\partial\hat{\Pi}/\partial x + \sigma\rho\Theta$. Top $\lambda_{\mathrm{T}} = 0$, bottom $\lambda_{\mathrm{T}} = 0.5$. For both cases $\sigma = 1$ and $\mathrm{Pr} = 0.72$.

5.6 Summary

This chapter was devoted to the analytic study of the first order boundary layer analysis of laminar natural convection above a uniformly heated horizontal and slightly inclined semi-infinite plate. Slight inclinations to horizontal were introduced in the formulation through the nondimensional parameter σ. With a positive or a negative value of σ, corresponding to a positive or negative inclination respectively, the effects of slight inclination to horizontal were studied in detail.

It is known that when the inclination is negative, a separation occurs in the boundary layer flow accompanied by flow reversal. This is due to buoyancy forces opposing the flow. Therefore, the initial focus was on negative inclination and three separate studies were carried. The first study investigated the effect of variable fluid properties (once more introduced in the formulation through the dimensionless parameter λ_{T}) on the position of the separation point. It was found that the position of the separation point, x_s, moves downstream from the leading edge of the plate with increasing values of λ_{T}, and a function $x_s = f(\lambda_{\mathrm{T}})$ was suggested.

Within the second investigation the effect of Pr on the position of the separation point was considered. Thus, under the Boussinesq approximation, a detailed numerical study was performed and resulted in the conclusion that by increasing the value of Pr the position of the separation moves closer to the leading edge. Once more this behaviour was captured by suggesting a function $x_s = f(\mathrm{Pr})$. The position of the separation points obtained in this work, for a varying Prandtl number, deviate from those published in [69]. This was attributed to the use of a continuous transformation for the boundary layer equations in [69], which as a consequence resulted in a different set of nonsimilar equations. On a theoretical basis the separation of the boundary layer implies that no similarity regime is approached as $x \to \infty$, and therefore a continuous transformation might not be a suitable choice. Consequently it seems reasonable to expect that the results obtained here are trustworthy. In the final analysis regarding negative inclination, the effect of the inclination parameter σ was briefly considered. Positions of separation points were obtained for different values of σ. As expected the separation point was shown to move downstream from the leading edge as the value of the negative inclination parameter increases.

In the final part of this chapter positive inclination ($\sigma > 0$), was considered. We concluded that variable property effects have a milder effect on the flow. Also, an examination in connection with the indirect pressure gradient $-\partial\hat{\Pi}/\partial x$ term, and its significance when compared with the tangential component of the buoyancy force, was carried out and an order of magnitude study was performed. From the analysis it was found that the pressure gradient term at around $\xi = 8$ is of order $\mathcal{O}(10^{-2})$ and the tangential buoyancy term fully dominates the driving of the flow.

Chapter 6

Hot Plate Experiment

6.1 Introduction

An ambitious experiment was designed with the collaborators and carried out by the sponsor (AWE). The scope of the experiment was to test the theoretical model of the horizontal plume and assist in its improvement. Based on top hat formalism, and a strong assumption on the entrainment hypothesis which resembles the one commonly used for the classic non Boussinesq plume i.e.

$$w_{\mathrm{e}} = -\alpha_h f_h(r) U \quad \text{with} \quad f_h(r) = (\frac{\rho}{\rho_{\mathrm{e}}})^{1/2}, \tag{6.1}$$

answers concerning the actual value of α_h were expected to be obtained, while the validity of the 'R-S like', functional part of the entrainment hypothesis $i.e. f_h(r)$ could be assessed and if necessary, modified according to the experimental findings. Furthermore in searching for the missing puzzle of the model, that being connecting the classic plume model with our horizontal attached plume model, analysis of the experimental data could serve as a guide for the right direction.

In trying to categorise the 'hot plate' experiment, one could easily assign it into the family of round turbulent pure plume experiments, given the source and environmental conditions defining it (i.e. no momentum at the source just buoyancy, still and unstratified ambient surrounding the source), which is a partly correct statement. Even though a pure plume is generated its focus would lie far from the source where self similarity is expected or established. Instead in our experiment attention is primarily directed in the region close to the source where the flow is expected to be predominantly attached and horizontal. The fully established vertical part of the flow far from the source is of secondary interest. In that way it bears similarities to natural convection experiments above flat horizontal surfaces, though the nature of the experiment is completely different since in the heart of classic natural convection experiments is the viscous sublayer located just above the plate which here is not of a theoretical interest.

Pure plumes are especially hard to realise experimentally and when attempted normally they are generated by a heated wire, a pad, a heated coil, a flame or a line of flames [17], and pool fires. In most cases though they are generated by a source of momentum and buoyancy and are studied far from the source where the buoyancy is fully dominant. One of the first vertical plume experiments dates back to 1952 and is due to Rouse et al. [76], while the work of George et al. [27] must be mentioned. A review of experimental data until 1980 is given by Chen and Rodi [17], more recent work is from Kotsovinos [50] and Shabir & George [82].

The source of the plume in our experiment was chosen to be a heated aluminium plate of 60cm diameter. While this should have been a good choice difficulties arose in the conduct of the experiment, as will be explained. Since it is not uncommon for many natural convection experiments even in the laminar limit (which implies smaller diameters and much lower temperatures) to suffer from problematic insulation or even convective flow from below the plate. As became apparent from our analysis problems with insulation were manifested. In addition the controlling as well as the heating of the plate turned out to be inappropriate. In what concerns the visualisation of the flow, the particle feeding to the flow was poor, while there were serious problems with the video data and no calibration was carried out. The need for the conduct of the experiment in one go did not help, since a quick analysis would probably have indicated where improvements could be made. The serious technical difficulties revealed above, had an impact on the delicate flow that was set to be modelled, something that was demonstrated in the huge amount of problematic data, whose analysis turned out to be a rather time consuming process. Most importantly though, due to the uncertainty incorporated within the data, we were unable to arrive at any conclusions with confidence.

On the brighter side, a newer experiment is being initiated at the time that this work is being written up, so that the valuable experience gained will be an asset. In addition methodologies and techniques developed here for analysing the data, suitable for representing the horizontal plume, should be applicable to a better set of experimental data. Therefore in what follows we shall begin with the introduction of the experimental apparatus and the methodology followed, while a more detailed description of difficulties faced and efforts made to overcome them is given. A thorough analysis of the horizontal plume flow is given while the chapter concludes with two brief sections, one dedicated to the numerical simulation of the experiment using the two equation turbulence models $(k-\epsilon)$ and $(k-\omega)$ [99], both implemented in COMSOL Multiphysics 3.5a. In addition a discussion is provided concerning modifications required so as to better predict the buoyant flow. The final section of the chapter that closes the main work of this thesis is dedicated to the visualisation of the flow using particle image velocimetry PIV.

6.2 Methodology and experimental apparatus

A round plume was generated by heating an aluminium plate of radius 30 cm, placed within a hole cut in the centre of a 150 cm × 150 cm aluminium housing plate, itself housed in a 300 cm × 300 cm wooden compartment. The power supply was controlled through brief injections of current so that the temperature (monitored by four thermocouples placed at the bottom of the plate) would remain close to a target temperature. Additionally, the power supply was monitored and recordings of current and voltage were taken so that the average power to the plate could be obtained. Care was taken to minimise external flow disturbances that could affect the plume flow, while insulation was used below and around the plate to minimise heat loss, and to avoid flow effects of convection from the bottom of the plate. The temperature of the plate at the surface was verified by taking Infrared (IR) pictures.

Fourteen different experiments were conducted for different target plate temperatures varying from 25°C to 240°C as (in °C)

$$25,\quad 30,\quad 35,\quad 40\quad 45,\quad 50,\quad 60,\quad 80\quad ,100,\quad 120,\quad 150,\quad 180,\quad 210\quad 240. \tag{6.2}$$

The temperature field above the plate was measured by moving an array of 12 thermocouples positioned vertically at different heights above the plate as

$$1, \quad 2, \quad 3, \quad 5 \quad 7, \quad 10, \quad 14, \quad 20 \quad ,30, \quad 50, \quad 80, \quad 120.$$

with all positions measured in cm. An additional thermocouple was placed outside the plume flow and was dedicated to measuring the ambient temperature, accompanied by a relative humidity sensor. The thermocouples and the humidity sensor were connected to a data logger, sampling at a frequency of 1Khz.Thermocouple recordings were made in two passes. For the first pass readings were taken at the following locations in the order

$$0 \quad 12 \quad 18 \quad 25 \quad 0 \quad -12 \quad -18 \quad -25$$

all in cm from the centre of the plate. The duration of each reading was 60 seconds and the shifting of position took place every 80 seconds. The second pass was taken at a more detailed set of positions given in order as

$$0 \quad 4 \quad 8 \quad 12 \quad 15 \quad 18 \quad 21 \quad 23 \quad 25 \quad 26 \quad 27 \quad 28 \quad 29 \quad 30 \quad 35$$

$$0 \; -4 \; -8 \; -12 \; -15 \; -18 \; -21 \; -23 \; -25 \; -26 \; -27 \; -28 \; -29 \; -30 \; -35$$

in cm from the edge of the plate. Once more the duration of the measurements lasted for 60 seconds at each position and the movement of the array to the next station, was carried out every 80 seconds. A detailed description of the experimental setup is given in the drawings presented in Figures 6.1 and 6.2.

Concerning the visualisation of the flow, an analytic schematic diagram is given in Figure 6.2. Talcum powder was used for the visualisation, while the particles were placed at the top of two oscillating speakers, which were carefully placed so that the feeding of powder into the plume flow took place with minimal possible disturbance. A sheet of light along the centreline of the plate, was created by lights positioned on opposite sides of the apparatus, far enough away to ensure that the beam was narrow while the convection caused by the lights did not interfere with the flow within it. After the completion of each experiment the surface of the plate was cleaned of talcum powder so that the emissivity of the plate was not affected when thermal images were taken. Two high resolution digital cameras were placed at different heights the lowest focused on the flow in the region near the surface of the plate, while the higher one captured a wider image of the flow.

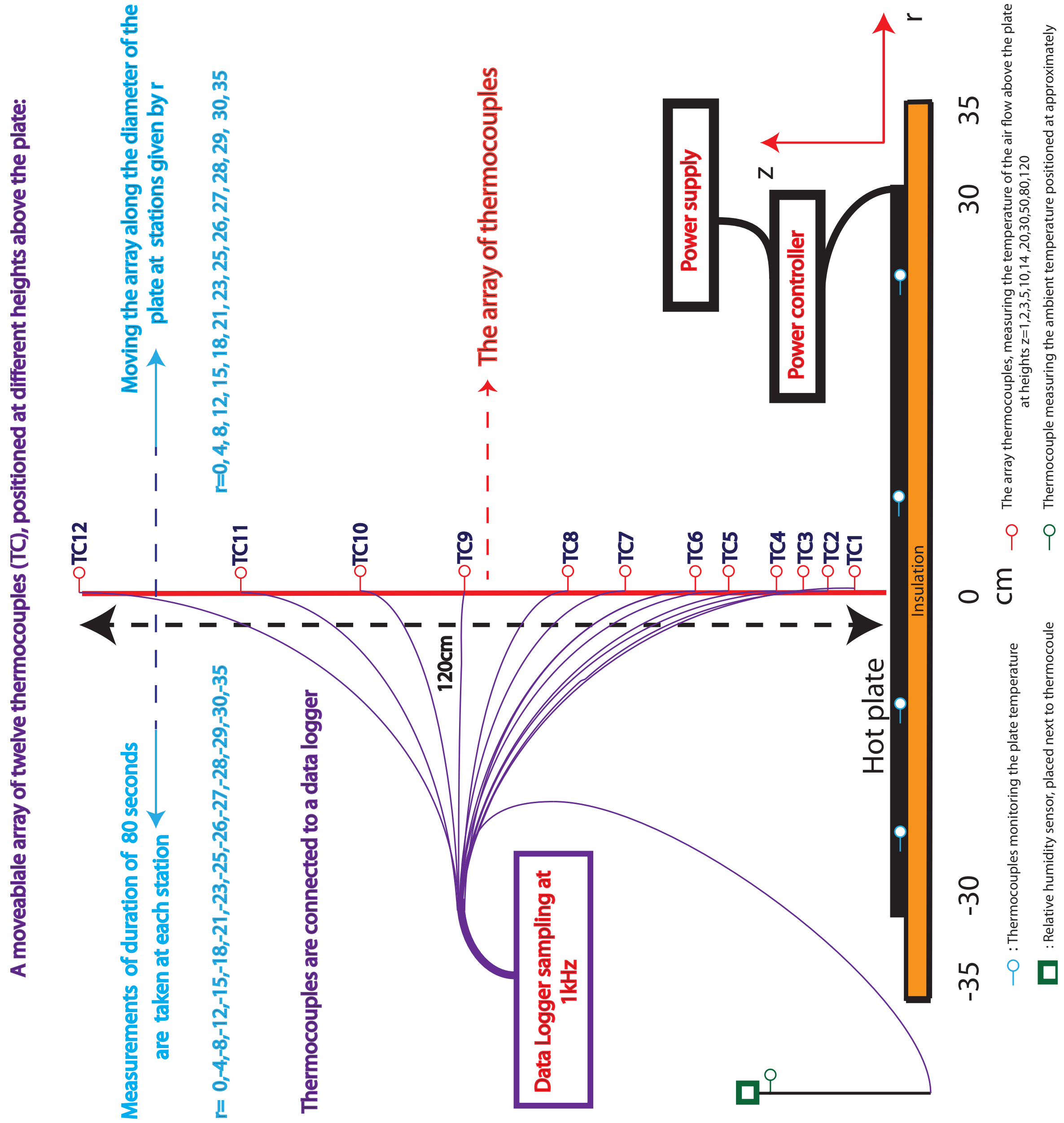

Figure 6.1: Thermocouples setup

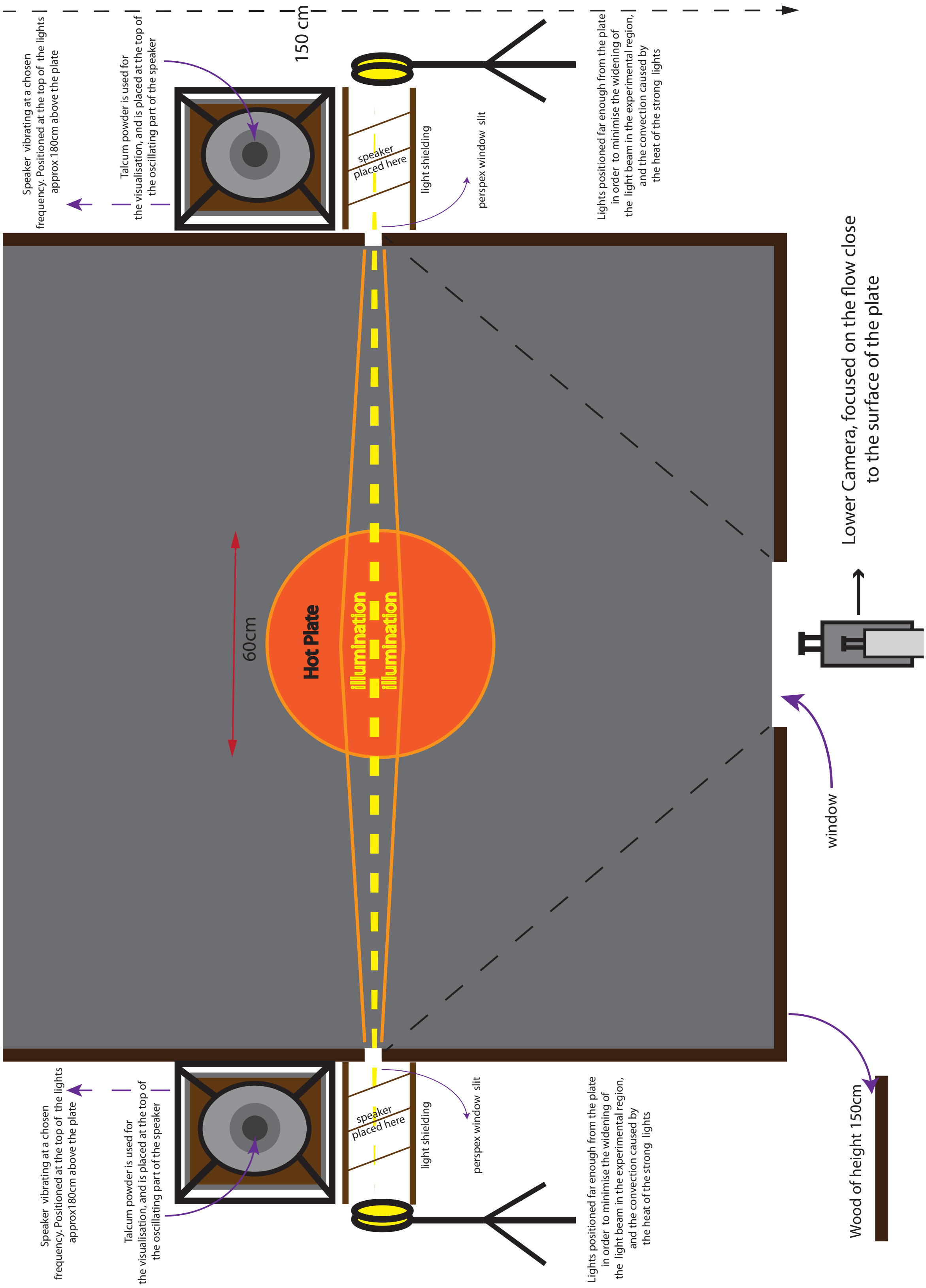

Figure 6.2: Visualisation of the flow

6.3 Technical difficulties

The instantaneous measurements obtained by the thermocouples are denoted as $T(r, z, t)$. In addition the ambient temperature data gathered by the readings obtained by a thermocouple safely positioned within ambient will be denoted by $T_{\mathrm{e}}(t)$. The possible presence of stratification was not measured. Unfortunately the ambient information was obtained by just one thermocouple positioned at a height of about 10cm above the plate so no actual information concerning the stability of the ambient can be concluded. A code was written for the collection of the data and the generation of the averages of, $T(r, z, t)$, $T_{\mathrm{e}}(t)$, $T(r, z, t) - T_{\mathrm{e}}(t)$, the median of $T_{\mathrm{e}}(t)$, $T(r, z, t) - T_{\mathrm{e}}(t)$ standard deviation of $T(r, z, t) - T_{\mathrm{e}}(t)$, in addition to the $\max\{T(r, z, t) - T_{\mathrm{e}}(t)\}$, and $\min\{T(r, z, t) - T_{\mathrm{e}}(t)\}$, while the results were output as 12×30 matrices positions. The columns of data in the matrices were used to represent the thermocouple data for different positions at a fixed z height, and the rows indicated data at the positions along r. In that way $\mathbf{Data}(1,\ 1)$ would correspond to the thermocouple positioned at height 1cm above the plate at $r = -35$cm.

From the measurements (assuming negative vertical stratification in temperature) it must be expected that

$$\lim_{\substack{r\to\infty \\ z\to\infty}} T = T_{\mathrm{e}}, \tag{6.3}$$

with $r \to \infty$ and $z \to \infty$ implying locations outside the hot plume within the experimental setup. In that way for all data-sets recorded, the simultaneously measured $T(r, z, t) - T_{\mathrm{e}}(t)$ should tend to zero as (r, z) moves towards ambient air. The ambient temperature varied slowly with time so that it should be reasonable to assume that $T_{\mathrm{e}}(t) = \bar{T}_{\mathrm{e}}$, therefore once the $T(r, z, t) - T_{\mathrm{e}}$ is averaged so as to remove the turbulent fluctuations i.e. $\overline{T(r, z, t) - T_{\mathrm{e}}} = \overline{\Delta T}(r, z)$ the result is independent of time and varies only with position.

In analysing the data the first problem encountered is demonstrated in the top left image in Figure 6.3, which is the surface plot for $\overline{\Delta T}$ obtained for the experiment at target temperature 25°C with $\bar{T}_{\mathrm{e}} = 16.81$°C. It can be observed that at greater heights the thermocouples indicate higher temperatures which was unexpected. The reason for this might be assigned to a stratification of the ambient but this was unlikely since this was the first experiment performed so there would not be enough time for a thermal build up. A possibility could be that the lights used for the visualisation of the flow were creating thermal layers, but then again for the temperature measurement the light sheet was turned off, and care was taken to address that problem in the design of the experiment. A third, and very likely possibility is that thermocouples were not recording in the same way. Unfortunately the thermocouples were not calibrated to test, or correct for, this possible source of error. In addition the thermocouples

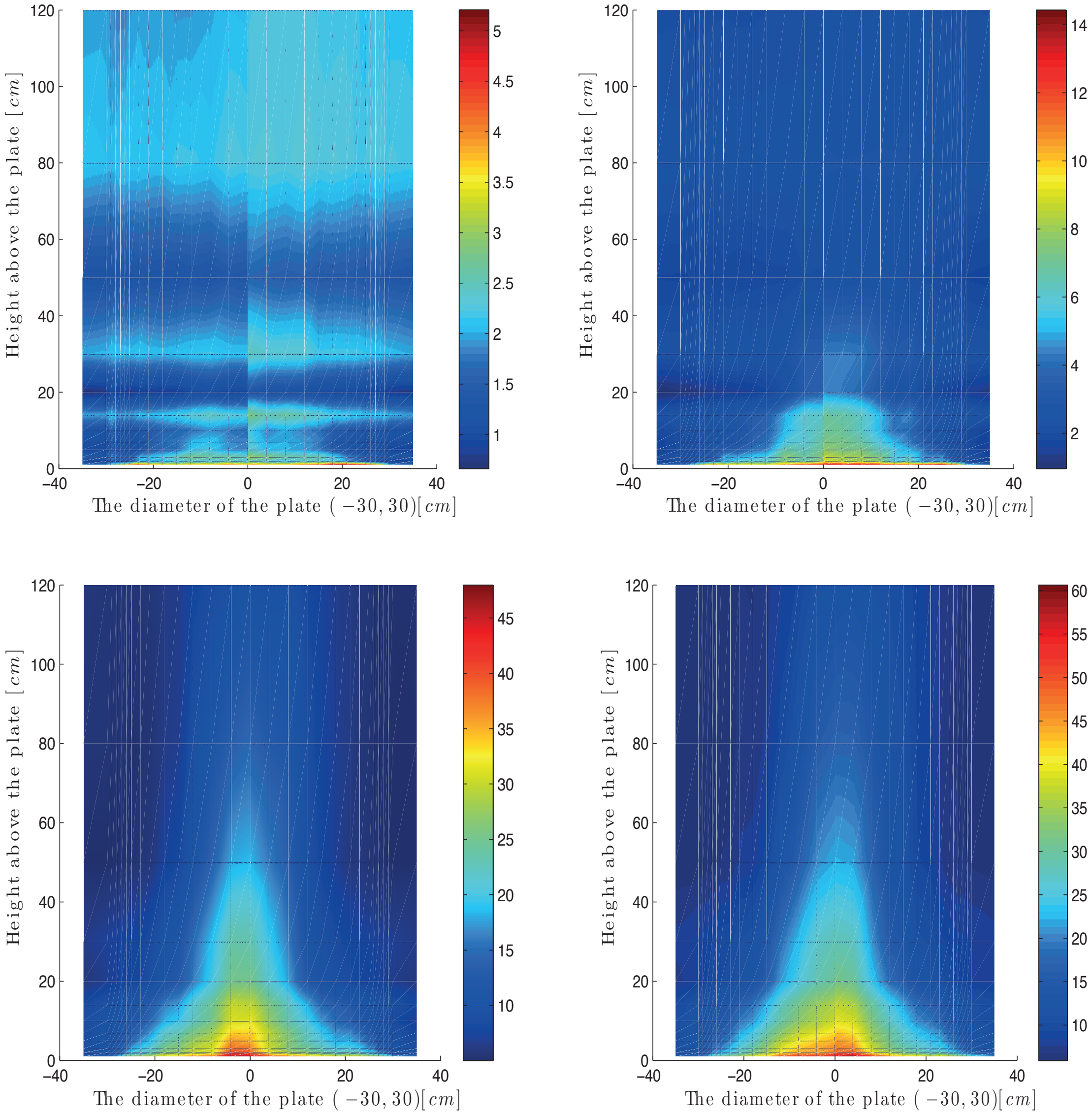

Figure 6.3: Surface plot of the mean distribution of Temperature. The instantaneous measurement of ambient temperature is subtracted from instantaneous measurements of the plume temperature. Moving clockwise the following cases of approximate plate temperature are considered: 25°C, 60°C, 210°C and 180°C.

used for the measurement of the experiment were (K-type), best suited to the measurement of large temperature variation of the order of 500°C to 1000°C, while for the experiment the order of the temperature variations were only of the order of one to ten degrees. To overcome the above discrepancy a calibration was imposed by using the 25°C experiment as a base-line. An offset of temperatures was obtained for every thermocouple (TCi with $i = 1 \ldots 12$) in the following way. If a thermocouple i was

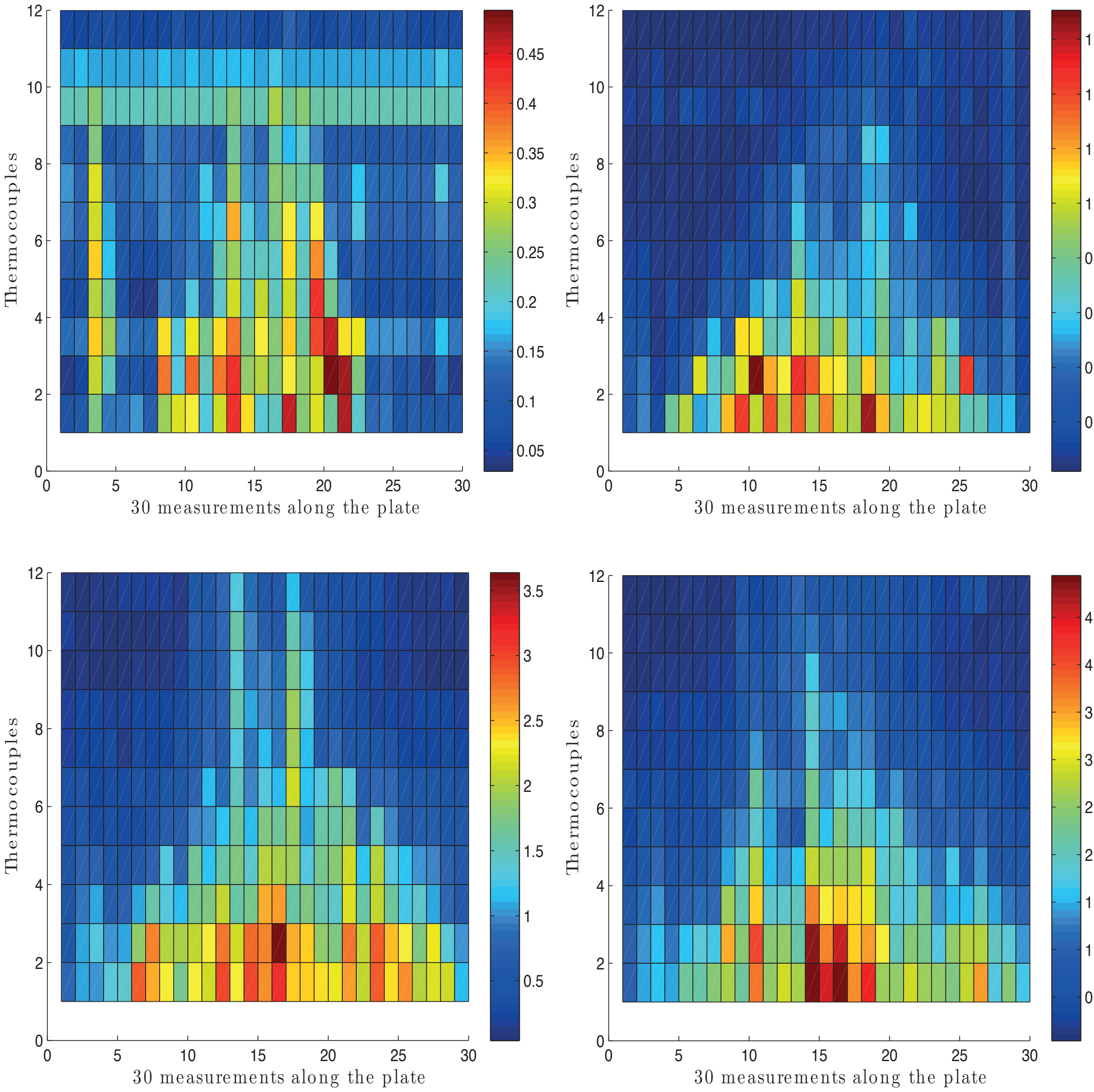

Figure 6.4: Plot of the standard deviation.Rows representing thermocouples, whilst columns represent the measurement positions along the plate. Moving clockwise the following cases of approximate plate temperature are considered: 25°C ,60°C, 210°C and 180°C

found to measure an 'ambient' temperature of $T_{\mathrm{e,i}}$, while the more distant thermocouple well into the ambient was measuring ambient T_{e} the difference $OF_i = T_{\mathrm{e,i}} - T_{\mathrm{e}}$ was determined and used to correct all the measurements of that thermocouple in subsequent runs. The corrections were then applied to the average measurements $\overline{\Delta T}$, so that result presented in the following sections will be based on these corrections.

Study of the IR images indicated another serious problem, this time regarding the heating and the insulation of the plate. Figure 6.5 is indicative. As can be observed for temperatures above 100°C, the heating and the insulation of the plate were problematic. At the target temperature of 120°C, the temperature distribution on the plate is far from uniform, while above that experiments based on higher target temperatures indicate a collapse of the insulation. For that reason further discussions concerning experiments at target temperatures above 100°C are abandoned. The final problem is the method used for heating the plate. Very brief pulses were provided to the plate once the temperature of one of the four thermocouples monitoring the plate fell below a preset target temperature, adjusted according to each experiment. Even though these pulses were recorded accurately, this method of heating is not a steady

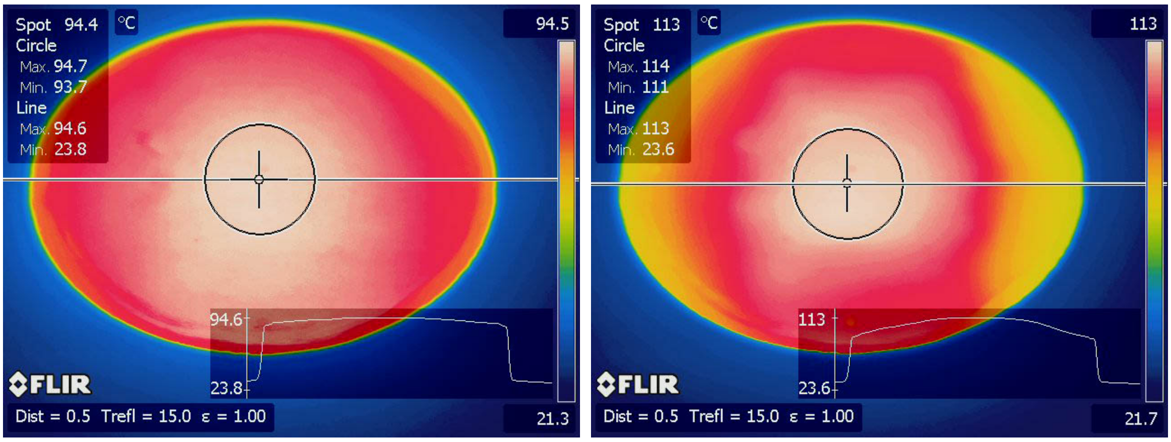

(a) 100°C (b) 120°C

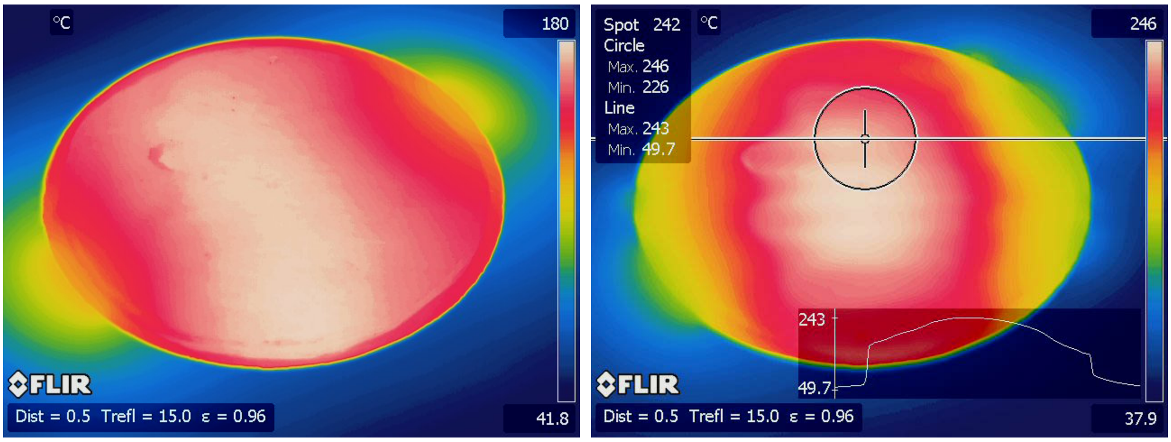

(c) 180°C (d) 240°C

Figure 6.5: IR images for experiments at different target temperatures.

process. Study of the power data as shown in Figure 6.7 revealed that mean heating

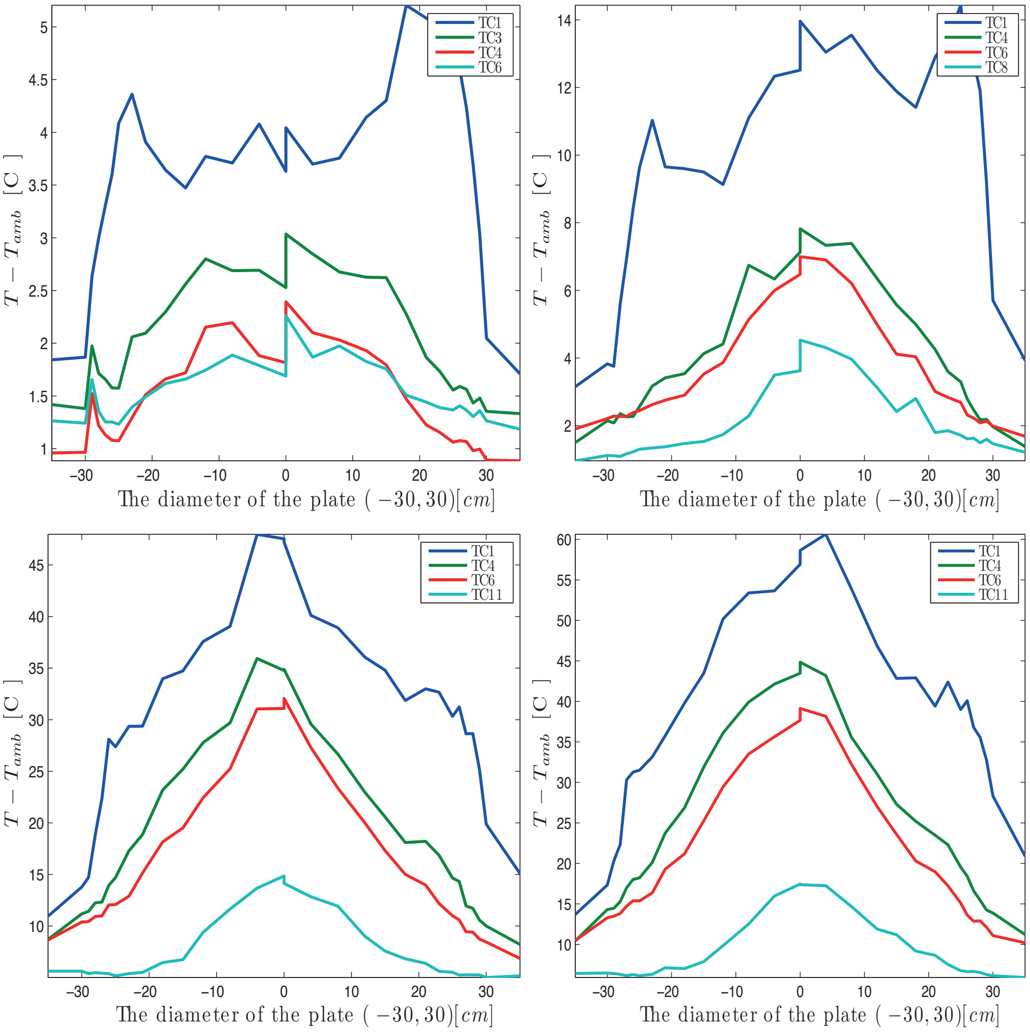

Figure 6.6: Plots of the temperature profiles at fixed height. $TC(i)$ with $i = 1 \dots 12$ is the corresponding thermocouple. Moving clockwise the following cases of approximate plate temperature are considered: 25°C ,60°C, 210°C and 180°C

rates were in transient for significant parts of the duration of the experimental time, which means that measurements made throughout this transient process introduced further uncertainty in the accuracy of the data. Another concern is illustrated in the (d) image given in Figure 6.5. The image was probably taken shortly after a pulse of energy was injected into the plate, which makes it clear that the method of heating used must have introduced short term and non uniform bursts in the rate of heat transfer from the plate to the air above the average. The pulses injected into the plate were responsible for the large values of standard deviation observed in Figure 6.4, while the asymmetry present in the profiles seen in Figure 6.6, may also be a result of the heating method adopted.

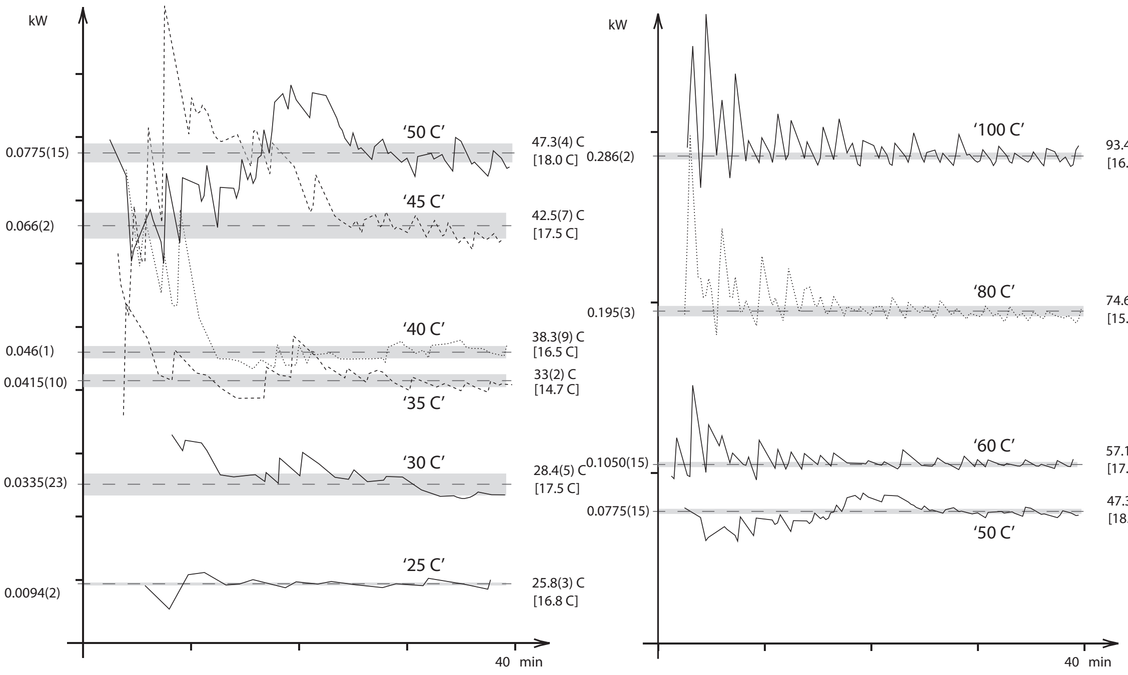

(a) (b)

Figure 6.7: Calculations of averaged power injected as thermal energy into the air. The numbers shown on the right of each plot give the surface temperature of the plate estimated from the thermal images supplied (with error margins). No thermal image was supplied for target temperature of 35°C for which a coarser estimate of surface temperature is made. Additional errors might arise for other temperatures since many of the thermal images would have been taken before the heating of the plate had reached thermal equilibrium. Average ambient temperatures during each experimental run are shown [in square brackets]. Number on the left are the average power conducted into the air, estimated near the end of each run, after allowing for radiative losses.

The average power to the plate obtained after allowing for radiative losses is given in the following table. In order to further proceed with the analysis, the asymmetry of the data was removed by using an even transformation. Averages obtained from measurements taken from symmetric positions on either side of the centre of the plate were averaged, and the mean value obtained was used to replace the actual measurements (i.e. Figure 6.8)

T_{w} [°C]	25	30	35	40	45	50	60	80	100
Q [kW]	0.0094	0.0335	0.0415	0.046	0.066	0.0775	0.1050	0.195	0.286

Table 6.1: Averaged power injected as thermal energy into the air for different target plate temperatures T_{w}.

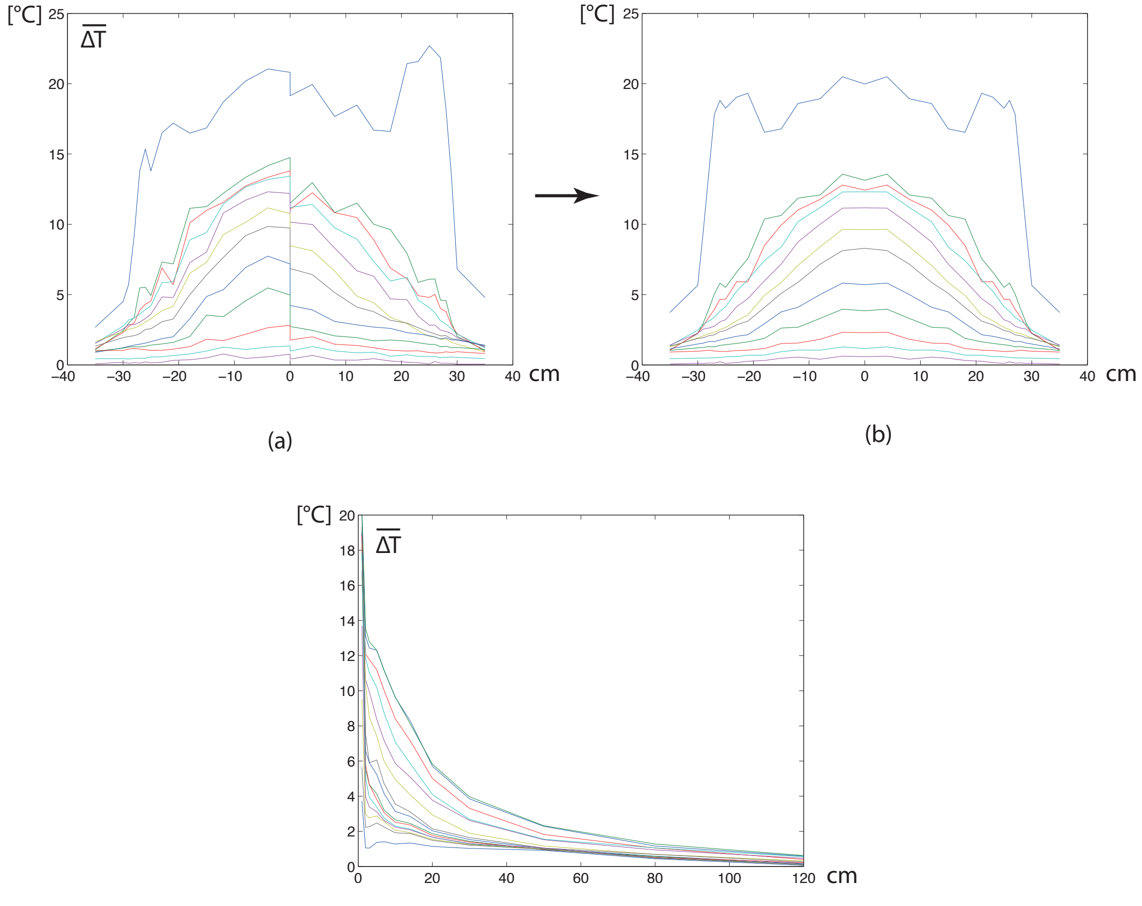

(a)

(b)

(c)

Figure 6.8: Averaged measurements are shown for the target plate temperature of 100°C.(a) Variation of $\overline{\Delta T}$ for every thermocouple along the diameter of the plate (b) Symmetric transformation of the data (c) Variation of $\overline{\Delta T}$ with height (i.e each line corresponds to fixed r position) for the symmetric data obtained.

The study of the vertical plume will not be pursued here, since the inconsistency of the data considered and the lack of information concerning the stratification of the ambient makes the analysis fruitless. Therefore the focus in analysing the data lies directly in developing a methodology suitable for the horizontal plume flow.

6.4 Analysis of the horizontal plume data

In formulating the theoretical horizontal plume model in **Chapter 2** for the turbulent flow above a circular horizontal disk, after neglecting viscous forces (i.e. large Grashof number Gr flows are of interest), and integrating the conservation equations for mass momentum and energy expressed in terms of the mean flow variables, four parameters of major importance were singled out. The mass flux V, the momentum flux M, the energy flux B and a forcing term F responsible for the horizontal driving of the flow, all defined as

$$\begin{aligned} V = 2\pi r \int_0^\infty \bar{\rho}\bar{u}\,\mathrm{dz}, \quad M = 2\pi r \int_0^\infty \bar{\rho}\bar{u}^2\,\mathrm{dz}, \\ B = 2\pi r \int_0^\infty \bar{\rho} c_\mathrm{p} \bar{T}\bar{u}\,\mathrm{dz}, \text{ and } F = 2\pi r \int_0^\infty \frac{\partial P}{\partial r}\,\mathrm{dz}. \end{aligned} \tag{6.4}$$

Furthermore the mass entrained into the system is defined as $V_{in} = -2\pi r \rho_\mathrm{e} w_\mathrm{e}$, while the energy entrained and provided through heat flux q, is expressed as $-2\pi r(q + \rho_\mathrm{e} \mathrm{c_p T_e w_e})$, with w_e being the the velocity at which ambient fluid is engulfed into the horizontal flow. In that way the conservation principles for mass, energy and momentum were specified as

$$\frac{\mathrm{dV}}{\mathrm{dr}} = V_{in}, \quad \frac{\mathrm{dB}}{\mathrm{dr}} = B_{in} \quad \text{and} \quad \frac{\mathrm{dM}}{\mathrm{dr}} = -F. \tag{6.5}$$

In addition the pressure outside the plume (i.e. $z > h$, with h being the height of the horizontal flow) was assumed purely hydrostatic whilst inside the plume was given as

$$P = P_0 - \rho_\mathrm{e} g z - \int_z^\infty (\rho_\mathrm{e} - \rho)\mathrm{d}\tilde{\mathrm{z}}, \tag{6.6}$$

so that the radial pressure gradient is

$$P_r = -\frac{\partial}{\partial r} \int_z^\infty (\rho_\mathrm{e} - \rho)\mathrm{d}\tilde{\mathrm{z}}, \tag{6.7}$$

which finally results in F being expressed as

$$F = 2\pi r \int_0^\infty \left(\frac{\partial}{\partial r} \int_z^\infty (\bar{\rho} - \rho_\mathrm{e})\mathrm{d}\tilde{\mathrm{z}} \right) \mathrm{dz} = 2\pi \mathrm{r} \frac{\partial}{\partial \mathrm{r}} \int_0^\infty \int_\mathrm{z}^\infty (\bar{\rho} - \rho_\mathrm{e})\mathrm{d}\tilde{\mathrm{z}}\mathrm{dz}. \tag{6.8}$$

In that way conservation equations given in (6.5) take the following form

$$\frac{\mathrm{d}}{\mathrm{dr}}\int_0^\infty r\bar{\rho}\bar{u}\,\mathrm{dz} = -r\rho_{\mathrm{e}}w_{\mathrm{e}} \tag{6.9a}$$

$$\frac{\mathrm{d}}{\mathrm{dr}}\int_0^\infty r\bar{\rho}\bar{u}^2\,\mathrm{dz} = -r\,\frac{\partial}{\partial r}\int_0^\infty\int_z^h(\bar{\rho}-\rho_{\mathrm{e}})\mathrm{d\tilde{z}dz} \tag{6.9b}$$

$$\frac{\mathrm{d}}{\mathrm{dr}}\int_0^\infty r\bar{u}\,\mathrm{dz} = -r(\frac{q}{\rho_{\mathrm{e}}\mathrm{c_p}\mathrm{T_e}}+w_{\mathrm{e}}) \tag{6.9c}$$

Embracing the top hat formulation so that

$$\bar{\rho} = \begin{cases}\rho & \text{if } z \le h\\ \rho_{\mathrm{e}} & \text{if } z > h\end{cases} \qquad \bar{u} = \begin{cases}U & \text{if } z \le h\\ 0 & \text{if } z > h\end{cases} \tag{6.10}$$

leads to the governing equations

$$\frac{\mathrm{d}}{\mathrm{dr}}\left[r\rho Uh\right] = -r\rho_{\mathrm{e}}w_{\mathrm{e}}, \tag{6.11a}$$

$$\frac{\mathrm{d}}{\mathrm{dr}}\left[r\rho U^2h\right] = \frac{1}{2}rg\,\frac{\mathrm{d}}{\mathrm{dr}}\left[(\rho_{\mathrm{e}}-\rho)h^2\right], \tag{6.11b}$$

$$\frac{\mathrm{d}}{\mathrm{dr}}\left[rUh\right] = -r(\frac{q}{\rho_{\mathrm{e}}\mathrm{c_p}\mathrm{T_e}}+w_{\mathrm{e}}), \tag{6.11c}$$

or expressed in terms of density deficiency $\delta = \rho_{\mathrm{e}} - \rho$ as

$$\frac{\mathrm{d}}{\mathrm{dr}}[r(\rho_{\mathrm{e}}-\delta)Uh] = -r\rho_e w_{\mathrm{e}}, \tag{6.12a}$$

$$\frac{\mathrm{d}}{\mathrm{dr}}[r(\rho_{\mathrm{e}}-\delta)U^2h] = \frac{1}{2}r\mathrm{g}\frac{\mathrm{d}}{\mathrm{d}r}[\delta h^2], \tag{6.12b}$$

$$\frac{\mathrm{d}}{\mathrm{dr}}[rUh] = -r(w_{\mathrm{e}}+\frac{q}{\rho_{\mathrm{e}}c_{\mathrm{p}}T_{\mathrm{e}}}). \tag{6.12c}$$

Equations (6.11), (6.12) are based on the theoretical assumption that top hat shape functions can properly represent the horizontal part of the flow. However in the context of the experimental measurements and their analysis, a more general form of distributions needs to be considered. Beginning with the introduction of a profile variable

$$\eta = \frac{z}{H(r)}, \tag{6.13}$$

where $H(r)$ represents a local height scale for the attached horizontal flow and a distribution function Φ for which

$$\Phi(0) = 1, \quad \text{and} \quad \int_0^\infty \Phi(\eta)\,\mathrm{d}\eta = 1 \Rightarrow \int_0^\infty \Phi(\eta)\,\mathrm{dz} = \mathrm{H}. \tag{6.14}$$

In addition further properties for the distribution function are L, L_2 and L_3, defined as

$$L = \int_0^\infty \int_\mu^\infty \Phi(\eta)\,\mathrm{d}\eta\,\mathrm{d}\mu, \quad \mathrm{L}_2 = \int_0^\infty \Phi^2(\eta)\,\mathrm{d}\eta, \quad \text{and} \quad \mathrm{L}_3 = \int_0^\infty \Phi^3(\eta)\,\mathrm{d}\eta. \quad (6.15)$$

The actual form of the distribution functions is to be determined from the experimental data. Since no reliable information can be be extracted from the video data (even though their analysis is pursued in the last section of the chapter where a qualitative behaviour is presented) we are left with limited options concerning the appropriate distribution function for the mean velocity. Therefore in what follows the mean properties of both density deficit $\bar{\delta}$ and the horizontal velocity $\bar{u}$ are presumed to be represented by the same shape function Φ as

$$\bar{\delta} = \delta_h(r)\Phi(\eta), \quad \text{and} \quad \bar{u} = -U_h\Phi(\eta). \quad (6.16)$$

On physical grounds the above assumption implies that the same turbulent mixing processes transfer mass and velocity. Arguably a more suitable choice might have been to presume that the momentum and the mass are described by the same distribution function, since the Boussinesq approximation is not adopted. Nevertheless experimental results studied here, indicate that the flow is not far from being Boussinesq so that the differences would be small, weighted down by the levels of uncertainty in the experiments carried out.

Introduction of the distributions given in (6.16) into the general form equations given in (6.9), results in the following set of equations

$$\frac{\mathrm{d}}{\mathrm{dr}}[r(\rho_\mathrm{e} - \delta_h L_2)U_h H] = -r\rho_e w_\mathrm{e}, \quad (6.17a)$$

$$\frac{\mathrm{d}}{\mathrm{dr}}[r(\rho_\mathrm{e} L_2 - \delta_h L_3)U_h^2 H] = r\mathrm{g}\frac{\mathrm{d}}{\mathrm{d}r}[\delta_h L H^2], \quad (6.17b)$$

$$\frac{\mathrm{d}}{\mathrm{dr}}[rU_h H] = -r(w_\mathrm{e} + \frac{q}{\rho_\mathrm{e} c_\mathrm{p} T_\mathrm{e}}). \quad (6.17c)$$

The above equations correspond to the ‘top hat’ ones given in (6.12), if $\delta_h = \delta$, $U_h = u$, $L_2 = L_3 = 1$ and $L = 1/2$. For a general form distribution Φ the analogous ‘top hat like’ equations can be obtained by initially directing attention towards equations (6.12a)–(6.17a) and (6.12c)–(6.17c). It can be deduced that equivalence is obtained when $\delta = L_2\delta_h$ and $U_h H = Uh$. Additionally by setting $U_h = \sigma_1 U$, and $H = \sigma_2 h$, noting that $\sigma_1\sigma_2 = 1$ and further assuming that the derivatives of L_2 and L w.r.t r can be neglected, then from equations (6.12b)–(6.17b) σ_1 and σ_2 are evaluated as

$$\sigma_1 = \left(\frac{2\,L}{L_2^2}\right)^{1/3} \quad \text{and} \quad \sigma_2 = \left(\frac{L_2^2}{2\,L}\right)^{1/3}. \tag{6.18}$$

Therefore the equivalent top hat equations for a general form profile are thus given as

$$\frac{\mathrm{d}}{\mathrm{dr}}[r(\rho_\mathrm{e} - \delta)Uh] = -r\rho_e w_\mathrm{e}, \tag{6.19a}$$

$$\frac{\mathrm{d}}{\mathrm{dr}}[r(\rho_\mathrm{e} - \lambda\delta)U^2h] = \frac{1}{2}r\mathrm{g}\frac{\mathrm{d}}{\mathrm{d}r}[\delta h^2], \tag{6.19b}$$

$$\frac{\mathrm{d}}{\mathrm{dr}}[rUh] = -r(w_\mathrm{e} + \frac{q}{\rho_\mathrm{e}c_\mathrm{p}T_\mathrm{e}}), \tag{6.19c}$$

where $\lambda = L_3/L_2^2$.

If the Boussinesq approximation is embodied so that $\delta \to 0$, then the resulting equivalent top hat like system given in equation (6.19), matches the theoretical top hat system of equations given in (6.12). In the more general case considered here where the Boussinesq approximation is not adopted the parameter λ is present in the equations and equivalence can only be attained when $\lambda = 1$ or $L_2^2 = L_3$. Therefore by considering a general horizontal plume profile that is not top hat, introduces a profile dependent parameter in the model equations, representing deviation from top hat formalism. The theoretical work given in **Chapter 3** was based on the assumption that top hat profiles can adequately describe the horizontal part of the flow, therefore all results obtained were based on $\lambda = 1$. Analysis of the thermocouple data indicate that an exponential distribution $\Phi(\eta) = \exp(-\eta)$ is a likely candidate for the representation of the density deficit data (or equivalently the density data) and since the same distribution is adopted for the horizontal velocity then

$$\bar{\delta} = \delta_h(r)\exp(-\eta), \quad \bar{u} = U_h(r)\exp(-\eta). \tag{6.20}$$

For the presumed exponential distribution $\Phi(\eta) = \exp(-\eta)$, additional properties given in (6.15) are evaluated as

$$L = 1 \quad L_2 = \frac{1}{2}, \qquad L_3 = \frac{1}{3} \quad \text{so that} \quad \lambda = \frac{4}{3}. \tag{6.21}$$

Consequently since $\lambda > 1$, departures from the theoretical analysis provided earlier are expected. Nevertheless the nature of the equations is not altered significantly provided that the resulting value of λ for any preferred distribution remains an $\mathcal{O}(1)$ term, as in the case considered here. Finally in fitting to the experimental data using the distributions given in (6.20), the corresponding 'top hat like' variables h and δ can be estimated as

$$h = 2H, \quad U = \frac{U_h}{2}, \quad \delta = \frac{\delta_h}{2}. \tag{6.22}$$

In what follows, the focus will lie in the analysis of the experiments based on target plate temperatures of 50°C, 60°C, 80°C and 100°C. In studying the horizontal part of the flow exponential fits of the form given in (6.20), were obtained in a least squares sense for the density deficit and seem to provide a moderately reasonable approximation in the region of interest. The fitting to the density deficit thermocouple data is presented in Figure 6.9. Furthermore the variation of the values obtained for δ_h along the radius of the plate, from the exponential fits are given in Figure 6.10, where in addition a symmetric polynomial of the form

$$\delta_h = \hat{\delta_0} + \hat{\delta}_2 r^2 + \hat{\delta}_4 r^4. \tag{6.23}$$

is fitted to the data. The reasoning behind the polynomial fit is to become clear once the theoretical model is tested on how well it approximates the experimental data given in the following section.

6.5 Testing the model

Having obtained the equivalent 'top hat like' system of equations given in equations (6.19), this section is concentrated on testing behaviour of the theoretical model in describing the experimental findings. We shall begin by rewriting the equations (6.19) in terms of density and further multiply equation (6.19c) with ρ_e, to obtain

$$\frac{\mathrm{d}}{\mathrm{dr}}[r\rho U h] = -r\rho_\mathrm{e} w_\mathrm{e}, \tag{6.24a}$$

$$\frac{\mathrm{d}}{\mathrm{dr}}[r(\rho_\mathrm{e} - \lambda(\rho_\mathrm{e} - \rho)U^2 h] = \frac{1}{2} r \mathrm{g} \frac{\mathrm{d}}{\mathrm{d}r}[(\rho_\mathrm{e} - \rho))h^2], \tag{6.24b}$$

$$\frac{\mathrm{d}}{\mathrm{dr}}[r\rho_\mathrm{e} U h] = -r(\rho_\mathrm{e} w_\mathrm{e} + \frac{q}{c_\mathrm{p} T_\mathrm{e}}). \tag{6.24c}$$

Subtraction of equations(6.24c)-(6.24a) and application of the entrainment hypothesis (i.e. $w_\mathrm{e} = \alpha_h(\frac{\rho}{\rho_e})^{1/2}\mathrm{U}$), to finally get

$$\frac{\mathrm{d}}{\mathrm{dr}}[r\rho U h] = -\alpha_h r(\rho_\mathrm{e}\rho)^{1/2} U, \tag{6.25a}$$

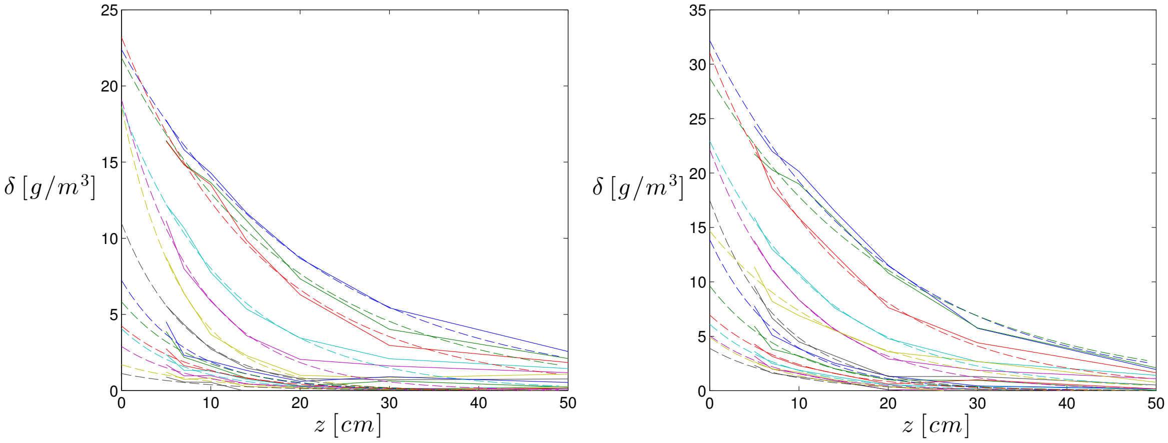

(a) 50°C (b) 60°C

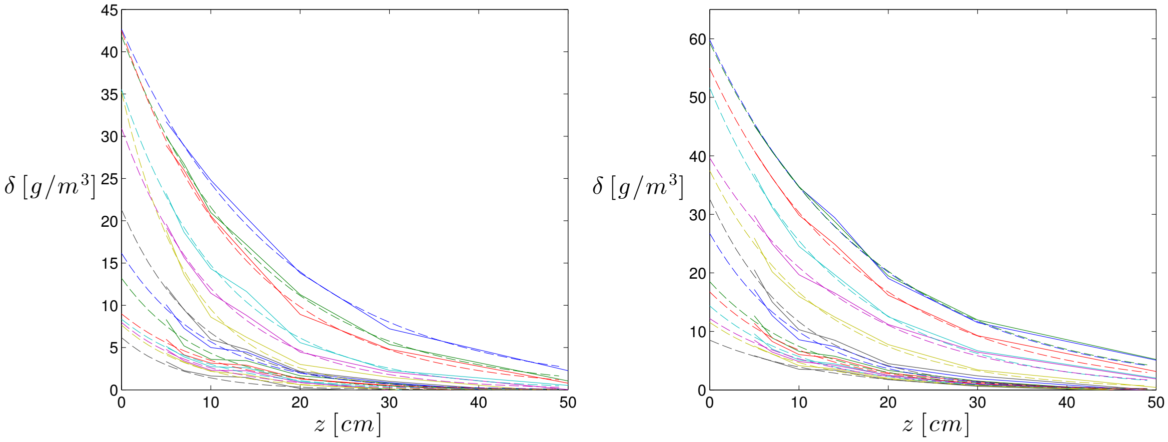

(c) 80°C (d) 100°C

Figure 6.9: Least squares exponential fits (dotted lines) to the experimental density deficit data.

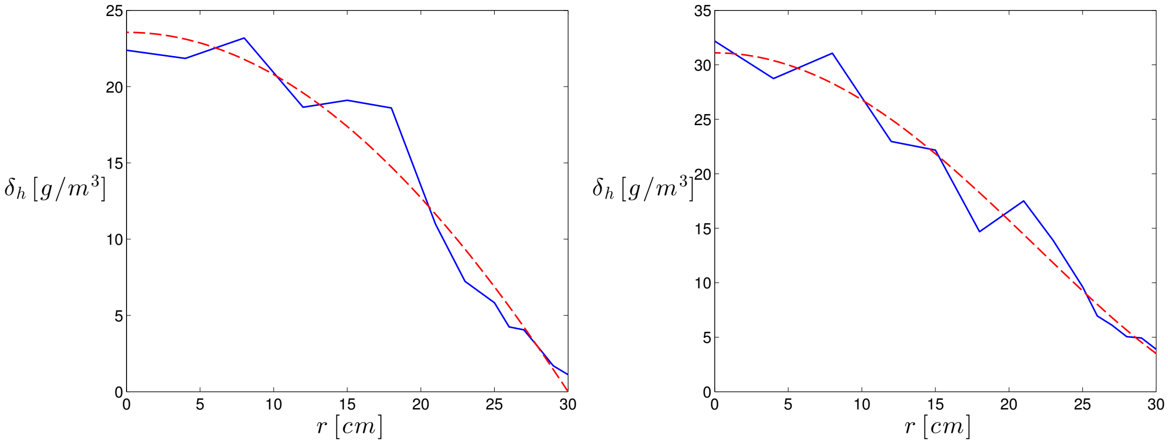

(a) 50°C (b) 60°C

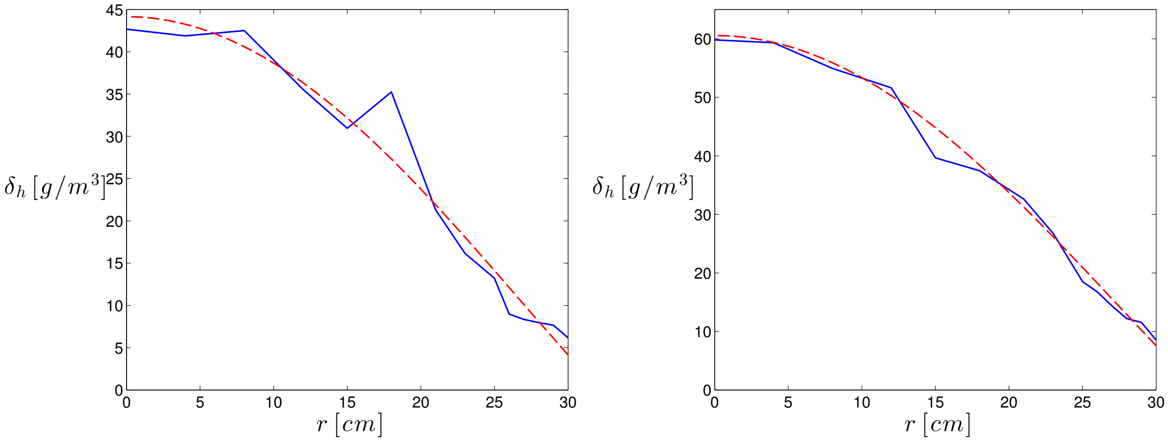

(c) 80°C (d) 100°C

Figure 6.10: Variation of δ_h with r and a best fit using least squares (dotted line).

$$\frac{\mathrm{d}}{\mathrm{dr}}[r(\rho_{\mathrm{e}} - \lambda(\rho_{\mathrm{e}} - \rho)U^2 h] = \frac{1}{2} r \mathrm{g} \frac{\mathrm{d}}{\mathrm{d}r}[(\rho_{\mathrm{e}} - \rho))h^2] \tag{6.25b}$$

$$\frac{\mathrm{d}}{\mathrm{dr}}[r(\rho_{\mathrm{e}} - \rho)Uh] = -r\frac{q}{c_{\mathrm{p}}T_{\mathrm{e}}}. \tag{6.25c}$$

The number of unknowns in the system of equations (6.25) is five, ρ, U, h, q and α_h whilst $\lambda = 4/3$. For the time being the entrainment coefficient α_h, is assumed to be known and given as $\alpha_h = 1/8$. This means that for the constant of entrainment in the horizontal flow, the numeric value widely used in vertical plumes, is assigned. By neglecting one unknown, the problem of shortage of equations is not diminished, one more equation is required for closure of the system. In searching for an additional equation, it should be remembered that the average power Q, provided to the plate has been estimated. By taking into account that information, one more equation appears in the form of an integral constraint for the heat flux q as

$$\int_0^L 2\pi r q \, \mathrm{dr} = \mathrm{Q}, \quad \text{with } L \text{ being the radius of the plate.} \tag{6.25d}$$

It is advisable before furthering discussion on the application of the theoretical model to the experimental data, to make the equations dimensionless. For the nondimensionalisation of (6.25), the following scales will be used

$$r = Lr', \quad h = L\alpha_h h', \quad U = \frac{Q}{2\alpha\pi L^2 \rho_{\mathrm{e}} c_{\mathrm{p}} T_{\mathrm{e}}} U' \quad q = \frac{Q}{\pi L^2}\acute{q}$$

$$\rho = \rho_e \rho' \quad \text{and} \quad \mathbf{a} = 4g\alpha_h^3(\rho_{\mathrm{e}} c_{\mathrm{p}} T_{\mathrm{e}})^2 \frac{\pi^2 L^5}{Q^2}. \tag{6.26}$$

The resulting equations after **dropping** primes for ease, are

$$\frac{\mathrm{d}}{\mathrm{dr}}[r\rho Uh] = -r\sqrt{\rho}U \tag{6.27a}$$

$$\frac{\mathrm{d}}{\mathrm{dr}}[r(1 - \lambda(1 - \rho)U^2 h] = \frac{1}{2}\mathbf{a}r\frac{\mathrm{d}}{\mathrm{dr}}[(1 - \rho)h^2] \tag{6.27b}$$

$$\frac{\mathrm{d}}{\mathrm{dr}}[r(1 - \rho)Uh] = -2rq. \tag{6.27c}$$

$$\int_0^1 rq \, \mathrm{dr} = \frac{1}{2}. \tag{6.27d}$$

This system of equations could be considered theoretically closed, provided that the form of q is known and suitable boundary conditions are given, so that it could then be treated numerically. Consequently it is necessary to open a discussion concerning the boundary conditions that are suitable for the experiment, before touching aspects of the numerical methodology to be used. In developing the theoretical model we had assumed constant heat flux q. The number of unknowns were three, namely U, h and ρ, while the problem was treated as an IVP, at $r = 1$. The initial conditions for the dependent variables were given as $h(1) = U(1) = \rho(1) = 0$. In addition, the singular behaviour of the system exhibited at $r = 1$, required a local analysis in the limit of $r \rightarrow 1$ to be performed. Truncated power series approximations valid in that vicinity had to be obtained, before a numerical solution could be attempted. The situation in the experiment is rather different, the number of unknowns has increased to four (not including α_h) with the addition of q, whilst in trying to formulate the problem as an IVP, experimental results indicate that the initial condition $\rho(1) \rightarrow 0$ cannot be used, since the variations in density are small with respect to the ambient density. Furthermore we have no prior knowledge of what the initial condition for $q(1)$ should be. To add to the trouble, the experiment indicates that the height of the plume and consequently the velocity, are not actually zero at the edge of the plate. This is likely to be connected with the insulation of the heated plate. As discussed earlier and shown in the thermal images, the area surrounding the plate is also heated to some degree, something that results in an additional weaker flow external to the boundaries of the plate. That secondary external flow acts as a perturbation to the actual flow under consideration. Nevertheless in what follows the effects of the incoming weak flow outside the edge of the heated plate will be neglected. In that way initial conditions for the velocity and the height of the attached flow imposed at the edge of plate remain unchanged when compared to the theoretical model, and are given as $h(1) = 0$ and $U(1) = 0$. The initial condition for the density is available from the experimental data, being $O(1)$ quantity, while the initial condition for the heat flux, still remains undefined.

Forcing the constraints for height and velocity to zero at the edge of the plate, results in a singularity at the edge of the plate. In the usual manner a local analysis has to carried out, around $r = 1$ before numerics can be considered. Unforeseen, local analysis reveals that the behaviour for all dependent variables at the edge of the plate, require only knowledge of the value of the density at the edge of the plate.

Assuming that the local behaviour of the dependent variables at the edge of the plate is of the form

$$\text{As } r \to 1\ \rho \sim \hat{\rho},\ U \sim \hat{U}(1-r)^a,\ h \sim \hat{h}(1-r)^b,\ q \sim \hat{q}(1-r)^c. \tag{6.28}$$

substitution of (6.28) into (6.27) results in $b = 1, a = c = 1/2$. So that

$$U \sim \hat{U}\sqrt{(1-r)},\ h \sim \hat{h}(1-r),\ q \sim \hat{q}\sqrt{(1-r)} \tag{6.29a}$$

with

$$\hat{h} = \frac{2}{3\sqrt{\hat{\rho}}},\ \hat{U}^2 = \frac{\mathbf{a}(1-\hat{\rho})}{3\sqrt{\hat{\rho}}(1-\lambda(1-r))} \text{ and } \hat{q} = \frac{(1-\hat{\rho})\hat{U}}{2\sqrt{\hat{\rho}}}. \tag{6.29b}$$

It is clear from the above results that knowledge of $\hat{\rho}$ suffices for the provision of initial conditions at $r(1^-)$. The system of differential equations is now reformulated with an introduction of a new dependent variable given as

$$m(r) = r\rho(r)u(r)h(r). \tag{6.30}$$

Keeping in mind that the local behaviour of m is also known from (6.28), three differential equations in terms of m, u, and ρ, plus the unchanged integral constraint for q are obtained as

$$\frac{\mathrm{d}m}{\mathrm{dr}} = -r\sqrt{\rho}u, \tag{6.31a}$$

$$\frac{\mathrm{d}\rho}{\mathrm{dr}} = \frac{r\left(u\left(\rho-1\right)+2q\sqrt{\rho}\right)\rho^{3/2}}{m}, \tag{6.31b}$$

$$\frac{\mathrm{d}u}{\mathrm{dr}} = \frac{u\,\Psi}{\Omega}, \tag{6.31c}$$

$$\int_0^1 rq\,\mathrm{dr} = \frac{1}{2}, \tag{6.31d}$$

while Ψ and Ω are given as

$$\Psi = 2\left(\sqrt{\rho}u + 2\left(1-\lambda\right)q\right)u^3\rho^2r^3 + \Big(2q\left(\rho-2\right)+\left(\rho-1\right)\sqrt{\rho}u\Big)\mathbf{a}\rho m r^2 + 2\mathbf{a}m^2\left(\rho-1\right) \tag{6.31e}$$

$$\Omega = 2mr\Big(\left(\lambda\left(\rho-1\right)+1\right)u^3\rho r + m\mathbf{a}\left(1-\rho\right)\Big) \tag{6.31f}$$

Nevertheless, there are further details that needs to be addressed, before a numerical process can be set up. The form of the heat flux q is still unknown, while the estimated power into the plate Q, is used in the nondimensionalisation of q as well as in the definition of the nondimensional parameter **a**. Provided that the estimates for the power are accurate enough, the parameter **a** contains another unknown of great interest in our study, namely the constant of entrainment α_h, which so far has been treated as known. Furthermore the scaling of the height of the plume h also makes use α_h. To sum up, there is a need to deal with a problem of five unknowns, after the inclusion of the constant of entrainment, with the use of three differential equations and an integral constraint. The fitting to the experimental data provides us with the information for the density deficit δ, or equivalently for the density ρ and for the height of the horizontal flow. Further, by fitting a fourth order symmetric polynomial to the experimental fits for the density deficit δ_h variation along r, knowledge for the density deficit at each point $r \in [1\,,0]$ rather than the discrete measurement fixed positions is achieved. The computational domain under consideration is $r \in [r_h,\, 1^-]$ with r_h being the value of r at which the horizontal model ceases to be valid ($r_h = 0.3$ is assumed), while 1^- is approximated by 0.9999. The domain [0.3, 0.999] is partitioned into subintervals created as

$$r_{i+1} = r_i - k \quad \text{for } i = 2, 3 \ldots n-1, n \quad \text{and } k = \frac{r_h - 1}{n-1}$$
$$\text{while} \quad r_1 = 0.9999 \quad \text{and} \quad r_2 = \frac{89}{90}. \tag{6.32}$$

Taking $n = 63$ or $k = 1/90$, 62 equal subintervals are generated plus the first one from $[89/90, 0.9999]$.

Reflecting on the asymptotic behaviour of q around $r = 1$ (6.29) we can further suppose that the heat flux can be expressed in the following functional form

$$q = \sqrt{1-r}\left(\hat{q}_i + \frac{r - r_i}{r_{i+1} - r_i}(\hat{q}_{i+1} - \hat{q}_i)\right). \tag{6.33}$$

With $\hat{q}_i$ and $\hat{q}_{i+1}$ representing the constant values of $\hat{q}$ at r_i and r_{i+1} . In other words linear interpolation is assumed for $\hat{q}$ at each subinterval. Now by differentiating q an additional differential equation valid for $\forall r \in [r_i, r_{i+1}]$ is introduced i.e.

$$\frac{\mathrm{d}q}{\mathrm{dr}} = \sqrt{1-r}\left(\frac{\hat{q}_{i+1} - \hat{q}_i}{r_{i+1} - r_i}\right) - \frac{1}{2}(1-r)^{-\frac{1}{2}}\left(\hat{q}_i + \frac{r - r_i}{r_{i+1} - r_i}(\hat{q}_{i+1} - \hat{q}_i)\right). \tag{6.34a}$$

In addition the constants $\hat{q}_i$,$\hat{q}_{i+1}$ can be written as ODEs

$$\frac{\mathrm{d}\hat{q}_i}{\mathrm{dr}} = 0, \quad \frac{\mathrm{d}\hat{q}_{i+1}}{\mathrm{dr}} = 0 \quad \forall\, r \in [r_i, r_{i+1}]. \tag{6.34b}$$

The introduction of three additional differential equations is purely for reasons of numerical formulation. The behaviour of the dependent variables m, q, ρ and U from $r = 1$ to $r = 0.9999$, is that described by the local analysis, therefore knowledge of the dependent variables exists at $r = 0.9999$. Having created this one dimensional grid, for each closed subinterval $[r_{i+1}, r_i]$, the number of unknowns is six, namely $\rho, u, m, q, \hat{q}_i$ and $\hat{q}_{i+1}$. Not neglecting the integral constraint, for each subinterval the following integral is introduced

$$t_i = -\int_{r_i}^{r_{i+1}} rq\,\mathrm{dr}. \tag{6.34c}$$

The system of equations can now be considered theoretically closed (i.e. six differential equations and six unknowns) once suitable boundary conditions are provided. The numerical formulation followed is almost straightforward, and it will only make use of the information of the data fit to the density deficit δ_h, or more accurately the least squares fit to the density deficit. The starting point has to be the local analysis, as it was shown initial conditions can be provided in $r_1 = 0.9999$ i.e $r = 1^-$ using (6.28), for q, m, u and ρ. For the constants $\hat{q}_1$ is not hard to see that that by setting $r = r_1$ into (6.33) that $q(r_1) = \sqrt{1 - r_i}\hat{q}_1$ so that

$$\hat{q}_1 = \frac{(1 - \hat{\rho})\hat{U}}{2\sqrt{\hat{\rho}}}. \tag{6.35}$$

It is clear that no information can be given for $\hat{q}_2$, when trying to formulate the problem as an IVP, for that reason the problem will be formulated as shooting one. At $r = r_2$ knowledge of $\delta_h(r_2)$, or equivalently of $\rho(r_2)$, allows us to provide a guess (with the objective of us fitting results, to the experimental data) β_1 as an initial condition for the $\hat{q}_2$, i.e. $\hat{q}_2(r_1) = \beta_1$, and set up an iterative process, in which improved estimates of β_1 are made, by shooting from r_1 to r_2 until the value obtained for $\rho(r_2)$ agrees with the fitted value to the experimental data. Once the process is complete, numerical information for all variables is obtained in $[r_1, r_2]$, and the integral $t_1 = -\int_{r_1}^{r_2} rq\mathrm{dr}$ is numerically evaluated. The same procedure is repeated in all the remaining subintervals. Once the computations are concluded, a check condition is applied

$$\Big|\sum_{i=1}^{n} t_i + \int_0^{r_h} rq_n\,\mathrm{dr} - \frac{1}{2}\Big| < 10^{-3}. \tag{6.36}$$

The above condition represents nothing else than the integral constraint. The second term on the l.h.s incorporates an assumption that the heat flux from $r_h = 0.3$ to $r = 0$

remains constant. As mentioned earlier an additional unknown is contained in the system of equations, through the nondimemensional parameter $\mathbf{a} = f(\alpha, Q)$. Provided that Q is estimated correctly, then $\mathbf{a}$ can be considered to be only a function of α i.e. $\mathbf{a} = \mathbf{F}(\alpha_\mathbf{h})$. If (6.36) is not satisfied then the value of $\mathbf{a}$ is altered (which means that α is altered), and the whole computational process is repeated again, until 6.36 is satisfied. In that way the constant of entrainment α_h which initially was set to be equal to 1/8; also calculated so as to obtain a good fit to the experimental data. In that way all the unknowns are determined and the theoretical model can be compared to the experimental results.

Alternatively because the dimensionless plume height also depends on α_h as seen in (6.26), the value of α_h could be estimated so as to arrive at a best match between the dimensional experimental heights $H(r)$ and the modelled equivalents. Using the value of α_h obtained in that way, it could also be applied in the definition of the $\mathbf{a}$ to recover the heat flux so that a comparison could be made with the value obtained using the power data.

6.5.1 Numerical results

Provided that the estimates for the heat flux into the plate are accurate enough, for the four experiments considered here, namely target plate temperatures of 50°C, 60°C, 80°C and 100°C numerical computations indicate that fulfilment of the integral constraint is achieved for values of $\mathbf{a}$ and consequently for values of the constant of entrainment α_h, listed in Table 6.2

Target plate temperature (°C)	$\mathbf{a}$	α_h
50°C	6.838×10^7	1.513
60°C	2.84×10^7	1.382
80°C	9.57×10^6	1.453
100°C	3.437×10^6	1.333

Table 6.2: Values obtained for the constant of entrainment, based on the assumption of accurate estimates of the power to the plate.

It must be recalled that for the exponential distribution chosen the ‘top hat like’ equations were obtained after the employment of definitions given in equation (6.22), which when combined with (6.26) results in

$$\alpha_h = \frac{2H}{Lh'}, \quad Q = 2\pi(\rho_\mathrm{e} \mathrm{c}_\mathrm{p} T_\mathrm{e})\left(\frac{g\alpha_h^3 L^5}{\mathbf{a}}\right)^{1/2}, \quad U = \left(\frac{Lg\alpha_h}{\mathbf{a}}\right)^{1/2} U'. \tag{6.37}$$

Introduction of a correction dimensional parameter ϵ [m], for the nondimensional height of the plume h' such that $H \approx \epsilon h'$, enables the matching of the height obtained numerically with the one obtained from the experimental data, where possible. In Figure 6.11 a demonstration is given. In doing so, the constant of entrainment α_h can be estimated, as $\alpha_h = 2\epsilon/L$. Knowledge of the constant of entrainment will then be used for calculating the heating power entering the plate using the second equation in (6.37). Analytical results are presenter in Table 6.3.

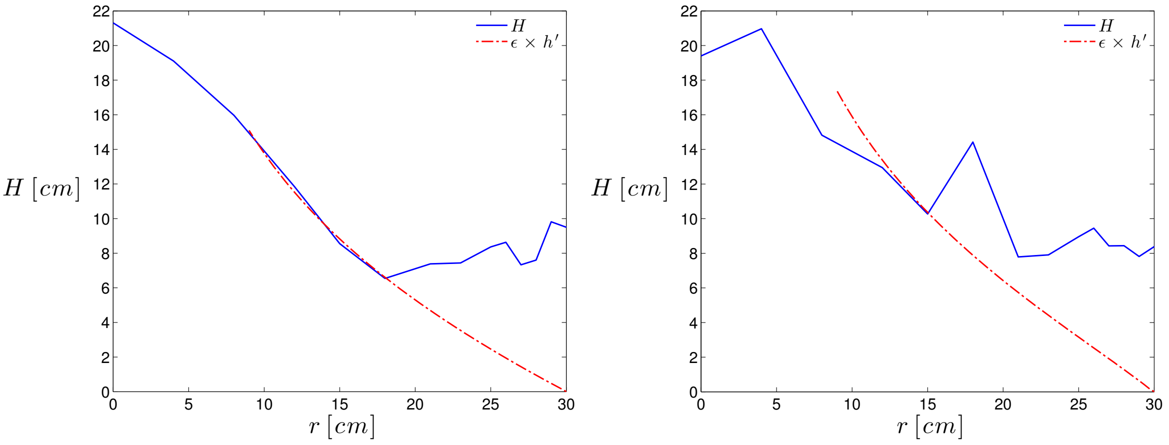

(a) 50°C (b) 60°C

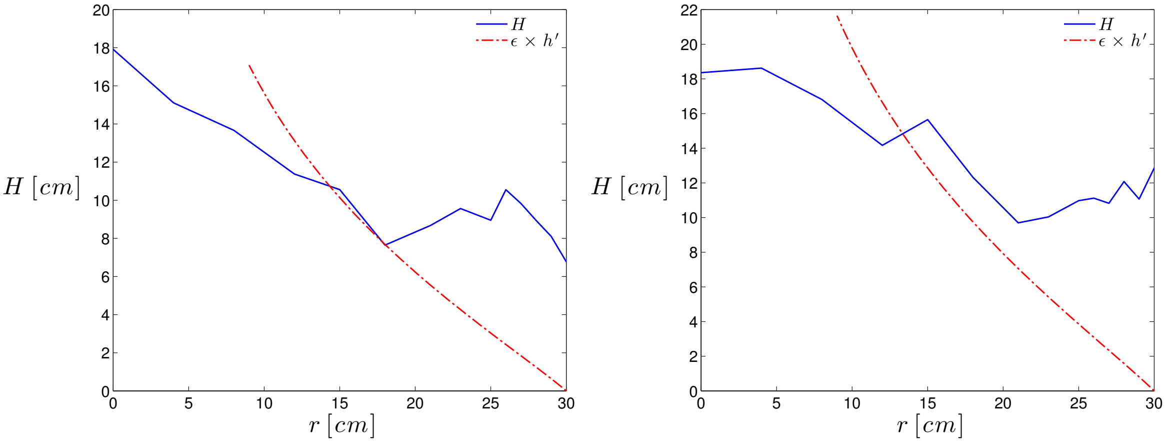

(c) 80°C (d) 100°C

Figure 6.11: Nondimensional computed plume height h', is modified by the parameter ϵ, so as to match the experimental height H.

Looking at the results obtained when the experimental height data are not considered the theoretical model provides a constant of entrainment that is around 1.5

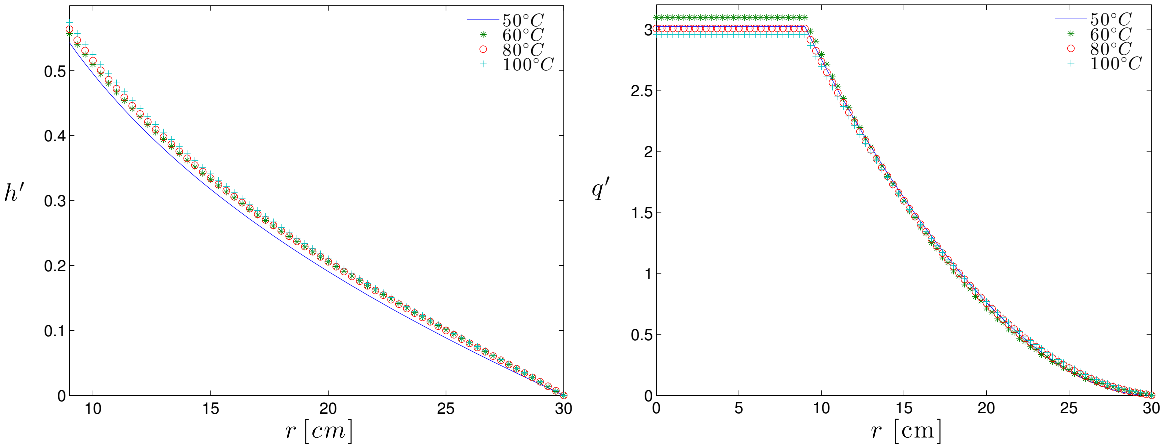

(a) Computed nondimensional height of the plume h'

(b) Computed nondimensional heat flux q'

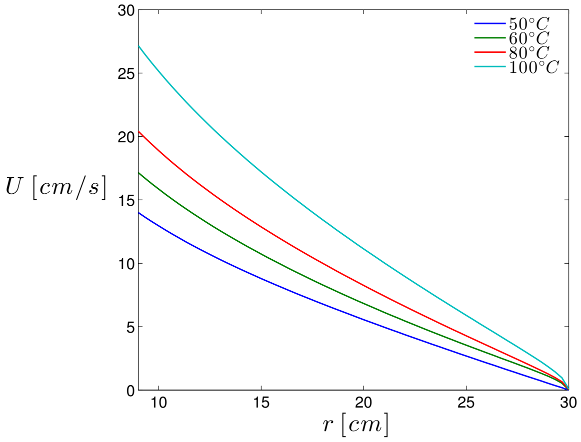

(c) Dimensional computed velocity U

Figure 6.12: Computed horizontal flow parameters for different target plate temperatures.

Target plate temperature (°C)	**a**	α_h	Q [W]	Q_{est} [W]	ϵ [cm]
50°C	6.838×10^7	1.853	105	77.5	27.8
60°C	2.84×10^7	2.08	194	105	31.2
80°C	9.57×10^6	2.021	320	195	30.3
100°C	3.437×10^6	2.513	740	286	37.7

Table 6.3: Results obtained for the constant of entrainment after fulfilling numerically the integral constraint for the average power to the plate. Once the value of **a** is recovered a plume height correction parameter is introduced so that computed and experimental height of the plume match. Use of that parameter leads us to the numeric value of the constant of entrainment α_h, which enable us to evaluate average power to the plate Q and compare it with the estimates Q_{est}.

while the value of **a** is large. When the matching of computational and experimental height is attempted the value of the constant of entrainment increases and is around two. Therefore in both case the value is much larger than the one expected for the vertical plume flow (i.e 1/8). When using height data to estimate α_h the values of the heating power are significantly higher than the estimates obtained from the power data, by a margin that seems to be beyond any usual experimental error. Clearly by revisiting Figure 6.11, it can be observed that in all cases, experimental data indicate that the height of the plume at the edge of the plate varies from 8cm to around 12cm. Due to insulation problems clearly seen in infrared pictures the actual size of the area heated is larger than the one actual modelled. Therefore the real flow taking place can roughly be described as the one above a larger plate of unknown size, being at a higher non-uniform temperature than the environment and surrounding the actual experiment plate. For example in Figure 6.13, infrared images for the experiment at target plate temperature of 100°C presented. Ambient temperature measurements indicate that the mean ambient temperature for the experiment is $T_{\text{e}} = 16.4$°C, though the infrared images manifest the problem, since the minimum temperature recorded in the region surrounding the plate is $T = 21.3$°C. That surely must result in an asymmetric external flow moving towards the edge of the plate and acting as a perturbation on the actual flow modelled. It is therefore expected that a horizontal plume structure is already in existence around the edge of the plate, which explains why the measured experimental heights H are significantly different from zero at $r = 30$cm. Moreover, the height profiles seen in Figure 6.11 show effects that are not consistent with the generation of a plume only over the heated plate.

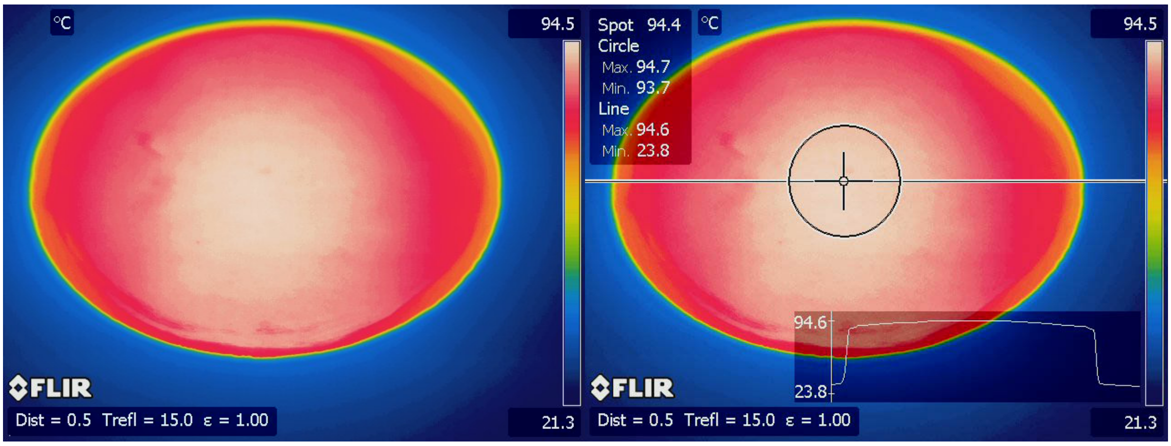

(a) (b)

Figure 6.13: IR images for the experiment at target temperature of 100°C .

Concluding, it is practically impossible to arrive at acceptable conclusions from the results obtained here since the experiment clearly failed to produce flow that the theoretical model was built to represent. It is therefore unfortunate but no useful information can be extracted w.r.t the entrainment hypothesis and the constant of entrainment, used for the horizontal plume flow. A major failing of the experiment was in maintaining a steady energy supply to the plate. Coupled with the problematic visualisation of the flow and especially the really poor quality of the videos capturing the whole flow (practically of no use), very little information can be obtained for the transition of horizontal buoyant current to vertical plume structure.

Nevertheless the methodology used here is appropriate and ready to be applied whenever better experimental data are available. Generation of a pure plume structure (no momentum at the source) does not seem to have been achieved in these laboratory experiments. Difficulties arise due to relatively small flow velocities, which makes the flow sensitive to unsteadiness in the energy supply rate and to outside disturbances, and which in turn are hard to measure [17]. Therefore in designing a future experiment, a few important features of the current experiment need addressing.

- Accurate monitoring and control of the source conditions.
- A vertical array of thermocouples positioned at different heights and in the ambient so that the stratification of the ambient can be monitored.

An important characteristic of the classic plume flow is that the rate at which buoyancy is added at the source must, for a neutral environment, be equal to the buoyancy integral at each height [26] . That is because for an ideal gas conservation of energy implies conservation of buoyancy so that the integrals of these quantities must equal the values at the source [82]. It is critical therefore that the conditions at the source, are carefully monitored so that problems faced here for the analysis of the horizontal flow are not repeated, while the analysis of the classic plume should allow for comparison of the buoyancy integrals with the source conditions. Stratification of the ambient is difficult to avoid in a laboratory generated plume, due to to long time scales that the experiments need to achieve statistical equilibrium, causing an inversion layer to be built up at the ceiling. The need for an array of well-calibrated thermocouples placed in the ambient and at heights covering the actual plume measurements is needed for determining the degree to which stratification causes warmer ambient fluid to be entrained into the plume as well as reducing buoyancy. Following [17] by defining a parameter S as

$$S = -\frac{g}{\rho_{\mathrm{e,s}}}\frac{\mathrm{d}\rho_{\mathrm{e}}}{\mathrm{dz}}, \tag{6.38}$$

where $\rho_{\mathrm{e,s}}$ is the density at the height of the source while ρ_{e} is the local density, then depending on the value of S, the following cases are defined; the environment is stably stratified when $S > 0$, neutrally stratified or unstratified when $S = 0$ and unstably stratified when $S < 0$. In a realistic laboratory environment the condition $S \to 0$ is ideal for stratification effects to be neglected.

- Reexamination of the time scales of the flow so as to ensure that statistically stable averages at different heights are present.
- A reassessment concerning the source
- The particle feeding for the visualisation flow.

For completeness the final two brief sections of this Chapter are dedicated to the numerical simulation of the experiment using $k - \epsilon$ and $k - \omega$ turbulence models, and the visualisation of the flow using particle image velocimetry (PIV) analysis.

6.6 Numerical simulation of the experiment using $k-\epsilon$ and $k-\omega$ turbulence models

Two equation models for turbulence have become increasingly popular over the last few decades specifically the $k-\epsilon$ and $k-\omega$ models accompanying the ever increasing computational power. Their foundations though date back to Kolmogorov and Prandtl [99]. With k representing the specific turbulence kinetic energy, ϵ the specific dissipation and ω the specific dissipation rate. The closure of the averaged Navier Stokes equations is obtained by computing the eddy viscosity μ_T using k and ϵ or k and ω. The dimensions of the above stated parameters are given as k $[L^2/T^2]$, ω $[T^{-1}]$, ϵ $[L^2/T^3]$ while for μ_T the dimension are $[M/L^4T]$. With M representing mass, L length and T time. On dimensional grounds therefore the eddy viscosity is modelled as

$$\mu_T = \rho C_\mu \frac{k^2}{\epsilon} \quad \text{in Standard}\, k-\epsilon, \tag{6.39a}$$

$$\mu_T = \rho \frac{k}{\omega} \quad \text{in} \quad k-\omega, \tag{6.39b}$$

with a closure coefficient given as $C_\mu = 0.09$. The eddy viscosity closure therefore introduces two additional transport equations depending on the chosen model. For a detailed description the reader can refer to the textbook of Wilcox [99].

There is an active discussion in the turbulence modelling community concerning modifications necessary to the classic $k-\epsilon$ turbulence model in order to successfully describe free buoyant plumes [8] [100] [65] [54]. The reason being that when the standard form of the $k-\epsilon$ is used to model round buoyant plume flows it over-predicts the velocities and temperature variations along the line of axisymmetry resulting in thinner widths for the velocity and the Temperature. An additional term is normally inserted in the turbulent kinetic energy equation, representing buoyancy production and different methods are followed to model it, but this is outside the scope of this short section.

We shall apply the standard $k-\epsilon$ and $k-\omega$ model to numerically simulate the target temperature experiment of 100°C. The numerical simulation is carried in COMSOL Multiphysics 3.5a using the Chemical Engineering module and the $k-\epsilon$ $k-\omega$ models.

Due to the problematic nature of the data collected, as reported in this chapter, a simulation of the HS1 experiment of Nam and Bill [65] was carried out so as to determine the the behaviour of COMSOL, presented in Figure 6.14 The results obtained when

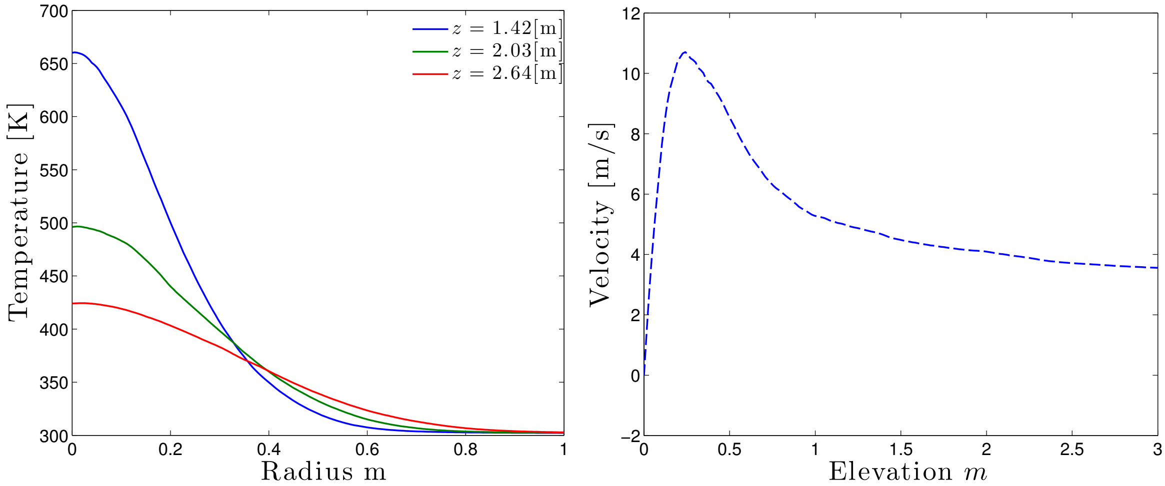

(a) (b)

Figure 6.14: $k - \epsilon$ simulation of HS1 experiment [65]. Pool fire of diameter 0.688 m and heat flux 440.1 kW/m^2. (a) Temperature variation at fixed height along the radius. (b) Velocity variation along the axis of symmetry.

compared to the ones given in [65], indicate that there is a reasonable agreement with the temperature profiles. The situation is slightly different concerning the variation of the velocity along the axis of symmetry, but only close to the source from zero to approximately one, where significantly higher velocity is obtained. Further above, the results obtained are satisfactory.

Turning attention to the simulation of the experiment of target plate temperature 100°C, we are faced with the problem of what might be the correct boundary conditions at the source and next to the source. IR images indicate that the temperature is not uniform, while the area next to the plate due to problems with insulation is at a higher temperature than the ambient. In addition the thermocouple readings indicate that at heights of 1cm above the plate the temperature is under 40°C. Given the uncertainties introduced in the numerical formulation by the lack of neat boundary conditions, it was decided that at the bottom of a square domain of length 1.5m which is used for the two-dimensional axisymmetric simulation, a uniform temperature condition of 40°C is suitable and will be imposed on the plate, while a thermal insulation condition is applied to the remaining part of that boundary. For the top boundary, convective heat flux and normal flow conditions are imposed while tangential velocities are set to zero. Similar constraints apply for the right boundary only with the difference that ambient temperature is imposed. Finally for the left boundary axial symmetry conditions are imposed.

In the $k-\epsilon$ model, initial computations carried, were based on the standard closure coefficients given in [99], but results obtained were unsatisfactory, since the temperature variation along the centerline was found to be significantly higher than the experimental measurements indicate. For that it was decided to change the value of the closure coefficients C_μ and σ_k as in [65]. Therefore $C_\mu = 0.09$ was changed to $C_\mu = 0.18$ and $\sigma_k = 1$ to $\sigma_k = 0.85$. With respect to the data, least squares Gaussian fits for the mean profiles of the temperature of the form

$$T = T_{\mathrm{v}} \exp \frac{-r^2}{B^2}, \tag{6.40}$$

were obtained and presented in Figure 6.15.

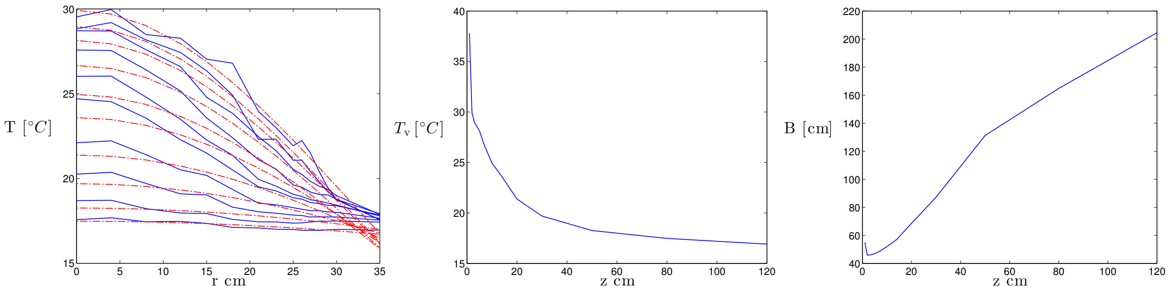

(a) (b) (c)

Figure 6.15: (a) Least squares Gaussian fit to the mean temperature data, (b) Variation of T_{v} with height, (c) variation of B with height.

A comparison between numerical simulations using $k-\epsilon$, $k-\omega$ with the experimental results, is given in Figures 6.16 and 6.17. No profound conclusions can be drawn from the current analysis, other than that a simple modification in the closure constants of the $k-\epsilon$ model, result in a solution that improves the fit to the data . It must be noted that before the change in the parameters the behaviour obtained from the $k-\epsilon$ model did not differ significantly from the one produced here by the $k-\omega$ model. The uncertainty in the data, in addition to the fact that the numerical simulation corresponds to a controlled experiment, makes any further analysis of little value.

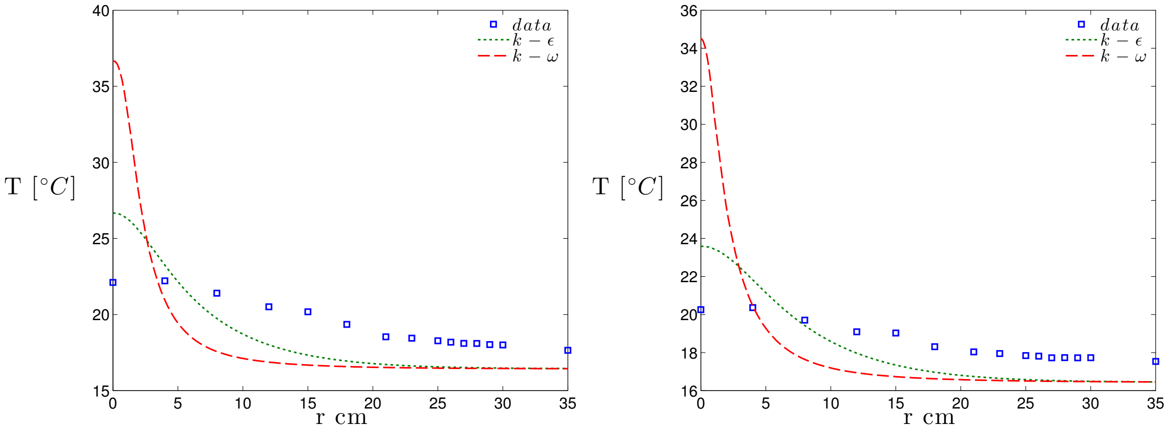

(a) $z = 20$cm (b) $z = 30$cm

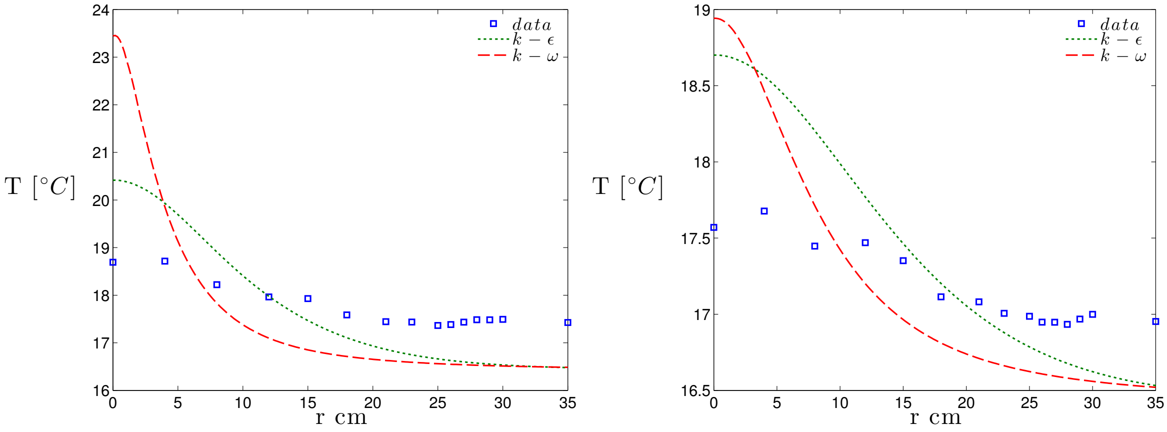

(c) $z = 50$cm (d) $z = 80$cm

Figure 6.16: Radial variation of the mean temperature at a fixed height.

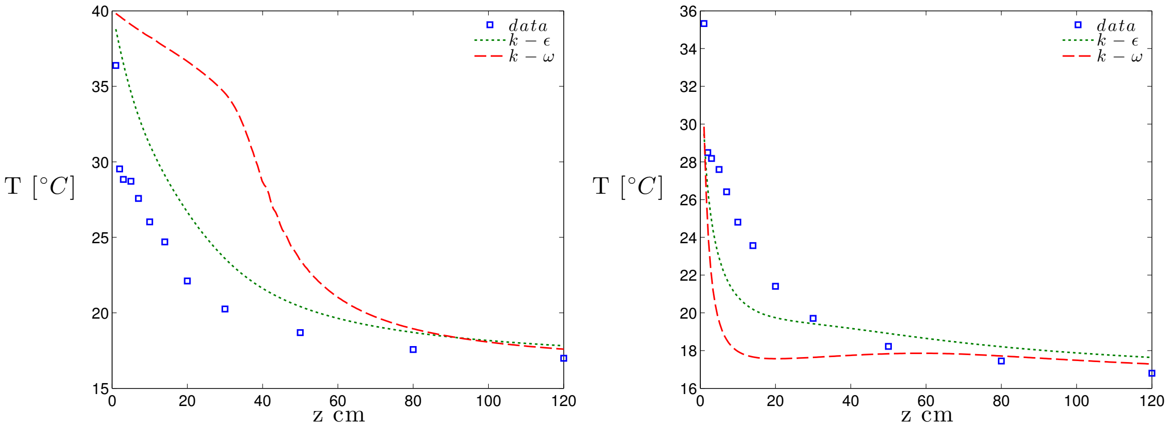

(a) $r = 0$cm (b) $r = 8$cm

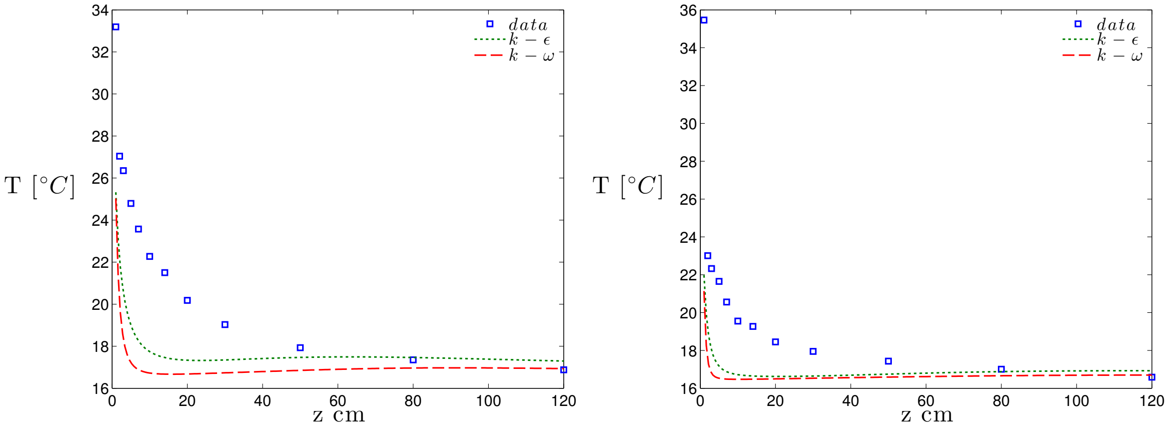

(c) $r = 15$cm (d) $r = 23$cm

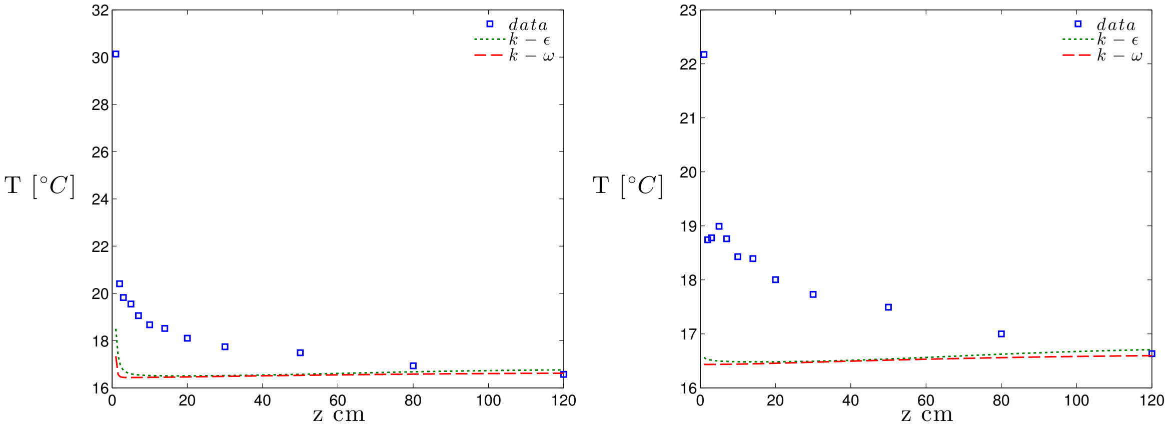

(e) $r = 28$cm (f) $r = 30$cm

Figure 6.17: Fixing r ($r = 0$ cm being the centre of the plate) the variation of temperature with height is plotted.

6.7 Visualisation of the flow

6.7.1 Particle image velocimetry (PIV)

In this final section of the chapter the analysis of the video data is attempted. Numerous problems encountered in the process and the analysis made this far from straightforward. As mentioned earlier, two high resolution cameras were supposed to record the flow, each one suitably placed, for the collection of information serving different purposes. The role of the lower camera, as shown in the schematic diagram given in Figure 6.2 was to record the flow just above the plate, while the camera positioned above was meant to capture the complete flow field. Snapshots obtained from original video files are shown below in Figure 6.18. Unfortunately the quality of information contained in videos obtained from the top camera, responsible for providing information for the velocity field of the whole experiment was poor. Adding the fact that there was no length calibration to the images, forced us to abandon their analysis. Therefore in what follows the focus lies solely in the analysis of the velocity field just above the plate.

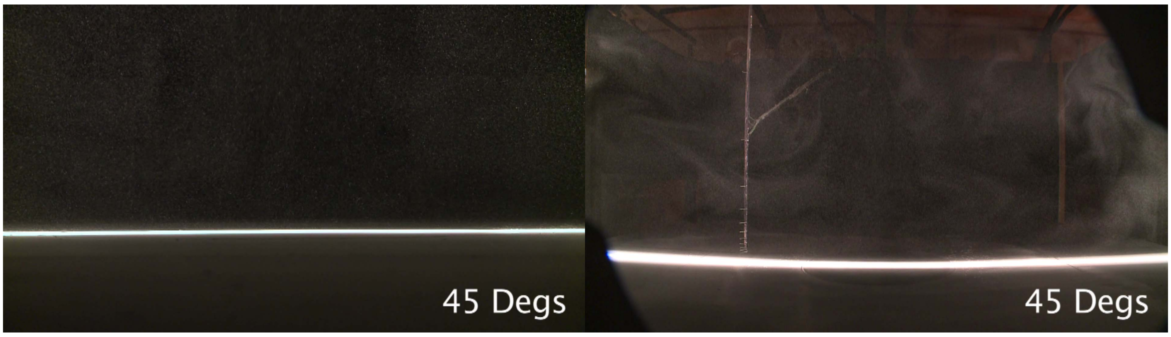

(a) (b)

Figure 6.18: Snapshots obtained from the original video files. (a) Camera focused on the flow just above the plate, (b) Camera capturing the whole flow field.

It was originally believed that a commercial software package for particle tracking velocimetry (PTV), could be used for the analysis. Serious problems with the format of the data led us to reconsider this and further our options. Instead we opted for the particle image velocimetry method (PIV), and two excellent open software PIV analysis tools MatPIV [37], [91], and PIVlab [94], were tested. Results presented here were obtained using PIVlab.

Briefly the principle of PIV lies on pattern matching. Given a pair of sequential images A and B obtained at times t_A and t_B respectively so that $\Delta t = t_B - t_A$. The procedure is to divide images A and B into sub-images or subwindows of side length (pixels) $N = 2^n$ (commonly $n = 4, 5, 6$). Once the partition of the images is complete then a subwindow from image A is compared with its corresponding subwindow in image B. That is carried out using cross-correlation so that a displacement pattern is uncovered. Given this information for displacement and the time that it took to happen, velocity information can be recovered. Detailed theoretical background of the method can be found in [37] and [71].

It is often the case that the contrast between particle and background is not up to the desired level, so that contrast enhancement techniques were applied [75], [21], in order to address the problem. Additionally the presence of bright spots caused by intense scattering from larger seed particles can also lead to erroneous cross-correlation, so that intensity capping [84] is recommended. For the purposes of our analysis image prepossessing was carried, in the form of masking and contrast enhancement while capping was introduced in PIVlab.

6.7.2 Results and discussion

Results obtained for two target temperature experiments are presented here, the one at 60°C and the other at 100°C. For target temperature 60°C, 100 frames were used for the calculation of the averages (i.e.$(3.333s)$). Instead for the experiment at target temperature 100°C, a more extensive analysis of 500 frames was carried. Finally for the calibration the length of the image was assumed to be 80cm, which is a reasonable approximation. The lack of calibration, the non uniform seeding of particles into the flow, (videos indicate abundance of particles just from one side and at cases of higher density than should be ideal) and the fact that the recording could have been of a better quality, make the results not very accurate.

In spite of the difficulties, results obtained suggest that the basic structure of the flow proposed theoretically by the horizontal plume model is correct. In all cases studied, there is a horizontal inflow moving from outside the plate (the edge if the boundary conditions where neat) towards a region around the centre, where it turns to vertical. The transition to vertical flow seems to happen through the meeting of the horizontal streams with strong vortex rolls as can be seen in Figures 6.23 and 6.24. Interestingly, and as was suspected a stagnation point seems to be present just below the region where the vertical flow arises (Figure 6.20). Furthermore looking at the behaviour of the vertical component of the velocity Figure 6.22, there are three dominant regions, one central, one moving upward and two ‘symmetric’ parts moving in the opposite direction and indicating that there is a structure entraining vertically.

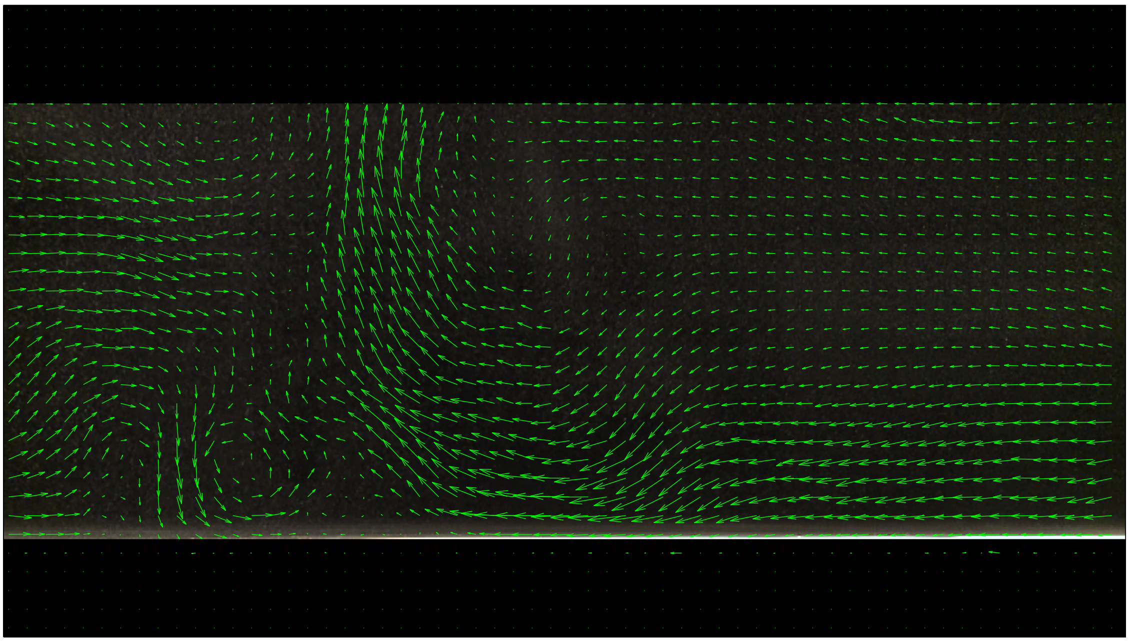

(a)

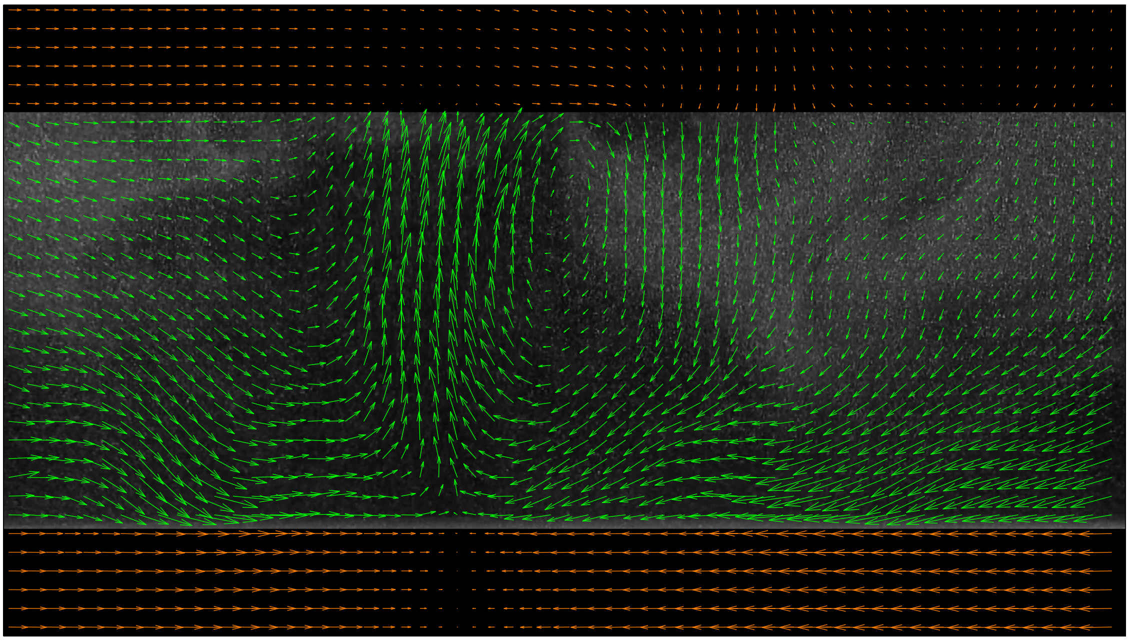

(b)

Figure 6.19: (a) Vector field at target temperature of 60°C, (b) Vector field at target temperature of 100°C.

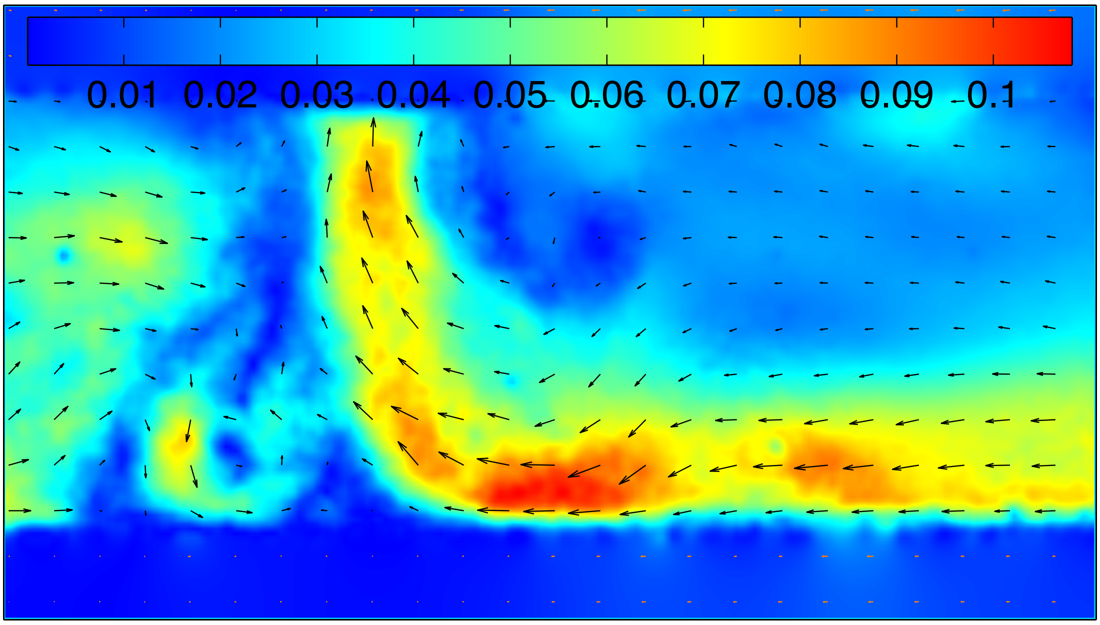

(a)

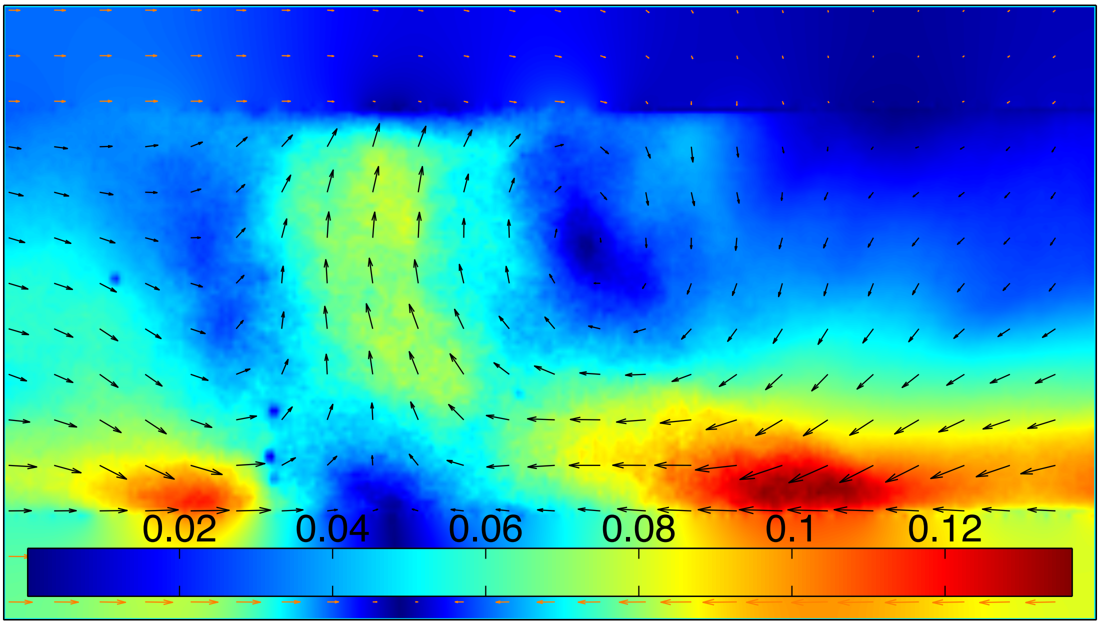

(b)

Figure 6.20: (a) Velocity field at target temperature of 60°C, (b) Velocity field at target temperature of 100°C, [m/s].

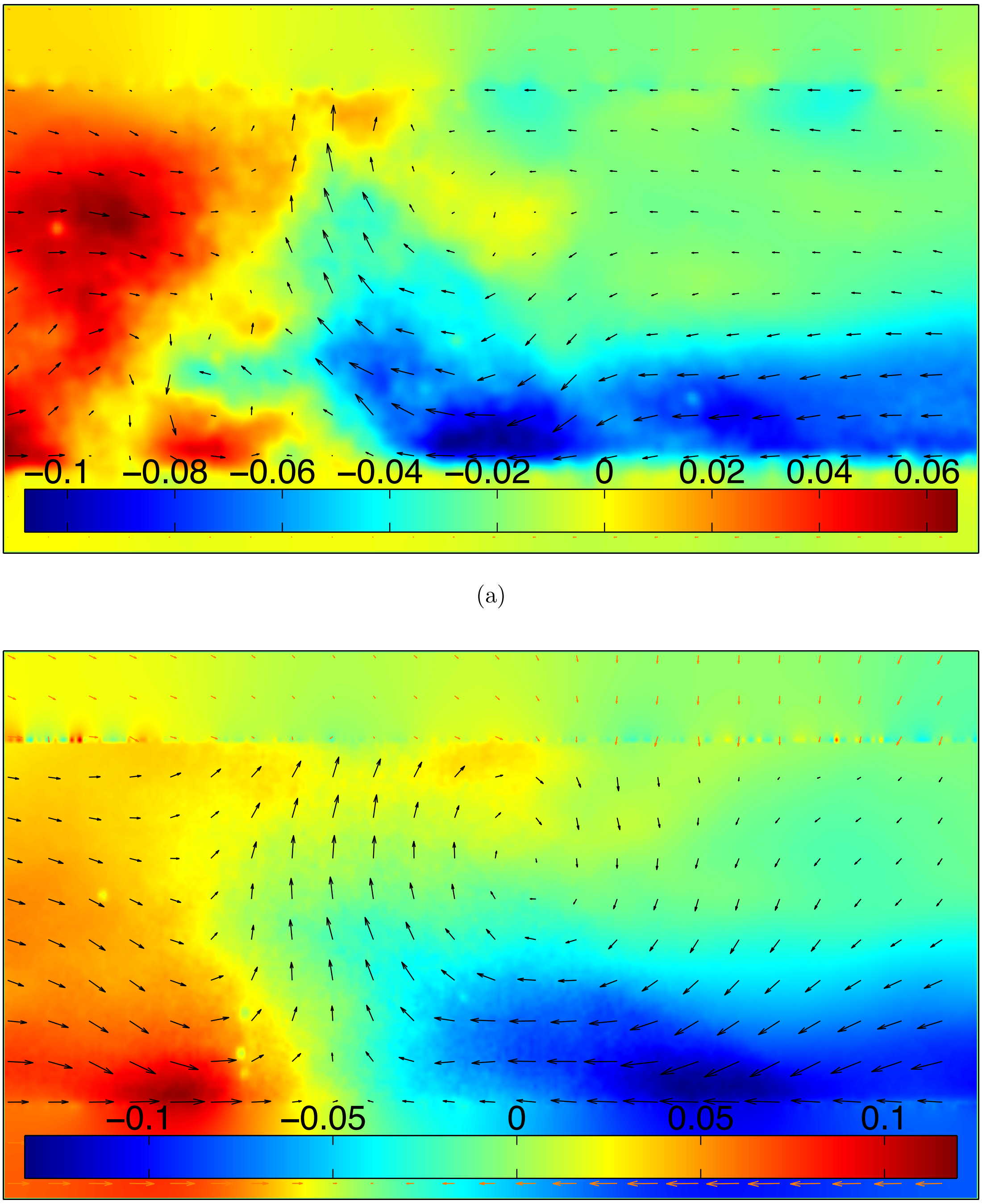

(a)

(b)

Figure 6.21: (a) Horizontal component of velocity at target temperature of 60°C, (b) Horizontal component of velocity at target temperature of 100°C, [m/s].

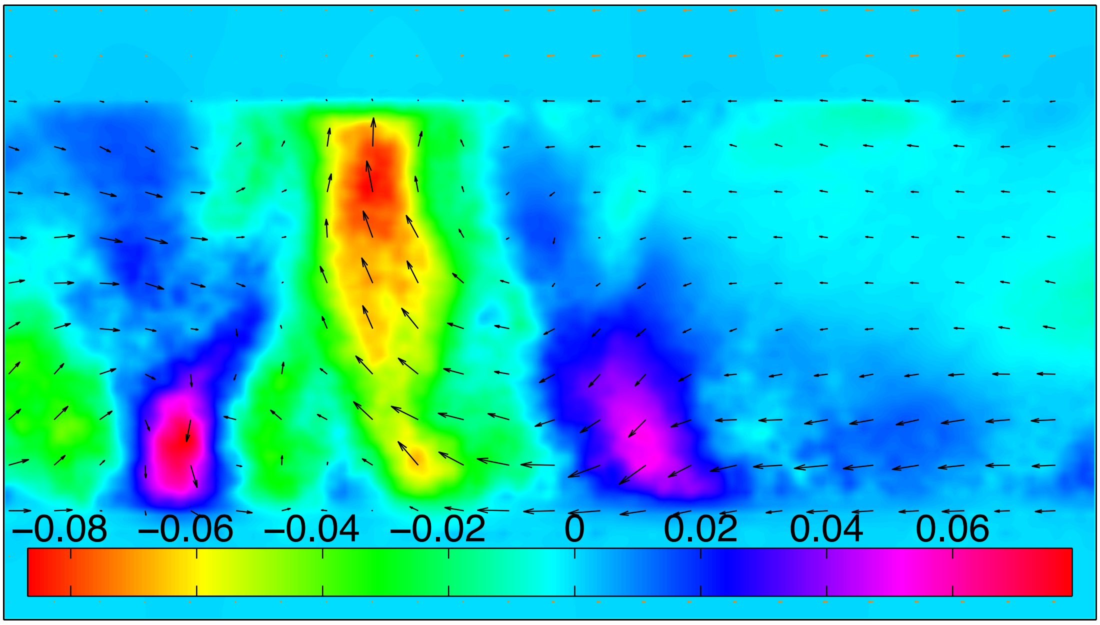

(a)

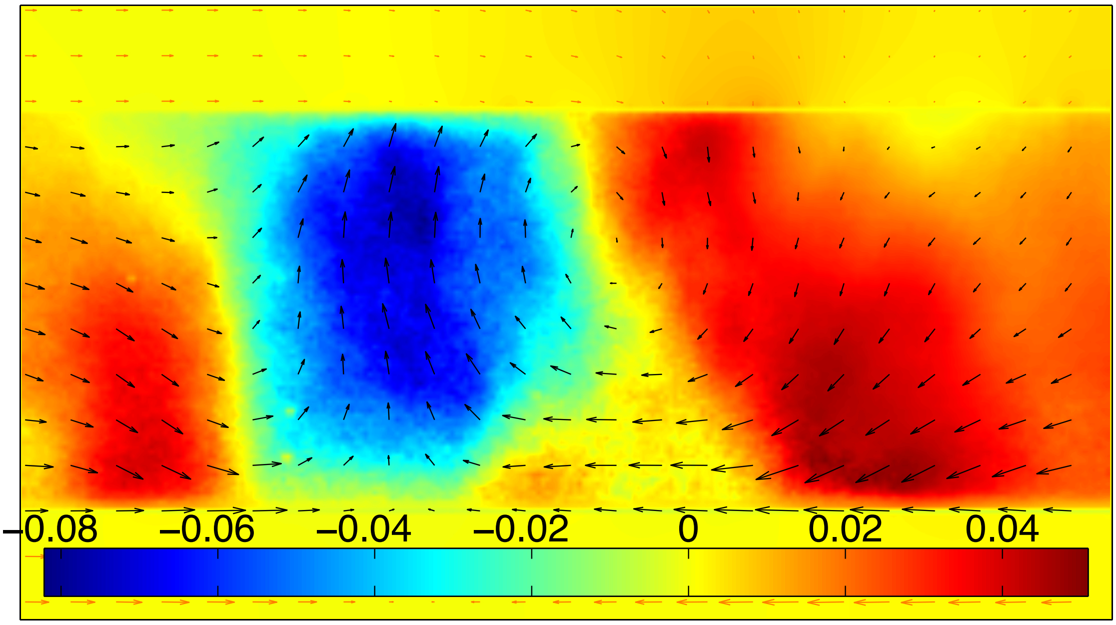

(b)

Figure 6.22: (a) Vertical component of velocity at target temperature of 60°C, (b) Vertical component of velocity at target temperature of 100°C, [m/s].

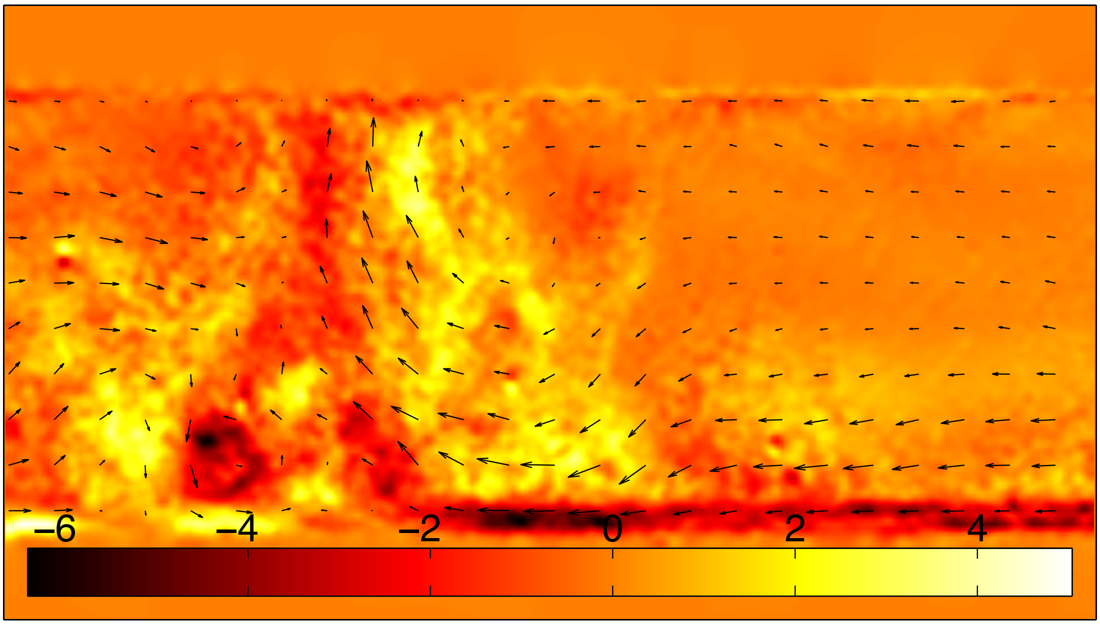

(a)

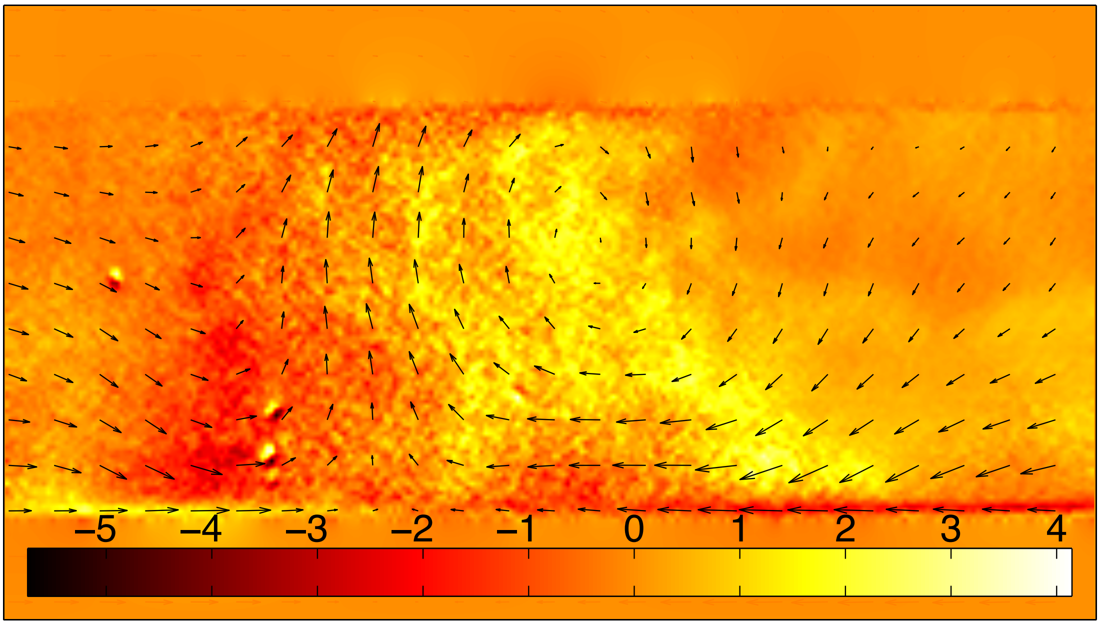

(b)

Figure 6.23: (a) Vorticity for the experiment at target temperature of 60°C, (b) Vorticity for the experiment at target temperature of 100°C, [1/s].

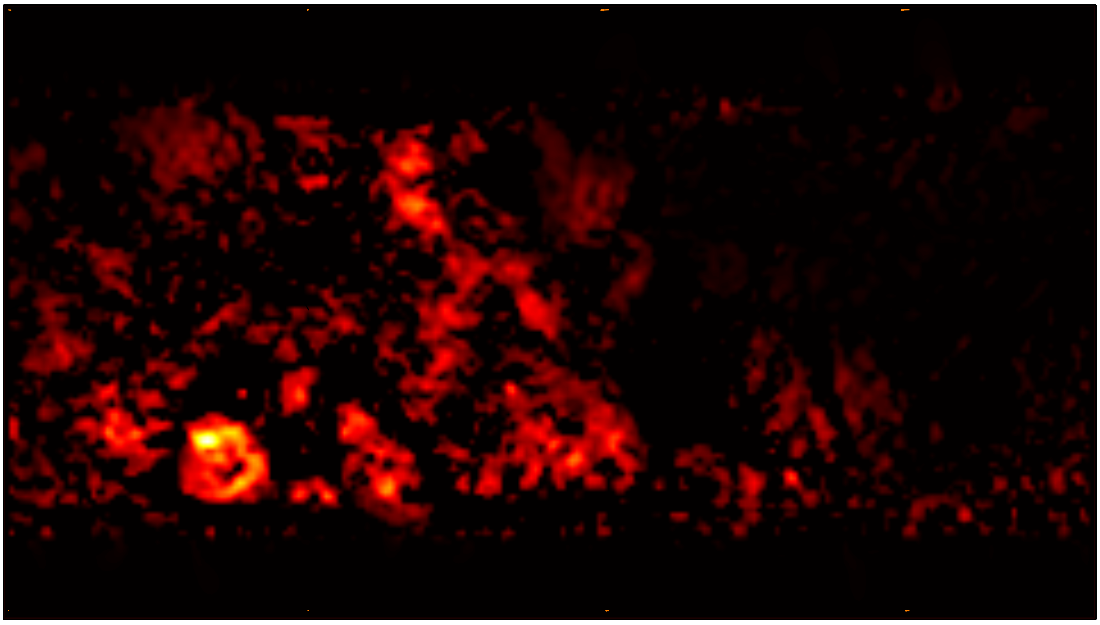

(a)

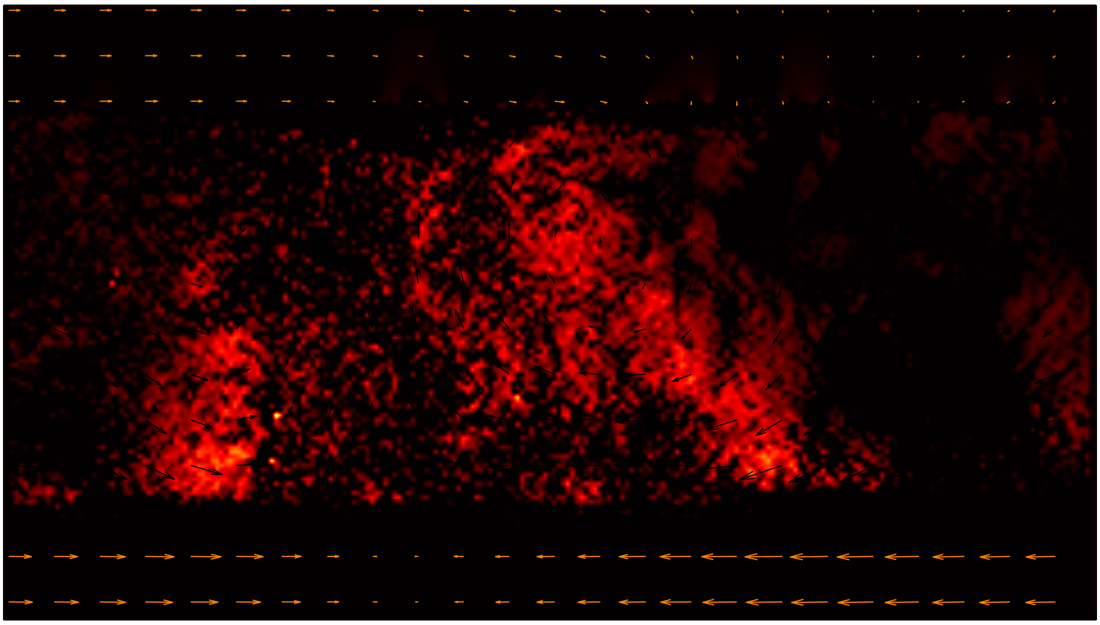

(b)

Figure 6.24: (a)Vortex locator at target temperature of 60°C, (b) Vortex locator at target temperature of 100°C.

(a)

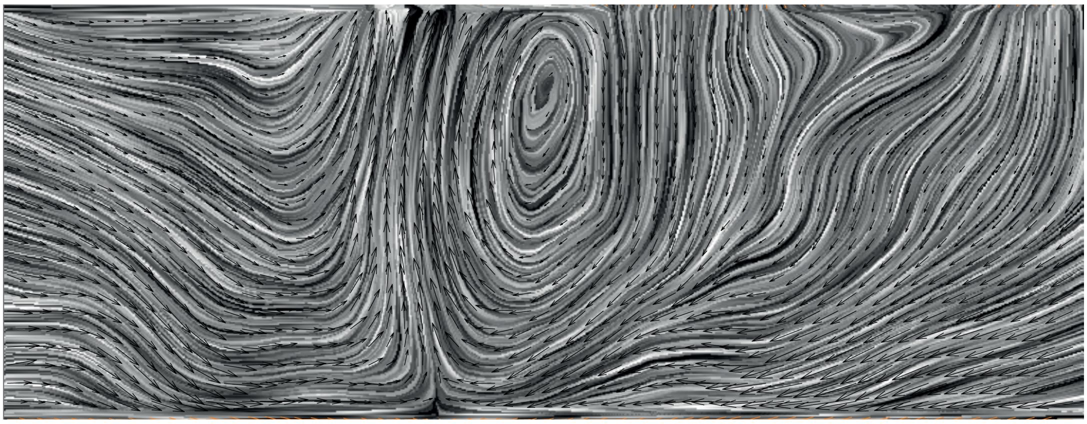

(b)

Figure 6.25: (a) Target temperature of 100°C (b) Target temperature of 60°C Representation of the velocity vector field using the line integral convolution method (LIC) [5]

Chapter 7

Conclusions

Figure 7.1: Plume generated by a spiral ignition in a 4 ha plot in South Africa in June 2012.

In the heart of this thesis was the development of a theoretical model that could describe the buoyant flow above large area fires. Classic plume theory assumptions must fail close to an impermeable heat source of large area firstly on dimensional grounds since the characteristic length of the source is an important parameter that is neglected. Most importantly classic plume theory fails to describe the attached and indirectly induced horizontal buoyant currents, observed above large area fires. These currents move inwardly from the edges of the area (independently of the geometry) and at certain locations depending on the wind, the topography, and the fuel, collide and separate to give rise to the roots of a vertical buoyant structure, the well known plume. Any independently formed plumes resulting from these collisions unite under the coanda effect at some height above the surface to then form a dominant rising plume.

Therefore a formal description for the buoyant flow above a large area fire, must include the attached horizontal buoyant currents mentioned above. Due to the complexity of such a turbulent flow and an endeavour to produce a model that predicts the gross features of such a flow, simplifications were introduced in the modelling. Firstly combustion and radiation effects were neglected while the geometry considered, was that of a circular disk of radius L (axisymmetric flow), supplied by constant heat flux q. In addition the environment was assumed unstratified and still, so that the modelling could solely focus on the free convective flow above the fire, disregarding external driving factors.

For the description of the buoyant flow above a circular region of large radius L, a radical approach was suggested. *The flow field must be divided into three regions. A region where the flow is predominantly horizontal and attached to the surface, a transition region from horizontal to vertical where separation of the attached current takes place, and a region where vertical flow is established and classic plume theory can be applied.*

For the description of the horizontal buoyant currents a ‘horizontal plume’ model was developed. Based on conservation principles of mass, momentum and energy, accompanied by the adoption of ‘top hat’ formalism, as well as an entrainment hypothesis that resembled the one used for the classic non-Boussinesq plume, a set of a differential algebraic system equations was obtained. In their nondimensional form, the set of governing model equations were shown to contain a parameter $\mathbf{a}$, of nature similar to Richardson number Ri, which we termed as the modified Richardson number for the horizontal plume. The parameter $\mathbf{a}$, being analogous to the physical radius L, implies that above large area fires that parameter would be large. An analytical numerical study of the model equations accompanied by a detailed asymptotic study of the limit $\mathbf{a} \to \infty$ was then performed. Uniformly valid second order semi-analytical approximations were obtained are were shown to provide an excellent agreement when compared with numerical solutions for values of $\mathbf{a}$[1] ranging from 10^2 to 10^6.

Since the vertical part of the flow can adequately be described by classic plume theory, the missing puzzle for a 'complete model' for the description of the buoyant flow above large area fires, is the one that describes the transition of the predominantly horizontal flow (horizontal plume model) into the predominantly vertical flow (classic plume model). Recall that the horizontal plume model ceases to be valid as the centre of the area is approached. Thus far discussions concerning the transition have been carefully avoided. A large part of the research was devoted to finding a way of modelling the transition so that a 'universal' plume model could be obtained. Efforts were however fruitless, and are not described here because they would elongate this thesis unnecessarily without contributing anything new. All approaches were based on the assumption that a smooth transition from horizontal to vertical takes place. This can be thought as, horizontal streams that move inwardly and towards the centre of disc being 'gently' decelerated and pushed away, since a stagnation point must be located at the centre of the plate.

For laminar natural convection above horizontal surfaces, the separation is due to mechanisms of gravitational instability or the dominance of buoyancy force over the pressure gradient that initiated the driving of the flow. Within the horizontal plume model equations, the flow is driven by the radial pressure gradient $1/2 \times g[(\rho_\mathrm{e} - \rho)h^2]_r$ and so that the velocity is accelerating towards infinity as $r \to 0$, since there is nothing to stop the flow. This is not physical and that is why the validity of the model ceases as the centre of the disk is approached. An additional dynamical pressure component within the hot plume gases must act, so as to stop the horizontal flow and deflect it upwards.

Another way of thinking of this intermediate region is by abandoning the idea that a 'gentle' smooth transition takes place and think of the deflection process as involving an abrupt pressure jump. This is a crude approach, but it provides relevant scales in

---

[1] It must be noted that excellent agreement was also demonstrated when $\mathbf{a}$ is of $\mathcal{O}(10^7)$, $\mathcal{O}(10^8)$ and should be expected for all larger values

this region. It can be considered that the pressure in the hot plume gases increases abruptly above its local hydrostatic level by a uniform amount throughout a disc of radius r_c (taken to be significantly smaller than L) and height H_c. The height H_c should be the height of the plume at $r = r_c$, where the mean density is $\rho_c \approx \rho_0$ and the incoming radial velocity is $u = u_c$. Within the disc the density can be taken to remain constant with the pressure jump being sufficient to almost stop the horizontal flow while causing an acceleration of a vertical flow out of the top of the disc. If the pressure jump and density are the same at the top and at the sides of the disc then the mean vertical velocity w_c, with which the fluid leaves the top of the disc should have the same value as u_c. Conservation of mass requires then that

$$2\pi r_c H_c \rho_c u_c = \pi r_c^2 \rho_c w_c \quad \text{so that} \quad r_c = 2H_c. \tag{7.1}$$

That is that the transition from horizontal to vertical flow can be expected to take place at a radius r that is twice the height h.

Unfortunately due to numerous technical difficulties arising in the conduct of a ‘hot plate’ experiment, and the resulting uncertainty in the data, we have not been able to reach to any conclusions with confidence. Nevertheless methodologies and techniques developed here should be applicable to the a new experiment that is being initiated at the time that this work is being written up. PIV analysis of the data indicates that the broad structure of the flow proposed theoretically in this thesis is appropriate. Once the data of the new experiment are available, the numerous assumptions included in the theoretical horizontal plume model will need to be revisited, starting with the top hat formulation as well as the form of the entrainment hypothesis.

The remainder of this thesis was devoted to the study of two classic problems, the first order boundary layer analysis of laminar natural convection above a uniformly heated horizontal and slightly inclined semi-infinite plate, and the first order laminar boundary layer flow above a uniformly heated horizontal circular disc of radius a. In both cases variable property effects were introduced in the formulation through the nondimensional parameter λ_{T}, with $\lambda_{\mathrm{T}} = 0$ corresponding to the Boussinesq approximation. For both problems a fourth order series approximation valid at the edge of the semi-infinite and the edge of the circular plate were obtained. The effect of the parameter λ_{T} was extensively studied; the missing initial condition for all orders and for values of $\lambda_{\mathrm{T}} = 0, 0.1 \ldots 4$, obtained via shooting techniques, are given in Appendix A and Appendix B. In addition for the circular disc, the effect of Pr when the Boussinesq approximation is adopted was studied for all orders.

Analytically for the semi-infinite plate, effects of slight inclination to horizontal were introduced in the formulation through a nondimensional parameter σ. A positive or a negative value of σ corresponding to a positive or negative inclination respectively. For the case of negative inclination it is known that separation occurs in the boundary layer flow, accompanied by flow reversal. That is because the buoyancy forces are opposing the flow. An analytical study was carried with respect to the effect of variable property effects on the position of the separation point in order to build upon what is known when the Boussinesq approximation is used. A best fit to the computations, obtained by least squares, suggests that the position of the separation point x_s varies with λ_{T} as shown below. It must be noted that this representation is valid for Prandtl number $\mathrm{Pr} = 0.72$, and inclination parameter $\sigma = -1$, while x_{s_0} is the position of the separation point obtained by Jones [38] for the Boussinesq case.

$$x_s = x_{s_0} + A\,\lambda_{\mathrm{T}}^{B}, \quad \text{where} \quad A = 7.2240, \quad B = 1.2649 \quad \text{and} \quad x_{s_0} = 3.705. \tag{7.2}$$

In a similar manner, by making the Boussinesq approximation (i.e. $\lambda_{\mathrm{T}} = 0$) and fixing $\sigma = -1$, the effect of Prandtl number on the position of the separation point was studied. It was found that a function of the form

$$x_s = A + B_1 e^{-C_1 \mathrm{Pr}} + B_2 e^{-C_2 \mathrm{Pr}}, \tag{7.3a}$$

where

$$A = 1.5693, \quad B_1 = 3.8734, \quad C_1 = 0.7346, \quad B_2 = 11.7838, \quad C_2 = 10.7508. \tag{7.3b}$$

is suitable for representing $x_s = f(\mathrm{Pr})$. In addition by fixing $\lambda_{\mathrm{T}} = 0$ and $\mathrm{Pr} = 0.72$ the effect of the inclination parameter was studied, and the following was obtained. At this point it should be mentioned that the points of separation obtained here with varying Prandtl number are different from those published in [69]. This is because

σ	-1.2	-1.1	-1	- 0.9	-0.8
x_s	2.7216	3.1550	3.705	4.4003	5.3526

Table 7.1: Position of the separation point x_s, for different values of σ while $\lambda_{\mathrm{T}} = 0$ and $\mathrm{Pr} = 0.72$.

a continuous transformation was used in [69] for the boundary layer equations which results in a different set of nonsimilar equations. On a theoretical basis when the inclination is negative, separation of the boundary layer takes place which implies that no similarity regime is approached as $x \to \infty$, and therefore a continuous transformation might not be suitable choice. Consequently it seems reasonable to expect that the results obtained here should be trustworthy.

When the inclination was set to positive ($\sigma > 0$), variable property effects turned out to have a milder effect on the flow. Finally an investigation concerning the indirect pressure gradient $-\partial\hat{\Pi}/\partial x$ term, and its significance when compared with the tangential component of the buoyancy force was carried out and an order of magnitude study was performed. It was found that the pressure gradient term at around $\xi = 8$ is of order $\mathcal{O}(10^{-2})$ and the tangential buoyancy term fully dominates the driving of the flow.

Directing attention towards the steady laminar boundary layer flow above an isothermal circular disc, an extensive numerical study was performed. A finite difference scheme was developed for the solution of the PIDEs using the Keller-Box method. In addition we defined a ‘compressed’ Dorodnitsyn-Howarth transformation for the Boundary layer equations and the numerical solution was obtained via FEM using COMSOL Multiphysics 3.5a.

Further work is required in terms of boundary layer analysis in the region close to the centre of the circular plate where singular behaviour is exhibited, while the work of [56],[57] can be used as a guide. In addition a parametric study with a varying Grashof number for the full Navier Stokes equations needs to be performed and the form of the relationship $\mathrm{Nu} = \mathrm{f}(\mathrm{Gr})$ need to be investigated. Having established the numerical tools for the analysis of this flow it is believed that a new study for both problems can be performed, but this time the boundary condition imposed on the plate will be that of constant heat flux q rather than constant temperature T_w, while variable property effects will also be retained in the formulation.

Bibliography

[1] J.A.D. Ackroyd. Stress work effects in laminar flat-plate natural convection. *Journal of Fluid Mechanics*, 62(04):677–695, 1974.

[2] J.A.D. Ackroyd. Laminar natural convection boundary layers on near-horizontal plates. *Proceedings of the Royal Society of London. Series A, Mathematical and Physical Sciences*, 352(1669):249–274, 1976.

[3] G.K. Batchelor. Heat convection and buoyancy effects in fluids. *Quarterly Journal of the Royal Meteorological Society*, 80(345), 1954.

[4] G.K. Batchelor. *An Introduction to Fluid Dynamics.* Cambridge University Press, 1967.

[5] B.Cabral and L.C. Leedom. Imaging vector fields using line integral convolution. In *Proceedings of the 20th annual conference on Computer graphics and interactive techniques*, pages 263–270. ACM, 1993.

[6] C.M. Bender and S.A. Orszag. *Advanced mathematical methods for scientists and engineers: Asymptotic methods and perturbation theory*, volume 1. Springer Verlag, 1978.

[7] T.S. Van Den Bremer and G.R. Hunt. Universal solutions for boussinesq and non-boussinesq plumes. *Journal of Fluid Mechanics*, 644:165, 2010.

[8] C.P. Brescianini and M.A. Delichatsios. New evaluation of the k-epsilon turbulence model for free buoyant plumes. *Numerical Heat Transfer Part A: Applications*, 43(7):731–751, 2003.

[9] G.A. Briggs. *Plume rise.* US Atomic energy commission, 1969.

[10] G.A. Briggs. *Plume rise predictions.* American Meteorological Society, 1975.

[11] R.L. Burden and J.D. Faires. *Numerical Analysis. 8th.* Thomson Brooks/Cole, 2001.

[12] T. Cebeci and P. Bradshaw. *Physical and Computational Aspects of Convective Heat Transfer.* Springer Verlag, 1984.

[13] T. Cebeci and J. Cousteix. *Modeling and Computation of Boundary-Layer Flows: Laminar, Turbulent and Transitional Boundary Layers in Incompressible and Compressible Flows.* Springer, 2005.

[14] T. Cebeci, H.B. Keller, and P.G. Williams. Separating boundary-layer flow calculations. *Journal of Computational Physics*, 31(3):363–378, 1979.

[15] T. Cebeci, J.P. Shao, F. Kafyeke, and E. Laurendeau. *Computational fluid dynamics for engineers.* Springer, 2005.

[16] T. Cebeci and A.M.O Smith. *Analysis of turbulent boundary layers*, volume 15. New York, Academic Press, 1974.

[17] C.J. Chen and W. Rodi. *Vertical turbulent buoyant jets: a review of experimental data*, volume 4. Pergamon, 1980.

[18] J. Cousteix and J. Mauss. *Asymptotic analysis and boundary layers.* Springer Verlag, 2007.

[19] M. Dehghan. Efficient techniques for the second-order parabolic equation subject to nonlocal specifications. *Applied Numerical Mathematics*, 52(1):39–62, 2005.

[20] M.A. Delichatsios. Strong turbulent buoyant plumes. I. Similarity. *Combustion Science and Technology*, 24(5):191–195, 1980.

[21] P.A. Dellenback, J. Macharivilakathu, and S.R. Pierce. Contrast-enhancement techniques for particle-image velocimetry. *Applied Optics*, 39(32):5978–5990, 2000.

[22] M. Van Dyke. *Perturbation methods in fluid mechanics*, volume 9. Parabolic Press Stanford, California, 1975.

[23] G. Fairweather and R.D. Saylor. The reformulation and numerical solution of certain nonclassical initial-boundary value problems. *SIAM Journal on Scientific and Statistical Computing*, 12(1):127–144, 1991.

[24] T.K. Fanneløp and D.M. Webber. On buoyant plumes rising from area sources in a calm environment. *Journal of Fluid Mechanics*, 497:319–334, 2003.

[25] B. Gebhart, Y. Jaluria, R.L. Mahajan, and B. Sammakia. *Buoyancy-induced flows and transport.* Hemisphere Publishing Corporation, 1988.

[26] W.K. George. Governing equations, experiments, and the experimentalist. *Experimental Thermal and Fluid Science*, 3(6):557–566, 1990.

[27] W.K. George, R.L. Alpert, and F. Tamanini. Turbulence measurements in an axisymmetric buoyant plume. *International Journal of Heat and Mass Transfer*, 20(11):1145–1154, 1977.

[28] W.N. Gill, D.W. Zeh, and E.D. Casal. Free convection on a horizontal plate. *Zeitschrift für Angewandte Mathematik und Physik (ZAMP)*, 16:539–541, 1965.

[29] R.J. Goldstein, E.M. Sparrow, and D.C. Jones. Natural convection mass transfer adjacent to horizontal plates. *International Journal of Heat and Mass Transfer*, 16(5):1025–1035, 1973.

[30] J.O. Hinze. *Turbulence.* McGraw-Hill, New York, 1975.

[31] L. Howarth. Concerning the effect of compressibility on laminar boundary layers and their separation. *Proceedings of the Royal Society of London. Series A, Mathematical and Physical Sciences*, 194(1036), 1948.

[32] G.R. Hunt and T.S. Van Den Bremer. Classical plume theory: 1937–2010 and beyond. *IMA Journal of Applied Mathematics*, 76(3):424–448, 2011.

[33] G.R. Hunt and N.G. Kaye. Virtual origin correction for lazy turbulent plumes. *Journal of Fluid Mechanics*, 435:377–396, 2001.

[34] R. Hunt and G. Wilks. Continuous transformation computation of boundary layer equations between similarity regimes. *Journal of Computational Physics*, 40(2):478 – 490, 1981.

[35] R.B. Husar and E.M. Sparrow. Patterns of free convection flow adjacent to horizontal heated surfaces. *International Journal of Heat and Mass Transfer*, 11(7):1206–1208, 1968.

[36] Y. Jaluria. *Natural convection: heat and mass transfer*. Pergamon Press, 1980.

[37] J.Grue, P.L.F. Liu, and G.K. Pedersen. *PIV and water waves*, volume 9. World Scientific Publishing Company Incorporated, 2004.

[38] D.R. Jones. Free convection from a semi-infinite flat plate inclined at a small angle to the horizontal. *The Quarterly Journal of Mechanics and Applied Mathematics*, 26(1):77, 1973.

[39] E. Kaminski, S. Tait, and G. Carazzo. Turbulent entrainment in jets with arbitrary buoyancy. *Journal of Fluid Mechanics*, 526:361–376, 2005.

[40] N.B. Kaye. Turbulent plumes in stratified environments: A review of recent work. *Atmosphere-ocean*, 46(4):433–441, 2008.

[41] H.B. Keller. Numerical methods for two-point boundary-value problems. 1968.

[42] H.B. Keller. A new difference scheme for parabolic problems. In *Numerical Solution of Partial Differential Equations, II (SYNSPADE 1970) (Proc. Sympos., Univ. of Maryland, College Park, Md., 1970)*, pages 327–350. Academic Press, 1971.

[43] H.B. Keller. Numerical methods in boundary-layer theory. *Annual Review of Fluid Mechanics*, 10:417–433, 1978.

[44] H.B. Keller and T. Cebeci. Accurate numerical methods for boundary layer flows i. two dimensional laminar flows. In *Proceedings of the second international conference on numerical methods in fluid dynamics*, pages 92–100. Springer, 1971.

[45] H.B. Keller and T. Cebeci. Accurate numerical methods for boundary layer flows ii. two dimensional turbulent flows. *AIAA Journal*, 10(9), 1972.

[46] J. Kevorkian and J.D. Cole. *Multiple scale and singular perturbation methods*, volume 114. Springer Verlag, 1996.

[47] K. Kitamura, X.A. Chen, and F. Kimura. Turbulent transition mechanisms of natural convection over upward-facing horizontal plates. *Transactions of the Japan Society of Mechanical Engineers. B*, 65(640):4033–4040, 1999.

[48] K. Kitamura and F. Kimura. Heat transfer and fluid flow of natural convection adjacent to upward-facing horizontal plates. *International journal of heat and mass transfer*, 38(17):3149–3159, 1995.

[49] K. Kitamura and F. Kimura. Fluid flow and heat transfer of natural convection over upward-facing, horizontal heated circular disks. *Heat TransferAsian Research*, 37(6):339–351, 2008.

[50] N.E. Kotsovinos. Temperature measurements in a turbulent round plume. *International journal of heat and mass transfer*, 28(4):771–777, 1985.

[51] L.D Landau and E.M Lifshitz. *Fluid Mechanics 2nd edition, Course of Theoretical Physics Volume 6.* Pergamon Press, 1987.

[52] J.H.W. Lee and V. H. Chu. *Turbulent jets and plumes: a Lagrangian approach.* Springer, 2003.

[53] M. Lesieur. *Turbulence in fluids.* Springer, 2008.

[54] K. Van Maele and B. Merci. Application of two buoyancy-modified k-[epsilon] turbulence models to different types of buoyant plumes. *Fire Safety Journal*, 41(2):122–138, 2006.

[55] D. Meade, B. Haran, and R. White. The shooting technique for the solution of two point boundary value problems. *Maple Technical Newsletter*, 3(1), 1996.

[56] J.H. Merkin. Free convection above a heated horizontal circular disk. *Zeitschrift für Angewandte Mathematik und Physik (ZAMP)*, 34(5):596–608, 1983.

[57] J.H. Merkin. Free convection above a uniformly heated horizontal circular disk. *International journal of heat and mass transfer*, 28(6):1157–1163, 1985.

[58] G. Michaux and O. Vauquelin. Solutions for turbulent buoyant plumes rising from circular sources. *Physics of Fluids*, 20:066601, 2008.

[59] B.R. Morton. Forced plumes. *Journal of Fluid Mechanics*, 5, 1959.

[60] B.R. Morton. Modeling fire plumes. In *Tenth Symposium (International) on Combustion*, pages 973–982, 1965.

[61] B.R. Morton. The choice of conservation equations for plume models. *Journal of Geophysical Research*, 76(30):7409–7416, 1971.

[62] B.R. Morton and J.H. Middleton. Scale diagrams for forced plumes. *Journal of Fluid Mechanics*, 58, 1973.

[63] B.R. Morton, G.I. Taylor, and J.S. Turner. Turbulent gravitational convection from maintained and instantaneous sources. *Proceedings of the Royal Society of London. Series A, Mathematical and Physical Sciences*, pages 1–23, 1956.

[64] T.Y. Na. *Computational methods in engineering boundary value problems(Book).* New York, Academic Press, 1979.

[65] S. Nam and R.G. Bill. Numerical simulation of thermal plumes. *Fire Safety Journal*, 21(3):231–256, 1993.

[66] A.H. Nayfeh. *Introduction to perturbation techniques.* Wiley-VCH, 2011.

[67] L. Pera and B. Gebhart. Natural convection boundary layer flow over horizontal and slightly inclined surfaces. *International Journal of Heat and Mass Transfer*, 16(6):1131 – 1146, 1973.

[68] A.B. Pippard. *Elements of Classical Thermodynamics: For Advanced Students of Physics.* Cambridge University Press, 1957.

[69] I.I. Pop and D.B. Ingham. *Convective heat transfer: mathematical and computational modelling of viscous fluids and porous media.* Pergamon Press, 2001.

[70] C.H.B. Priestley and F.K. Ball. Continuous convection from an isolated source of heat. *Quarterly Journal of the Royal Meteorological Society*, 81(348):144–157, 1955.

[71] M. Raffel, C.E. Willert, and J. Kompenhans. *Particle image velocimetry: a practical guide.* Springer Verlag, 1998.

[72] F.P. Ricou and B.P. Spalding. Measurements of entrainment by axial symmetric turbulent jets. *J. Fluid Mechanics*, 11:21–32, 1961.

[73] G.G. Rooney and P.F. Linden. Similarity considerations for non-Boussinesq plumes in an unstratified environment. *Journal of Fluid Mechanics Digital Archive*, 318:237–250, 2006.

[74] Z. Rotem and L. Claassen. Natural convection above unconfined horizontal surfaces. *Journal of Fluid Mechanics*, 39(01):173–192, 1969.

[75] G.I. Roth and J. Katz. Five techniques for increasing the speed and accuracy of piv interrogation. *Measurement Science and Technology*, 12(3):238, 2001.

[76] H. Rouse, C.S. Yih, and H.W. Humphreys. Gravitational convection from a boundary source. *Tellus*, 4(3):201–210, 1952.

[77] A.I. Ruban. *Lecture Notes in Perturbation Techniques in Fluid Mechanics.* University of Manchester, 2006.

[78] P.L. Sachdev. *Nonlinear Ordinary Differential Equations and Their Applications.* Monographs and Textbooks in Pure and Applied Mathematics. MARCEL DEKKER, INC, 1991.

[79] J. Schetz. *Boundary Layer Analysis.* Englewood Cliffs, NJ, Prentice Hall, 1993.

[80] H. Schlichting and K. Gersten. *Boundary Layer Theory.* Springer, 2000.

[81] W. Schmidt. Turbulent propagation of a stream of heated air. *Z Angew Math Mech*, 21:265–351, 1941.

[82] A. Shabbir and W.K. George. Experiments on a round turbulent buoyant plume. *Journal of Fluid Mechanics*, 275:1–32, 1994.

[83] L.F. Shampine, M.W. Reichelt, and J.A. Kierzenka. Solving index-i daes in matlab and simulink. *Siam Review*, pages 538–552, 1999.

[84] U. Shavit, R.J. Lowe, and J.V. Steinbuck. Intensity capping: A simple method to improve cross-correlation piv results. *Experiments in fluids*, 42(2):225–240, 2007.

[85] J.J. Shu and G. Wilks. An accurate numerical method for systems of differentio-integral equations associated with multiphase flow. *Computers & fluids*, 24(6):625–652, 1995.

[86] S. Siddiqa and M.A. Hossain. Conduction–convection–radiation effects on the flow of optically dense gray fluid over a horizontal circular disk. *Journal of Engineering Physics and Thermophysics*, pages 1–10, 2012.

[87] P.R. Slawson and G.T. Csanady. On the mean path of buoyant, bent-over chimney plumes. *Journal of Fluid Mechanics*, 28(2):311–322, 1967.

[88] J.H. Spurk. *Fluid Mechanics.* Springer Verlag, 1997.

[89] K. Stewartson. On the free convection from a horizontal plate. *(ZAMP)*, 9:276–282, 1958.

[90] K. Stewartson. *The Theory of Laminar Boundary Layers in Compressible Fluids.* Clarendon Press, Oxford Mathematical Monographs, 1964.

[91] J. K. Sveen. An introduction to matpiv v.1.6.1. Eprint no. 2, **ISSN** 0809-4403, Dept. of Mathematics, University of Oslo, 2004. http://www.math.uio.no/˜jks/matpiv.

[92] G.I. Taylor. Dynamics of a mass of hot gas rising in air. 1945.

[93] H. Tennekes and J.L. Lumley. *A First Course in Turbulence.* MIT Press, 1972.

[94] W. Thielicke and E.J. Stamhuis. Pivlab. Online.

[95] D.J. Tritton. *Physical fluid dynamics.* The Modern University Physics Series. Van Nostrand Reinhold Company L.t.d, second edition, 1977.

[96] J.S. Turner. Buoyant plumes and thermals. *Annual Review of Fluid Mechanics*, 1(1):29–44, 1969.

[97] J.S. Turner. *Buoyancy effects in fluids.* Cambridge University Press, 1979.

[98] F.M. White. *Viscous fluid flow, Third Edition.* McGraw-Hill International Edition, 2006.

[99] D.C. Wilcox. *Turbulence Modeling for CFD.* DCW Industries, Inc, 1998.

[100] J. Worthy, V. Sanderson, and P. Rubini. Comparison of modified k-? turbulence models for buoyant plumes. *Numerical Heat Transfer: Part B: Fundamentals*, 39(2):151–165, 2001.

[101] M. Zakerullah and J.A.D. Ackroyd. Laminar natural convection boundary layers on horizontal circular discs. *Zeitschrift für Angewandte Mathematik und Physik (ZAMP)*, 30(3):427–435, 1979.

[102] Y.B. Zeldovich. The asymptotic laws of freely-ascending convective flows. *Zhur. Eksper. Teor. Fiz*, 7:1463–1465, 1937.

Appendix A

Computed Initial Values For the Horizontal Circular Plate

λ_{T}	$G_0(0)$	$\Theta_0'(0)$	$f_0''(0)$
0	-1.73493	-0.35726	0.97795
0.1	-1.71517	-0.36171	1.02505
0.2	-1.69674	-0.36595	1.07082
0.3	-1.67946	-0.36999	1.11538
0.4	-1.66322	-0.37387	1.15884
0.5	-1.64789	-0.37758	1.20129
0.6	-1.63340	-0.38115	1.24280
0.7	-1.61966	-0.38459	1.28343
0.8	-1.60659	-0.38791	1.32326
0.9	-1.59415	-0.39112	1.36233
1	-1.58227	-0.39422	1.40068
1.1	-1.57091	-0.39723	1.43837
1.2	-1.56003	-0.40015	1.47543
1.3	-1.54960	-0.40299	1.51190
1.4	-1.53958	-0.40574	1.54780
1.5	-1.52994	-0.40843	1.58316
1.6	-1.52065	-0.41104	1.61802
1.7	-1.51170	-0.41359	1.65240
1.8	-1.50306	-0.41607	1.68631
1.9	-1.49471	-0.41850	1.71979
2	-1.48663	-0.42087	1.75284
2.1	-1.47881	-0.42319	1.78549
2.2	-1.47123	-0.42546	1.81775
2.3	-1.46388	-0.42768	1.84964
2.4	-1.45675	-0.42986	1.88118
2.5	-1.44983	-0.43199	1.91237
2.6	-1.44310	-0.43408	1.94323
2.7	-1.43655	-0.43613	1.97377
2.8	-1.43018	-0.43815	2.00401
2.9	-1.42397	-0.44012	2.03394
3	-1.41793	-0.44206	2.06359
3.1	-1.41204	-0.44397	2.09296
3.2	-1.40629	-0.44585	2.12206
3.3	-1.40068	-0.44769	2.15090
3.4	-1.39520	-0.44950	2.17949
3.5	-1.38985	-0.45129	2.20783
3.6	-1.38462	-0.45305	2.23593
3.7	-1.37951	-0.45478	2.26381
3.8	-1.37451	-0.45648	2.29145
3.9	-1.36961	-0.45816	2.31888
4	-1.36482	-0.45981	2.34610

Table A.1: Computed initial values to leading order for circular and semi-infinite plate[†]

[†] It should be recalled that to leading order the similarity equations describing the flow above the semi-infinite plate were recovered. Therefore the computed initial values listed above are also valid for the semi-infinite plate.

λ_{T}	$G_1(0)$	$\Theta_1'(0)$	$f_1''(0)$
0	-0.25443	0.05009	-0.60402
0.1	-0.25100	0.05053	-0.63108
0.2	-0.24783	0.05096	-0.65744
0.3	-0.24489	0.05138	-0.68314
0.4	-0.24216	0.05179	-0.70824
0.5	-0.23961	0.05219	-0.73279
0.6	-0.23721	0.05258	-0.75683
0.7	-0.23496	0.05295	-0.78039
0.8	-0.23283	0.05332	-0.80349
0.9	-0.23082	0.05368	-0.82618
1	-0.22890	0.05403	-0.84847
1.1	-0.22708	0.05437	-0.87039
1.2	-0.22535	0.05470	-0.89196
1.3	-0.22369	0.05502	-0.91319
1.4	-0.22211	0.05534	-0.93410
1.5	-0.22059	0.05565	-0.95472
1.6	-0.21913	0.05596	-0.97505
1.7	-0.21774	0.05625	-0.99510
1.8	-0.21639	0.05655	-1.01490
1.9	-0.21509	0.05683	-1.03444
2	-0.21384	0.05711	-1.05375
2.1	-0.21263	0.05739	-1.07282
2.2	-0.21146	0.05766	-1.09168
2.3	-0.21033	0.05792	-1.11032
2.4	-0.20924	0.05818	-1.12876
2.5	-0.20818	0.05844	-1.14701
2.6	-0.20715	0.05869	-1.16506
2.7	-0.20615	0.05894	-1.18293
2.8	-0.20518	0.05918	-1.20063
2.9	-0.20424	0.05942	-1.21816
3	-0.20332	0.05966	-1.23552
3.1	-0.20243	0.05989	-1.25272
3.2	-0.20156	0.06012	-1.26977
3.3	-0.20071	0.06034	-1.28666
3.4	-0.19988	0.06057	-1.30341
3.5	-0.19908	0.06078	-1.32003
3.6	-0.19829	0.06100	-1.33650
3.7	-0.19752	0.06121	-1.35284
3.8	-0.19677	0.06142	-1.36905
3.9	-0.19604	0.06163	-1.38513
4	-0.19532	0.06183	-1.40110

Table A.2: Computed initial values to second order.

λ_{T}	$G_2(0)$	$\Theta_2'(0)$	$f_2''(0)$
0	-0.22642	0.03285	0.03629
0.1	-0.22319	0.03304	0.03936
0.2	-0.22022	0.03324	0.04231
0.3	-0.21749	0.03343	0.04515
0.4	-0.21495	0.03363	0.04789
0.5	-0.21259	0.03382	0.05055
0.6	-0.21038	0.03402	0.05312
0.7	-0.20830	0.03421	0.05563
0.8	-0.20635	0.03440	0.05807
0.9	-0.20450	0.03458	0.06045
1	-0.20275	0.03476	0.06278
1.1	-0.20109	0.03495	0.06505
1.2	-0.19951	0.03512	0.06728
1.3	-0.19800	0.03530	0.06946
1.4	-0.19656	0.03547	0.07160
1.5	-0.19519	0.03564	0.07371
1.6	-0.19387	0.03581	0.07577
1.7	-0.19260	0.03597	0.07781
1.8	-0.19138	0.03614	0.07981
1.9	-0.19021	0.03630	0.08178
2	-0.18908	0.03645	0.08372
2.1	-0.18799	0.03661	0.08563
2.2	-0.18693	0.03676	0.08751
2.3	-0.18591	0.03691	0.08937
2.4	-0.18493	0.03706	0.09121
2.5	-0.18397	0.03720	0.09302
2.6	-0.18305	0.03735	0.09481
2.7	-0.18215	0.03749	0.09658
2.8	-0.18128	0.03763	0.09833
2.9	-0.18043	0.03777	0.10006
3.0	-0.17961	0.03790	0.10177
3.1	-0.17881	0.03804	0.10346
3.2	-0.17803	0.03817	0.10514
3.3	-0.17727	0.03830	0.10680
3.4	-0.17653	0.03843	0.10844
3.5	-0.17581	0.03856	0.11006
3.6	-0.17510	0.03868	0.11167
3.7	-0.17441	0.03881	0.11327
3.8	-0.17374	0.03893	0.11485
3.9	-0.17309	0.03905	0.11642
4	-0.17244	0.03917	0.11797

Table A.3: Computed initial values to third order.

λ_{T}	$G_3(0)$	$\Theta_3'(0)$	$f_3''(0)$
0	-0.21199	0.02115	0.03282
0.1	-0.20897	0.02120	0.03557
0.2	-0.20621	0.02125	0.03823
0.3	-0.20367	0.02132	0.04079
0.4	-0.20131	0.02139	0.04326
0.5	-0.19912	0.02146	0.04567
0.6	-0.19707	0.02154	0.04801
0.7	-0.19514	0.02162	0.05029
0.8	-0.19333	0.02170	0.05251
0.9	-0.19161	0.02178	0.05468
1	-0.18999	0.02186	0.05681
1.1	-0.18845	0.02195	0.05889
1.2	-0.18698	0.02203	0.06093
1.3	-0.18559	0.02211	0.06293
1.4	-0.18425	0.02220	0.06489
1.5	-0.18297	0.02228	0.06682
1.6	-0.18175	0.02237	0.06871
1.7	-0.18057	0.02245	0.07058
1.8	-0.17944	0.02253	0.07241
1.9	-0.17835	0.02261	0.07422
2	-0.17730	0.02269	0.07600
2.1	-0.17629	0.02277	0.07776
2.2	-0.17531	0.02285	0.07949
2.3	-0.17436	0.02293	0.08120
2.4	-0.17345	0.02301	0.08289
2.5	-0.17256	0.02309	0.08456
2.6	-0.17170	0.02316	0.08620
2.7	-0.17086	0.02324	0.08783
2.8	-0.17005	0.02331	0.08944
2.9	-0.16927	0.02339	0.09103
3	-0.16850	0.02346	0.09260
3.1	-0.16776	0.02353	0.09416
3.2	-0.16703	0.02361	0.09570
3.3	-0.16632	0.02368	0.09723
3.4	-0.16563	0.02375	0.09874
3.5	-0.16496	0.02382	0.10023
3.6	-0.16431	0.02389	0.10171
3.7	-0.16367	0.02396	0.10318
3.8	-0.16304	0.02402	0.10464
3.9	-0.16243	0.02409	0.10608
4	-0.16183	0.02416	0.10751

Table A.4: Computed initial values to fourth order.

Appendix B

Computed Initial Values for the Semi-Infinite Plate

To leading order the computed initial values for the semi-infinite plate (i.e. $G_0(0)$, $\Theta_0'(0)$ and $f_0''(0)$) are the same as those given in **Appendix A** in Table A.1.

λ_{T}	$G_1(0)$	$\Theta_1'(0)$	$f_1''(0)$
0	0.23574	-0.05563	0.51822
0.1	0.22145	-0.05325	0.50676
0.2	0.20885	-0.05113	0.49642
0.3	0.19764	-0.04921	0.48702
0.4	0.18760	-0.04747	0.47843
0.5	0.17855	-0.04589	0.47053
0.6	0.17036	-0.04444	0.46324
0.7	0.16290	-0.04310	0.45647
0.8	0.15608	-0.04187	0.45018
0.9	0.14982	-0.04072	0.44430
1	0.14405	-0.03966	0.43878
1.1	0.13872	-0.03866	0.43360
1.2	0.13378	-0.03773	0.42872
1.3	0.12918	-0.03686	0.42411
1.4	0.12489	-0.03604	0.41975
1.5	0.12088	-0.03526	0.41561
1.6	0.11712	-0.03453	0.41167
1.7	0.11360	-0.03384	0.40792
1.8	0.11028	-0.03318	0.40435
1.9	0.10716	-0.03256	0.40093
2	0.10420	-0.03196	0.39766
2.1	0.10141	-0.03140	0.39453
2.2	0.09877	-0.03086	0.39153
2.3	0.09626	-0.03034	0.38864
2.4	0.09388	-0.02985	0.38587
2.5	0.09161	-0.02937	0.38320
2.6	0.08945	-0.02892	0.38062
2.7	0.08740	-0.02848	0.37814
2.8	0.08543	-0.02806	0.37574
2.9	0.08355	-0.02766	0.37343
3	0.08176	-0.02727	0.37119
3.1	0.08004	-0.02690	0.36902
3.2	0.07839	-0.02654	0.36691
3.3	0.07681	-0.02619	0.36488
3.4	0.07529	-0.02586	0.36290
3.5	0.07383	-0.02553	0.36098
3.6	0.07243	-0.02522	0.35912
3.7	0.07108	-0.02492	0.35730
3.8	0.06978	-0.02462	0.35554
3.9	0.06853	-0.02434	0.35383
4	0.06732	-0.02406	0.35216

Table B.1: Computed initial values to second order.

λ_{T}	$G_2(0)$	$\Theta_2'(0)$	$f_2''(0)$
0	-0.04618	0.00529	0.01046
0.1	-0.04068	0.00464	0.01118
0.2	-0.03614	0.00411	0.01166
0.3	-0.03235	0.00366	0.01197
0.4	-0.02915	0.00329	0.01215
0.5	-0.02642	0.00297	0.01223
0.6	-0.02408	0.00270	0.01225
0.7	-0.02205	0.00246	0.01222
0.8	-0.02027	0.00226	0.01215
0.9	-0.01871	0.00208	0.01205
1	-0.01733	0.00192	0.01193
1.1	-0.01611	0.00178	0.01180
1.2	-0.01502	0.00166	0.01166
1.3	-0.01404	0.00155	0.01150
1.4	-0.01315	0.00145	0.01134
1.5	-0.01235	0.00136	0.01118
1.6	-0.01163	0.00127	0.01102
1.7	-0.01097	0.00120	0.01086
1.8	-0.01036	0.00113	0.01070
1.9	-0.00981	0.00107	0.01053
2	-0.00930	0.00102	0.01038
2.1	-0.00884	0.00096	0.01022
2.2	-0.00841	0.00092	0.01006
2.3	-0.00801	0.00087	0.00991
2.4	-0.00764	0.00083	0.00976
2.5	-0.00729	0.00079	0.00962
2.6	-0.00697	0.00076	0.00948
2.7	-0.00667	0.00072	0.00934
2.8	-0.00639	0.00069	0.00920
2.9	-0.00613	0.00067	0.00907
3	-0.00589	0.00064	0.00894
3.1	-0.00566	0.00061	0.00881
3.2	-0.00544	0.00059	0.00869
3.3	-0.00524	0.00057	0.00856
3.4	-0.00505	0.00055	0.00845
3.5	-0.00487	0.00053	0.00833
3.6	-0.00470	0.00051	0.00822
3.7	-0.00453	0.00049	0.00811
3.8	-0.00438	0.00047	0.00800
3.9	-0.00424	0.00046	0.00790
4	-0.00410	0.00044	0.00780

Table B.2: Computed initial values to third order.

λ_T	$G_3(0)$	$\Theta_3'(0)$	$f_3''(0)$
0	0.00685	-0.00016	-0.00735
0.1	0.00550	-0.00008	-0.00661
0.2	0.00449	-0.00003	-0.00598
0.3	0.00371	0.00001	-0.00542
0.4	0.00310	0.00003	-0.00494
0.5	0.00262	0.00005	-0.00451
0.6	0.00223	0.00006	-0.00414
0.7	0.00192	0.00007	-0.00381
0.8	0.00166	0.00007	-0.00352
0.9	0.00145	0.00007	-0.00327
1	0.00127	0.00007	-0.00303
1.1	0.00112	0.00007	-0.00283
1.2	0.00100	0.00007	-0.00264
1.3	0.00089	0.00007	-0.00247
1.4	0.00080	0.00007	-0.00232
1.5	0.00072	0.00007	-0.00218
1.6	0.00065	0.00007	-0.00206
1.7	0.00059	0.00006	-0.00194
1.8	0.00053	0.00006	-0.00184
1.9	0.00049	0.00006	-0.00174
2	0.00044	0.00006	-0.00165
2.1	0.00041	0.00006	-0.00157
2.2	0.00038	0.00005	-0.00149
2.3	0.00035	0.00005	-0.00142
2.4	0.00032	0.00005	-0.00136
2.5	0.00030	0.00005	-0.00130
2.6	0.00028	0.00005	-0.00124
2.7	0.00026	0.00005	-0.00119
2.8	0.00024	0.00004	-0.00114
2.9	0.00022	0.00004	-0.00109
3	0.00021	0.00004	-0.00105
3.1	0.00020	0.00004	-0.00101
3.2	0.00018	0.00004	-0.00097
3.3	0.00017	0.00004	-0.00093
3.4	0.00016	0.00004	-0.00090
3.5	0.00015	0.00004	-0.00087
3.6	0.00014	0.00003	-0.00084
3.7	0.00014	0.00003	-0.00081
3.8	0.00013	0.00003	-0.00078
3.9	0.00012	0.00003	-0.00076
4	0.00012	0.00003	-0.00073

Table B.3: Computed initial values to fourth order.